Thermally activated processes and electronic properties of size selected Ag clusters and grown metal islands on C_{60} functionalized surfaces

Dissertation

Zur Erlangung des Doktorgrades der
Naturwissenschaften
vorgelegt von

STEFANIE DUFFE

angefertigt am
Lehrstuhl Experimentelle Physik I
der Fakultät Physik der Technischen Universität Dortmund

März 2009

TABLE OF CONTENTS

1 INTRODUCTION

Most of the intersting phenomena in physics can not be experienced by human senses - like x-rays, radioactivity and in general properties and interactions on the atomic scale. Only the use of detectors or microscopes enables an approach to the microcosm. On the way to solid state physics - the world which can be experienced with human senses - another field of interest is hidden. A group of atoms - named *cluster* - changes the physical properties of a special element depending on the number of atoms per cluster. Generally the term “cluster” denotes a group of the same or similar elements gathered or occurring closely together.

This is a *bottom-up* approach to cluster physics, a large field in solid state physics, which became popular in the 1980s. One purpose of the research was to study the gradual development of collective phenomena which characterize a bulk solid, e.g. the color of a body, its electrical conductivity, its ability to absorb or reflect light, and magnetic phenomena. It was found that collective phenomena break down for very small cluster sizes. The approach from the bulk solid to a cluster is called *top-down* approach.

The study of atomic and molecular clusters also benefits the developing field of nanotechnology. If new materials are to be made out of nanoscale particles, such as nanocatalysts [1,2], nanoscale electronics [3], sensors [4], magnetic recording devices [5] and quantum computers [6, 7], the properties of the nanoscale particles - the clusters - must first be understood.

Within this thesis size selected Ag clusters which were deposited on C_{60} functionalized surfaces were studied concerning their electronic properties, geometrical structure and thermal stability. The Ag cluster/C_{60} system was studied using scanning tunneling microscopy (STM), scanning tunneling spectroscopy (STS) and ultraviolet photoelectron spectroscopy (UPS). This project is a collaboration with the experimental group of BERND VON ISSENDORFF from Universität Freiburg and with MICHAEL MOSELER from Universität Freiburg, the Fraunhofer Institut and the Materials Research Center in Freiburg, respectively, who performs molecular dynamics (MD) simulations and atomistic calculations in addition to the experimental data. The project is part of the priority program SPP 1153: “*Clusters in Contact with Surfaces – Electronic Structure and Magnetism”* of the German Research Foundation (Deutsche Forschungsgemeinschaft – DFG) [8] combining theoretical and experimental investigations of the electronic and magnetic properties of clusters on surfaces. Additionally to size selected Ag clusters Ag and Pb islands grown on a C_{60} functionalized metal surface were investigated concerning their thermal stability and compared both to each other and to size selected Ag clusters.

One aim of our studies is the comparison of size selected clusters on surfaces with size selected clusters in a free beam which are investigated in the group of BERND VON ISSENDORFF with photoemission spectroscopy (Figure1.1).

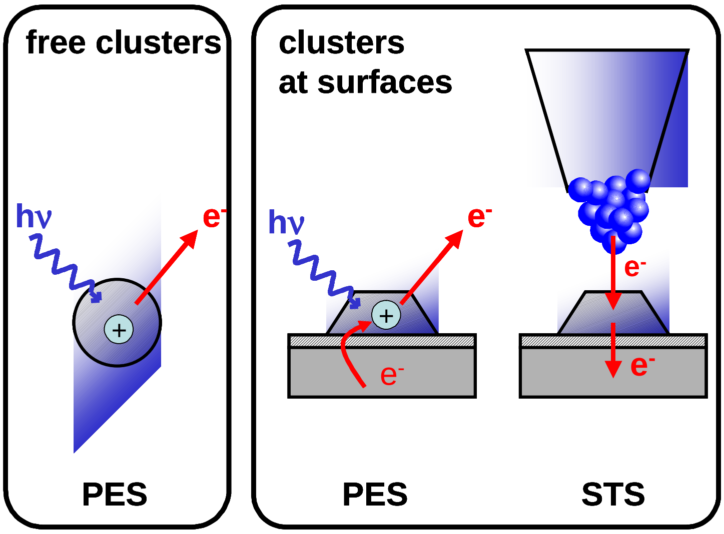

Figure1.1 : The Dortmund-Freiburg project: Photo emission spectroscopy (PES) of free clusters in comparison with PES, STM and STS studies of clusters on surfaces.

Photoemission spectra of free size selected Ag and other metal clusters taken in Freiburg show that every cluster size has a typical characteristic spectrum which identifies the cluster like a fingerprint. The choice of using silver as cluster material for the experiments presented within this thesis enables a direct comparison to the results of free size selected Ag clusters [9].

Geometrically magic clusters with closed atomic shells are well suited for the deposition on surfaces due to their stability and electronic and geometric properties, which were studied in detail by e.g. photoemission spectra. A soft landing of geometrically magic clusters on surfaces is nevertheless necessary to avoid fragmentation. Therefore, suitable substrates for the cluster deposition are C_{60} functionalized surfaces. Due to the van der Waals interaction between C_{60} molecules it works as a buffer layer and supports a soft landing. Additionally C_{60} has a diameter of about 1 nm and thus a large corrugation period which hinders cluster diffusion on the surface. The room temperature stability of C_{60} and the electronic decoupling of clusters from e.g. metal or graphite substrates are optimal conditions for the investigation of clusters on surfaces.

Another ambition of our studies is the utilization of clusters on surfaces for technical applications. In this context particularly the room temperature (RT) stability of supported nanostructures is of paramount importance. For instance metal particles on carbon nanosubstrates are of interest due to their important role in carbon nanotube growth [10] or as catalysts for various chemical reactions [11]. In particular the spectacular catalytic properties of metallic nanoclusters and nanoparticles are a current highlight due to their utility in catalytic converters, e.g. for the oxidation of CO to CO_2, or for the automotive industry (see subsection 2.1.5). Surprisingly the thermal robustness of this class of systems has not been studied systematically, neither by experiments nor by theory. In this thesis the RT stability of a well-defined representative of such metal/carbon nanosystems will be characterized in detail.

This content of this thesis is structured as follows:

Chapter 2 gives a general overview about the properties of free and supported clusters and the properties of fullerenes. The importance of clusters on surfaces for technical applications is emphasized by presenting the important role of clusters for catalysis.

Chapter 3 deals with the experimental setup which consists of a cluster deposition machine directly connected to a surface science facility (Omicron Nanotechnology GmbH) including STM, STS and high-resolution UPS.

In chapter 4 the experimental techniques STM, STS and UPS are described from an experimental and theoretical point of view.

After that, in chapter 5, the sample preparation is explained which includes the preparation of the substrate, the fullerene layer and the size selected clusters or grown metal islands.

The results concerning thermally activated processes and electronic properties of size selected Ag clusters and metal islands are presented in chapter 6. First STM images of C_{58} on HOPG and C_{60} on HOPG are compared which show the different structure and growth mechanism of C_{58} and C_{60}. Then the different orientations of C_{60} molecules on 1 and 2 monolayer (ML) C_{60} on HOPG and on Au(111) are presented. In the following section STM measurements and the thermal stability of size selected clusters and grown metal islands on HOPG or Au(111) surfaces functionalized with C_{60} are discussed. Finally the study of electronic properties of size selected clusters on surfaces with STS measurements and first UPS studies is presented.

Chapter 7 gives a summary about the results which were achieved within this thesis and an outlook on future experiments.

2 CLUSTERS AND FULLERENES

In this chapter the structure and properties of three dimensional clusters, two dimensional islands and fullerenes are introduced. The section on clusters gives a detailed overview as they are the main subject of this thesis.

2.1 Clusters

Cluster physics deals with the interesting transition from single atoms and molecules to bulk-like materials. Due to the fact that single atoms have quantized states but bulk material is defined by a band structure, clusters have - depending on their size - quantized or bulk-like properties. Thus clusters can be subdivided into four categories [12]:

- ***micro clusters*** with 3 to 13 atoms
- ***small clusters*** with 14 to 100 atoms
- ***large clusters*** with 100 to 1000 atoms
- ***micro crystallites*** with more than 1000 atoms

For micro clusters the methods and concepts of molecular physics are applicable and for $N \leq 12$ (N = number of atoms per cluster) all atoms are localized at the cluster surface. The properties of small clusters can not be completely described by molecular physics anymore and there exist a lot of isomers. For the properties of large clusters a gradual transition to solid state physics is visible which becomes more apparent for micro crystallites.

In this thesis the properties of *metallic* clusters or particles are investigated, which are of great interest for cluster physics [13, 14, 15]. Metals can be described by the metallic bonding model. This kind of bonding describes the interaction between the atom core ions and the delocalized conduction electrons, which are not associated with a single atom or with a covalent bond. This means that this sea of electrons is free to move and gives rise to properties such as conductivity.

A model which extends the description of the electronic structure of metallic clusters is the j*ellium model* [16, 17]. The first jellium model for clusters was introduced by CINI in 1975 [18]. It depicts the atomic core ions not as discrete objects but as smeared out charges which form a uniform static positive background. The electrons are assumed to move freely in this positive background which maintains charge neutrality. At zero temperature the system properties are dependent only on the charge density of electrons. In 1984 EKARDT and BECK described a *spherical* jellium model for the calculation of the work function of small particles [19, 20, 21, 22]. The first experimental indication of the validity of the jellium model for clusters was the mass spectrum of sodium clusters which is discussed in section 2.1.2. Although the assumption of delocalized electrons restricts the jellium model in a strict view to the first and second main group of the periodic table of the elements and partly to the first B group the jellium model for clusters describes many experimental observations qualitatively and sometimes even quantitatively. Most of all it leads to an interpretation of clusters with electronic “magic numbers”, which are presented in 2.1.2.

2.1.1 Size selected clusters

As explained in section 2.1, micro clusters or small clusters have quantized states whereas large clusters or micro crystallites are characterized by bulk-like properties. For this reason it is necessary to be able to select clusters by their size. Size selected clusters have an exactly defined number of atoms and thus special tailored electronic and geometric properties. Due to their stability the so called *magic* clusters play an important role in cluster physics and are the focus of the experiments which are presented in this thesis. The following sections introduce the properties of electronically and geometrically magic clusters.

2.1.2 Electronically magic clusters

The first observations of electronically magic clusters were made in 1982 by M. Kappes [23] and in 1984 and 1985 by W. D. Knight [24, 25]. The magic cluster sizes became apparent in mass spectra of small sodium and potassium clusters by peaks with a very high intensity which is plotted versus the cluster mass (see Figure 2.1).

PEDERSON et al. also observed the shell structure which is due to electronically magic clusters for sodium clusters with up to 3000 constituent atoms [26]. The stability of electronically magic clusters results from the high binding energy of the electrons in closed electron shells in a cluster. The pronounced peaks for the clusters Na_2, Na_8, Na_{20}, Na_{40} and Na_{58}… correspond to 2, 8, 20, 40 and 58… electrons per cluster and it takes higher energies to remove or to add an electron. Clusters with an additional atom, i. e. an additional electron, which starts to fill a new shell, are less stable and thus show lower intensities.

Figure 2.2 shows the kinetic energy of the electrons and the effective jellium potential according to the spherical jellium-background model for a Na_{20} cluster [12]. The energy levels represent the cluster shells which can be filled with a total number of maximum 8, 18, 20, 34, 40… electrons. The lettering *s, p, d, f* of the energetic levels stands for the angular quantum number according to atomic physics and the number in brackets represents the number of electrons per level. On the one hand this potential of electrons in a spherical jellium-background can be compared with the Woods-Saxon potential for nucleons [28] which describes both neutrons and protons as Fermi gas.

On the other hand there is an analogy to the periodic table of the elements [29, 30], as depicted in Figure 2.3. This “Electronic Periodic Table” for clusters can be constructed by filling the electronic shells in the different periods. The monovalent clusters (Na_3,

Na_9…) and halide clusters like Na_7, Na_{17}… reveal enhanced reactivity due to a single electron (monovalent) or a missing electron (halide) in the outer shell. The clusters on the right side are the electronically magic clusters with closed shells.

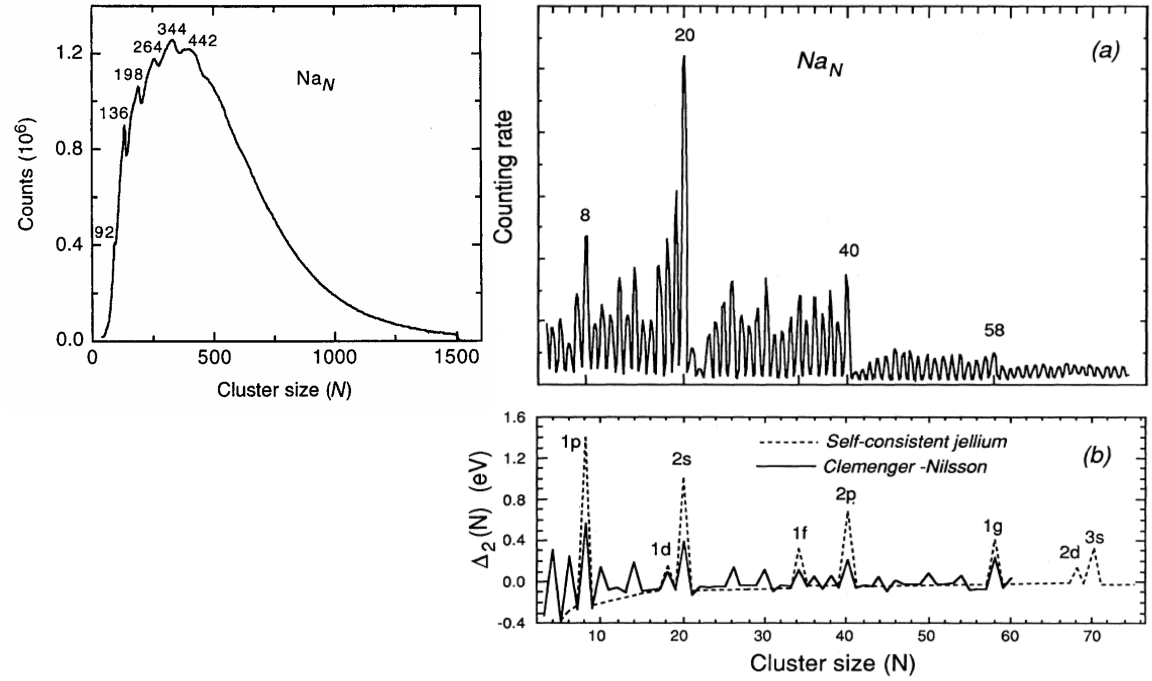

Figure 2.1: Left: mass spectrum of large sodium clusters with up to 1500 atoms [26]. Right: (a) mass spectrum of small sodium clusters [24], (b) dashed line: calculation using Woods-Saxon potential [24], solid line: calculation using the ellipsoidal shell (Clemenger-Nilsson) model [27] (see text).

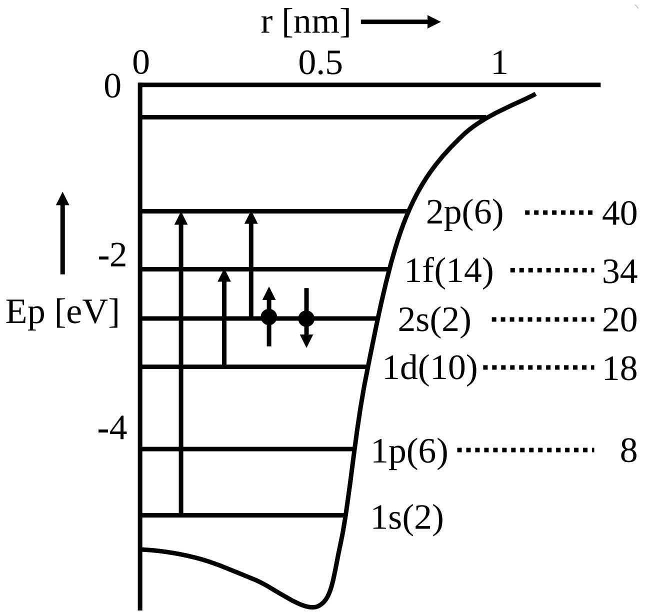

Figure 2.2: Kinetic energy of the electrons of a Na_{20} cluster according to the spherical jellium-background model.

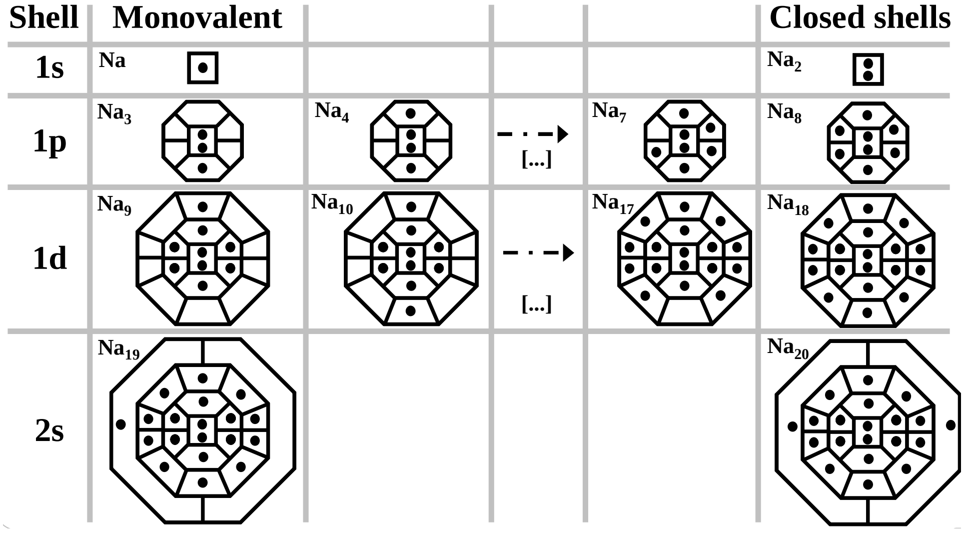

Figure 2.3: The shell model for sodium clusters.

The simple jellium model assumes that all clusters are spherical which is only true for clusters with closed shells due to fully occupied energy levels. Other cluster sizes have a non-spherical shape due to the asymmetric distribution of the electrons in the clusters. This mechanism is called *Jahn-Teller effect* [31, 32] and was studied in detail for nuclei by Nilsson [33, 34]. The model which includes the electron configuration of the non-spherical clusters is the *Clemenger-Nilsson model* [35]. The physical principle is that for clusters with open shells the total energy can be lowered by distorting the cluster and thereby lifting the degeneracy in the electronic shells in the spherical confirmation. In Figure 2.4 the Nilsson diagram shows the cluster energy levels as a function of the distortion parameter δ. For $\delta = 0$ the clusters are spherical. Clusters with closed shells are on the vertical axis crossing the x-axis at zero and are highly degenerated. For distortion parameters $\delta < 0$ the clusters have the shape of an oblate ellipsoid, for $\delta > 0$ the clusters are shaped prolate. The degeneracy has been shifted and the energy levels split up into sublevels respectively subshells. For $\delta \to 0$ the overlap of the sublevels increases. Thus electrons of non-spherical clusters are located in subshells and have a lower energetic level than electrons of spherical clusters. This explains not only the deviations of the ionization potential between theory and experiment [36], but also the minima for the ionization potential for some magic cluster sizes [12, 37].

Manninen et al. have shown theoretically that the electronic structure of a cluster not only depends on the number of electrons per cluster but also on the number of atoms [38]. For Na_{57}^- and Na_{59}^+, – both having a number of 58 electrons and showing the shell structure of the jellium model – they observed different energy gaps between the jellium subshells.

In this thesis the stability due to electronically magic numbers of positively charged Ag clusters are observed in a mass spectrum of small Ag_N^+ clusters as shown in Figure 2.5. The electron configuration of a single Ag atom is $[Kr]4d^{10}5s^1$. The 5s shell is filled with only one electron, so for Ag_2 there are two electrons in the outermost cluster shell which lead to more stability. In general for an odd number of electrons per cluster the cluster current is lower. For an even number of atoms per cluster the electron shells are closed, the cluster is more stable and the measured cluster current for these sizes is higher. In the case of positively charged Ag clusters with one missing electron as presented in Figure 2.5 the clusters with an odd number of atoms show a higher cluster current than the clusters with an even number of atoms. The peak corresponding to Ag_9^+shows the highest intensity in this spectrum because Ag_9^+ with a number of 8 electrons is an electronically magic cluster and therefore more stable than the other clusters which are visible in this spectrum.

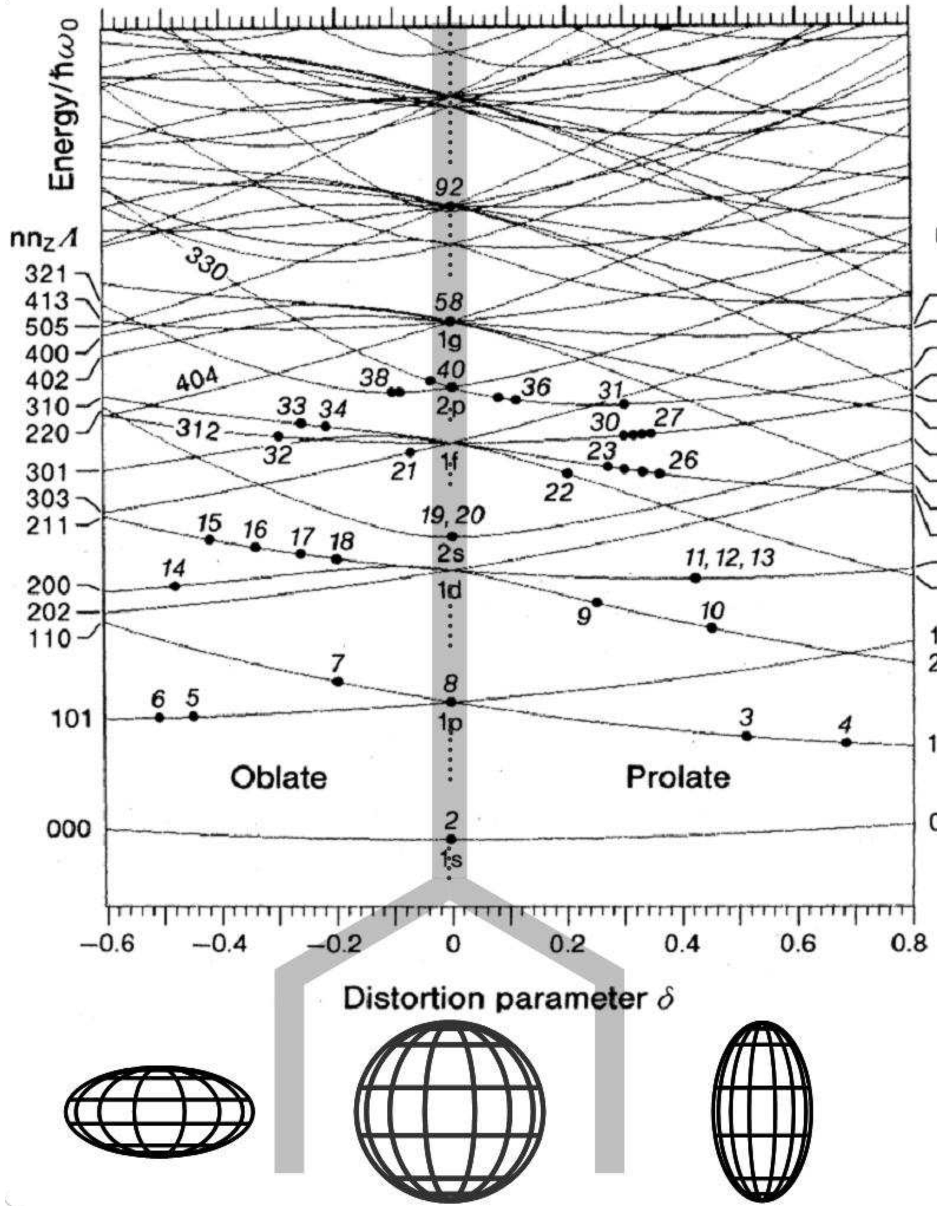

Figure 2.4: Nilsson diagram of cluster energy levels as a function of the distortion parameter δ [35].

Due to the fact that Ag and other coinage metals can be regarded to first order as d-shell perturbed s^1-electron clusters, much of the semi-quantitatively theoretical formalism used for alkali metals can be applied to them [39, 40]. Also the geometrical structure of Ag or other metal clusters is similar to alkali metals, as discussed in the next section.

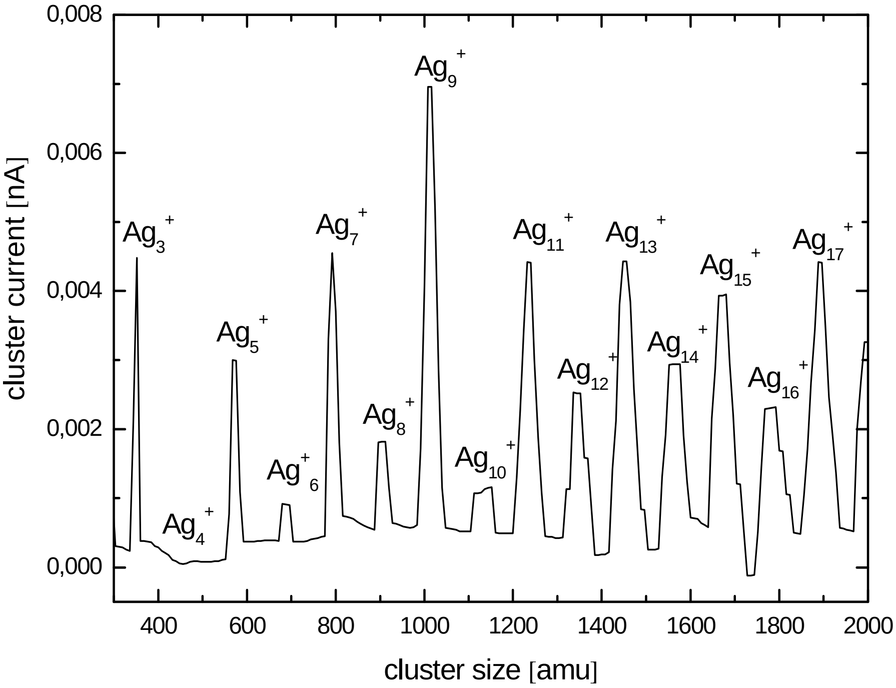

Figure 2.5: Mass spectrum from Ag_3^+ to Ag_{17}^+. The alternating height of the cluster current is due to closed or open outermost shells of the clusters.

2.1.3 Geometrically magic clusters

For small clusters the electronic structure dominates the properties of the clusters. For large clusters, e.g. in the case of sodium for clusters with 1500 or more atoms, periodicities in the cluster stability due to the *geometrical* packing of atoms into closed shells were discovered by MARTIN et al. [42] and STAMPFLI et al. [43,44]. The transition from dominantly electronic shell to atomic shell determined magic numbers happens at a certain cluster size n_{cr}, which is much smaller for crystallinelike clusters than for liquidlike clusters for which the atomic surface structure is washed out [43]. For Na and Ag the shell closings can be correlated with the construction of MACKAY icosahedra [45] which are also formed by rare gas clusters with closed atomic shells [46, 47].

Figure 2.6 presents a mass spectrum of Xe clusters with magic numbers due to the geometrical structure of the clusters. Xe_{13}, Xe_{55} and Xe_{147} have geometrically closed shells and form Mackay icosahedra with higher stability as other cluster sizes. The icosahedron is the structure of the platonic bodies which result from FRIEDEL's rule: *The cluster structure that has the largest number of next neighbor bonds has the highest bonding energy and hence, is the most stable of all structures* [12] (Figure 2.6).

Clusters with 13 atoms build the smallest icosahedra, where one atom in the middle is surrounded by two 5-fold caps consisting of six atoms. For the next size - a cluster with 55 atoms - the 42 additional atoms build the second shell around the icosahedron with 13 atoms. In general the number of atoms N which is necessary to form an icosahedron with *k* shells is defined by

$$N = 1 + \sum_{i=1}^{k} (10\,i^2 + 2) \qquad (2.1)$$

In this thesis geometrically magic Ag_N clusters with N = 55, 147, 309, 561 and 923 were investigated (see Figure 2.7). The larger a cluster is the more decreases the percentage of atoms in the outer shell of a cluster. HALL et al. observed by electron diffraction from Ag particles an icosahedral structure for Ag_{5083} with 11 closed atomic shells [48]. For clusters with more than 10^4 atoms the fcc (face centered cubic) structure is energetically preferred compared to the icosahedral structure.

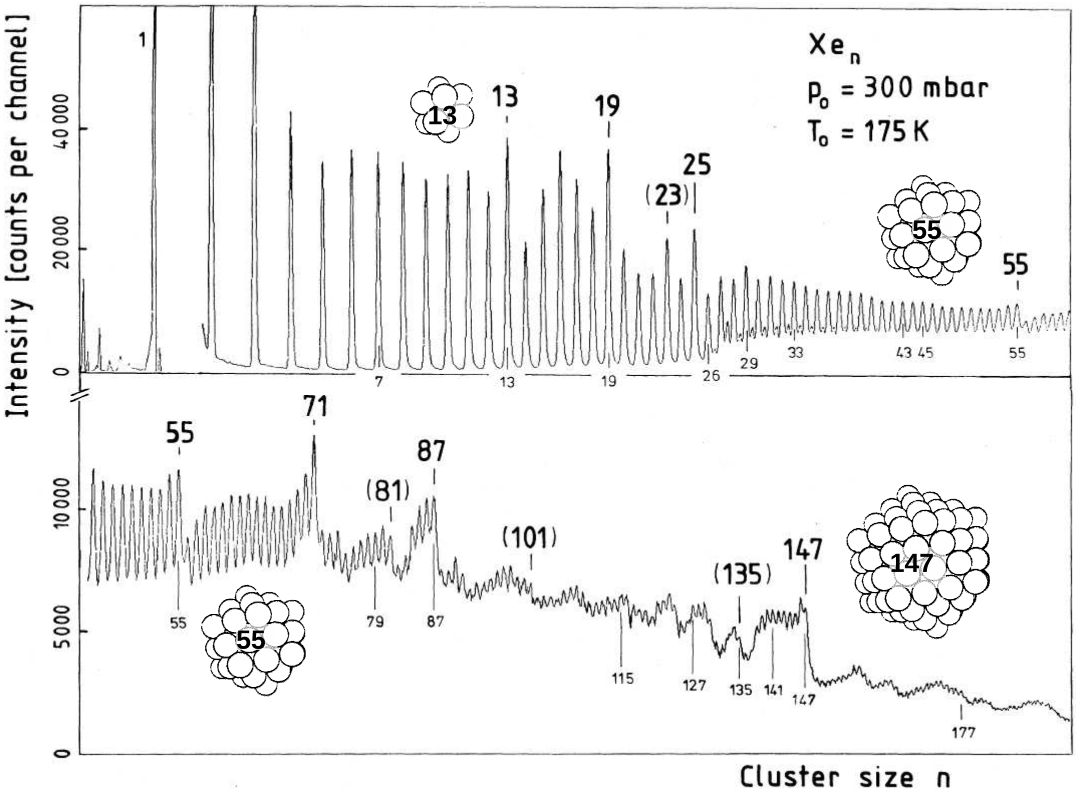

Figure 2.6: Mass spectrum of Xe clusters with geometrically magic cluster sizes (boldface). Brackets are used for numbers with less pronounced effects. Numbers below the curve indicate predictions or distinguished sphere packings [46].

For the investigation of size selected Ag clusters the cluster height after deposition on a surface is of great interest. As a simplification to compare measured cluster heights with theoretical values, an icosahedron is approximated by a sphere. In bulk material silver has an fcc structure with a lattice constant of a = 0.409 nm and 4 atoms per unit cell [49]. Thus the volume of a spherical Ag_N cluster equals

$$V_{Ag_N} = \frac{1}{4} \cdot a^3 \cdot N = \frac{4}{3} \cdot \pi \cdot \left(\frac{h_{Ag_N}}{2} \right)^3 . \qquad (2.2)$$

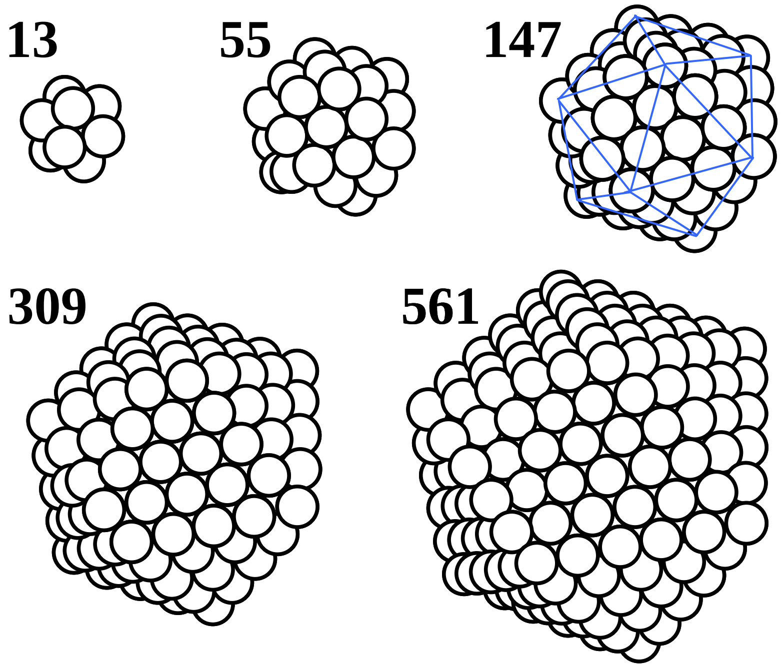

Figure 2.7: Rare gas, Na_N and Ag_N clusters with geometrically closed atomic shells form MACKAY icosahedra [45] consisting of 13, 55, 147, 309, 561 atoms, for which the 1st, 2nd, 3rd, 4th, 5th atomic shell is closed [50, 51].

The height of an Ag_N cluster with N atoms is therefore

$$h_{Ag_N} = 0.32\,nm \cdot \sqrt[3]{N}. \tag{2.3}$$

In Figure 2.8 the calculated cluster heights are plotted versus the number of atoms and the number of closed atomic shells, respectively by assuming a spherical cluster shape.

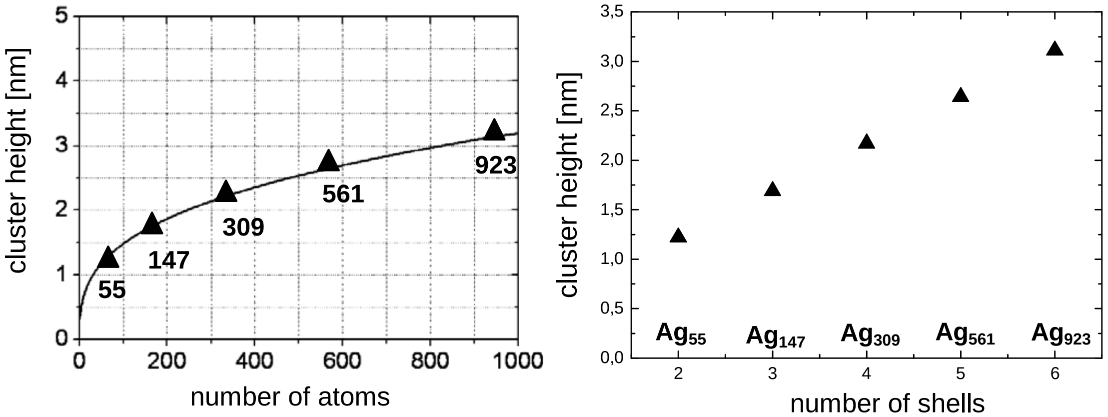

Figure 2.8: Calculated height of spherical clusters, left: according to the number of atoms, right: according to the number of atomic closed shells.

2.1.4 Free Clusters

As mentioned in chapter 1 the presented project is part of the priority program SPP 1153 within which we cooperate with BERND VON ISSENDORFF from Universität Freiburg. The group of BERND VON ISSENDORFF has made a comprehensive investigation of size selected negatively [52] and positively [53] charged sodium clusters by using photoelectron spectroscopy. The experimental study of free clusters together with molecular dynamics and density functional theory calculations by MICHAEL MOSELER allows for example predictions about the electronic [53] and geometric [54, 55] shell structure of Na clusters or the agreement with jellium model results and deviations due to thermal effects [52].

Furthermore multiply charged Al clusters were observed in photo emission spectra due to multiple electron emission, resulting in a so called *Coulomb staircase* [56] (see Figure 2.9). The Fermi edge shifts result from the Coulomb interaction between positively charged clusters and emitted electrons.

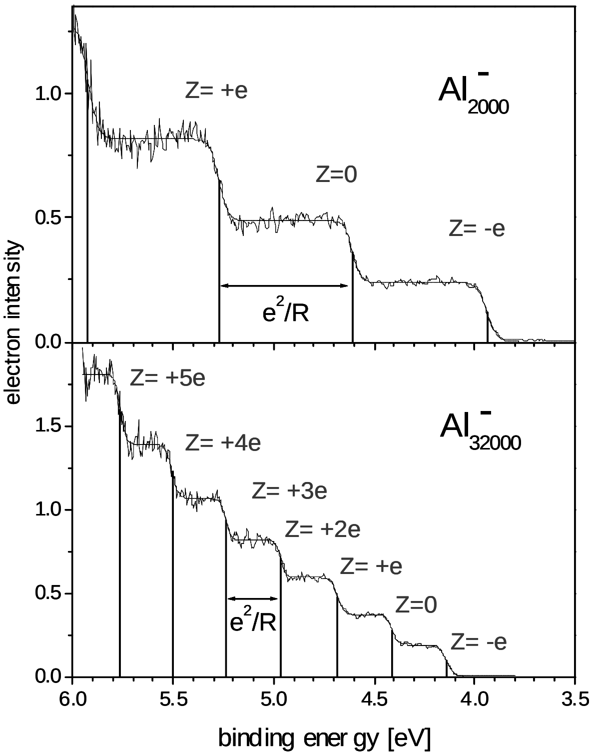

Figure 2.9: Photoelectron spectra of free size selected $Al_{2000}^{-}{}_{\pm 10}$ and $Al_{32000}^{-}{}_{\pm 150}$ clusters at a photon energy of $h\nu$ = 6.42 eV. Due to multiple electron emission the ionization thresholds of four different charge states of the smaller cluster can be observed (from Al_{2000}^{-} to Al_{2000}^{2+}) and of seven different charge states of the larger cluster (from Al_{32000}^{-} to Al_{32000}^{5+}) [56].

In general photo emission spectra of size selected clusters are like a fingerprint: every cluster material with a certain number of atoms per cluster has its own, characteristic photo emission spectrum. This becomes apparent in the photo emission spectra of copper (Cu_n^-), silver (Ag_n^-) and gold (Au_n^-) clusters [9] which are shown in Figure 2.10.

The spectra demonstrate that Cu_{55}^{-} and Ag_{55}^{-} exhibit highly degenerated states due to their icosahedral symmetry whereas other cluster sizes feature strongly perturbed electron shell structures as a consequence of lower symmetries. In contrast to Cu and Ag, Au clusters show completely different spectra due to strong relativistic bonding effects and exhibit a tendency to amorphous structures [9, 57].

For this reason geometrically magic icosahedral Ag clusters deposited on surfaces are well suited for the investigation concerning geometric and electronic properties of the cluster-surface system and interactions between clusters and surfaces.

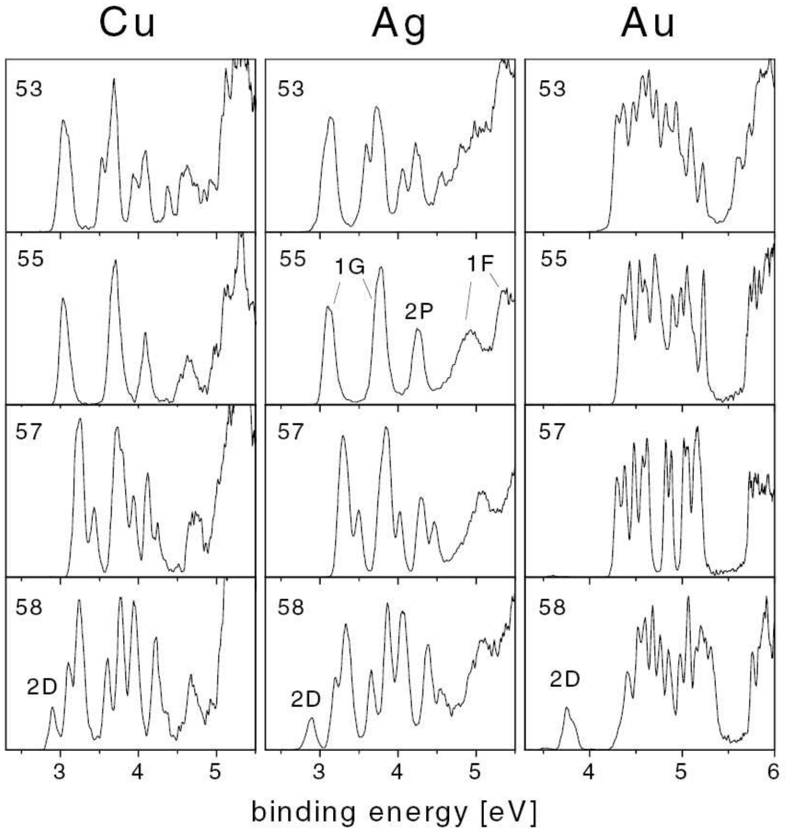

Figure 2.10: Photoelectron spectra of noble metal cluster anions, measured at a photon energy of 6.42 eV [9].

2.1.5 Examples for clusters on surfaces: catalysis

Some cluster materials have a superior position in the role of being nanocatalysts [1, 2]. The cluster material and the cluster size determine the catalytic activity. Two examples of Au_N nanocatalysts are presented in the following, which show the properties and the relevance of Au_N clusters for catalysis. Another example highlights the use of Pd_N nanocatalysts as catalytic converters in the automotive industry.

In a first example it will be shown that the reactivity of small gas-phase gold clusters with up to 30 atoms depends on the number of atoms N and the charge state of the clusters. Cluster anions with an even N show enhanced reactivity [58, 59]. These observations were confirmed and extended more recently [60, 61]. The group of GERD GANTEFÖR presents in [61] that Au_N^- clusters with an odd N do not react with O_2 in contrast to clusters with an even N up to Au_{20}^- which react with O_2. An interesting exception, which shows that the number of atoms per cluster drastically changes its chemical properties, is Au_{16}^- which breaks the odd–even alternating pattern. The anomalous absence of O_2 take-up for Au_{16}^- is visible in the mass spectrum in Figure 2.11. The explanation of this phenomenon give YOON et al. in [62].

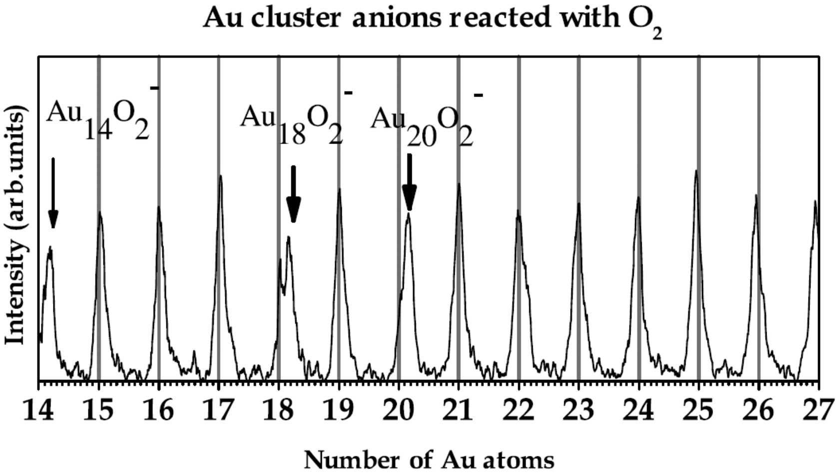

Figure 2.11: Mass spectrum of Au anion clusters after reacting with O_2. The grid lines correspond to the masses of pure Au clusters [61].

Several Au_N clusters like Au_{16} were found to have cage-like structures. The electronic properties of these cage-like structures cannot be described by the conventional jellium model, because the positive ions are located in a shell. Thus the so called *hollow* jellium model replaces the conventional jellium model, where the metal ions with a uniform positive charge background are located in a hollow spherical shell whereas the specific ionic structure is ignored. Within a hollow jellium model, the bare Au_{16}^- cluster lacks just a single electron for closure of the major 1d shell. This halogen-like situation underlies the high vertical detachment energy of Au_{16}^- and the corresponding low O_2 binding energy, as well as the experimental absence of $Au_{16}O_2^-$ (see Ref. [61]). On the other hand, both Au_{18}^- and Au_{20}^- behave in an alkali-like manner (the former in the hollow and the latter in the filled jellium model) with corresponding low vertical detachment energy values and high reactivities towards O_2.

The second example highlights the properties of one certain cluster size, namely Au_{55}. Quite recently MARK TURNER et al. observed that Au_{55} clusters are efficient and robust catalysts for the selective oxidation of styrene by dioxygen [63]. The Au_{55} clusters are supported on chemically and electronically inert materials and can adsorb and activate O_2 for selective oxidation, presumably by dissociating O_2 to yield O adatoms [64, 65] that initiate the reaction with styrene molecules. The oxidation products are styrene epoxide, benzaldehyde and acetophenone. Larger Au particles on inert supports or extended Au surfaces are incapable of catalysing this oxidation process. Other cluster materials like silver [66, 67] and zeolites containing cobalt [68, 69] are well known to activate O_2 and efficiently epoxidize styrene with O_2 alone.

The use of catalysts for the automotive industry is a further hot topic. The improvement of the life time of catalytic converters, particularly the lowering of the light-off temperature of the catalytic converter is of great interest. Due to the high temperature of around 250°C it takes up to two minutes for catalytic converters until they work properly. For this reason most of the harmful substances are emitted during this cold starting period. A possibility to lower the light-off temperature is given in [70] and was studied by soft-landing of small Pd_N clusters onto an MgO(001) surface containing a surface F center, (from german *Farbzentrum* = oxygen vacancy). When adsorbed on magnesia, surface defects serve as strong trapping centres for the clusters that maintain their open valence shells and finite spin moments [71]. Model-catalytic experiments and ab initio simulations indicated that a Pd_4 cluster adsorbed at a surface color centre (FC) of the magnesia support can be catalytically active for CO oxidation with a direct CO_2 formation, which is illustrated in Figure 2.12. B, C und D show the three energetically preferred positions of O_2 on Pd_4 with adsorption energies from 0.8 up to 1.0 eV. For large palladium particles with some 100.000 atoms, as they are used in conventional catalytic converters, the dissociation barrier amounts to around 1.0 eV. For only some atoms there is a decrease of the activation energy of 0.5 eV (D,F,E), implying that the reaction on Pd_N should be experimentally realized below room temperature.

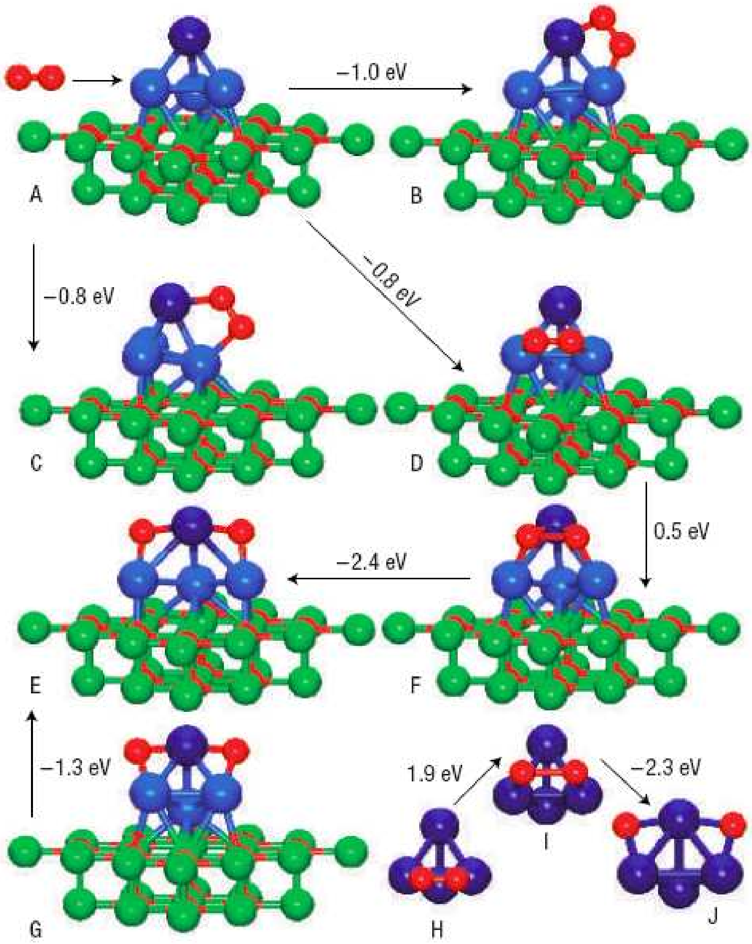

Figure 2.12: A: Pd_4 (blue) on MgO (green/red) with an oxygen vacancy; B-D: with molecularly adsorbed O_2; E: ground state of O_2Pd_4/MgO(FC); F, transition state between D und E; G, final state after O_2 dissociation on a static Pd_4, i.e. in the geometry as in A; H-J, dissociation in gas phase [70].

2.2 Fullerenes

Due to the fact that for the experiments which are presented in this thesis size selected Ag clusters and metal islands were deposited on C_{60} layers, the properties of fullerenes are introduced in this section. In particular C_{60} and C_{58} which were investigated by STM studies are presented in more detail.

Fullerenes are spherical or ellipsoidal carbon molecules and the third well-known allotrope of carbon. The different forms or allotropes of carbon also include diamond, the hardest naturally occurring substance, and graphite, one of the softest known substances. Related structures are plane carbon sheets (graphene) [72, 73], cylindrical carbon nanotubes [74], carbon nanobuds - a composition of nanotubes and fullerenes [75, 76] - and carbon nanofibers [77]. Fullerenes are nowadays commonly synthesized and used in research. Studies about fullerenes were published in 1970 by EIJI OSAWA in Japanese language who predicted their existence by calculations [78, 79]. The experimental detection in molecular beam experiments of fullerenes in 1984 (Figure 2.13) by HARALD W. KROTO, RICHARD E. SMALLEY et al. [80] lead to the noble prize in 1996. On the way to detect or synthesize fullerenes LEO PAQUETTE was the first one who synthesized a $C_{20}H_{20}$ dodecahedrane in 23 steps from the cyclopentadienide anion [81, 82].

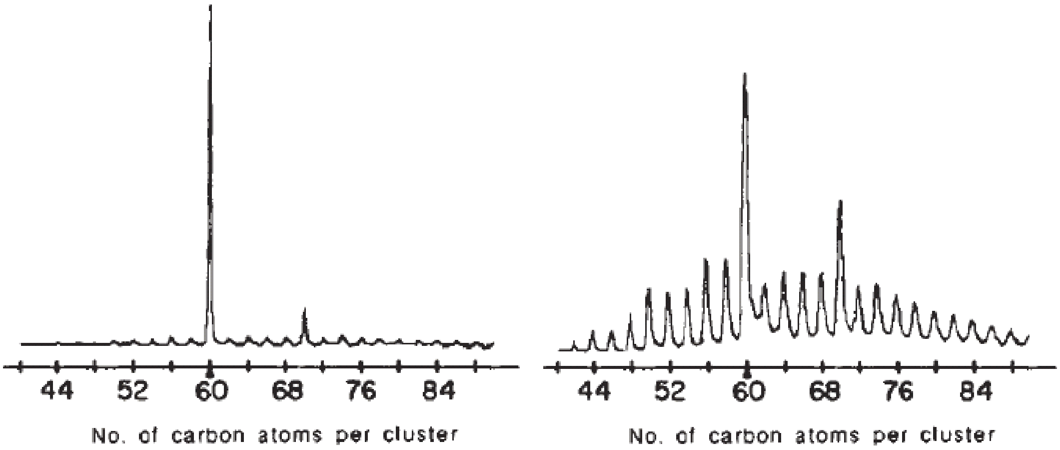

Figure 2.13: Time-of-flight mass spectra of carbon clusters prepared by laser vaporization of graphite and cooled in a supersonic beam with high (left) and lower helium pressure (right) [80].

The most stable fullerenes are C_{60}, C_{70}, C_{76}, C_{80}, C_{82}, C_{84}, C_{86}, C_{90} and C_{94}. Fullerenes are produced by vaporizing graphite in an inert atmosphere through an electric arc maintained between two electrodes [83, 84]. The carbon vapor is quenched in an inert gas and a part of the small clusters self-assemble to produce fullerenes. A new process for the production consisting of treating carbon powders through a 3-phase thermal plasma is presented in [85]. A detailed description of the production of C_{60} and C_{70} is given in [86].

2.2.1 The Buckminster fullerene C_{60}

The most stable and best studied fullerene is C_{60}. It is called Buckminster fullerene or *Buckyball* in honor of the architect RICHARD BUCKMINSTER FULLER whose geodesic buildings look very similar to the structure of a C_{60} molecule. Geometrically, C_{60} is a truncated icosahedron, with 20 hexagons and 12 pentagons with an average diameter of around 0.7 nm and an outer diameter including the p-electrons of around 1 nm [87]. For the hexagons and pentagons there are 1812 possibilities to form closed cage-like structures, but only one stable configuration is observed which is formed in such a way that no two pentagons share an edge but are surrounded only by hexagons (see Figure 2.14). All isolated “classical” fullerenes conform to the isolated pentagon (IPR) rule [88] which requires that all twelve pentagons in a fullerene are separated from each other by intermediate hexagons which leads to an ambiguous aromatic character and thus a high stability of the fullerene cages. C_{60} is the smallest IPR fullerene [89]. Solid C_{60} (fullerite) with an fcc crystal structure at RT was discovered in 1990 by W. KRÄTSCHMER et al. [90]. Raman spectra show that the interactions in crystalline C_{60} are van der Waals-like [91]. Therefore a C_{60} film is well suited as a buffer layer for the soft landing of clusters.

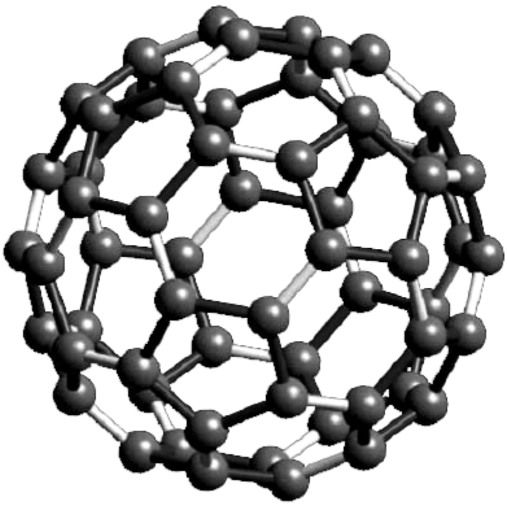

Figure 2.14: The C_{60} molecule: a truncated icosahedron with 12 pentagons and 20 hexagons.

A close packed hexagonally arranged film of C_{60} has a corrugation period of around 1 nm which hinders the cluster diffusion on the C_{60}. C_{60} is also helpful to decouple the clusters electronically from the substrate and there are interesting interactions of C_{60} and metals. An interesting phenomenon was observed by HEBARD et al. who found that C_{60} fullerites doped with potassium are superconducting at 18 K [92]. The experimental investigations and results which were achieved within this thesis containing the different orientations of C_{60} molecules on an Au(111) and HOPG (highly orientated pyrolytic graphite) surface and the structure and properties at room temperature (RT) and low temperatures are discussed in detail in section 6.2.

2.2.2 The C_{58} fullerene

Classical C_n fullerenes which obey the IPR rule are all-carbon cage molecules comprising twelve pentagonal and $n/2–10$ hexagonal rings (n = number of carbon atoms). All such cages form weakly van der Waals bound semiconducting molecular solids [88]. Smaller carbon cages as C_{60}, being the largest IPR fullerene, must either have adjacent pentagons (AP) or even nonclassical structures containing, e.g., heptagonal rings. Non-IPR carbon cages are thought to exhibit reduced stability due to considerably increased steric strain and weakened π conjugation especially at the adjacent pentagon sites [93]. Density functional theory (DFT) based calculations predict that covalent links between adjacent pentagon sites of neighboring non-IPR cages should be strong and the activation barriers for cage-cage bonding quite low, thus favoring the formation of polymeric network solids. The largest non-IPR fullerene is the C_{58} molecule, which contains two candidates for the most stable ground-state isomer of C_{58} (see Figure 2.15 a)), according to DFT calculations [94]. $C_{58}(1)$ contains three pairs of adjacent pentagons (3-2AP) separated by hexagons whereas $C_{58}(2)$, an “unconventional” structure, exhibits one heptagon and two chains of three adjacent pentagons (1 HP + 2 C3AP) [94]. For $C_{58}(1)$ and $C_{58}(2)$, the steric strain energy associated with adjacent pentagons is expected to lead to significantly lower chemical stability than for C_{60}. Thus the pentagon junctions (and in the case of $C_{58}(2)$ also the heptagon) should correspond to high reactivity sites. A C_{58} dimer, where two AP bind to each other, is shown in Figure 2.15 b).

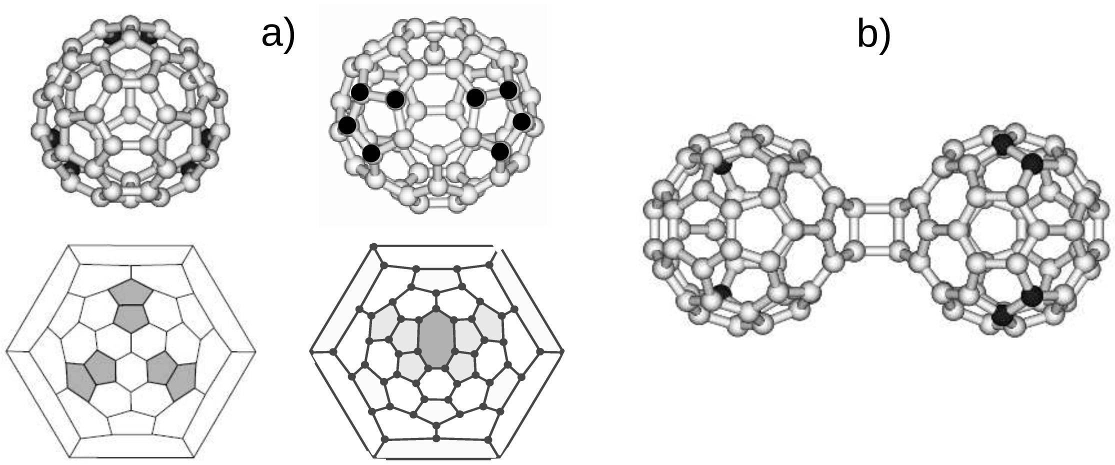

C_{58} Isomer 1 (C_{3v}) **C_{58} Isomer 2 (C_s)** **C_{58} 1 (C_{3v}) dimer**

Figure 2.15: a) Structures of the energetically favored isomers of C_{58}. Two views are given: the spherical shape of each fullerene, where carbon atoms linking two pentagons are marked in black, and the two-dimensional Schlegel diagram with neighbored pentagons or the heptagon colored in grey. b) structures of computed C_{58} dimer, where 2AP binds to 2AP. Pictures taken from [95].

The C_{58}/HOPG samples, which were investigated within this thesis in comparison to C_{60} films, were prepared by DANIEL LÖFFLER from the group of ARTUR BÖTTCHER from the physical chemistry department of Universität Karlsruhe. The sample preparation is discussed in section 5.2.2, the results and STM images taken in Dortmund are presented in chapter 6.

3 EXPERIMENTAL SETUP

In 2005 a high transmission cluster deposition machine was developed and built at Technische Universität Dortmund in cooperation with BERND VON ISSENDORFF from Universität Freiburg. The cluster deposition machine is connected by a valve to a low temperature (LT) ultra high vacuum (UHV) surface science facility [96] which was manufactured by the Omicron Nanotechnology GmbH.

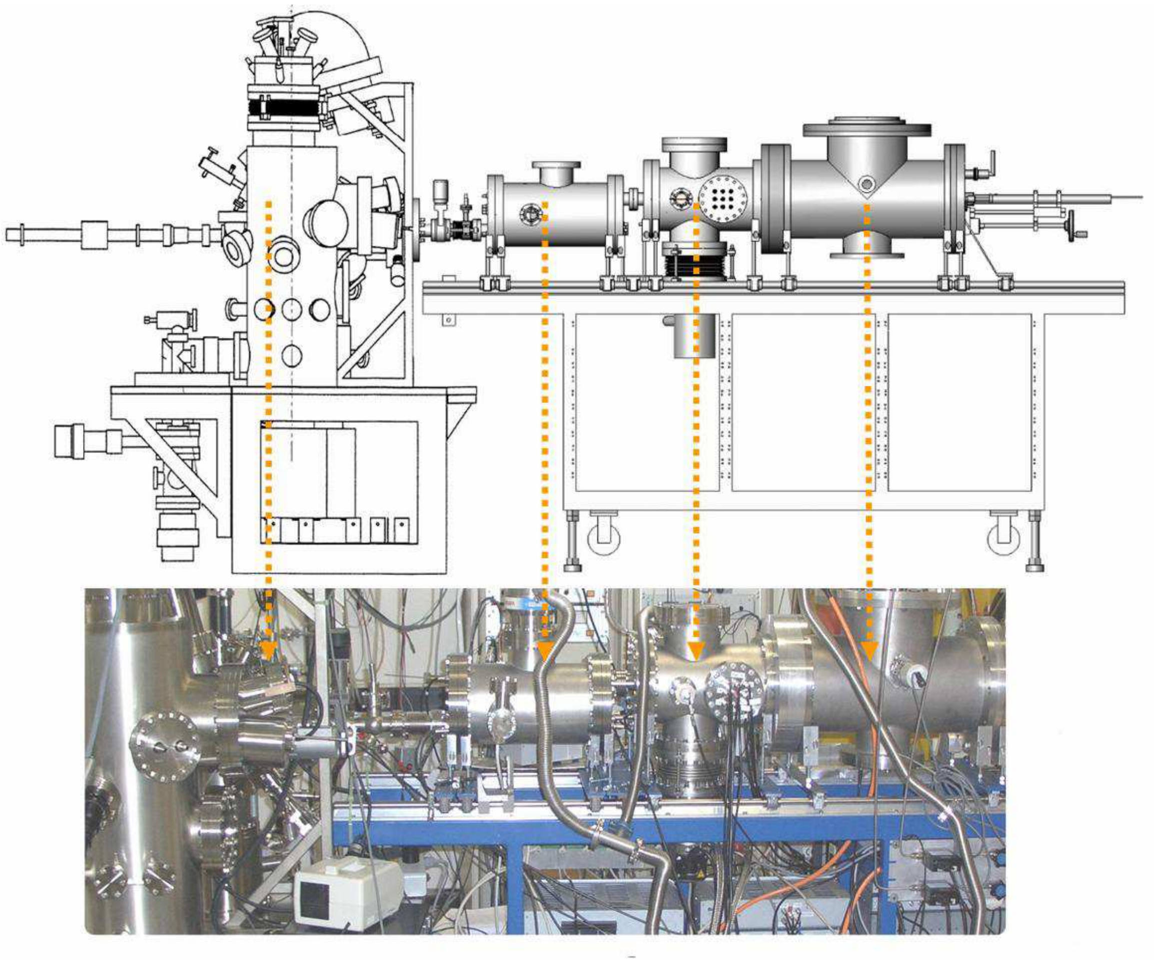

Figure 3.1: Drawing and photograph of the experimental setup of the cluster deposition machine which is connected to the Omicron LT-UHV surface science facility.

The unique combination of a cluster deposition machine and a surface science facility that includes both in situ LT STM / STS and UPS [97] holds a large research potential.

3.1 The cluster deposition machine

The last chapter has shown that a mass selection of clusters is very promising and worthwhile to investigate the electronic and geometric properties of nanoparticles. For the production of size selected Ag clusters a cluster deposition machine is used, which consists of a magnetron sputter gas aggregation source [98], an acceleration chamber including a cryo pump and an infinite range high resolution time-of-flight mass selector [99] as shown in Figure 3.2.

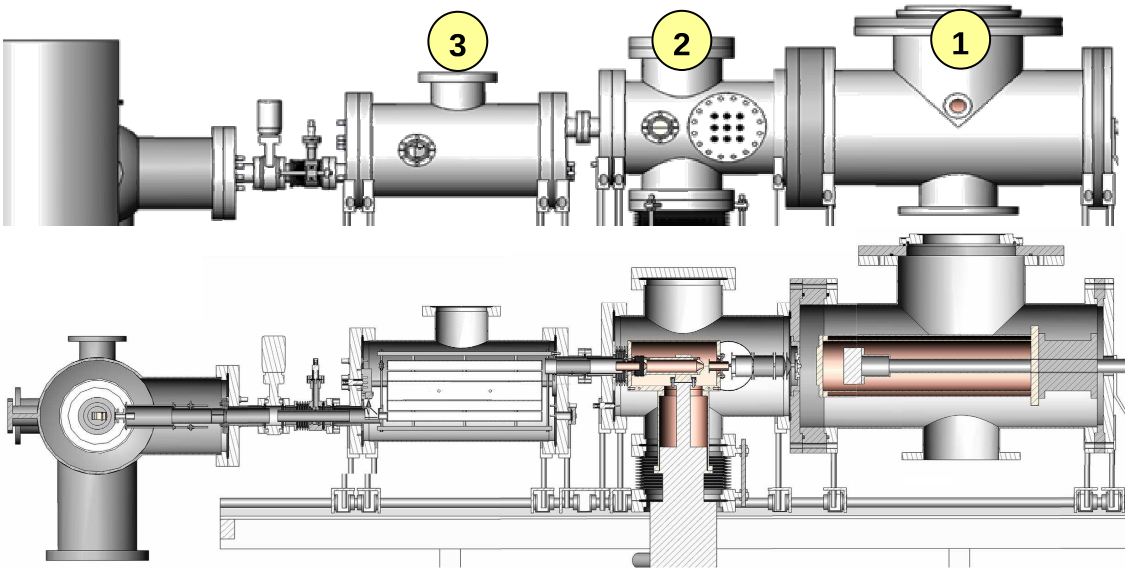

Figure 3.2: Top: The cluster deposition machine including a magnetron sputter gas aggregation source (number 1), an acceleration chamber with a cryopump (number 2) and a time-of-flight mass selector (number 3). Below: cross section of the cluster deposition machine.

The three stages of the cluster deposition machine are presented in the following sections. A detailed description of the cluster deposition machine was worked out in [28] and [100].

3.1.1 The magnetron sputter gas aggregation source

The type of source which was used to produce Ag clusters combines two processes: the magnetron sputtering of atoms from a silver target and the gas aggregation of these atoms in order to form clusters. This cluster source was first introduced by the group of H. Haberland [98] and is illustrated in Figure 3.3.

A magnetron sputtering cathode is mounted inside a liquid-nitrogen-cooled double-wall aggregation tube with an inner diameter of 10 cm and a movable magnetron-sputter-discharge head and is operated with a mixture of helium (He) and Argon (Ar). The liquid nitrogen (LN_2) flows trough a flow cryostat which surrounds the cluster source and protects the magnetron cathode from overheating for high powers from 5 W to 20 W. It is possible to operate the magnetron cathode without cooling between 1 W and 4 W.

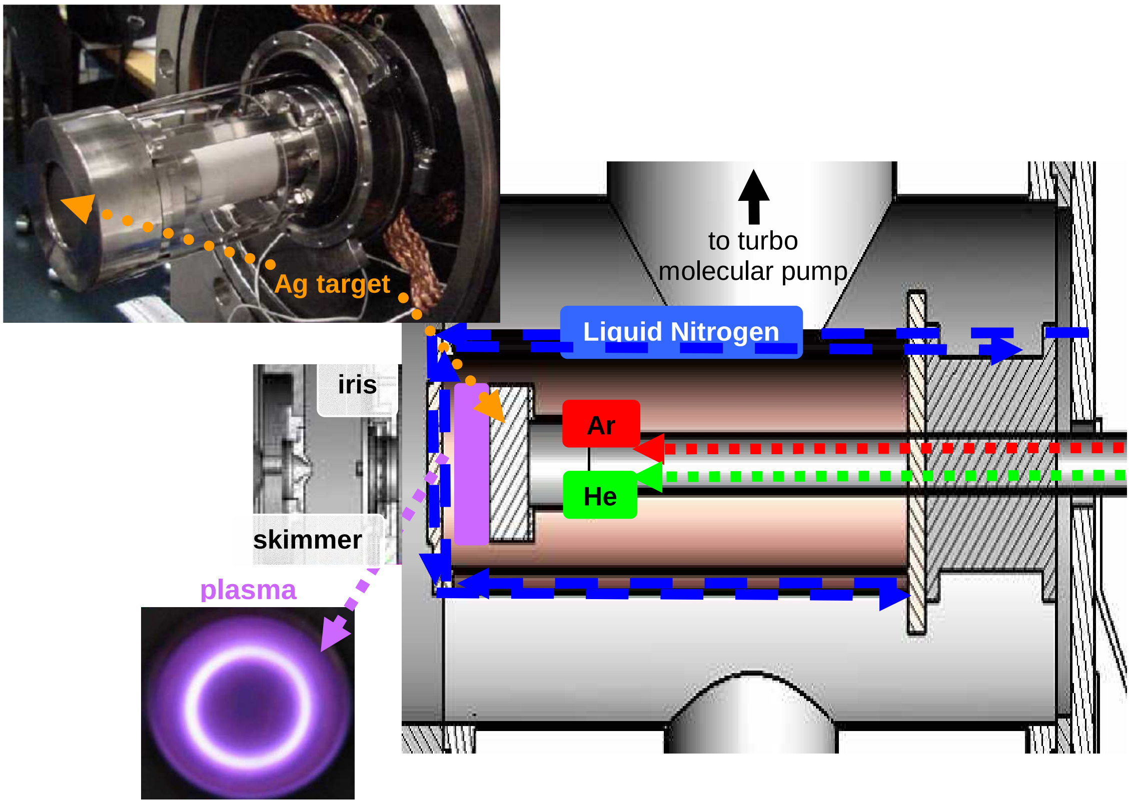

Figure 3.3: Pictures and scale drawings of the magnetron sputter gas aggregation source. The picture on the left top shows the magnetron head, on the left bottom the plasma produced by the magnetron head is depicted.

The sputtering process works as follows: a mixture of He and Ar is introduced into the chamber, whereas the Ar directly flows over the sputter target. Helium is introduced into the aggregation region between target and iris. Typical gas fluxes are $\Phi_{Ar} = 100$ sccm (standard cubic centimetres per minute, where "standard" means flux at a normal pressure of 1 bar and room temperature) and $\Phi_{He} = 200$-400 sccm. The magnetron cathode is formed by a cylindrical magnet behind the target which can be biased up to 1.2 kV. The electric field accelerates the Ar, which is ionized by secondary electrons in front of the magnetron cathode, towards the target and Ag atoms are ejected from the Ag target. The theory of the sputtering process is described in detail in [101]. Due to the influence of the magnetic field the electrons are forced to cyclotron orbits, where they ionize more Ar atoms and, together with the ionized Ar atoms, build a plasma torus (Figure 3.3). The ejected Ag atoms leave the discharge region and enter the aggregation region where they collide with both Ar and He atoms which leads to coalescence of the atoms and thus cluster formation. This process is illustrated schematically in Figure 3.4.

The cluster beam then passes the iris (Figure 3.3) which has an adjustable diameter and is focused by the ring lens, which reduces the loss of clusters, towards the skimmer (Figure 3.3). The cluster size can vary from one atom to several thousands of atoms and depends on different parameters: the aggregation distance between magnetron cathode and iris, the electrical discharge power and the pressure inside the aggregation tube which depends on the gas fluxes and the opening of the iris. For small clusters the aggregation length has to be short and the pressure in the aggregation zone, given by the ratio of gas flux and the cross section of the iris, should be small and vice versa.

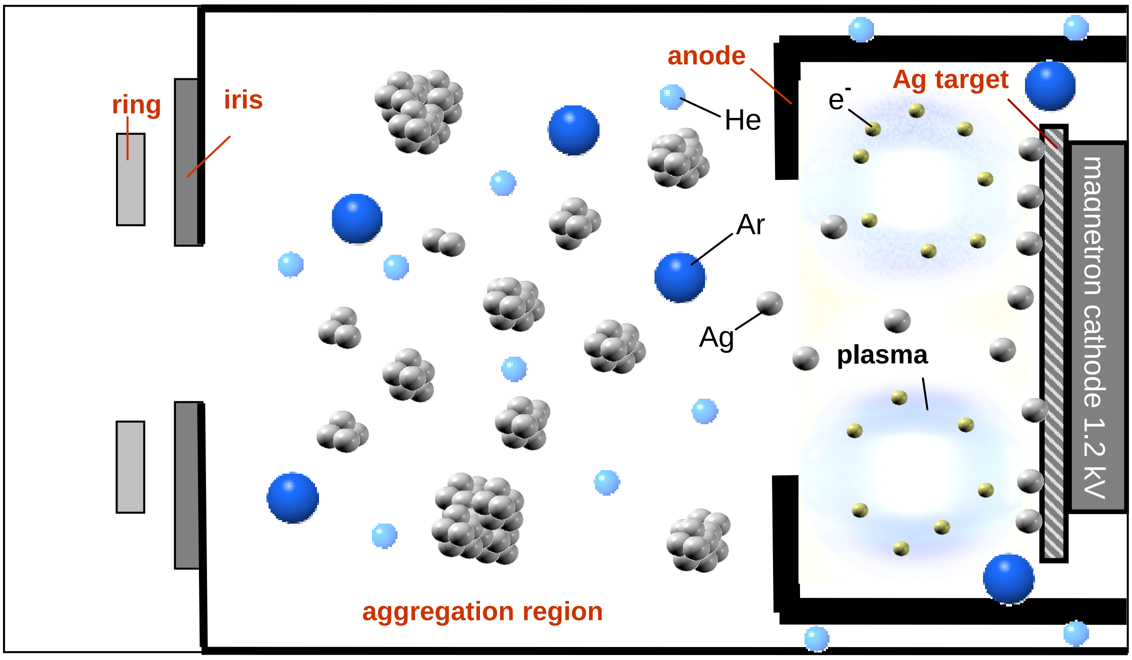

Figure 3.4: Schematic illustration of the sputter and coalescence process in the source chamber. Due to Ar ion bombardment Ag atoms are ejected from the target and collide with the Ar and He atoms in the aggregation regions which leads to cluster formation.

A turbo molecular pump evacuates the source chamber, so that the final pressure in the LN_2 cooled chamber is in the order of 10^{-8} mbar without gas load and in the order of 10^{-2} mbar with gas load. Due to the high ionization degree and charge transfer processes in the magnetron plasma discharge 40 % - 60 % of the clusters are positively or negatively charged. The experiments within this thesis were carried out using positively charged clusters. For this reason negative voltages are applied to all electrodes after the iris and the ring lens.

3.1.2 The acceleration chamber

The skimmer with an aperture of 2 mm (Figure 3.3, Figure 3.5) separates the core of the diffuse cluster beam, connects the source with the acceleration chamber and can be biased from 0 up to –50 V. If the applied voltage is higher than about –10 V electron discharges are possible. Therefore it is better to apply zero bias or low negative voltages to the skimmer. After that the cluster beam, which contains a broad size distribution of clusters, is accelerated and collimated by a set of ion optics consisting of four lenses. The shape and dimensions have been designed and were optimized by CHUNRONG YIN [100] using the ion and electron simulation program SIMION 3D^{TM} 7.0 [102]. The last electrode of the ion optics is set to –500 V, the floating voltage of the apparatus, which is applied to the electrodes that are not used to bend, focus or accelerate the cluster beam. Four deflector plates (x–, x+, y–, y+) can be used to bend the cluster beam in x- and y-direction and guide it to the field free region inside the cryo tube (see Figure 3.5).

The cryo tube is part of the cryo pump system that consists of two cooling stages made of copper. Within 2.5 h the first cooling stage cools down to 30 K, the second cooling stage to a temperature of 10 K. Such low temperatures are necessary to freeze out most of the Argon, water and other impurities. The cooling, achieved by adiabatically expanding helium, which is pumped through the pipes of the cryo pump with a pressure of 15 bar. The first stage serves as a thermal shield for the second one. More details about the function and physical principles of a cryo pump are given in [28]. The acceleration chamber is additionally pumped by a turbo molecular pump. During operation the pump provides a pressure of 10^{-6} mbar, in the stand-by modus a pressure of around 10^{-8} mbar. After passing the cryo tube the clusters leave the acceleration chamber and enter the time-of-flight mass selector, which is presented in the following section.

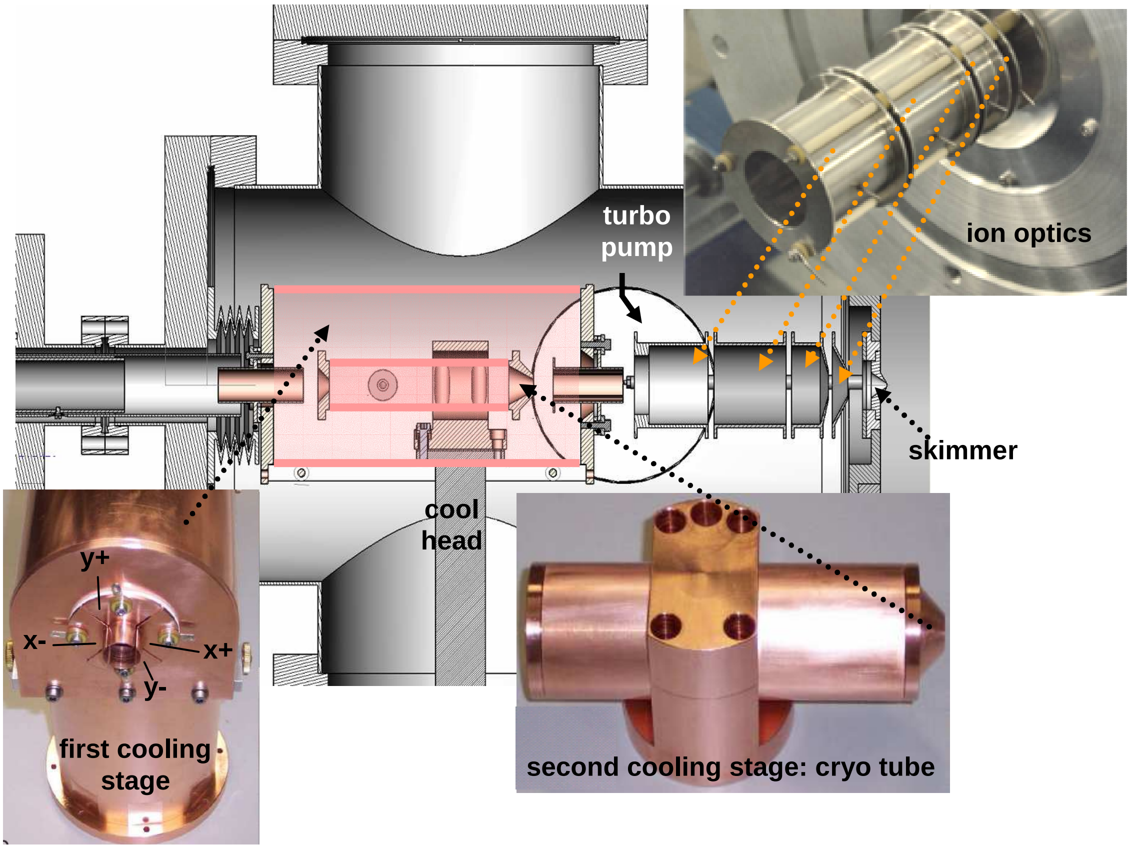

Figure 3.5: Drawing and pictures of the acceleration chamber. The cluster beam enters the chamber through the skimmer, is focused by the ion optics and bended by the x-y deflector. Argon, water and other impurities are frozen out at the cryo tube.

3.1.3 The mass selector

The mass selector of the cluster deposition machine is a special infinite range high transmission semi continuous time-of-flight mass selector, which was constructed by BERND VON ISSENDORFF [99]. With the right choice of parameters the transmission of the mass selector can be close to 100 % for the selected size and is thus much larger than for conventional time-of-flight mass selectors. The practically infinite selectable mass range can not be achieved by magnetic sector or quadrupole mass selectors. A schematic view of the setup and function of the mass selector gives Figure 3.6.

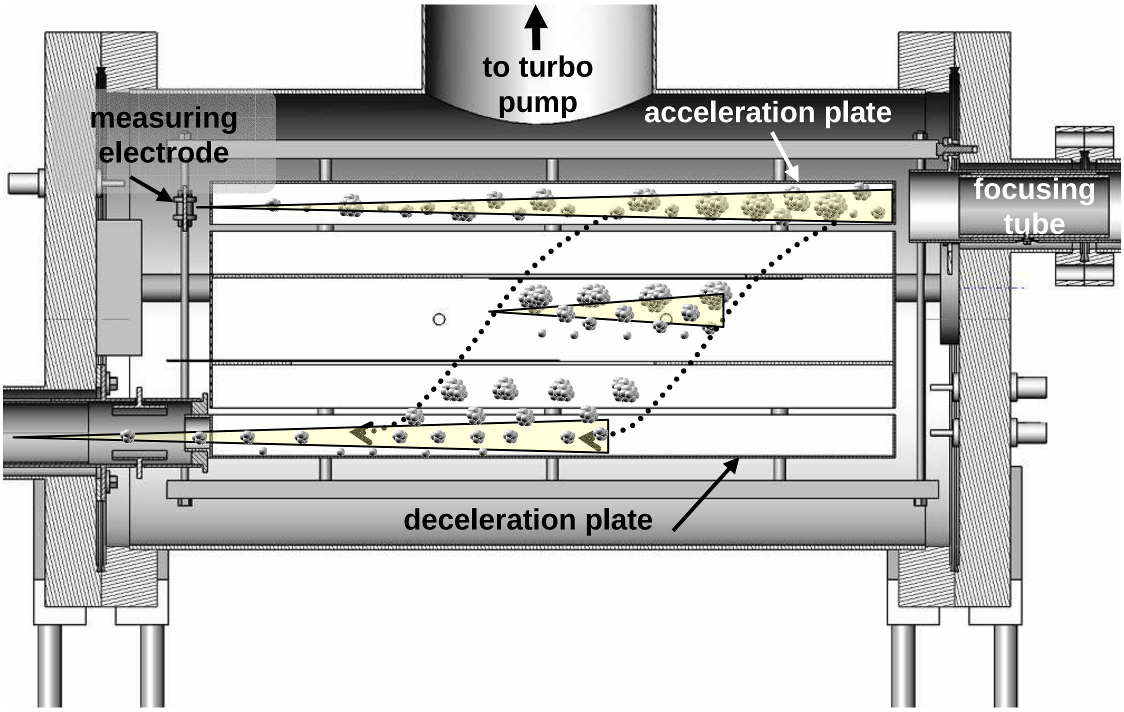

Figure 3.6: Schematic of the mass selector chamber.

When the cluster beam enters the mass selector chamber, it can be focused on a measuring electrode which is mounted at the top end of the mass selector. Up to here, the cluster beam consists of a broad spectrum of cluster sizes, which is given by the cluster sizes which were produced by the source. As explained in section 3.1.1 the produced sizes depend on the parameters like aggregation length, aperture of the iris and He/Ar ratio. Besides the cluster beam contains not only positively charged clusters but also neutral clusters. The probability of *simply* positively charged clusters is much higher than the probability of the existence of *multiply* charged clusters, so nearly all clusters are simply positively charged or neutral. The function of the mass selector relies on the time-of-flight principle, but differs from the time-of-flight mass selection which is normally used. After entering the upper region of the mass selector, the cluster beam is displaced perpendicular to its original direction through a slit aperture due to an electric pulse of the pulse length τ_p from the acceleration plate (Figure 3.6). During the drift time τ_d the cluster beam splits up into several cluster beams and each beam contains a single cluster size. This phenomenon is due to mass inertia – all clusters have the same charge, but different masses – thus smaller clusters drift down faster than larger clusters. After the drift time the clusters pass a second identical slit aperture and a second pulse from the deceleration plate with the same length τ_p in the opposite direction as the first pulse stops the movement downwards. The clusters keep their original lateral velocity during the whole displacement process. Thus the selected clusters leave the mass selector through an exit slit, keeping the original focus, whereas the other cluster masses remain in the mass selector. After a waiting time τ_w the pulsing sequence starts again. Schematic illustrations of the pulse sequence and the drifting process of the cluster beam are shown in Figure 3.7.

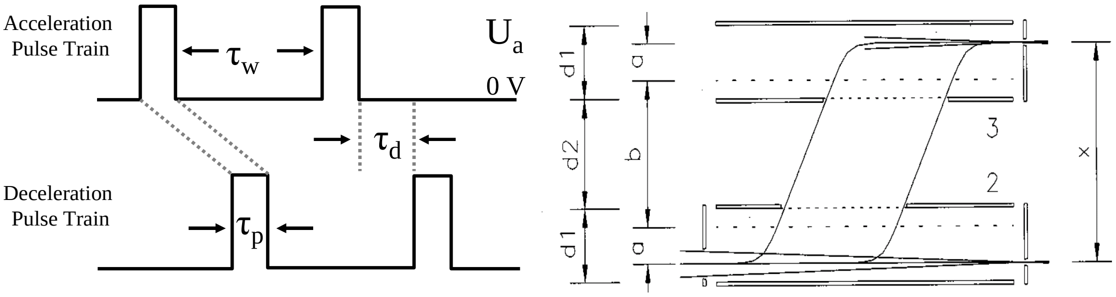

Figure 3.7: Left: schematic of the sequence of the high voltage pulses, right: schematic illustration of the cluster beam drifting process, caused by the high voltage pulses [99].

The selected cluster mass is given by the equation

$$m = \frac{e \cdot U_p}{x \cdot d_1} \cdot \left(1 + \frac{\tau_p}{\tau_d}\right) \cdot \frac{1}{f^2}, \tag{3.1}$$

where $e \cdot U_p$ is the energy gained by the voltage pulse ($U_p = 863$ V), x the total beam displacement (0.1 m), d_1 the plate separation (0.04 m) – see Figure 3.7 – and f the frequency. The times τ_d, τ_p, and τ_w are multiples of the period of the frequency generator, thus the times have to be divided by this frequency to get the real times. To convert the cluster mass in atomic mass units (amu) one has to divide m by the mass of a proton ($1.67 \cdot 10^{-27}$ kg). By varying the frequency one can define the selected mass. The lower f is the larger are the selected clusters, which need more time to drift due to their larger mass. As the movement of the ions perpendicular to their original beam direction is independent of their forward velocity, mass resolution and calibration do not depend on the ion beam energy.

3.1.3.1 Mass resolution and error tolerance

Figure 3.8 shows a mass spectrum which was measured with a Faraday cup in the preparation chamber of the surface science facility (see section 3.2). It is visible that for cluster sizes between Ag_{60}^+ to Ag_{70}^+ single mass peaks are barely visible. For higher cluster sizes the peaks overlap.

A mass spectrum of large clusters from Ag_{100}^+ to Ag_{1500}^+ is shown in Figure 3.9. For such large cluster sizes no single mass peaks are visible, but a broad distribution which represents the clusters that are produced by the magnetron sputter source. The mass selector cuts out a small region of this distribution and is able to select a special cluster size with an error of maximally 1 %.

In the following it is explained how the very small error of < 1 % for the accuracy of the mass selection is connected to the mass spectrum shown in Figure 3.8. In [28] it was shown that single mass peaks can be fitted by a Gaussian

$$f(x) = \frac{A}{w\sqrt{\pi/2}} \cdot \exp(-2\frac{(x-x_c)^2}{w^2}). \tag{3.2}$$

A is the area under the Gaussian, x_c the maximum of the Gaussian and $w = 2\sigma$ is the width of the Gaussian which is defined by the two inflection points. Besides, the width is defined as $w = FWHM/\sqrt{\ln 4}$, where $FWHM$ denotes the full width at half maximum. The mass resolution is defined as

$$\frac{m}{\Delta m} = \frac{x_{c,i}}{w_i}. \tag{3.3}$$

where $x_{c,i}$ is the position of the maximum of the Gaussian and w_i its width. The mass resolution of the mass selector used here is independent of mass, i.e. $m/\Delta m$ = const.

For $w = 1$ three pairs of Gaussians (red and blue) and their respective sum curve (black) are plotted in Figure 3.10. The x-axis represents the number of atoms in a mass spectrum. The red and blue Gaussians on the left are shifted by 1.8 σ, the pair of Gaussians in the middle are shifted by 2 σ and the pair on the right by 2.2 σ. The sum curves demonstrate that one can identify two different peaks, if the single Gaussians are shifted by more than 2 σ. The plateau in the sum curve consisting of two Gaussians shifted by 2 σ lets assume that it consists of two Gaussians, but only the sum curve on the right, which has been shifted by more than 2 σ shows two maxima.

In [28] it was also shown that strongly overlapping mass peaks can be fitted on the one hand by a sum of Gaussians

$$g(x) = \frac{A}{w\sqrt{\pi/2}} \sum_n \exp(-2\frac{(x-x_n)^2}{w^2}), \tag{3.4}$$

with $x_n = n$ and on the other hand by a cosine

$$c(x) = 1 + a \cdot \cos(2 \cdot \pi \cdot x) \tag{3.5}$$

if the boundary area is neglected.

In this case of mass spectra with an x-axis representing the number of atoms per cluster, the maxima of the mass peaks are shifted by 1 (1 atom) and the sum curve shows an oscillation (Figure 3.11).

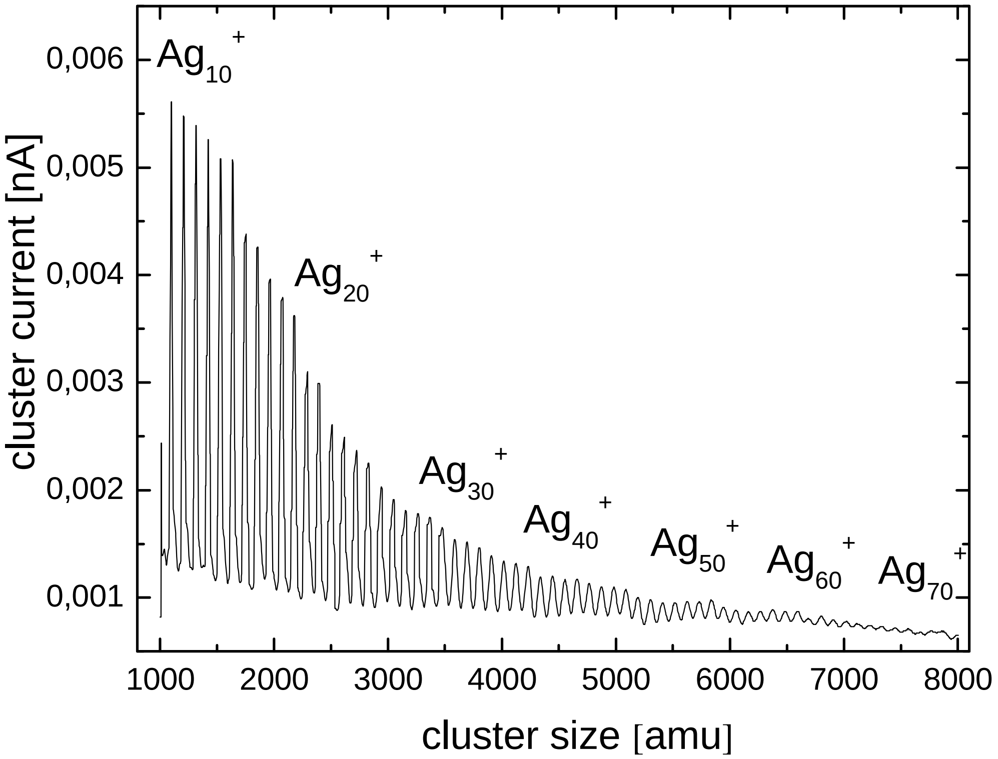

Figure 3.8: Mass spectrum of Ag_{10}^+ to Ag_{70}^+, measured with the Faraday cup in the preparation chamber of the surface science facility. A single Ag atom has an atomic weight of 107.87 ≈ 108 amu.

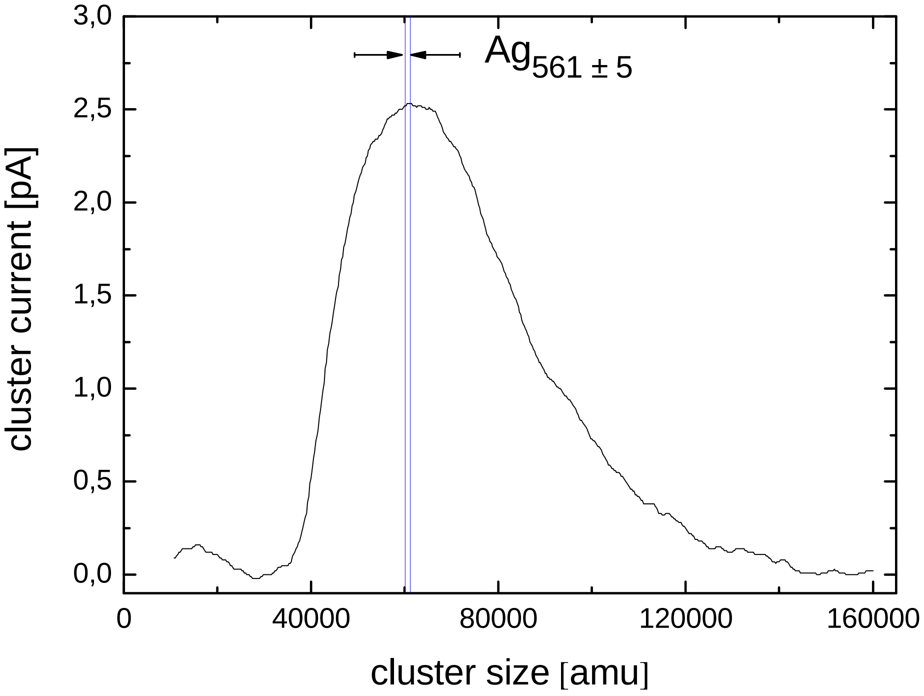

Figure 3.9: Mass spectrum of Ag_{100}^+ to Ag_{1500}^+. The mass selector cuts one size out of the broad distribution.

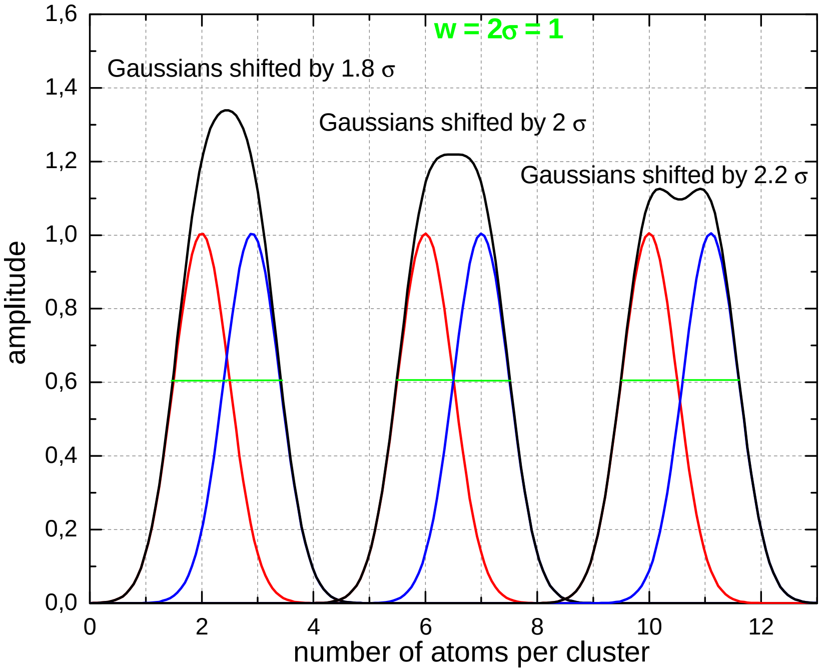

Figure 3.10: Three pairs of Gaussians (for N = (2,3); (6,7) and (10,11)), shifted by 1.8 σ, 2 σ and 2.2 σ and their respective sum curves.

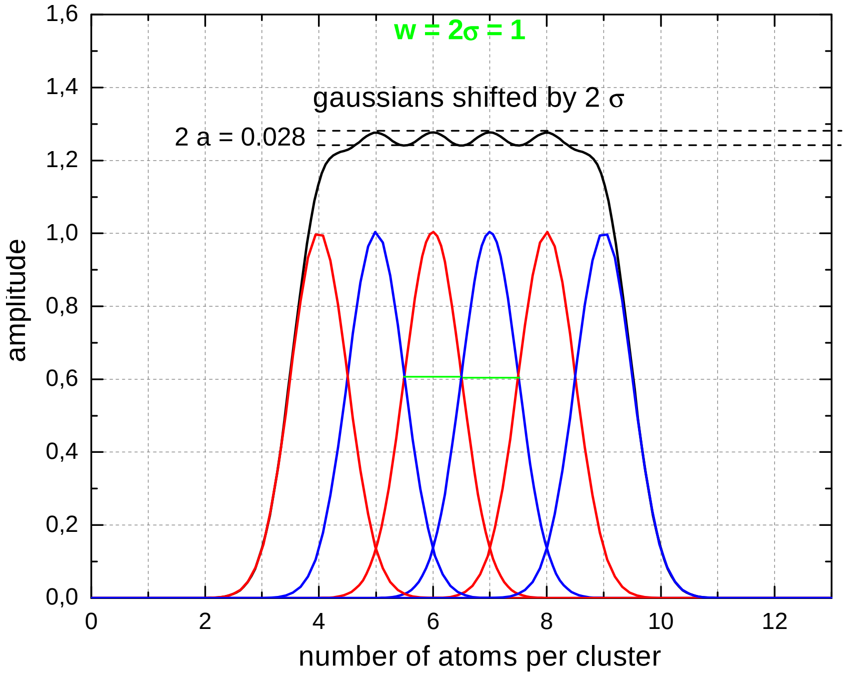

Figure 3.11: Gaussians shifted by 2 σ to each other and the corresponding sum curve, which shows an oscillation.

In [28] it was shown that in a region with constant *w* the mass spectrum can be fitted by a sum of Gaussians as well as by a cosine, if *w* is equal or larger than around 0.5. The relative mass resolution $m/\Delta m$ is constant for the mass selector used here, which means that *w* becomes larger for a higher number of atoms per cluster. The relation between *w* and *a*, the amplitude of the cosine, was calculated in [28] and is shown in Figure 3.12. The smaller *w* is, the larger is the amplitude *a* because the mass peaks are well separated from each other.

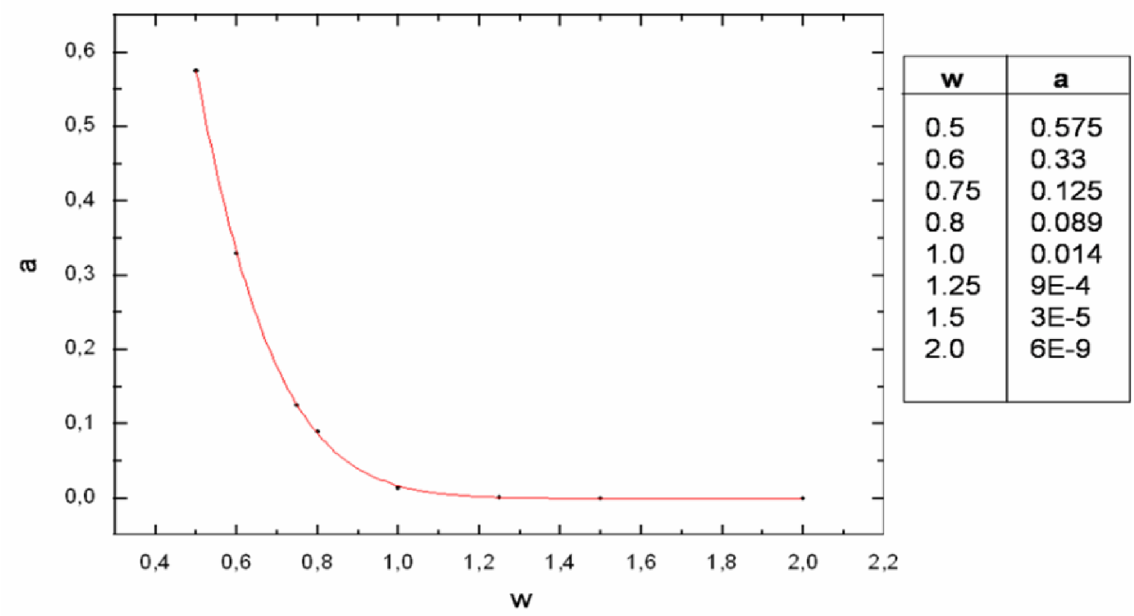

w	a
0.5	0.575
0.6	0.33
0.75	0.125
0.8	0.089
1.0	0.014
1.25	9E-4
1.5	3E-5
2.0	6E-9

Figure 3.12: Amplitude *a* of the cosine as function of the width *w* of the sum of the Gaussians [28] *w* = 1→ *a* = 0.014 corresponds to Figure 3.11.

For $w = 1$, which is the case for already strongly overlapping peaks, *a* has a value of 0.014, which is around 1 % of *w*, still large enough to distinguish the mass peaks from each other (Figure 3.12). For larger *w*, *a* converges exponentially to zero and consequentially one cannot distinguish the mass peaks anymore. The reason for the selected mass having an error of < 1 % is explained in the following.

For Ag_N with N = 50 single mass peaks are still clearly visible. Thus, for the selected cluster mass $m = x_{c,I} = 50\, m_{Ag}$ (50 times the mass of an Ag atom), $w_i = 2\sigma_i$ is less or equals 1 m_{Ag}. Since the relative mass resolution $m/\Delta m$ is constant, it follows generally:

$$\frac{m}{\Delta m} = \frac{x_{c,i}}{w_i} = \frac{x_{c,i}}{2\sigma_i} > \frac{50\, m_{Ag}}{1\, m_{Ag}} = 50 \tag{3.6}$$

and thus

$$\sigma_i < x_{c,i}/100\,. \tag{3.7}$$

This means that each cluster size is selected at least with

$$m = \overline{m} \pm 1\sigma \tag{3.8}$$

$$= \overline{m} \pm 1\%\,. \tag{3.9}$$

3.2 The surface science facility

The Omicron LT-UHV surface science facility consists of an analysis chamber containing the LT scanning tunneling microscope (STM) and a preparation chamber [96]. The chambers are connected by a valve which is opened if samples are transported with the manipulator, an x-y-z sample translator. A liquid helium (LHe) flow cryostat provides cooling with full 360° of rotation. The manipulator contains three sample holders which are shown in Figure 3.13: a sample holder which is heatable up to 600°C (HB holder), a sample holder which can be cooled down to T = 10 K (LT holder) [103] and a sample holder for the in situ preparation of the STM tip (TP holder). Both chambers are pumped by ion getter and titan sublimation pumps to base pressures in the 10^{-11} mbar range. The preparation chamber is additionally pumped by a turbo pump. In the preparation chamber tips and samples can be heated and sputtered as well as be exposed to various evaporation sources and gases. Besides, the Faraday cup for the cluster current measurement is located in the preparation chamber, as depicted in Figure 3.14.

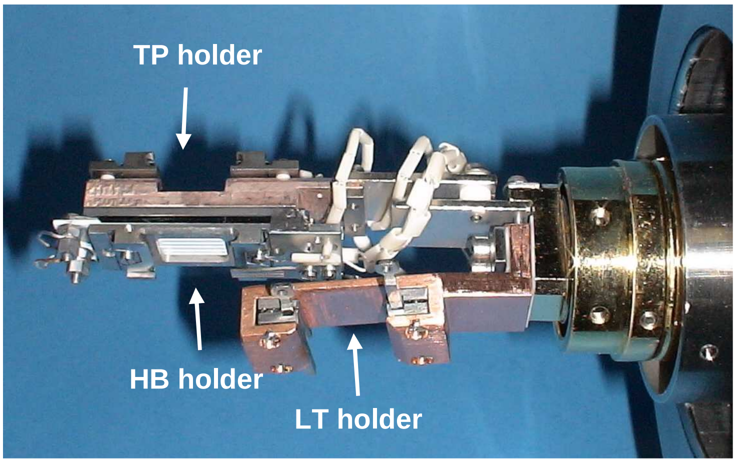

Figure 3.13: Picture of the HB, LT and TP sample holder attached to the manipulator.

The Faraday cup consists of two electrically isolated boxes. The cluster current enters the inner box of the Faraday cup, connected to a picoamperemeter, through a 4 mm large hole. The outer box works as shielding. It is possible to use a channeltron ion multiplier, if the cluster current is too low to measure it directly. The construction details of the Faraday cup are explained in [28].

A high-resolution photoelectron analyzer and a He discharge lamp which allow photo electron spectroscopy measurements are attached to the preparation chamber [97]. The analysis chamber contains in the STM block an LHe bath cryostat surrounded by an LN_2 dewar (see Figure 3.14). Six samples can be put inside a storage carousel in the analysis chamber, which can be cooled to LN_2 temperature. The STM can be cooled down to 5 K, if the inner bath cryostat is filled with LHe, or down to 77 K, by filling the cryostat with LN_2. The advantage of an STM cooled to 5 K is the small thermal drift, only 0.2 nm/h, but the handling is more complex than for an LN_2 cooled cryostat.

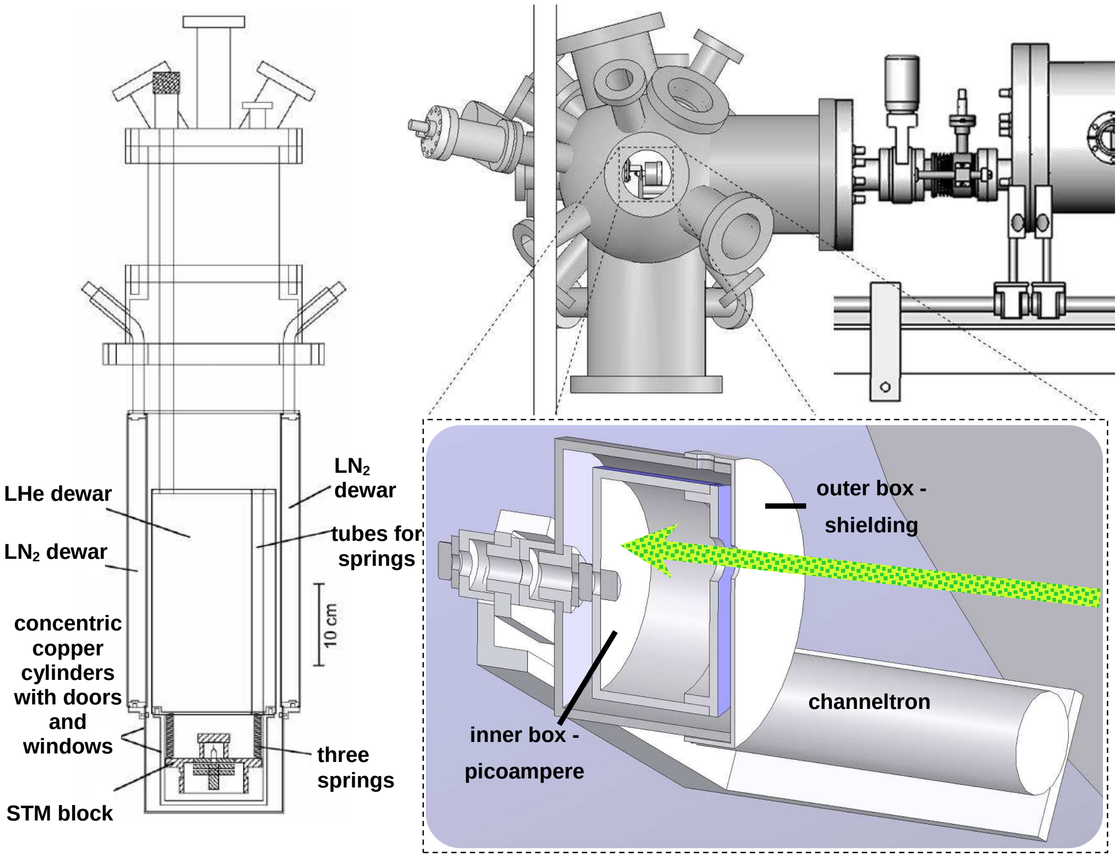

Figure 3.14: Left: Schematic of the analysis chamber of the surface science facility, right: preparation chamber with the Faraday cup.

3.2.1 The C_{60} evaporator

Attached to the preparation chamber is a custom-built C_{60} evaporator, which contains a crucible made of quartz glass with solid C_{60} powder resistively heated up to 450°C. The C_{60} sublimates through an aperture, which can be closed by a shutter during the start of the heating process and opened while evaporating C_{60} onto the sample. The C_{60} evaporator was planed and constructed by TORSTEN RICHTER, who in detail explained the technical and physical properties of the C_{60} evaporator, the evaporation process and the appropriate parameters in [104]. Photographs of the setup of the C_{60} evaporator are shown in Figure 3.15.

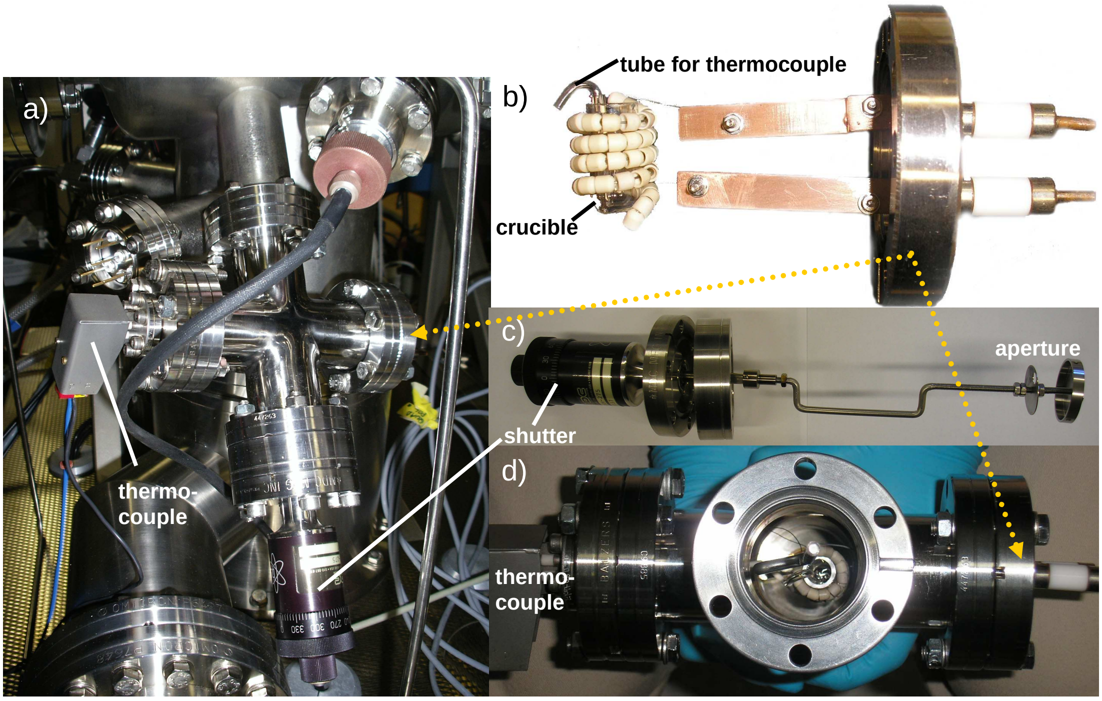

Figure 3.15: a) C_{60} evaporator as attached to the preparation chamber, b) C_{60} evaporator with ceramic shielded heating wire around the quartz glass crucible. The small tube is used for a thermocouple, which measures the temperature of the C_{60}, c)+d) setup of the C_{60} evaporator system with crucible, shutter, aperture and thermocouple.

3.2.2 The evaporator with integrated flux monitor

A second evaporator which is attached to the preparation chamber is the evaporator with integrated flux monitor (EFM) which was used within this thesis to evaporate silver and lead (Pb). The evaporator allows an in situ flux measurement utilizing the flux of ionized atoms produced by the electron-beam heating of the tantalum (Ta) crucible filled with Ag or Pb. Figure 3.16 shows photographs of the evaporator.

The EFM is surrounded by a cooling shroud, a water cooled copper cylinder. The crucible is connected with the external power supply by a barrel connector and a slide bearing. Opposite to the crucible, which represents the anode, there is a filament (cathode) and an ion collector which serves as a flux monitor. The filament emits electrons which are accelerated to the crucible due to a high voltage of 800 V. The electron bombardment heats up the crucible and the Ag or Pb evaporates.

A small part of the evaporated atoms is ionized by the electron bombardment. Measured with the ion collector this can be used to determine the atom flux after a corresponding calibration (cf. section 6.4.1.1).

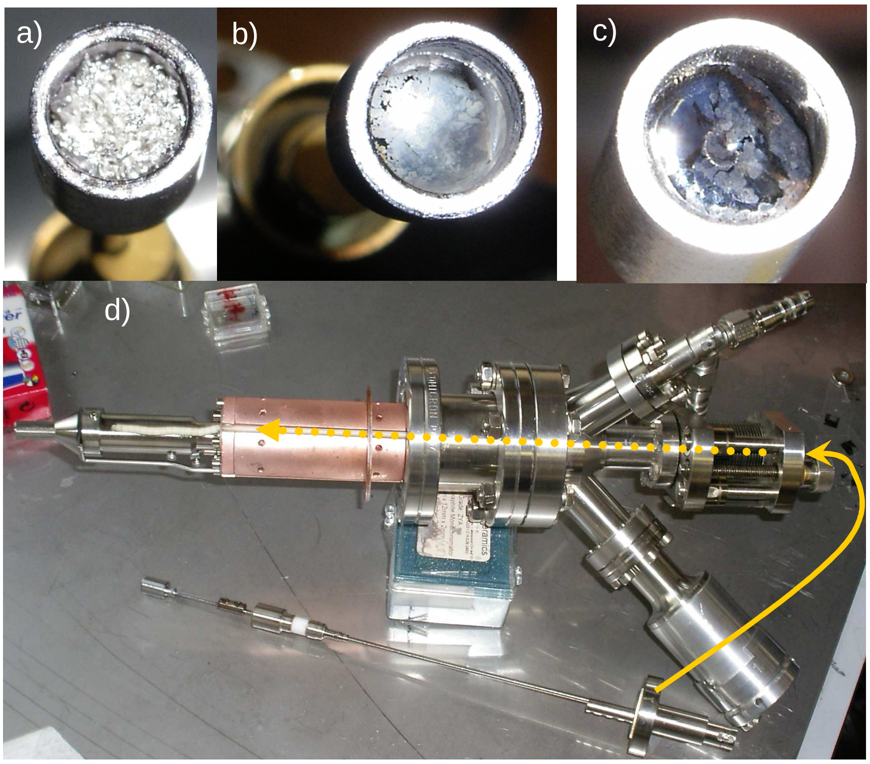

Figure 3.16: a) Ta crucible filled with Ag granulate, b) Ta crucible with melted Ag, c) Ta crucible with melted Pb, d) complete setup of the evaporator.

4 EXPERIMENTAL TECHNIQUES

In this chapter the experimental techniques which were used within this thesis are presented. The geometric and electronic properties of size selected Ag clusters and grown Ag or Pb islands as well as C_{58} and C_{60} were studied by scanning tunneling microscopy, scanning tunneling spectroscopy and ultraviolet photoelectron spectroscopy.

4.1 Scanning tunneling microscopy

STM is a powerful tool to investigate the electronic and geometric properties of solid-state surfaces. An STM produces a topographic image in real space of conducting and semi-conducting materials down to atomic resolution. This method was developed by GERD BINNIG and HEINRICH ROHRER [105, 106, 107] in 1982, who got the noble prize together with ERNST RUSKA in 1986.

For STM a sharp tungsten or platinum-iridium tip is used to investigate a conducting or semi-conducting sample. To prepare an extremely sharp tunneling tip, a piece of tungsten wire is electrochemically etched in KOH or NaOH. After that follows a cycle of in situ sputtering, heating and self-sputtering. The tip is approached to the sample down to less than one nanometer distance between tip and surface. This distance represents a potential barrier for electrons. Due to the quantum mechanical tunneling effect a tunneling voltage between tip and substrate leads to a tunneling current through the barrier. Depending of the polarity of the tip-sample bias, the electrons flow from the occupied states of the tip to the unoccupied states of the surface or vice versa. Piezo electric crystals move the tip over the sample in an area of some square nanometers to a few square micrometers. There are two possibilities to get a direct image of the sample: it is possible to record the local variations of the tunneling current while the distance between tip and sample remains constant (constant height mode). This method has the disadvantage that the tip could collide with large objects on the sample surface which results in a destruction of the tip and/or the surface. The mostly used method is the constant current mode, which is based on recording the variations of the local z-position of the tip relatively to the surface, while the tunneling current is constant. STM enables to measure the height of an object with adequate precision, but it is not possible to measure the width of an object with STM. This is due to the fact that the width is always a convolution of the shape of the tip and the scanned object. Figure 4.1 illustrates this effect schematically.

The basic principle of the function of an STM is the quantum mechanical tunneling effect which was independently discovered and explained by G. GAMOW [110] and E. U. CONDON together with R.W. GURNEY [108, 109] in 1928.

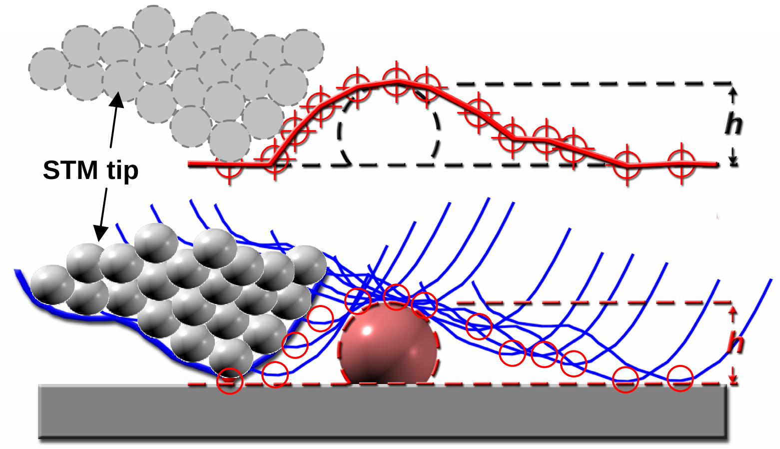

Figure 4.1: Top: line profile of a surface scanned by an STM tip and broadening effect due to the convolution of tip shape and object on the surface. Bottom: Trajectory and shape of the STM tip which leads to the line profile at the top.

The first experimental observation of the tunneling effect was made by R. W. Wood in 1897 [111], who could not explain the phenomenon yet. Within quantum mechanics, the wave function of an object with a kinetic energy E_{kin} has a non-zero probability to penetrate (*tunnel*) into a barrier, e.g. a potential well, with the height V_0, if $E_{kin}<V_0$. This process is impossible within classical physics. Inside the potential well the wave function decays exponentially, which results in a plane wave with small amplitude on the other side of the potential well. The tunneling process is visualized in Figure 4.2.

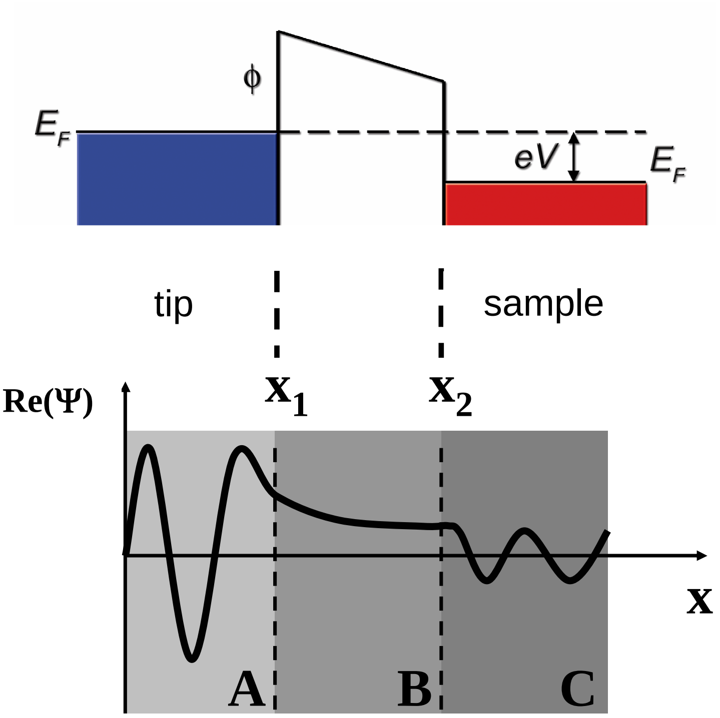

Figure 4.2: Top: model of a one dimensional potential well between tip and sample, which have an equal work function Φ. Bottom: a wave (A) penetrates a potential barrier, decays exponentially (B) and leaves the barrier with a smaller amplitude than before (C).

If the wave function of a second object on the other side of the barrier also penetrates the barrier, the wave functions of the two objects overlap and an exchange of electrons becomes possible. An approximation for this two-electrode-tunneling through a trapezoidal potential barrier was developed by H. BETHE and A. SOMMERFELD in 1933 [112] and was improved by R. HOLM and B. KIRSCHSTEIN [113, 114]. In 1963 J. SIMMONS calculated a general tunnel current density for all kinds of potential barriers including field emission [115]. In 1961 J. BARDEEN calculated the transition rate from an eigenstate describing an electron on one side of the barrier to an eigenstate describing this electron on the other side of the barrier [116]. Based on the work of J. BARDEEN, J. TERSOFF and D. R. HAMANN developed a theory for the tunneling process applicable especially for the STM [117, 118]. Since the microscopic structure of the tip is not known, they modelled it as a locally spherical potential well, where it approaches nearest to the surface. A schematic picture of the tunneling tip as modeled by J. TERSOFF and D. R. HAMANN is shown in Figure 4.3.

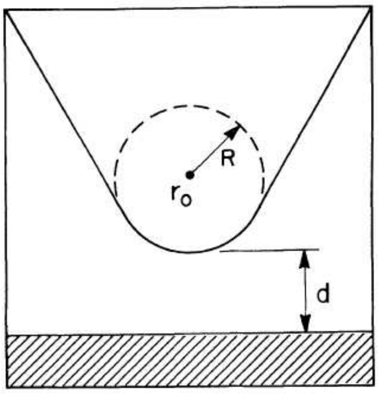

Figure 4.3. Schematic illustration of the tunneling geometry of Tersoff and Hamann [117, 118]. d is the distance of the nearest approach, r_0 is the center of the curvature of the tip.

An STM image does not directly picture the atoms on the surface, but the local electronic density of states (LDOS) at the sample surface close to the Fermi energy. The DOS of the tip and the DOS of the scanned surface influence the STM image. For low voltages the tunneling current I is proportional to the voltage V, the density of states of the tip $\rho_{tip}(E_F)$ and the density of states of the sample at the position r_0, i.e. $\rho_{sample}(\vec{r}_0, E_F)$:

$$I \propto V \cdot \rho_{tip}(E_F) \cdot \rho_{sample}(\vec{r}_0, E_F) \tag{4.1}$$

Because the DOS of the surface states decays exponentially in the vacuum ($\rho(\vec{r}_0, E_F) \propto \exp(-2qd)$), the tunneling current I can be written as

$$I \propto \exp(-2qd) \text{ with } q = \sqrt{\frac{2m}{\hbar^2}\bar{\phi}} \tag{4.2}$$

In this relation d is the distance between tip and sample, m the electron mass, $\hbar$ Planck's constant divided by 2π and $\bar{\phi}$ the average work function of tip and sample. Thus small changes of the distance between tip and sample lead to huge changes of the tunneling current.

For higher voltages, but still with $eV < \bar{\phi}$, one needs a different model to calculate the tunneling current. In this case all the different energies which are involved in the tunneling process contribute to the tunneling current:

$$I(d,V) \propto \int_0^{eV} \rho_{tip}(E - eV)\rho_{sample}(E)T(d,V,E)dE \tag{4.3}$$

T(d, E, V) is the transmission coefficient, which can be approximated (Wentzel-Kramers-Brillouin approximation [119, 120, 121]) for a trapezoidal tunneling barrier as

$$T(d,E,V) \propto \exp\left(-2d\sqrt{\frac{2m}{\hbar^2}\left[\bar{\phi} + \frac{eV}{2} - E\right]}\right). \tag{4.4}$$

For the case $eV > \bar{\phi}$ field emission effects occur [122, 123].

If an image is taken at a certain negative voltage –V at the sample, the image shows the occupied states with energies from the Fermi energy to eV below the Fermi energy. In contrast, in the case of positive voltages, only unoccupied states are imaged.

As already mentioned the height of an object on the surface is correlated with its local electronic density of states (LDOS) and determines the contrast of an STM image. One has to be careful by interpreting bright colors always as “higher objects” because the electronegativity of e.g. adsorbates plays an important role in defining the contrast of an STM image. In [124] and [125] it is shown experimentally and theoretically that adsorbates with low electronegativity, like carbon and sulfur, appear as bumps, whereas oxygen and fluorine, possessing a high electronegativity, are characterized by a depression with negative corrugation.

4.2 Scanning tunneling spectroscopy

In addition to topographic measurements, which give information about the geometrical structure of a surface, the STM can be operated in the spectroscopy mode in order to investigate the electronic properties of a surface, e.g. of a cluster. In this case the position of the tip is kept constant and the tunneling current *I* is measured dependent of the gap voltage *V*. Due to the fact that an electron transport only takes place from occupied to unoccupied states, a measured *I(V)* spectrum contains information about the local density of states of the sample. If occupied or unoccupied states are investigated, depends on the polarity of the voltage, which is visualized in Figure 4.4.

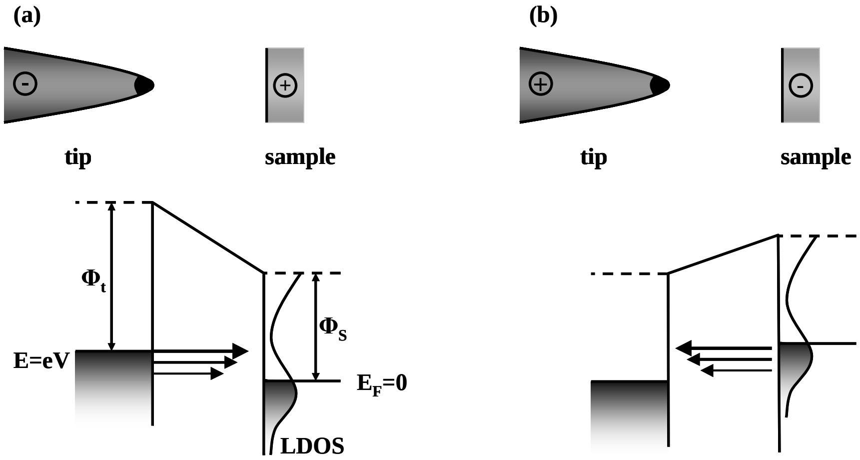

Figure 4.4: Principle of scanning tunneling spectroscopy (STS). a) For a positive sample voltage occupied states are investigated, b) a negative sample voltage leads to investigation of unoccupied states.

The local density of states of the sample can be calculated startin from equation (4.3) as the derivative *dI/dV*:

$$\begin{aligned}\frac{dI(d,V)}{dV} \propto & \left[e\rho_{tip}(E-eV)\rho_{sample}(E)T(d,V,E)\right]_{E=eV} \\ & + \int_0^{eV} \tfrac{d\rho_{tip}(E-eV)}{dV}\rho_{sample}(E)T(d,V,E)dE \\ & + \int_0^{eV} \tfrac{dT(d,V,E)}{dV}\rho_{tip}(E-eV)\rho_{sample}(E)dE\end{aligned} \tag{4.5}$$

The second term can be neglected due to the fact that there are no strong variations for ρ_{tip} for different energies. This is the case, if the tip does not have a dominant structure in the density of states for the investigated energies. For the interpretation of the STS data it is important that the influence of the tip is low and the properties of the measured structures are dominantly defined by the properties of the sample. If the transmission *T(d, V, E)* does not show any sharp structures, the third term can be neglected as well. Because equation (4.4) describes an exponential dependence on the energy for *T(d, V, E),* this condition is fulfilled. Thus only the first term defines the differential conductivity and it follows

$$\frac{dI(d,V)}{dV} \propto \rho_{tip}(0)T(d,V,eV)\rho_{sample}(eV)\,. \tag{4.6}$$

For the reason that mostly only the region close to the Fermi energy is investigated, *T(d, V, E)* is proportional to a constant background. The density of states of the tip for $E_F = 0$, $\rho_{tip}(0)$ is a constant as well, so the differential conductivity can be written as

$$\frac{dI(d,V)}{dV} \propto \rho_{sample}(eV)\,. \tag{4.7}$$

This shows that the interesting parameter is *dI/dV*, which gives information about the LDOS of the sample. By reversing the polarity of the voltage it is possible to investigate occupied and unoccupied states. It is very important that the distance *d* between tip and sample is constant. This is guaranteed by stabilizing the tip with activated loop gain by given “setpoint” values for tunneling voltage and current up to a stable scanning of the tip. Then the loop gain is switched off and the measurement of the *dI/dV* curve with constant z-piezo voltage starts. If the distance d for two different spectra is not identical due to varying conditions on different positions on the sample, it is possible that the spectra have different intensities and have to be normalized. The signal amplitude is defined by the set point (I, V) before the spectroscopy. For low voltages and high currents the signal-to-noise ratio increases, which unfortunately sometimes leads to instable tunneling conditions.

Several spectra for different lateral tip locations can be displayed as a set of voltage dependent *dI/dV* curves. Another possibility is to measure the differential conductivity with constant voltage as a function of the lateral sample position, as it was done in the past in experiments in Dortmund [159, 127, 128]. This results in STS maps, which each show the DOS of the sample with spatial resolution for a particular energy.

As an improved technique for the measurement of STS spectra it is possible to use a lock-in amplifier, which directly enables the measurement of *dI/dV* curves and further improves the signal-to-noise ratio [129]. This method replaces the measurement of *I(V)* curves with subsequent numerical differentiation. However, for the STS data taken within this work the lock-in detection method has not been an improvement and most of the spectra measured within this thesis were taken without the lock-in detection method.

4.3 Ultraviolet photoelectron spectroscopy

Another spectroscopy method used here is UPS, a surface sensitive analysis method, which enables the investigation of the occupied states of a sample. This technique is based on the photoelectric effect which was first discovered in 1887 by H. HERTZ [130] and W. HALLWACHS [131]. In 1899 J. J. THOMSON observed experimentally that the particles which are emitted by irradiating light onto a surface are electrons [132], whose existence was already predicted by GEORGE JOHNSTONE STONEY in 1874 [133]. In 1900 P. LENARD discovered that the energy of the emitted electrons depends on the frequency of the light and the irradiated material and is independent of the intensity of the light [134]. Finally A. EINSTEIN won the noble prize for the discovery that the photoelectric effect is based on the quantization of light [135]. Therefore the Einstein relation is the most important formula in this context:

$$E_{kin} = h\nu - \phi_s - E_B \tag{4.8}$$

E_{kin} is the kinetic energy of the electrons, h Planck’s constant, ν the light frequency, ϕ_s the work function of the sample and E_B the binding energy of the electron before emission.

About 1956 Kai Siegbahn developed x-ray photoelectron spectroscopy (XPS) for surface chemical analysis, using x-ray sources to study energy levels of atomic core electrons. The ultraviolet version of this technique (UPS) was developed by David W. Turner to study the photoelectron spectra of free molecules in the gas phase with a helium discharge lamp as photon source [136]. The method was later extended to the study of solid surfaces, where it is usually described as photoemission spectroscopy (PES). Figure 4.5 shows the principle of the XPS and UPS technique.

By irradiating a sample with light the photon energy is transferred to the electrons in the sample. If their energy is high enough to overcome the vacuum energy, the electrons are emitted and can be detected as function of their kinetic energy. The resulting spectra show broad or sharp peaks, which represent the different states or bands the electrons belong to. UPS is particularly sensitive to the surface region (to 10 nm depth) due to the short free mean path of the emitted photoelectrons. It is therefore used to study valence energy levels and chemical bonding, adsorbed species and their binding to the surface, as well as their orientation on the surface. The observed structures result from the energy dependency of the optical electron excitation, which correlates strongly to the combination of the DOS of the initial and final states of the electrons [137]. With increasing energy the structure in the final DOS decreases, so the intensity of the measured signal represents the occupied states of the sample (Figure 4.5).

In contrast to STS, UPS leads to an averaged spectrum of the states of the whole sample area which is irradiated with light and from where the electrons are collected.

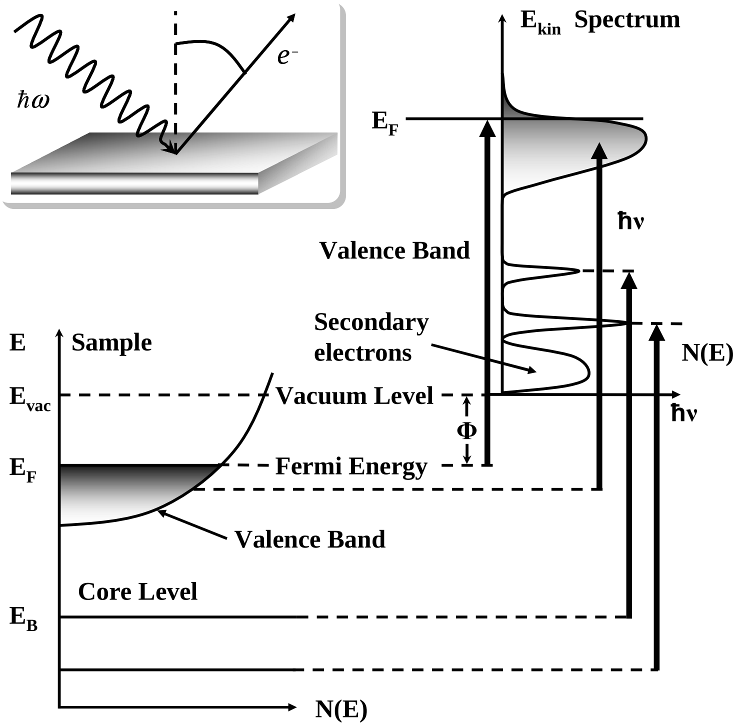

Figure 4.5: By irridiating a surface excited electrons are emitted. The detected electrons lead to a spectrum which is an image of the DOS of the sample.

5 SAMPLE PREPARATION

For the deposition and investigation of clusters on surfaces as well as for the controlled growth of metal islands or C_{60} films on surfaces it is necessary to have clean surfaces without adsorbates, a water film or other kinds of contamination. For this reason this chapter deals with the cleaning and preparation of the sample, from the bare substrate up to the complete sample system.

5.1 Sample substrate preparation

Within this thesis highly orientated pyrolytic graphite (HOPG) and gold on mica (Au/mica) were used as sample substrates. For the calibration of the Ag evaporator an Ag(111) single crystal was used. For each substrate there are special preparation steps, which have to be performed to get a clean surface.

5.1.1 Preparation of the HOPG substrate

HOPG has a layered structure with each graphene layer composed of a planar arrangement of hexagonal carbon rings. Therefore graphite is highly anisotropic. The trigonal bonding in each graphene sheet involves overlap of carbon sp^2 hybrid orbitals in the plane, whereas the overlap of carbon $2p_z$ orbitals produces delocalized rings of π electrons lying above and below each carbon ring, which makes graphite a good electrical conductor. The graphene layers are bonded to each other by weak van der Waals forces, so that they can easily slide one over another, which is why graphite is soft and slippery. HOPG is highly oriented with respect to the layer-stacking direction with an angular spread of the *c* axes of less than one degree. Every second carbon atom has a neighbor in the subjacent layer and thus has a different DOS as an atom without an subjacent neighbor. The lattice constant of HOPG is around 0.25 nm.

For HOPG being chemically inert it can be exposed to air without oxidizing and for the first preparation step of HOPG vacuum conditions are not necessary. By removing the upper layers of the HOPG sample with an adhesive tape one gets a plane and smooth surface.

The cleaved surface contains single atomic steps or steps of several atomic layers with a single step height of 0.34 nm [138]. As a second preparation step the HOPG sample is heated under UHV conditions for one hour (h) at T = 600°C to remove the water layer from the surface of the HOPG sample. After this procedure the HOPG sample is ready for being used for an evaporation or deposition experiment. Figure 5.1 shows a cleaved HOPG sample which is fixed by spot welded tantalum stripes onto an Omicron sample holder and an STM image of HOPG with atomic resolution.

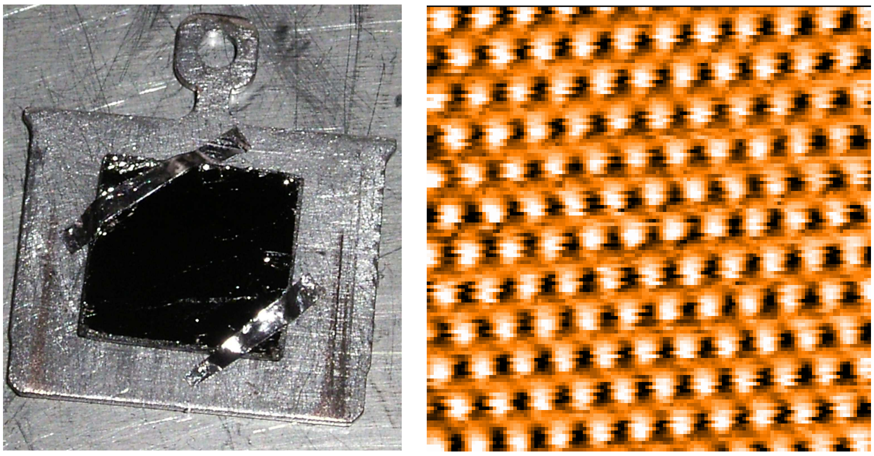

Figure 5.1: Left: Cleaved HOPG sample fixed onto an Omicron sample holder, right: 2×2 nm² STM image of HOPG.

In order to remove e.g. deposited clusters or a C_{60} film for a further experiment an ex-situ cleavage with adhesive tape is again necessary.

5.1.2 Preparation of the Au(111)/mica substrate

The Au/mica substrate has to be prepared differently than the HOPG substrate. The gold is oriented in (111)-direction and was evaporated on mica by the preparation laboratory of Technische Universität Dortmund. An STM image and a photograph of an Au/mica sample are visible in Figure 5.2.

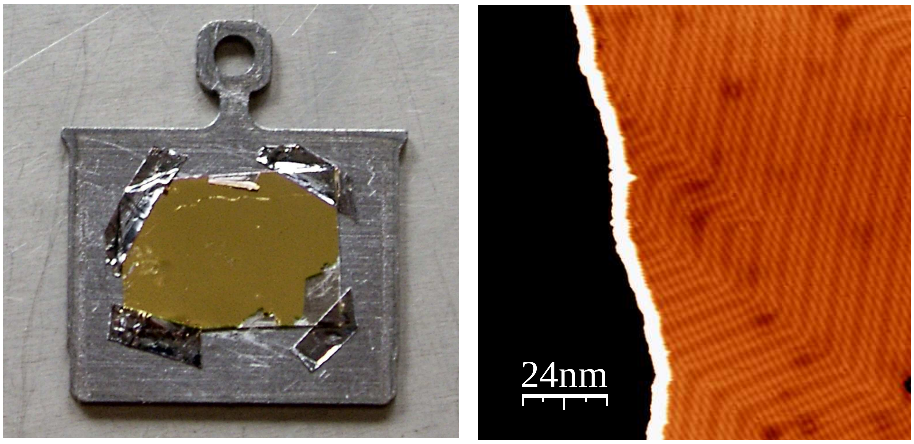

Figure 5.2: Left: Au/mica sample on an Omicron sample holder, right: 118×118 nm² STM image of an Au(111) surface imaged within this thesis. The typical 23×√3 herringbone reconstruction of Au(111) is visible [141]. More details about the properties of Au(111) can be found in [142].

Mica (from Latin: micare = to gleam) includes a group of sheet silicate minerals. The most prominent characteristic of mica is the highly perfect basal cleavage, which can be explained by the hexagonal sheet-like arrangement of its atoms. This atomically flat surfaces lead to the growth of µm sized crystallites with (111) orientation, if Au is evaporated on mica at T ≈ 500°C [139,140]. The flat (111) surfaces on top of these crystallites are used in the experiments here. After the exposure to air the Au/mica first has to be heated for 1 h at 500°C to desorb the water layer from the surface. Besides, impurity atoms which are located in the bulk of the sample diffuse to the surface. Then the Au/mica is sputtered for 1 h at RT with 1 keV Ar ions. This removes several monolayers of the gold sample in order to clean the surface from adsorbates. Due to the surface roughening by the Ar ions, the Au/mica has to be heated again for 45 minutes (min) at 300°C to heal the defects and flat the surface. The temperature of the second annealing step has to be lower to prevent the appearance of impurity atoms from the bulk at the sample surface. The Au/mica sample can be used for several experiments until the Au layer on mica becomes too thin for a further sputtering. The first heating step is only required after exposure to air, otherwise the sputtering process and annealing at 300°C is sufficient to get a clean Au/mica surface again.

5.1.3 Preparation of the silver single crystal

For the calibration of the Ag evaporator Ag was evaporated on an Ag(111) single crystal. Due to the fact that the Ag(111) single crystal was exposed to air, two heating-sputtering cycles were necessary to clean the surface. Both the RT sputtering and the heating procedures took 1 h. The heating temperatures were 550°C for the first heating and 500°C for the second heating. The two heating-sputtering cycles were followed by a last annealing step at 430°C for 1 h in order to heal the defects which were due to the sputtering.

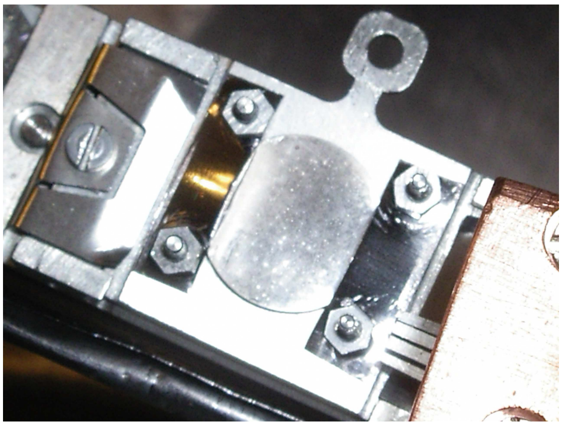

Figure 5.3: Ag(111) single crystal fixed with screws on an Omicron sample holder. The sample is positioned in the heatable sample holder of the manipulator of the surface science facility.

5.2 Preparation of the fullerene layer

The well prepared and clean sample surfaces are now ready for being covered with fullerenes. In the following sections the preparation steps are explained in detail.

5.2.1 Preparation of the C_{60} layer

As already mentioned in section 2.2.1, fullerenes, especially C_{60}, are well suited for the deposition of clusters due to their function as a buffer layer, their stability and inertness at RT, the electronic decoupling of the clusters from the substrate and the large corrugation period which hinders the cluster diffusion (see Figure 5.5 b)). The C_{60} molecules are deposited onto the sample surface by using the C_{60} evaporator, which is presented in section 3.2.1. Due to the different strength of interactions between C_{60}–Au(111)/mica and C_{60}–HOPG the preparation steps differ in some ways. The following STM images of C_{60}/Au(111) and C_{60}/HOPG were all taken within this thesis.

5.2.1.1 Evaporation of C_{60} on Au(111)

For the evaporation of C_{60} on Au(111)/mica the C_{60} evaporator is heated for 20 min up to the temperature of $T_{C60} \approx 440°C$ which corresponds to 17.15 mV measured with the thermocouple (see section 3.2.1). After that 1 monolayer (ML) C_{60} is evaporated on Au(111) by opening the shutter of the evaporator for 5 min, followed by an annealing of 1 ML C_{60}/Au(111) for 30 min at 250°C. The annealing is necessary to get an ordered C_{60} ML because due to the relatively strong interaction between C_{60} and Au(111) the C_{60} is not mobile enough to build an ordered structure at RT [143]. The disordered structure of the C_{60}/Au(111) system without annealing is demonstrated in Figure 5.4.

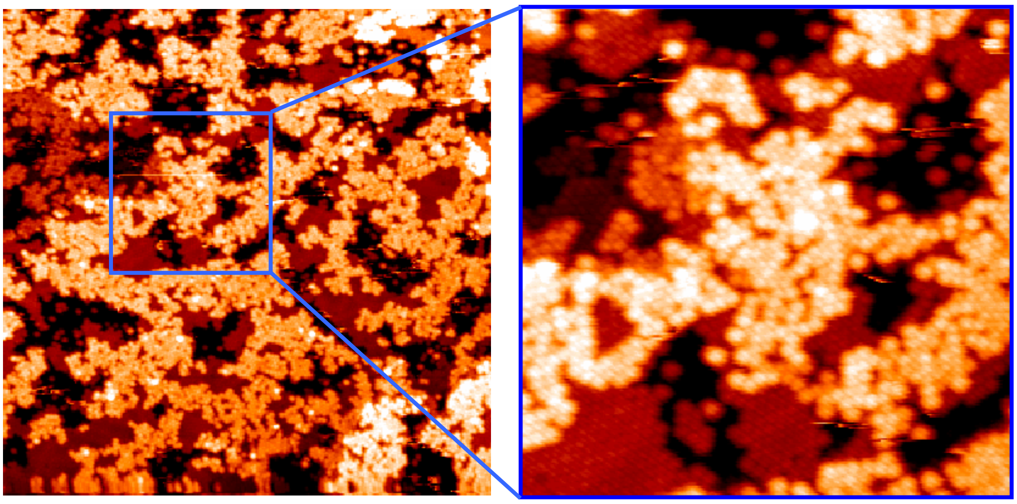

Figure 5.4: 150×150 nm² STM image (left) and 50×50 nm² STM image (right) of disordered C_{60}/Au(111).

Most of the experiments were carried out with slightly more than 1 ML C_{60} in order to have the possibility to study the thermally induced processes of size selected clusters on 1 and 2 ML C_{60}. Therefore, after the annealing process of 1 ML C_{60}/Au(111) less than an additional ML C_{60} is evaporated onto the sample. This time an annealing is not necessary because the C_{60}-C_{60} interaction is not as strong as the metal-C_{60} interaction, so that the C_{60} molecules of the second ML are able to form ordered islands on the first ML. STM images of a surface with ordered C_{60} taken at 77 K are depicted in Figure 5.5. The different orientations which are visible in Figure 5.5 c) are discussed in section 6.1.

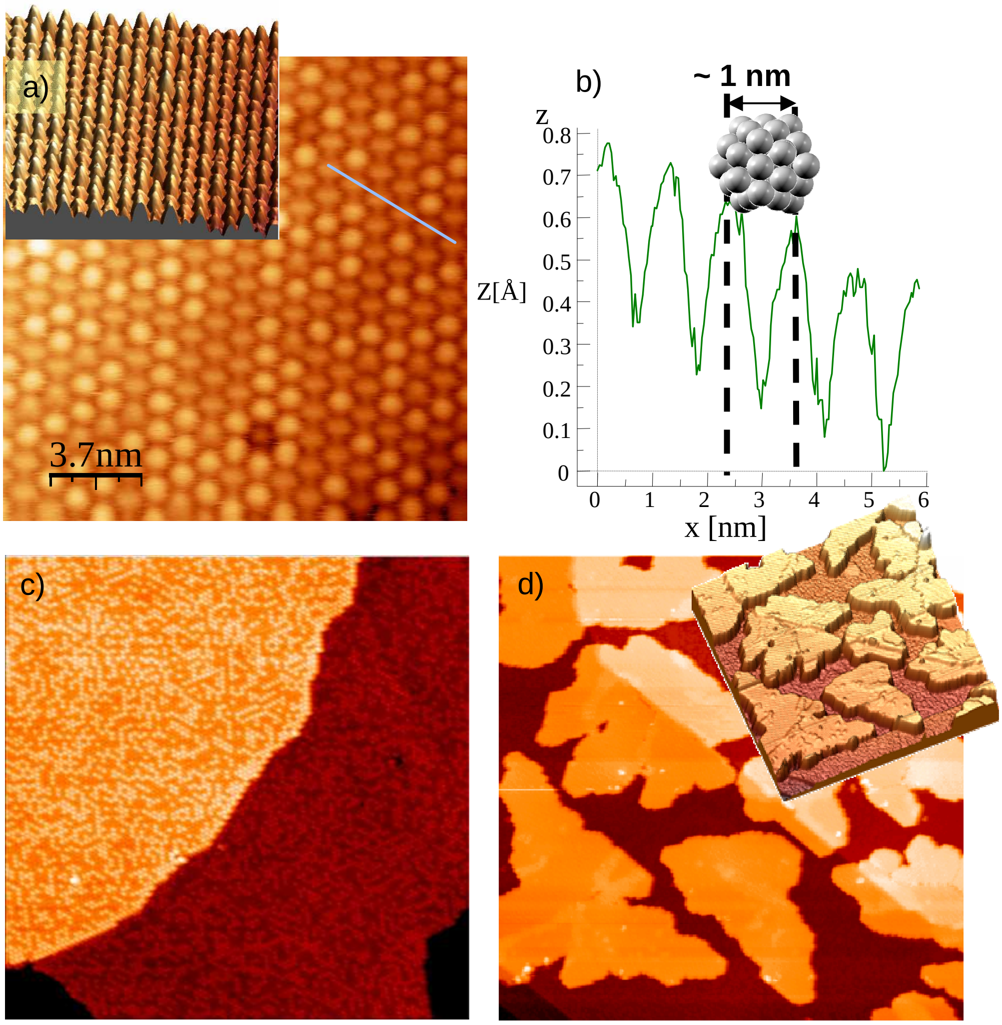

Figure 5.5: a) 2 D and 3 D view of an 18×18 nm² STM picture of 1 ML C_{60}/Au(111). The blue line marks the line profile, which is shown in b). c) 1 ordered ML C_{60} on large Au(111) planes, separated by an Au(111) step edge crossing from bottom-left to top-right (100 × 100 nm²). d) 2 D and 3 D view of 1 ordered ML C_{60} with islands of the second ML C_{60} (200 × 200 nm²). Here an Au(111) step edge runs from top-left to bottom-right.

5.2.1.2 Evaporation of C_{60} on HOPG

The growth mechanism of C_{60} on HOPG is different from the behavior of C_{60}/Au(111). The interaction between HOPG and C_{60} is very low, so that the C_{60} molecules form ordered islands at RT. Hence, an annealing is not necessary, similar to the evaporation of C_{60} on C_{60}/Au(111). Another aspect which makes the evaporation of C_{60} on HOPG easier and less time-consuming is that on large 1 ML planes islands of the second ML C_{60} are formed before the first ML C_{60} covers the whole HOPG sample. Thus the evaporation time of around 5 min is optimal to get large 1 ML C_{60} islands with smaller 2 ML islands and sometimes very small 3 ML islands. The typical lateral dimensions of the 1 ML islands are of the order of a few 10^4 square nanometers. Besides there are also free HOPG areas of the same size. Four STM images of C_{60}/HOPG taken at 77 K are shown in Figure 5.6.

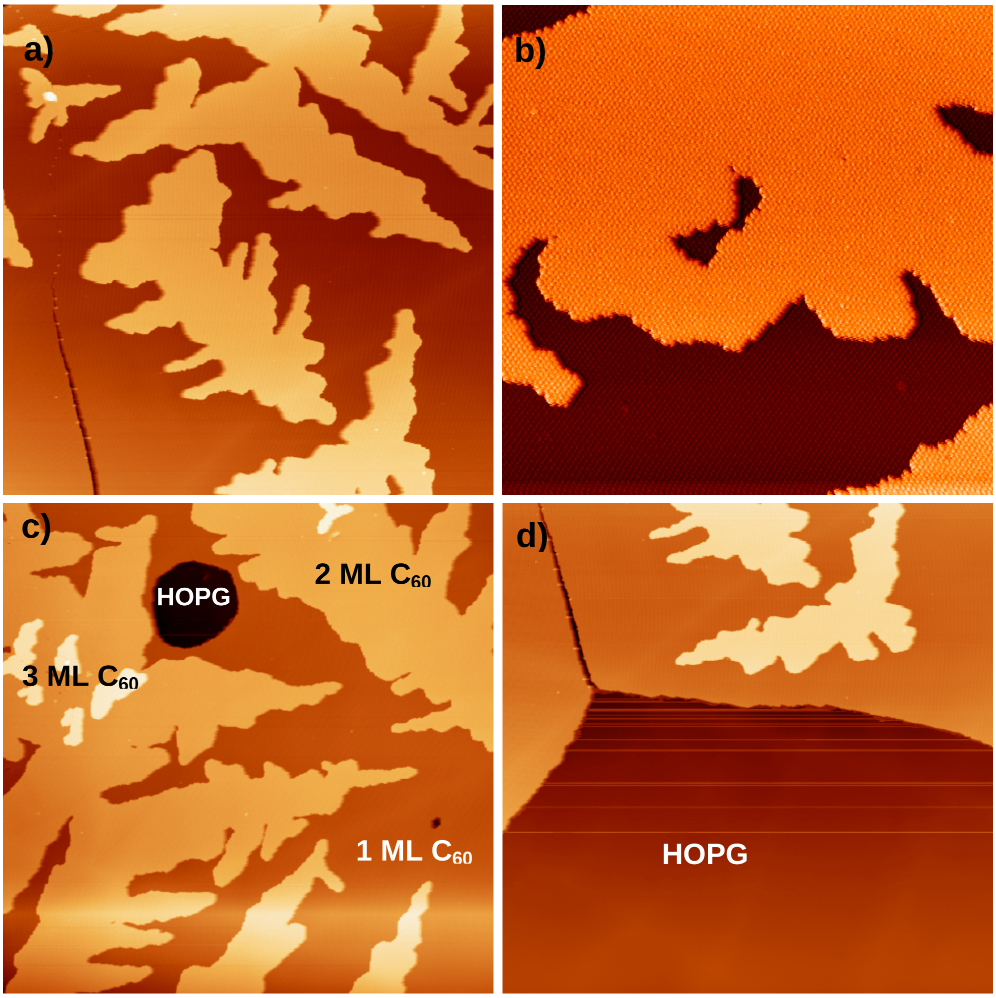

Figure 5.6: a) + c) 500×500 nm² STM image of C_{60}/HOPG, b) 100×100 nm² 3 D STM image (top view) of C_{60}/HOPG, d) 500×500 nm² STM image of C_{60}/HOPG showing islands of 1 ML C_{60}/HOPG with smooth edges and fractal shaped 2 ML C_{60} islands.

The 1 ML C_{60} islands are confined by smooth edges on the HOPG. The second and all subsequent layers adopt a fractal-dendritic shape [144, 145], as it is visible in Figure 5.6 d). The profound differences between the growth of the first ML C_{60} on HOPG and the subsequent C_{60} layers are caused by the restriction of the C_{60} mobility on the highly corrugated fullerene surfaces. The orientation of the fractal islands follows the hexagonal symmetry of the densely packed (111) surface of the fullerene lattice with an angle of 120° between the growth directions [144, 145]. The 2 ML C_{60} islands on Au(111) also have a fractal shape (Figure 5.5), but not as pronounced as on HOPG.

Within this thesis the thermal stability of clusters on C_{60}/Au(111) and C_{60}/HOPG was investigated. C_{60} islands on Au(111) are stable at RT due to the strong interaction of C_{60} with the metal surface [146]. Since the interaction between C_{60} and HOPG is very low, the RT stability of C_{60}/HOPG was checked by imaging the same surface area with STM at RT for several times and studying the variation of the shape of the C_{60} islands. The STM images in Figure 5.7 were measured consecutively at the same surface area and it took 34 min to take one image. Due to relatively high thermal drift at RT over 3 h of measurement the imaged area shifted for some ten nanometers from picture to picture.

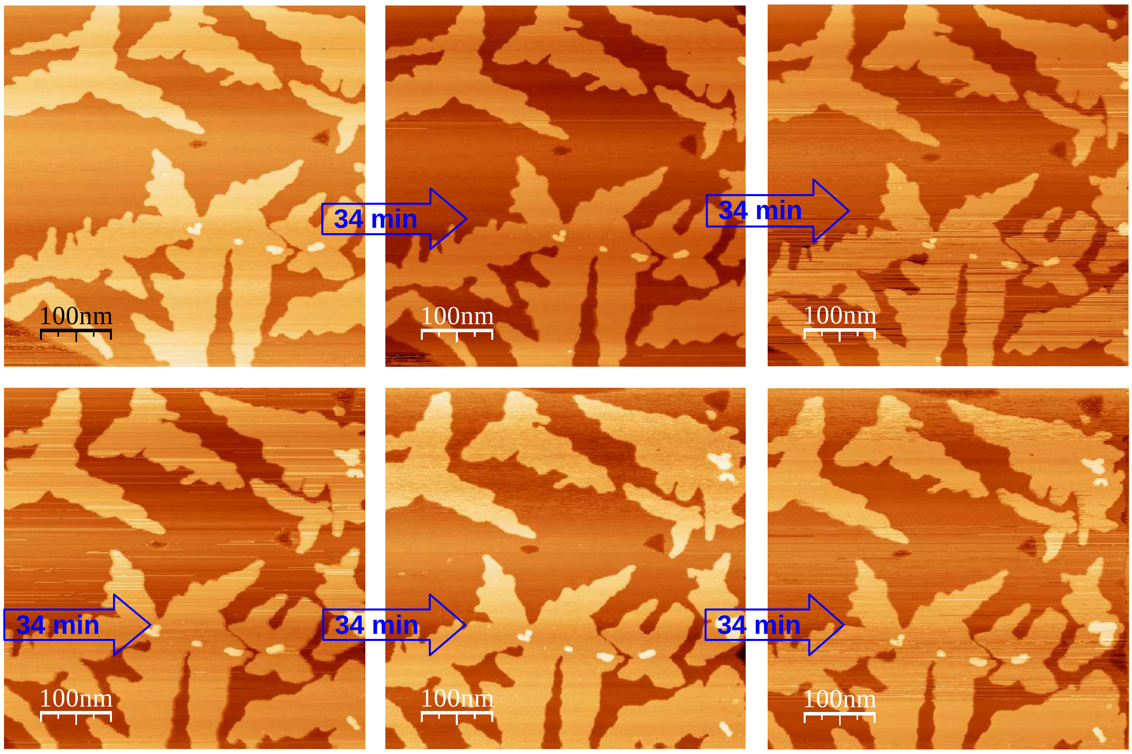

Figure 5.7: 500×500 nm² STM images of C_{60}/HOPG measured at RT. The pictures were taken consecutively at the same area to study the RT stability of C_{60}/HOPG.

As it is visible in Figure 5.7, the shape of the islands did not change noticeably. There were some indications that the shape of the edges of the 2 ML C_{60} islands changed in fine details, but in general the islands stayed stable for some hours at RT, which is an important aspect for the investigation of thermal activated processes of clusters on C_{60}. The thermal activated processes of single C_{60} molecules within an ordered C_{60} surface on Au(111) are discussed in section 6.2.3.

5.2.2 Preparation of the C_{58} layer

As mentioned in section 2.2.2 the C_{58} layers on HOPG were prepared by Daniel Löffler from the group of Artur Böttcher from the physical chemistry department of Universität Karlsruhe.

C_{58} ions were produced at RT under UHV conditions by electron-impact induced ionization/dissociation of C_{60} molecules using a Knudsen-type oven working at temperatures between 600°C and 700°C [147, 148, 149]. Impact ionization-dissociation was carried out using 70 eV electrons. Figure 5.8 shows a schematic drawing of the apparatus. The positive ions which were created in this way were guided by a series of electrostatic lenses through three stages of differential pumping, bent by 90° in an ion mirror, mass filtered in a quadrupole mass filter and then soft landed. The mass filter removes all undesired ions, in particular the abundant C_{60} molecules, but also smaller fragments. The ion mirror avoids a direct line of sight between source and target surface and prevents neutral fullerene molecules from reaching the surface.

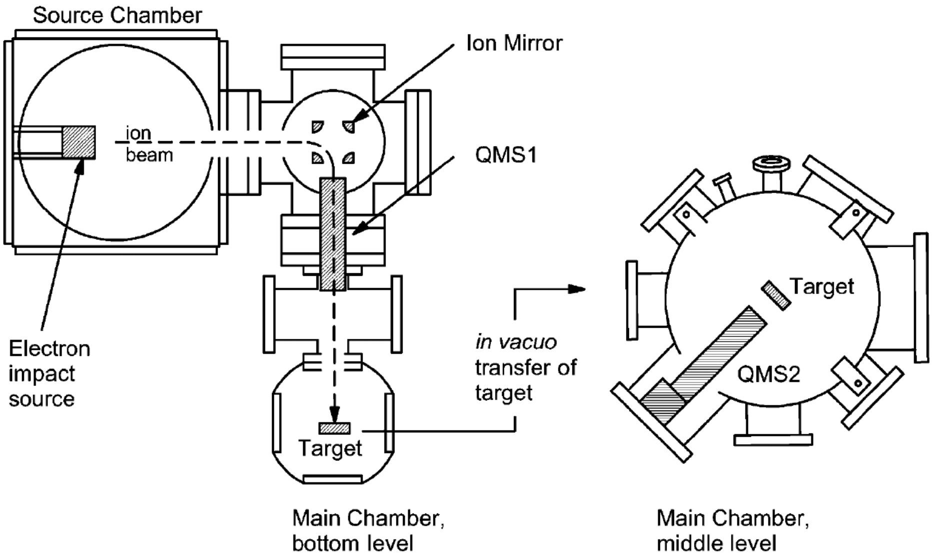

Figure 5.8: Experimental setup in Karlsruhe: the fullerene ion beam is created in an electron impact ionization source, bent by 90° in an ion mirror (electrostatic quadrupole), mass selected in a quadrupole mass filter, decelerated and soft landed on a HOPG surface [147].

In the final stage of the electrostatic system the mass selected ion beam is focused onto the HOPG and decelerated to a kinetic energy of 6 eV, (0.1 eV/carbon atom). The soft landing is crucial in order to avoid impact-mediated fragmentation as well as to maximize the effective sticking probability. The C_{58} flux during the deposition was kept constant at a level between 0.2 and 1 nA. The middle level of the main chamber (see Figure 5.8) is used to take desorption spectra of C_{58} by heating the sample up to 1000 K [147].

Within this thesis four C_{58}/HOPG samples were investigated, which differ in the C_{58} coverage. An overview about the coverage of the four C_{58}/HOPG samples is given in Table 5.1. The samples were prepared in Karlsruhe in the bottom level of the main chamber [148, 149], transferred into an exsiccator and transported to Dortmund. Since the samples had to be exposed to air when they were transferred from the apparatus in Karlsruhe to the exsiccator and from the exsiccator to the UHV surface science facility in Dortmund, the samples had to be annealed for 30 min at 200°C to desorb water and other adsorbates. Annealing the samples at lower temperatures before (100°C and 150°C for 30 min each) was not effective, as visible in STM images, due to contaminations which need higher temperatures to desorb. The STM images taken within this thesis of the four C_{58}/HOPG samples are shown and discussed in section 6.1.1.

Sample	**C_{58} ion dose**	**Number of C_{58} ions**
Sample 1	5 nAmin	$1.9 \cdot 10^{12}$
Sample 2	10 nAmin	$3.8 \cdot 10^{12}$
Sample 3	15 nAmin	$5.7 \cdot 10^{12}$
Sample 4	20 nAmin	$7.6 \cdot 10^{12}$

Table 5.1: C_{58} ion dose and number of C_{58} ions respectively of the four C_{58}/HOPG samples from Karlsruhe.

5.3 Ag cluster and metal island deposition

HOPG or Au(111) surfaces covered with ordered monolayers of C_{60} were used to deposit size selected Ag clusters or metal islands. The following sections explain the deposition process for size selected Ag clusters and the mechanism for the growth of islands from single evaporated metal atoms.

5.3.1 Deposition of size selected Ag clusters

5.3.1.1 Adjustment of the selectable Ag cluster mass

For the size selected clusters there are different conditions to guarantee a successful deposition on a sample. First one has to adjust the cluster size which shall be deposited. This is performed with the help of two Labview (Laboratory Virtual Instrument Engineering Workbench) programs, which were programmed by CHUNRONG YIN. The details of the operating mode of the Labview programs are explained in detail in [28] and [100]. Briefly, for the measurements of mass spectra one enters the start and end mass in atomic mass units (amu) as well as the step size for the mass detection and starts the measurement. For the deposition of a certain mass, the entered end mass is the cluster size which is permanently selected after the measurement of a mass spectrum, until the measurement of another mass spectrum is started again. For cluster sizes from Ag_{10} to about Ag_{70} single mass peaks are visible, as it is demonstrated in Figure 3.8. Hence, for the selection from Ag_{10} to Ag_{70} it is easy to find out the maximum of the corresponding mass peak and to define the mass in amu very precisely. Since the mass spectrum for larger cluster sizes is a broad distribution (see Figure 3.9), the mass scale for larger masses has to be calculated by extrapolation. The values for all focusing and accelerating voltages, the parameters of the cluster source etc. are adjusted differently for each experimental run by optimization of the cluster beam intensity, which also influences the position of the mass peaks. Therefore the peak position for Ag_1 does not always correspond to 108 amu. Furthermore the following peaks are shifted by a linear function with slightly varying slope. For this reason, before every deposition mass spectra have to be taken to check the position of the mass peaks. For the deposition of large masses a linear fit has to be made to find out which cluster mass in amu has to be chosen in the Labview program for a certain cluster size. Figure 5.9 shows several mass spectra, which were taken while adjusting the cluster current for the deposition of Ag_{561}.

An experimental run – with a clean cluster source, which is free of Ag residues, and a baked out mass selector – works as follows: One starts with selecting Ag atoms and molecules (Figure 5.9 a)) and adjusts the parameters in order to get the maximal cluster current. Then the cluster source has to be optimized for the production of not only atoms or molecules but clusters with three or more atoms (Figure 5.9 b)-f)). One always has to maximize the current for a cluster mass showing a dominant peak in the mass spectrum. This is necessary to get a high cluster current for larger masses. At least 1 pA before the optimization of the current for a certain mass is useful. Otherwise it is possible to lose the current during the variation of the parameters. Finally, after optimizing the source and all voltages for the production of large clusters, Figure 5.9 e) and f) demonstrate a mass spectrum with a maximal cluster current for Ag_{561}. As mentioned above one has to make an extrapolation to define the atomic mass unit which has to be used in the Labview program for large clusters, which do not show single peaks in the mass spectrum. An example for an extrapolation which is done with the help of a mass spectrum of Ag_4 to Ag_{43} is illustrated in Figure 5.10.

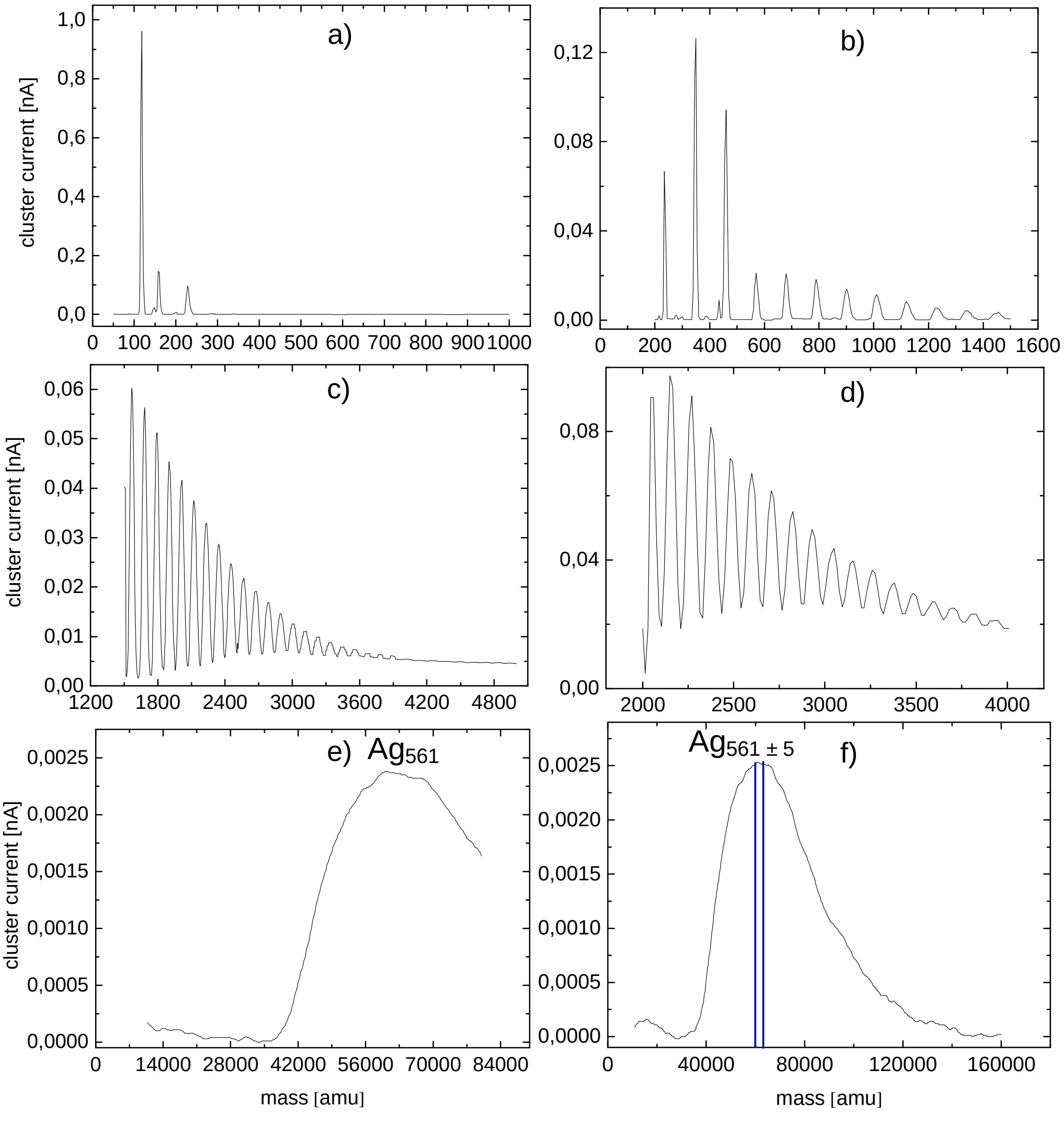

Figure 5.9: Adjustment of the cluster deposition machine for the deposition of Ag_{561}, illustrated by mass spectra from small clusters up to big clusters.

Figure 5.10 shows the linear fit for the calculation of an atomic mass unit for a certain cluster size, which was figured out by defining the atomic mass number of the marked peaks in the shown mass spectrum. For the deposition of Ag_{147}, Ag_{309}, Ag_{561} or Ag_{923} one replaces “N” by the corresponding number of atoms to get the cluster size in atomic mass units. In the calibration in Figure 5.10 the cluster sizes in atomic mass units for Ag_{147}, Ag_{309}, Ag_{561} or Ag_{923} are depicted in Table 5.2.

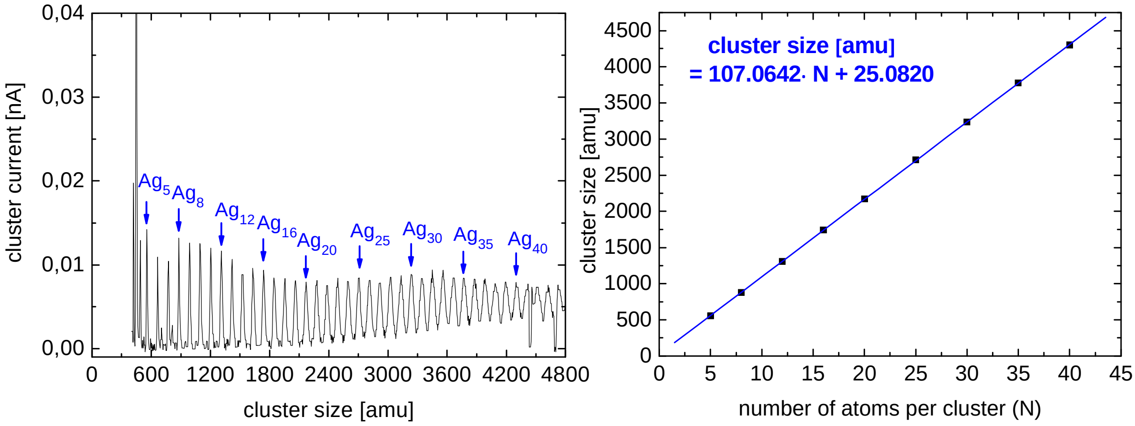

Figure 5.10: Linaer fit for the extrapolation to atomic mass units of large clusters, which do not show single mass peaks anymore.

Number of atoms per cluster (N)	Cluster size [amu]
147	≈ 15,764
309	≈ 33,083
561	≈ 60,088
923	≈ 99,379

Table 5.2. Cluster sizes in amu for different geometrically magic clusters for the linear extrapolation shown in Figure 5.10.

5.3.1.2 Cluster current and deposition time

After the adjustment and optimization of the cluster current for the cluster size which is deposited, the next step during an experimental run is defining the deposition time, which depends on the cluster current. The higher the cluster current is, the more Ag^+_N ions per time are deposited onto the sample and the shorter is the deposition time. A cluster current of 5 pA corresponds to $3.1 \cdot 10^7$ Ag ions per second. That means that on a $100\times100\ \mathrm{nm}^2$ area $9.9 \cdot 10^{-2}$ Ag ions per seconds are deposited assuming a typical diameter of the deposition spot of 2 mm. On the one hand the deposition time must not be too long to avoid a strong coalescence of the clusters, especially in the center of the deposition spot. On the other hand if the time is too short, there are not enough clusters and it may be hard to find them on the sample with STM.

The diameter of the deposition spot was measured by both passing the small hole of the Faraday cup through the cluster beam and by measuring different regions of the sample with STM. Both methods for several experiments have shown that the cluster beam can have a diameter of 2-3 mm It is further corroborated by UPS data in section 6.6.2. The experience during a number of deposition experiments has shown that the coverage with Ag clusters within the deposition spot on the sample is optimal if the product of cluster current $I_{cluster}$ and deposition time t_{depo} equals 200 pAmin:

$$I_{cluster} \cdot t_{depo} \overset{!}{\approx} 200\ \mathrm{pAmin}, \tag{5.1}$$

which corresponds to about 250 clusters / (100×100 nm²) for a spot diameter of 2 mm.

Typical deposition times are illustrated for the deposition of Ag_{55}, Ag_{68}, Ag_{80}, Ag_{147}, Ag_{309}, Ag_{561} and Ag_{923} in Table 5.3.

Cluster size	Cluster current [pA]	Deposition time [min]
Ag_{55}	10.25	20
Ag_{68}	8	40
Ag_{80}	16.5	12.5
Ag_{147}	5	41
Ag_{309}	27	7
Ag_{561}	16	10
Ag_{923}	8.5	27

Table 5.3 Cluster current and deposition time for several deposition experiments of different geometrically magic cluster sizes.

In some cases more than 200 pAmin were deposited, as for Ag_{68}, in order to obtain more clusters. This has the advantage that there are more clusters within an STM image, which leads to a faster analysis due to good statistics within only a few STM images. The disadvantage is that the clusters in the center of the deposition spot are coalesced, which has to be considered for the measurement and analysis. A deposition of less than 200 pAmin, as for Ag_{561}, leads to less or nearly no coalescence, but one needs more STM images for good statistics for the analysis.

With an optimal adjustment of all parameters of the cluster deposition machine, typical values for the cluster current are 1-3 nA for Ag atoms and some 10 pA for all larger clusters. The highest cluster current which was measured for Ag_{55} after optimizing the parameters was 93 pA and for Ag_{2130} 20 pA.

5.3.1.3 Distribution and diffusion of deposited clusters

For the STM images of size selected Ag clusters on C_{60} functionalized surfaces it was shown by comparison of the experimental results with statistical simulations that the clusters, which were deposited at 165 K, are uniformly distributed on the sample, as it is expected for a deposition experiment [150]. Besides, the simulations have shown that the clusters after deposition at 165 K do not coalesce due to thermal activation.

These are optimal conditions for the deposition and investigations of size selected Ag clusters. If the clusters were not uniformly distributed and would coalesce on the substrate after deposition, the complex setup for the mass selection would be dispensable. Another problem, which could destroy the mass selection, is the fragmentation of the cluster when they impinge on the sample. For this reason the clusters have to be soft landed, which is discussed in the following section.

5.3.1.4 Soft landing of size selected Ag clusters

To guarantee a soft landing on the substrate and to avoid fragmentations of the size selected clusters, a positive voltage is applied to the sample which decelerates the clusters, so that they are deposited with low kinetic energy. For small clusters as Ag_{13} and Ag_{55} one often has to apply a negative voltage to the sample in order to guarantee that all clusters reach the sample. To find out the voltage which has to be applied to the sample, the cluster current depending on the applied voltage is measured before a deposition by applying different voltages to the Faraday cup. Several of these current-voltage curves are shown in Figure 5.11.

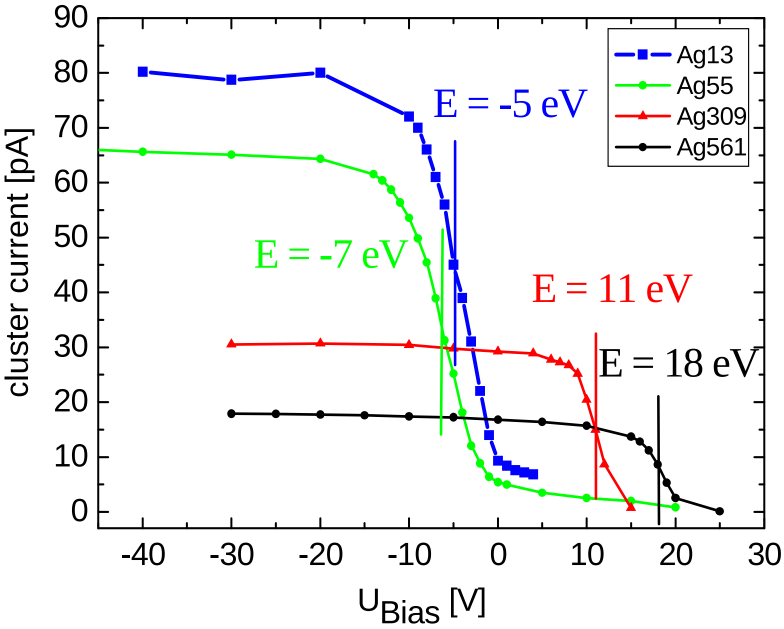

Figure 5.11: Cluster current vs. sample voltage for Ag_{13}, Ag_{55}, Ag_{309} and Ag_{561}. The lines mark the average kinetic energy of the clusters.

Up to a certain value of U_{Bias} the cluster current remains nearly constant. Then the cluster current decreases drastically and finally converges towards zero. The lines mark the average kinetic energy of the clusters. For Ag_{309} a cluster current of about 30 pA was measured for –40 V applied to the sample and to the Faraday cup, respectively. The cluster current is only the half (15 pA) for $U_{Bias} = 11$ eV. This means that half of the clusters do not have enough energy anymore to reach the sample.

For the deposition it is important that the kinetic energy of the clusters is low, but the cluster current as high as possible to reduce the deposition time. For depositions at 165 K and a pressure of 10^{-8} mbar during the deposition in the preparation chamber of the surface science facility (normally 10^{-11} mbar), where the sample is located, deposition times up to one hour are acceptable without contamination of the sample. For deposition at lower temperatures probably shorter deposition times are necessary. Although a large part of the 10^{-8} mbar during deposition is clean helium gas, recently these vacuum conditions were improved by a modification in the vacuum system of the cluster deposition machine. Even if the contamination of the sample is not a problem, short deposition times are more comfortable due to the fact that during the deposition all parameters, pressures and most of all the temperature of the source, which is cooled with LN_2, has to be checked. If the source becomes warm, impurity particles, which were frozen before, can reach the sample.

For a certain cluster size the total kinetic energy equals the average energy minus the energy which correlates to the applied voltage. In the case of Ag_{309} it was soft enough to deposit the cluster with the sample on ground potential, so that the total kinetic energy amounted to

$$E_{kin}(Ag_{309}{}^{+}) = (11-0)\ eV = 11\ eV \Leftrightarrow 0.036\ eV/atom \tag{5.2}$$

In general the average kinetic energy for larger clusters is higher than for smaller clusters. This is due to the fact that larger clusters get a higher kinetic energy by the velocity gained in the rare gas expansion in the cluster source, additionally to the energy they get due to the applied voltages in the cluster deposition machine.

5.3.2 Growth mechanism of metal islands

Additionally to the deposition of size selected Ag clusters, metal islands on C_{60} functionalized Au(111) were investigated. The metal islands are produced by evaporating Ag or Pb "atom-by-atom" by an evaporator with integrated flux monitor (EFM) which is presented in section 3.2.2. The mechanism of island growth by self organization of the evaporated atoms is demonstrated in Figure 5.12. When the atoms arrive at the surface, they hit an existing island (direct impingement) or diffuse between the existing islands, performing a random walk, until they hit another island after the typical path length λ_{diff}. The sizes of the islands increase, the more Ag atoms are captured. Due to the strong metal-metal interaction one can assume that the sticking coefficient between metal atom and metal island is 1, so that a later escape of an atom is negligible. It is also possible that atoms re-evaporate from the substrate directly, but the probability for this desorption process is quite low for the experiments presented here. Depending on the interaction between substrate and metal islands it is possible that molecules or small islands are mobile on the substrate and diffuse to step edges, defects or coalesce with other islands on the surface [151]. This is e.g. the case if one uses the pristine HOPG surface as substrate material due to the weak metal-HOPG interaction. The interaction between metals and C_{60} is stronger, as it is reported in several publications [152-156].

Another possibility to stabilize metal islands on surfaces is the growth of metal islands in nanopits, controlled defects which serve as nucleation centers for the metal atoms and islands. Several former studies of the cluster group in Dortmund deal with this topic [157-162].

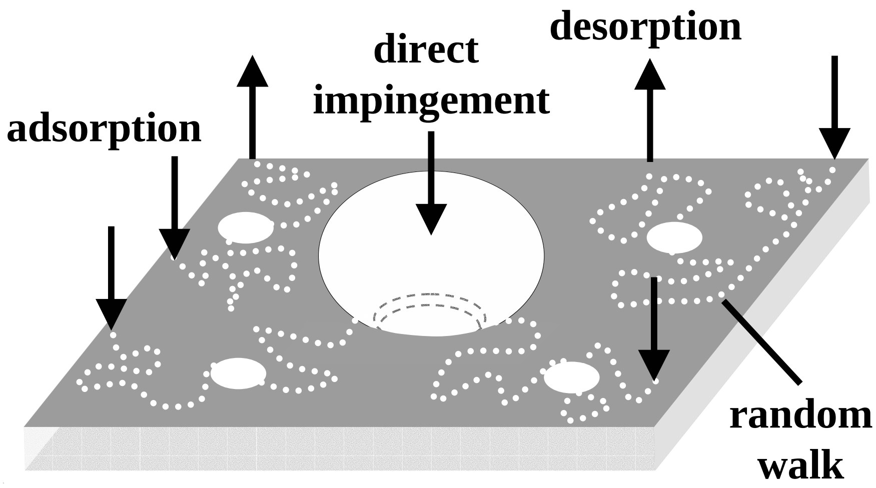

Figure 5.12: Schematic representation of the growth process and nucleation of metal islands on surfaces.

6 RESULTS AND DISCUSSION

In this chapter the experimental results which were obtained within this thesis are presented.

The first section deals with the problems of height measurements with STM and a calibration for a precise height measurement. After that the properties of C_{58}/HOPG, C_{60}/HOPG and C_{60}/Au(111) are discussed. Then the thermally activated decay of geometrically magic Ag clusters including atomistic simulations is introduced, followed by a section about Ostwald ripening of geometrically non-magic Ag clusters. The thermally induced ripening of Ag and Pb islands is presented in the next section, before STS and UPS spectra of size selected Ag clusters are shown and discussed.

6.1 Height measurement and calibration

6.1.1 Data analyzing

The analysis and preparation of the STM images was performed on the one hand with the software *WSxM* [172] developed by Nanotec, and on the other hand with the software *Scala SPM SO 2.2* of the STM workstation developed by Omicron. The cluster height is measured with *WSxM* by studying line profiles and measuring the difference between the top of the cluster and the surface level at the cluster onset. Clusters at step edges were neglected because it is often not observable if such clusters lie on the upper or lower terrace relative to the step edge. Histograms of surface heights in the STM image were performed with *Scala SPM SO 2.2*.

6.1.2 Calibration of the z-piezo of the STM

During the first measurements of the heights of geometrically magic Ag clusters it was striking that the measured cluster heights were around 10 % higher than the cluster heights which were calculated by assuming a spherical shape of the clusters. This phenomenon can be partially attributed to the different local density of states on the cluster and on the C_{60} which is measured with STM, but the discrepancy is too high to explain it only with the different LDOS of C_{60} and clusters [146, 195]. The corresponding STM measurements were performed at 77 K. Measuring the cluster heights at 5 K generates smaller values. Figure 6.1 shows height distributions of Ag_{309}, which were deposited on 1 and on 2 ML C_{60} on HOPG. The heights were measured at 77 K and at 5 K after annealing the sample for 12 h at RT to investigate the thermal stability and it was observed that the clusters stay stable after annealing. More details about the annealing of clusters/C_{60}/HOPG are presented in section 6.3.

The same effect of a smaller cluster height is obtained if the clusters are scanned at 77 K with very slow scan speed due to the fact that the z-piezo has more time to adjust its position including hysteresis and creep of the piezo material [163]. Figure 6.2 demonstrates this effect. Therefore the z-piezo voltage (which corresponds to the measured cluster height) needed on top of the cluster is lower for a slow scan speed.

It seems to be obvious that the calibration matrix for the z-piezo, which can be programmed within the software, is not correct for the temperature of 77 K, at least not for objects with a few nm height, e.g. the clusters. For different scanning temperatures (RT, 77 K and 5 K) there are different calibration matrices used at these temperatures.

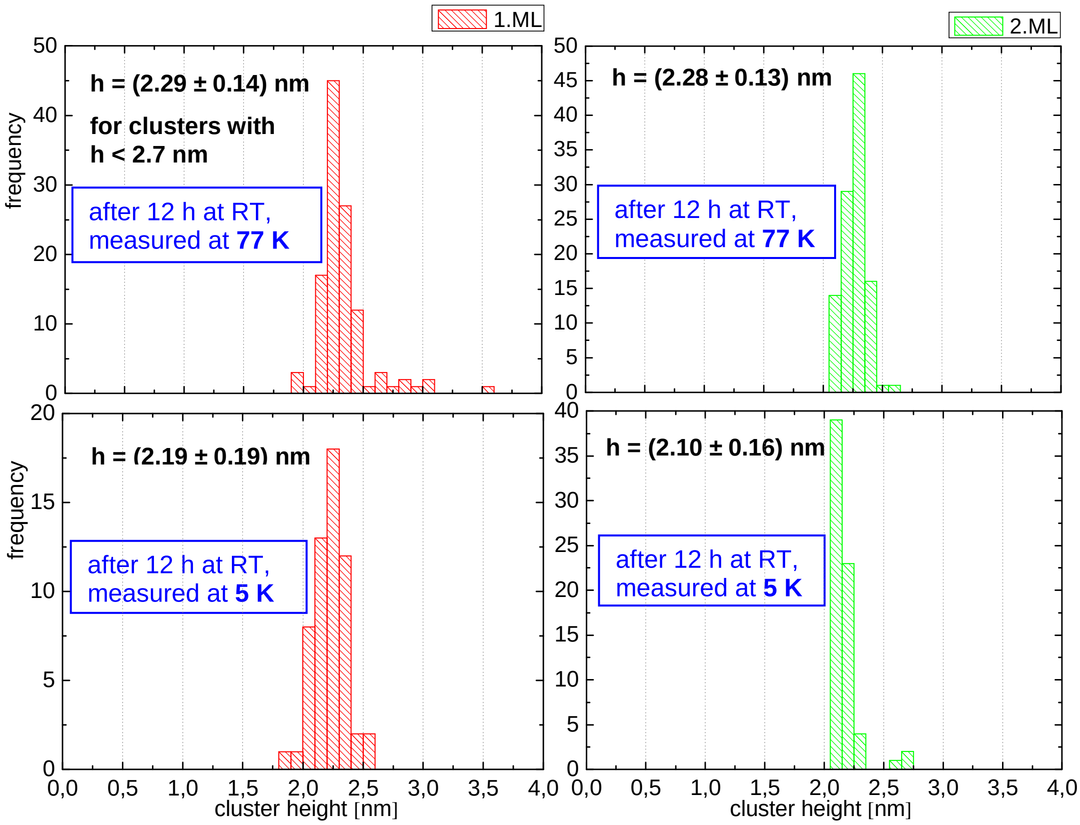

Figure 6.1: Height distributions of Ag_{309}/1 and 2 MLC_{60}/HOPG after 12 h at RT. The heights were measured at 77 K (top) and at 5 K (bottom). Larger clusters due to coalescence in a region with high cluster coverage do not contribute to the mean value of the cluster height (top left). The heights shown here are calculated with the former piezo scanner matrix for 77 K, before the calibration was used for all following data from section 6.2 on.

Thus a recalibration of the z-piezo for 77 K was made as follows. Usually the z-scale of the STM piezo is calibrated using monolayer steps with a few 0.1 nm height, e.g. on a metal surface. The accuracy of this calibration is limited to about 5%. In addition to statistical errors there are systematic differences for the step heights as compared to crystallographic data (see next section) Due to piezo nonlinearity, creep etc., the calibration has to be modified for larger height differences of several nm [163]. Therefore a multilayer C_{60} film (1ML … 4ML) on HOPG was used for the calibration of heights on a nm scale by measuring the heights with STM at 77 K. The step heights of $C_{60}(111)$ are given by the fcc lattice constant a_0 = 1.405 nm to $a_0/\sqrt{3}$ = 0.81 nm [164]. Using the former 77 K calibration the result of the height measurement is shown in Figure 6.3. A height histogram of an STM image of a multilayer C_{60} film on HOPG reveals peak distances of 0.91 nm instead of 0.81 nm. Thus, the C_{60} step heights are imaged 11 % higher. This was also the case for the size selected Ag clusters, whose heights are in the same order of magnitude.

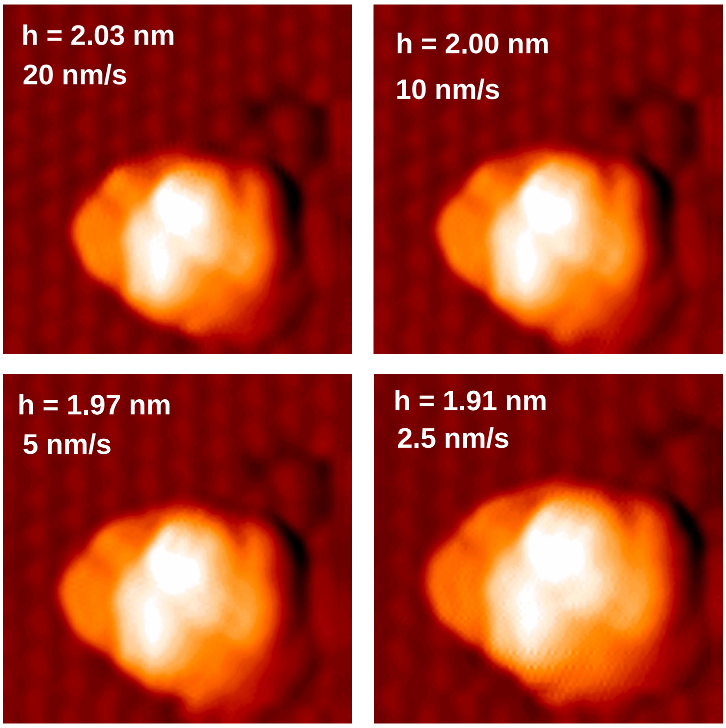

Figure 6.2: 10×10 nm² STM images of an Ag_{309} cluster/C_{60}/HOPG taken at 77 K with different scan speeds. Color and contrast are optimized to visualize the highest region of the cluster. The slightly different lateral sizes are due scan-speed dependent changes in the x-y-scale as visible by the period of the C_{60}. The height was not influenced by the tip shape, which is shown by heights measured for an again faster scan speed.

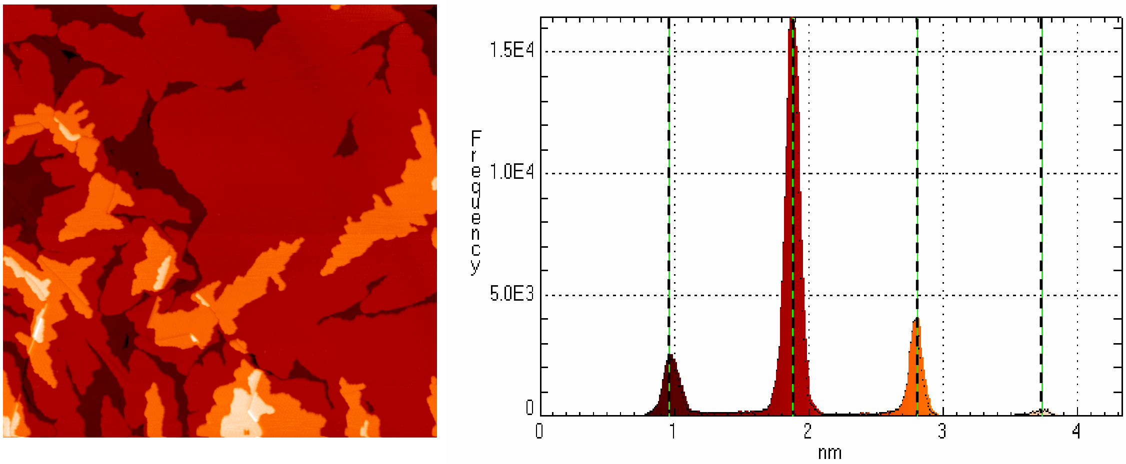

Figure 6.3: Left: 500×500 nm² STM image of a multilayer C_{60} film on HOPG. Right: corresponding height histogram.

The measured cluster heights which were presented in [165, 104, 150] are the heights without calibration and have to be corrected by a factor of 0.89. In all following data for 77 K from section 6.2 on the recalibrated piezo scanner matrix is used. Only the heights which are visible in line profiles show the raw data. The measurement of step heights of a multilayer C_{60} film at 5 K revealed that the calibration matrix for 5 K is correct within the experimental errors.

6.1.3 Step edges and lattice constant of Au(111)

The STM images of Ag clusters or islands on C_{60}/Au(111) show step edges of the Au substrate. For the correct interpretation of the images it is important to know the height of an Au(111) step edge. Due to different reasons, which are discussed in the following, it is difficult to define an exact value for the Au(111) step edge. The distance of the Au layers in (111) direction amounts to

$$d_{111} = 1/3 \cdot \sqrt{3} \cdot a_0 = 2.355\,\text{Å} \tag{6.1}$$

with the lattice constant of $a_0 = 4.0785$ Å at 25°C [166]. The interatomic distance of Au(111) is 2.8839 Å. At 5 K these parameters are < 1 % smaller [167] (maximally $\alpha_{Au,RT} \cdot T = 14.2 \cdot 10^{-6}/K \cdot 300\,K = 4.26 \cdot 10^{-3} \approx 0.4\,\%$. $\alpha_{Au,\,RT}$ is the thermal expansion coefficient of Au at RT), which can be neglected within the experimental errors of the STM. For the first few layers one has to consider relaxation effects, which lead to a different height of the step edges of the first layers [168]. Due to a missing next layer at the surface of a metal, the first layer is contracted towards the second layer which results in a smaller height d_{12} for the step edge. The following few layers are on the one hand contracted as well or on the other hand expanded towards the next layer. The theoretical results of the multilayer relaxation for Au(111) are illustrated in Table 6.1.

d_{12}	d_{23}	d_{34}
–3.54 %	0.57 %	–0.09 %

Table 6.1: Theoretical results of the multilayer relaxation for Au(111) surfaces in percent as the change from the bulk value of the spacings. Negative (positive) values indicate contraction (expansion) [168].

This means that one has to substract 3.54 % of 2.355 Å which amounts to 2.27 Å for the distance of the first pair of lattice planes. However, the relaxation close to a step edge may be different. Because the height measurement of the first pair of Au(111) planes with STM is influenced by the local density of states and includes the corrugation of the herringbone reconstruction, the experimental values for Au(111) step edges are higher than the theoretical value. C. E. D. CHIDSEY et al. measured a step edge height of 2.36 Å [169], V. M. HALLMARK et al. [170] as well as R. C. JAKLEVIC et al. [171] observed a height of 2.5 Å.

In Dortmund the heights of Au(111) step edges were measured using Au(111) line profiles (see Figure 6.4). Due to the fact that the former 77 K calibration was alright for Au(111) step edges, which are on an Å scale, the measured Au(111) heights were not calibrated with the factor of 0.89, which was used for calibration of heights on a nm scale.

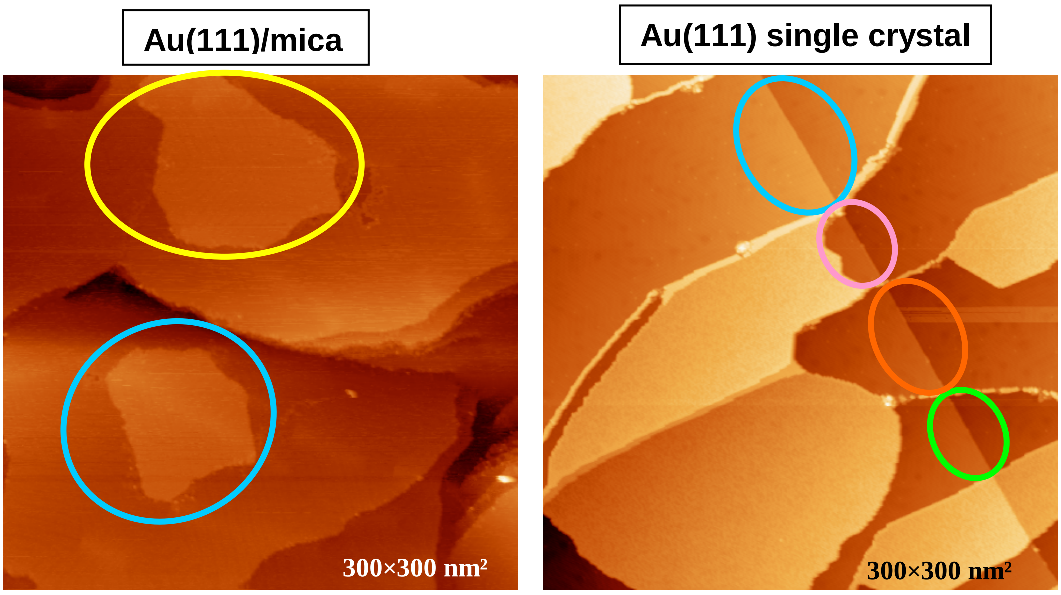

Region	Height	Error	Region	Height	Error
Blue	0.24126	0.00716	Blue	0.24975	0.00838
Yellow	0.24438	0.00752	Pink	0.24920	0.00865
			Orange	0.25674	0.00959
			Green	0.24362	0.00766
Mean value	**0.24310**	**0.00752**	**Mean value**	**0.24911**	**0.00889**

Figure 6.4: Heights of step edges of Au(111)/mica and an Au(111) single crystal measured at 77 K.

Figure 6.4 shows two STM images of Au(111)/mica (left image) and an Au(111) single crystal (right image). The heights of the step edges were measured in the colored regions and for the Au(111) single crystal and Au(111)/mica the mean value of the measured height of the step edges was calculated. For Au(111)/mica 112 line profiles were measured in the blue colored region and 161 in the yellow colored region, which represent the typical plateaus of an Au/mica surface. For the Au(111) single crystal line profiles along the straight step edge were measured. In the blue colored region 138 line profiles were measured, in the pink colored region 116, in the orange colored region 20 and in the green colored region 46. In summary, the mean value for the step edge height of Au(111)/mica is 0.243 ± 0.008 nm and for the Au(111) single crystal 0.249 ± 0.009 nm. These heights are approximately in agreement with the heights measured by CHIDSEY, HALLMARK and JAKLEVIC.

6.2 Properties of fullerene layers on surfaces

In this section the results and properties of fullerene layers on HOPG and Au(111) are presented. First STM images of C_{58}/HOPG are shown and explained and compared to

C_{60}/HOPG. After that the properties of C_{60}/Au(111) are presented. Especially the different orientations of C_{60}/HOPG and C_{60}/Au(111) are highlighted.

6.2.1 C_{58}/HOPG

The preparation of the C_{58}/HOPG samples is described in detail in subsection 5.2.2. As already mentioned, the four samples, which were investigated within this thesis as a comparison to the C_{60} films discussed in subsections 5.2.1.2 and 6.2.2, differ in the C_{58} coverage. They were exposed to a dose of 5 nAmin, 10 nAmin, 15 nAmin and 20 nAmin (see Table 5.1). STM images are depicted in Figure 6.5. The STM images of C_{58}/HOPG exposed to 5 nAmin look very similar to the samples which were exposed to 10 and 15 nAmin. Only the sample with the highest exposure of 20 nAmin shows a clearly higher coverage with C_{58}. Whereas 1 ML C_{60} forms compact round shaped islands, C_{58} arranges in fractal-like islands which decorate HOPG step edges as well as flat terraces. In [148] it was shown that the fractal-like growth is due to C_{58} forming a covalently bound polymeric network under the deposition conditions, which is still weak enough to allow back-transformation to monomers via heating.

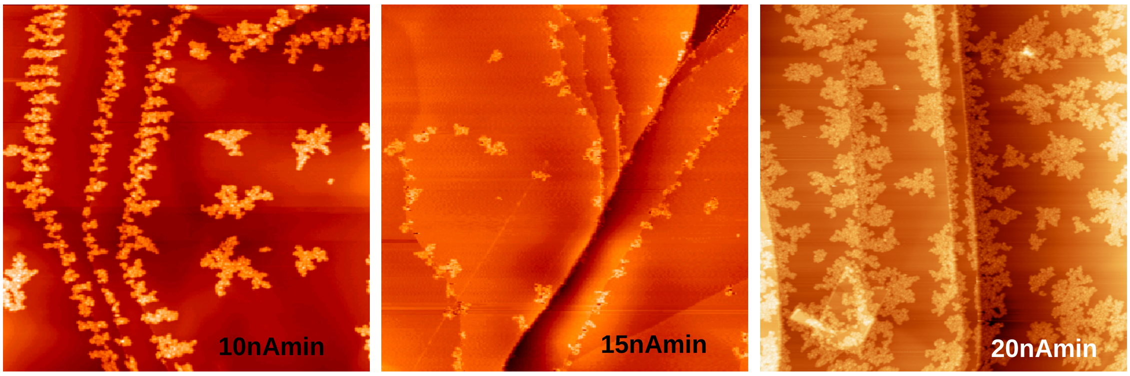

Figure 6.5: 1×1µm² STM images of C_{58}/HOPG exposed to a dose of 10, 15 and 20 nAmin.

C_{58} islands therefore form a very stable network, stabilized by significantly stronger fullerene-fullerene bonds than found for 1 ML C_{60} van der Waals films. The C_{58}-surface interactions are comparable to or even weaker than C_{58}-C_{58} interactions which is the decisive factor in C_{58} thin-film growth. A high sticking coefficient yields dendritic islands of low fractal dimension, whereas a low lateral sticking probability results in nearly circular densely packed islands, as observed for C_{60}. This observation is in agreement with the diffusion-limited aggregation (DLA) model for adsorbates [173]. Besides, higher lateral sticking coefficients are consistent with the higher chemical reactivity expected for the adjacent-pentagon-ring C_{58} cage structures, as well as for other non-IPR fullerenes, which all show a fractal-like island growth.

For increasing ion dose, the growth at step edges slows down while small compact islands begin to nucleate on terraces. This leads to a reduction of the catchment areas associated with islands at step edges. Increasing the dose further causes the initially small compact islands to become increasingly ramified (see Figure 6.5, right image) as predicted by DLA models [174]. More details and atomic force microscopy (AFM) images can be found in [147, 148 and 149].

Figure 6.6 shows STM images of C_{58}/HOPG exposed to a dose of 10 nAmin. With STM at 77 K a higher resolution of the C_{58} islands is obtained than with AFM, which becomes apparent especially in the smaller images. The images show regions of higher and lower LDOS, visible by brighter and darker colors. This might be due to different orientations of the C_{58} molecules relative to the surface. Another possibility is that the islands are not only two dimensional but start to grow in the third dimension which leads to higher regions within the C_{58} islands. This phenomenon is probable for a higher coverage of C_{58}. In Figure 6.7 two 500×500 nm² STM images of C_{58}/HOPG exposed to a dose of 10 nAmin and 20 nAmin, respectively, are shown. The different coverage and island shape are clearly visible. The STM image on the right lets assume that the islands are three dimensional due to the high coverage with C_{58}. In addition to STM images, STS spectra of C_{58}/HOPG could be interesting for future experiments to reveal the electronic structure in comparison to the electronic properties of C_{60}.

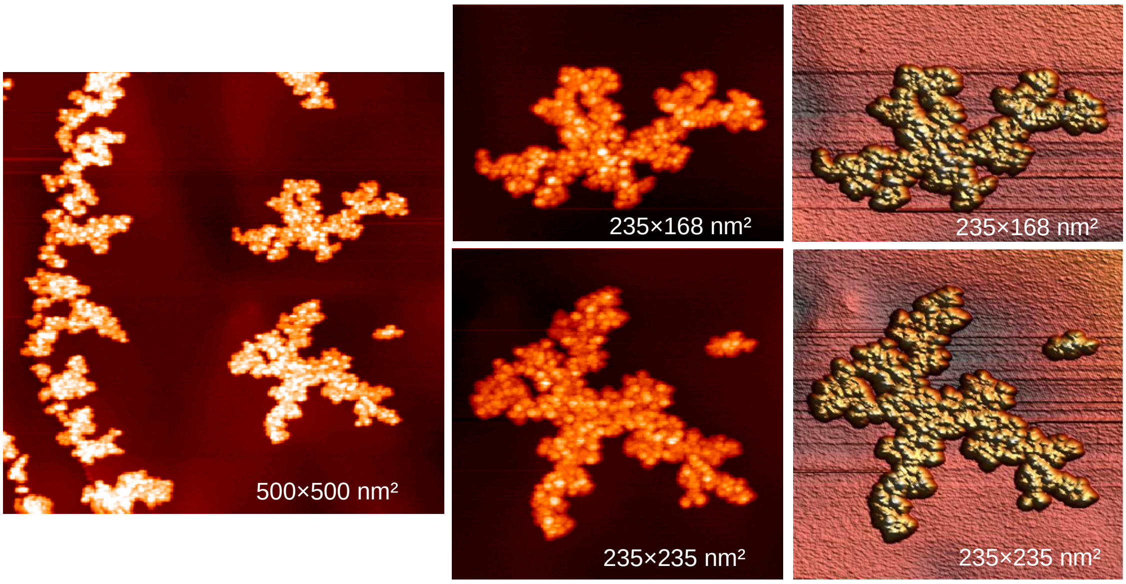

Figure 6.6: STM images of C_{58}/HOPG exposed to a dose of 10 nAmin. The images in the middle are extensions of the left image and are illustrated in 3D by the rightmost images.

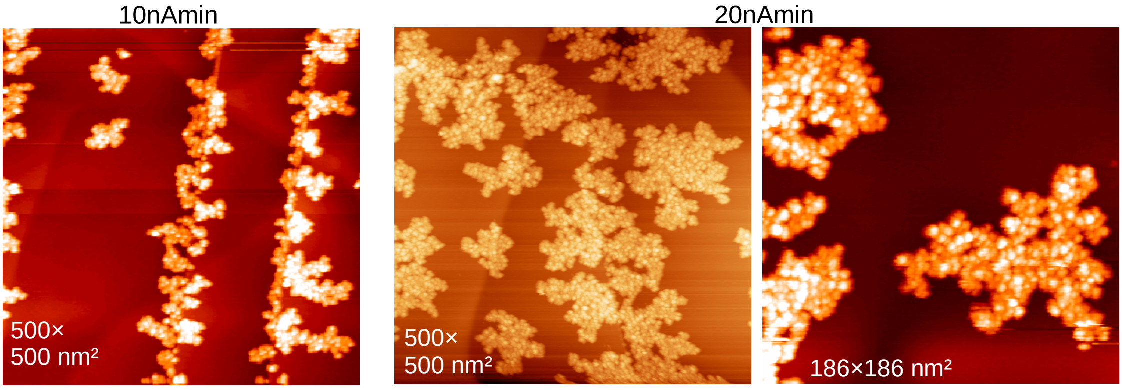

Figure 6.7: STM images of C_{58}/HOPG exposed to a dose of 10 (left) and 20 nAmin (middle and right). The different coverage is visible and the 3D island growth for high coverage.

6.2.2 C_{60}/HOPG

As discussed in subsection 5.2.1.2, the first ML C_{60} forms islands with smooth edges on HOPG due to the weaker C_{60}-C_{60} interaction in comparison to the strong C_{58}-C_{58} interaction. Besides, the interaction between C_{60} and HOPG is very weak. The second and all following ML C_{60} islands show a fractal-dendritic shape, following the hexagonal symmetry of the densely packed (111) surface (see Figure 5.6 and Figure 6.3).

In this subsection the molecular structure of 1 and 2 ML C_{60}/HOPG is discussed concerning the different orientations of the single C_{60} molecules. 1 and 2 ML C_{60}/HOPG were investigated at 5 K with STM using positive and negative tunneling voltages. At this temperature the thermal drift is very low. As explained in section 4.1, scanning with negative voltage images occupied states of the sample and vice versa. In Figure 6.8 four $10\times10\ \text{nm}^2$ STM images of 1 and 2 ML C_{60}/HOPG are shown, which were scanned using positive and negative voltages. The images are rendered in a varicoloured 3 D shading to point out the structure of the C_{60} molecules.

The STM tip has to be brought into a very sharp and stable condition by varying the tunneling current and voltage. A double-tip would smear out the structure of the C_{60} molecules. The stability is important because the same sample area is scanned using positive and negative voltages by reversing the polarity. This change could destroy the tip shape, if the tip shape is not stable enough. The images of 1 ML C_{60}/HOPG and of 2 ML C_{60}/HOPG were scanned subsequently at the same sample area with positive and negative voltage, respectively.

As it is visible in Figure 6.8, the 1 ML C_{60} molecules/HOPG all show the same orientation. They only differ for negative and positive voltages, which is due to the fact that only occupied or unoccupied states are imaged.

The images for 2 ML C_{60}/HOPG look different than for 1 ML C_{60}/HOPG. One clearly observes three different orientations of the 2 ML C_{60} molecules: a three-lobe and a dumbbell-like intramolecular pattern and a bright spherical pattern. This becomes apparent especially in the STM image which shows the unoccupied states of the 2 ML C_{60} molecules (Figure 6.8 c)). The three patterns are three or twofold symmetric or rather uniformly bright, which is indicated by hexagons, squares, and pentagons in Figure 6.8 c). This means that there are two possible in-plane orientations for the three-lobe pattern and three for the dumbbell-like pattern. WANG et al. have shown that at positive bias bright lobes correspond to pentagons of the C_{60} cage [176]. This is due to the fact that the pentagons have a lower electron density than the hexagons which show the highest intensity in STM images at positive tunneling voltage. Consequently, the patterns can be assigned to C_{60} adsorbed on a hexagon, a double bond in between hexagons and a pentagon. The enlarged different patterns are demonstrated in Figure 6.9, together with models of C_{60} molecules showing the different orientations [175].

G. SCHULL et al. showed that on Au(111) the three orientations of C_{60} molecules show different features in STS spectra due to different electronic properties [177].

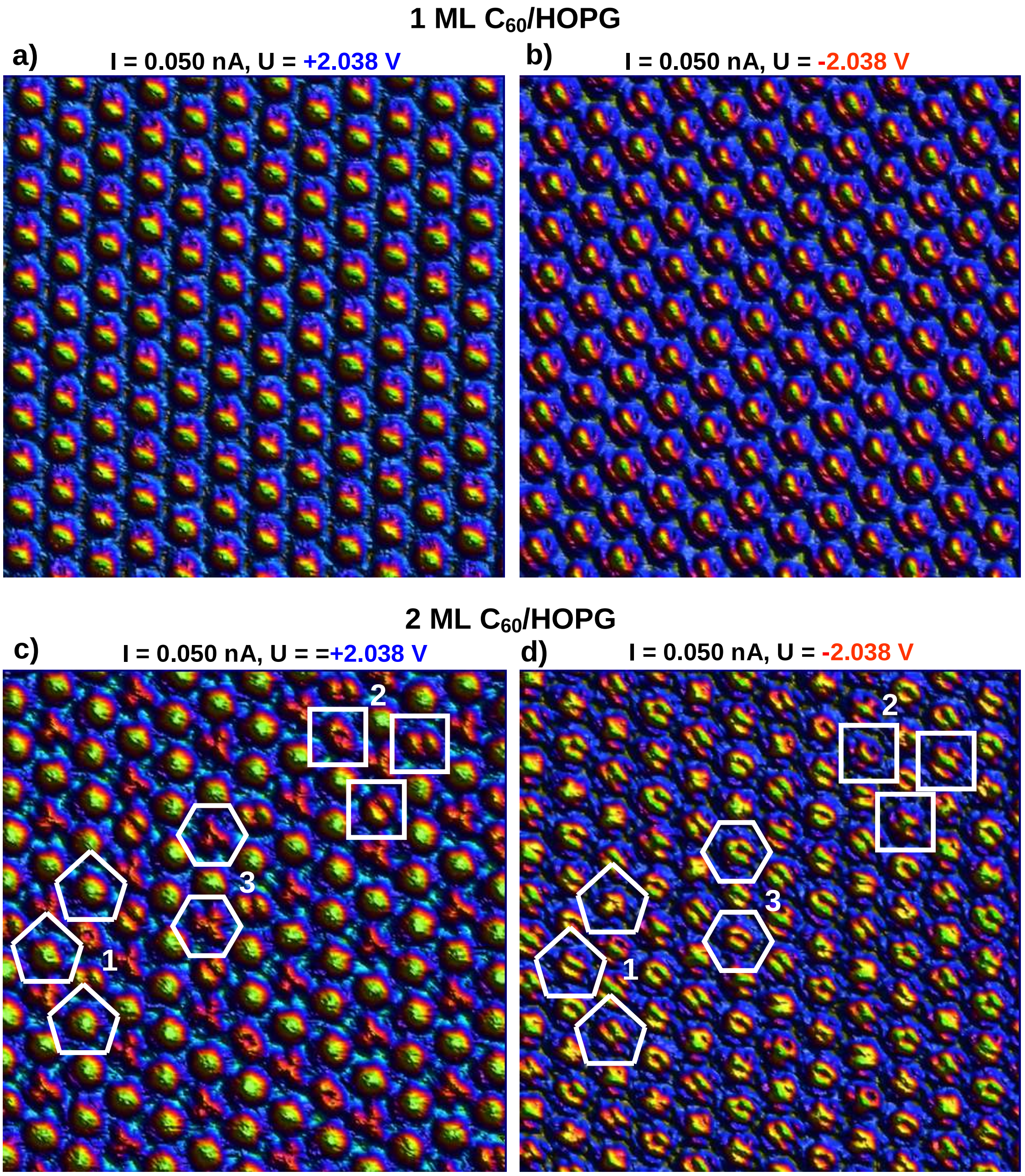

Figure 6.8: High-resolution 10×10 nm² STM images of 1 and 2 ML C_{60}/HOPG imaged at 5 K. The molecules show the same orientation for positive and for negative tunneling voltages.

Figure 6.8 d) shows the STM image of the occupied states of 2 ML C_{60}/HOPG, which also shows three different patterns. The same sample area as in the STM image of the unoccupied states is displayed, consequently the pentagons, squares and hexagons mark the same C_{60} molecules. The three-lobe intramolecular pattern for the unoccupied states is again a threefold symmetric pattern for the occupied states, the pattern which is uniformly bright is dumbbell-like in the case of occupied states and the pattern showing a dumbbell-like structure for the unoccupied states becomes slightly diffuse and differs for the three possible in-plane orientations. The different topography of C_{60} molecules for negative and positive tunneling voltages is similar to the one found in [178, 179], where the topography and structure of single C_{60} molecules on Au and Ag surfaces were investigated with STS, STM and theoretical methods. The STM image of the unoccupied states of C_{60}/HOPG is very sharp and the structures are clearly to identify, whereas in the STM image of the occupied states the patterns are smeared out a little bit. It is possible that the tip shape changed slightly by reversing the polarity. This becomes apparent especially for the three bright spots of the three-lobe structure, which often overlap.

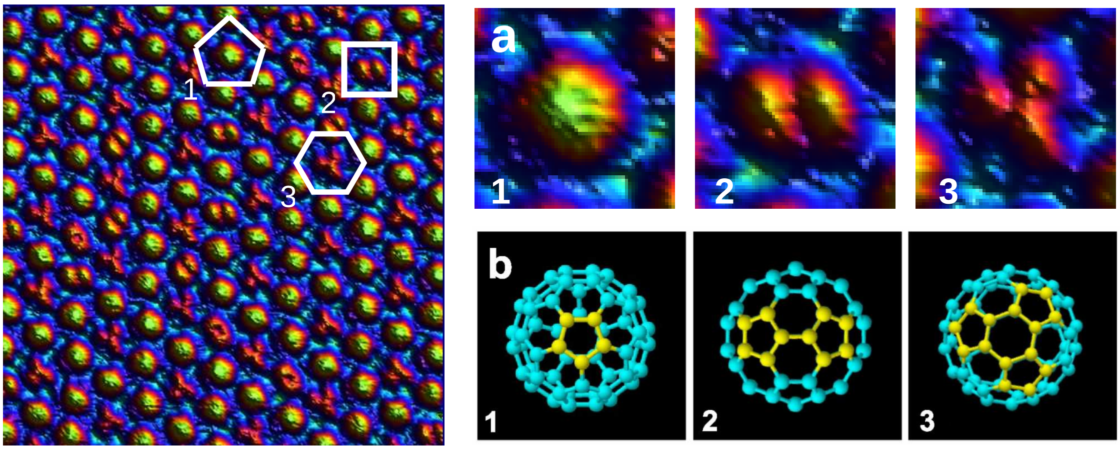

Figure 6.9:Left: 10×10 nm² STM image of unoccupied states of C_{60}/HOPG. Right: a) Enlarged images of the C_{60} molecules. b) Corresponding top view models. The regions which appear high in the STM image of unoccupied states are highlighted in yellow and belong to pentagonal rings of the C_{60} molecule [175].

The most fundamental question in this context is *why* the 2 ML C_{60} molecules/HOPG show three different patterns including in-plane orientations. To discuss and understand this topic the unoccupied states of 2 ML C_{60}/HOPG are considered. If one looks at the STM image carefully, one observes rows of C_{60} molecules consisting of uniformly bright spots with a few exceptions showing the dumbbell-like pattern. In the neighboring rows the three-lobe molecules alternate with the molecules showing bright spots or – in the case of the exceptions – with molecules showing the dumbbell-like pattern. Thus the C_{60} molecules with the three-lobe pattern are at defined positions in the lattice without any exceptions. This structure can be explained by the low temperature phase of C_{60} which forces the molecules to be rotationally ordered.

Due to the temperature dependence of the C_{60} bulk structure, the temperature range between 5 K and 320 K can be divided into three groups: phase I (260-320 K), phase II (90-260 K) and phase III (5-90 K) [180]. In the phase I region, the C_{60} bulk molecules rotate freely, effectively randomly and independently from each other, which was observed by x-ray [181], NMR [182, 183, 184], quasi-elastic scattering [185] and powder neutron diffraction [180] measurements. At RT a bulk C_{60} crystal adopts an fcc structure, space group $Fm\bar{3}m$ [181], with all four spherical C_{60} units being symmetry equivalent. In the temperature range of 90–260 K (phase II) the molecules in solid C_{60} lose two of their three degrees of rotational freedom, and the lattice structure is transformed into a simple cubic (sc, space group $Pa\bar{3}$), known as the rotational ordered phase. At the critical temperature of T_C = 260 K phases I and II coexist [180]. Heiney et al. observed a critical temperature of 249 ±1 K [181]. The lowering of the crystal symmetry is caused by the assignment of a local threefold axis to each of the four distinct molecules in a unit cell. This leads to two possible orientations for each C_{60} molecule, which are energetically favored. Briefly, the molecules on the face-centered sites and at the corners of the former fcc lattice structure become inequivalent due to the development of orientational order which leads to the simple-cubic order of solid C_{60} below T_C. Figure 6.10 illustrates this phenomenon.

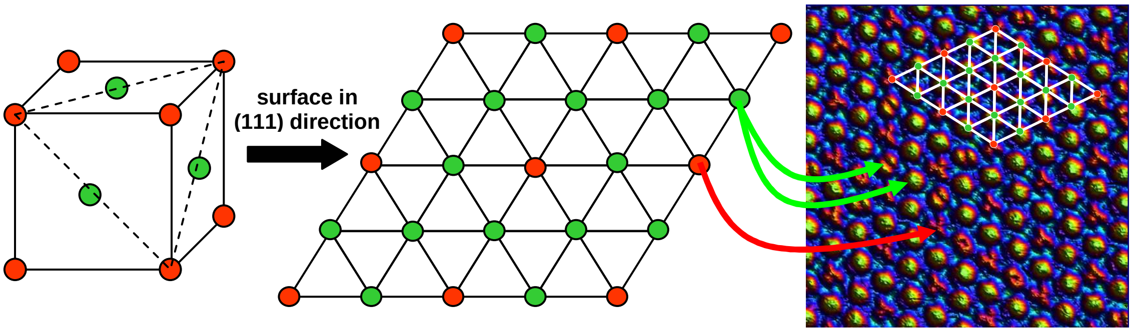

Figure 6.10: The C_{60} (111) lattice showing different orientations at low temperatures, which can be assigned to the orientations which were observed in the 10×10 nm² STM image of unoccupied C_{60} states.

Below 90 K the C_{60} molecules are frozen into a rotational frozen (glassy) phase. In this state the rotational freedoms of the molecules are totally lost; each molecule randomly occupies one of the two orientation-dependent local-energy minima. In an idealized ordered C_{60} solid electron-deficient regions (pentagons) face electron-rich regions (inter-pentagon bonds) of neighboring C_{60} units, which leads to optimal molecular electrostatic interactions and a reduction in the local symmetry and stabilizes the relative orientation of adjacent molecules [186]. Each C_{60} unit has six of its twelve pentagonal faces and six of its thirty inter-pentagon bonds facing its 12 nearest neighbors. This bonding interaction arises from the rigid anticlockwise rotation of the C_{60} unit at the origin of the unit cell around the (111) axis by 98°. The other three C_{60} molecules in the unit cell, centered on the cube faces, are similarly rotated by the same angle but about the other three (111) axes. For this reason the C_{60} molecules at the corners of the unit cell show the three-lobe intramolecular patterns while the molecules on the cube faces show a different orientation. WANG et al. studied a 10 ML thick C_{60} film on a Si(100) 2×1 surface and observed very similar intramolecular patterns for the C_{60} molecules as it is shown here for 2 ML C_{60}/HOPG. The difference to the STM image taken in Dortmund is that WANG et al. did not observe molecules showing bright spots, but only molecules with the three-lobe pattern and molecules with the dumbbell-like pattern including in-plane orientations [176]. This is possibly due to the fact that WANG et al. studied a C_{60} film which was completely decoupled from the substrate, whereas the 2 ML thick C_{60} film investigated within this thesis could still be influenced by the substrate. The bright spot C_{60} molecules were also observed for 1 ML C_{60}/HOPG and are possibly typical for a C_{60} film which interacts with the substrate. The molecules showing the dumbbell-like pattern seem to be typical for C_{60} molecules on face-centered positions of a unit cell in *solid* C_{60}. The STM image in [176] observed by WANG et al. does not show different in-plane orientations for the three-lobe C_{60} molecules either, but three in-plane orientations in (111) direction of the dumbbell-like

C_{60} molecules. This is due to the fact that the in-plane orientations of the three-lobe structure are defined by the orientations of the dumbbell-like structure due to energy minimization. In contrast, if the C_{60} molecules with the three-lobe pattern are surrounded by C_{60} molecules showing the bright spot pattern, there are different possibilities for the in-plane orientation of the three-lobe C_{60} molecules due to the fact that this arrangement is highly symmetric.

In solid C_{60} the high symmetry of the C_{60} molecules allows the interactions of adjacent molecules to be optimized identically for all 12 nearest neighbors. On the surface of a C_{60} solid the translational symmetry is broken. The molecules at the surface have only nine neighbors instead of 12 in the bulk. Nevertheless the STM images taken in Dortmund and taken in [176] show the existence of a 2×2 superlattice indicating that a crystal field involving nine nearest neighbors of C_{60} molecules is still capable of driving the molecules to an orientationally ordered state [187].

The results concerning the different orientations of C_{60} molecules/HOPG were achieved after evaporating C_{60} on HOPG at RT. The growth mechanism at RT and the shape of the C_{60} islands were discussed in detail as well as the step heights of a multilayer C_{60} film on HOPG. Due to the different electronic properties of C_{60} and HOPG the step height as measured with STM of 1 ML C_{60}/HOPG is 1 nm and 0.81 nm for the following monolayers. In contrast to the RT evaporation, the island shapes look different for the evaporation of C_{60} on HOPG at 100 K and subsequent RT annealing. In Figure 6.11 STM images of C_{60}/HOPG evaporated at 100 K and annealed for 1 h at RT are depicted.

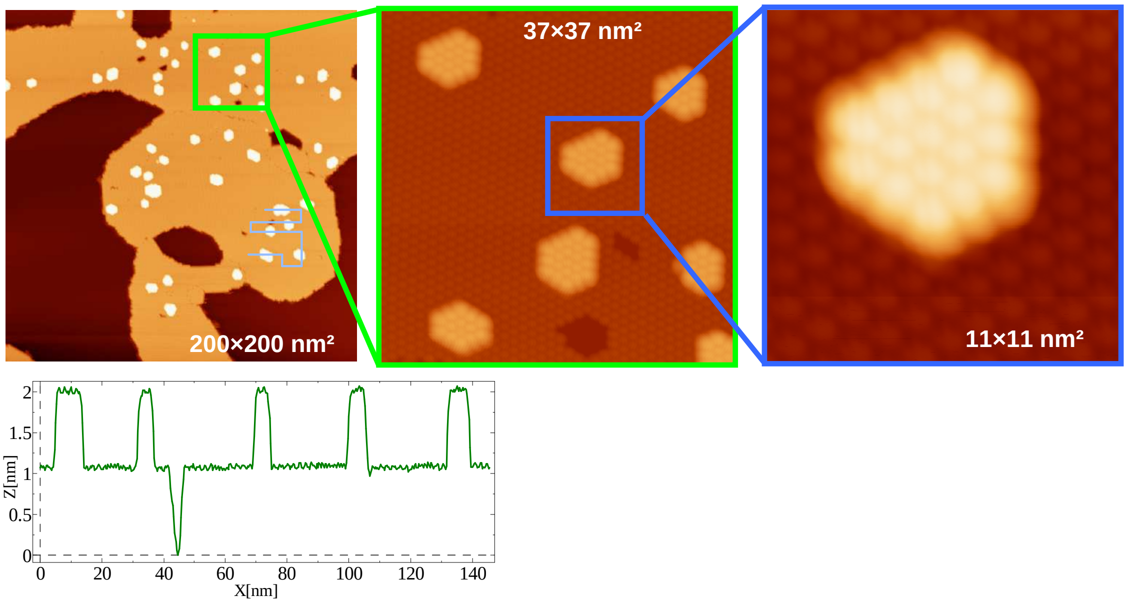

Figure 6.11: STM images scanned at 77 K and line profile of C_{60}/HOPG evaporated at 100 K and annealed for 1 h at RT.

The reason for the annealing of 1 h at RT was the following: Ag_{923} was deposited on the HOPG sample at low temperatures for taking UPS spectra (see section 6.6). The sample was kept at 100 K to avoid coalescence of the Ag_{923} clusters on the pristine HOPG substrate. C_{60} was evaporated followed by an annealing at RT to find out if there is an arrangement of clusters and C_{60}, which interacts stronger with metal clusters than with HOPG, which could lead to self assembled structures. An interesting arrangement of C_{60} molecules and clusters was not observed but on the free sample areas which were not covered with Ag_{923} the growth mechanism of C_{60} evaporated at low temperatures was studied.

In contrast to C_{60} evaporated on HOPG at RT, the first ML is not completely closed, but both small and large holes and fissures are visible, showing the pristine HOPG surface. The second ML C_{60} does not grow in a fractal like manner, but small hexagonal shaped islands grown in (111) direction are visible (see Figure 6.11). The line profile depicted in Figure 6.11 shows that the small islands on the first ML C_{60} have a height of around 0.81 nm. The reason for the different growth mechanism at low temperatures is the limited mobility of the C_{60} molecules. The higher the mobility of the C_{60} molecules, the higher the completeness and order of the first and second ML C_{60} and the larger the 1 and 2 ML C_{60} islands on HOPG.

6.2.3 C_{60}/Au(111)

In addition to C_{60} on HOPG, also the orientations of C_{60} molecules which were evaporated on Au(111) were studied. The different orientations of C_{60} on HOPG become apparent by investigating the intramolecular structure with STM at 5 K. The three different intramolecular orientations discussed in 6.2.2 were also found for 1 ML C_{60}/Au(111) [175]. In contrast to C_{60}/HOPG, different patterns due to a certain arrangement of C_{60} molecules with different orientations for 1 ML C_{60}/Au(111) can be found on a larger scale for certain areas of 1 ML C_{60} islands. Figure 6.12 displays the three different close-packed adsorbate phases C_{60}(1), C_{60}(2) and C_{60}(3) of 1 ML C_{60}/Au(111).

The black areas in Figure 6.12 represent the bare Au(111) surface, the white areas 1 ML C_{60} islands on a terrace which is an Au(111) step edge higher. The strong contrast is necessary to emphasize the different C_{60} patterns.

The crystallographic directions of C_{60}(2), which shows only some dark colored C_{60} molecules having a different orientation than the brighter C_{60} molecules, match those of the Au(111) surface. C_{60}(2) has a 38×38 unit cell containing 11 C_{60} molecules [143, 188]. In contrast, the C_{60}(1) surface has a stronger pattern with both dark and bright molecules representing different C_{60} orientations. In this structure the close-packed directions of the C_{60} run parallel to the Au(111) reconstruction lines and are assigned to a $(2\sqrt{3} \times 2\sqrt{3})$ R30° structure in which all C_{60} molecules are bonded at equivalent positions. The third pattern – C_{60}(3) – was published by the group of R. BERNDT in 2007 and is organized in a supramolecular $(\sqrt{589} \times \sqrt{589})$ R 14.5° lattice on Au(111). Its unit cell is composed of 49 molecules in a (7×7) array [175]. An STM image of this C_{60} superstructure is visible in Figure 6.13, together with pictures and explanations taken from Ref. [175].

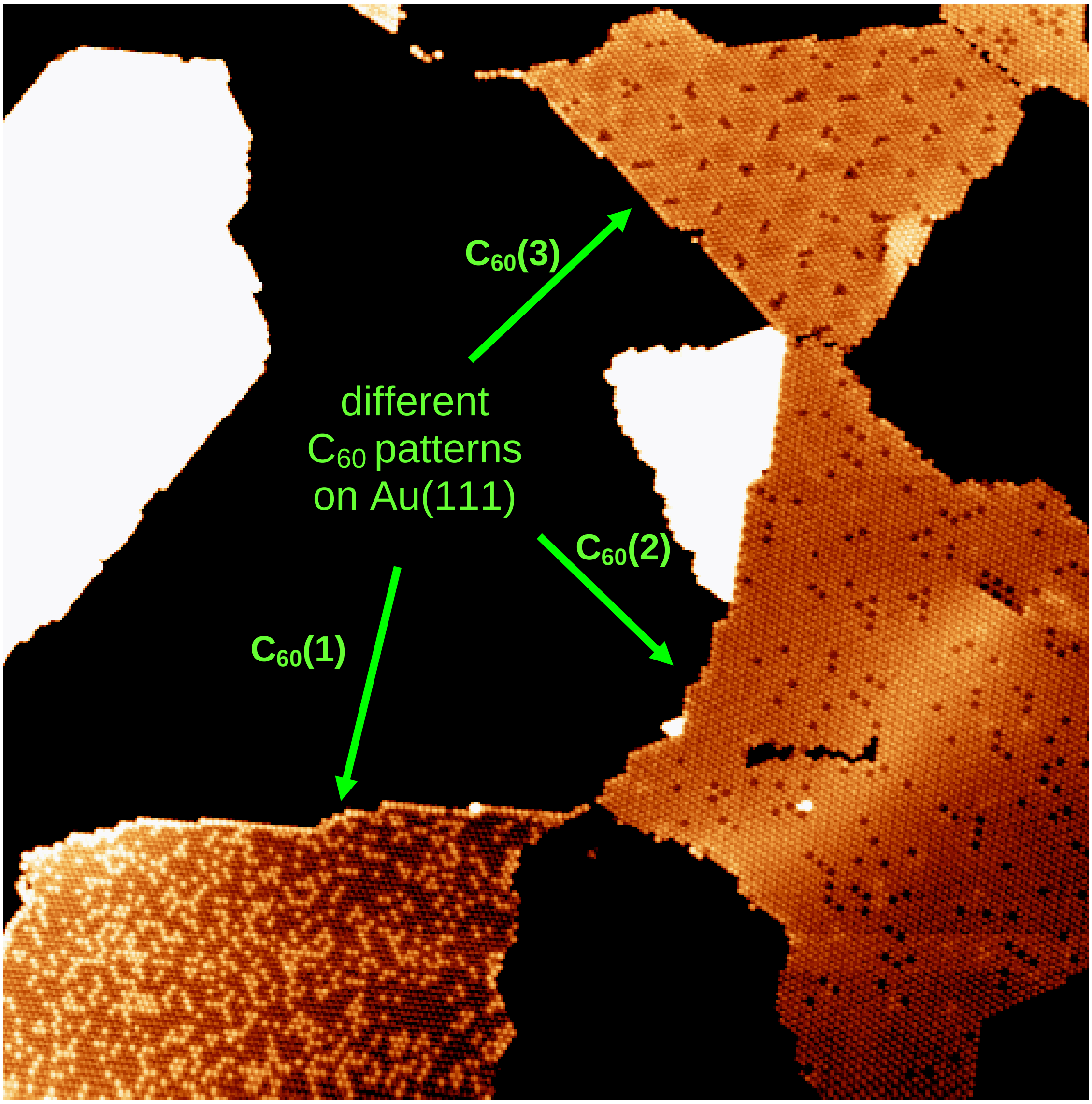

Figure 6.12: 162×164 nm² STM image taken within this thesis of the three patterns of 1 ML C_{60} molecules on Au(111) due to a certain arrangement of C_{60} molecules with different orientations.

The huge adsorbate unit cell is due to long range commensurability with the underlying Au(111) lattice. The orientation of the C_{60} molecules varies periodically resulting in a Moiré pattern. The darker C_{60} molecules in Figure 6.13 a), all showing threefold symmetry, suggest that several Au atoms are missing underneath. X. ZHANG et al. proposed that the regularly spaced dark spots are caused by some kind of surface re-organisation of gold atoms. Upon the adsorption of C_{60}, top layer gold atoms re-organize and the reconstruction of the clean Au(111) is lifted. Instead of atoms resuming to their bulk truncated positions they form an isotropically compressed close-packed layer under the influence of the C_{60} molecules [189].

Since the thermally activated decay of Ag clusters on C_{60}/Au(111) and C_{60}/HOPG was studied within this thesis, the RT stability of C_{60} molecules on Au(111) plays an important role. For this reason the RT stability of 1 ML C_{60}(1) on Au(111) – with its different orientations visible by dark and bright spots – was studied with STM at RT

[146]. The four STM images of C_{60}(1) on Au(111) in Figure 6.14 were measured at RT and are out of a larger series. They were consecutively measured at the same surface area and it took 22 min to take one image.

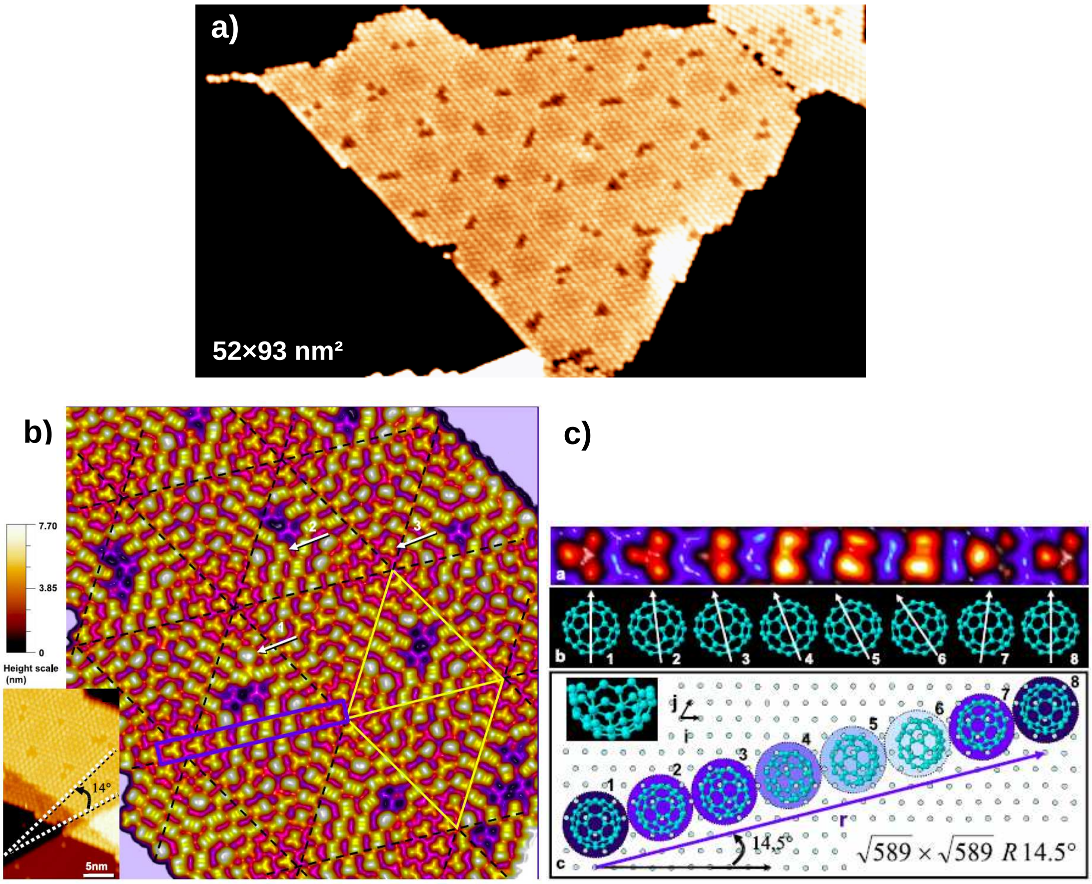

Figure 6.13: a) Detail of Figure 6.12: enlarged 52×93 nm² STM image of 1 ML C_{60}/Au(111) with C_{60} being organized in a ($\sqrt{589} \times \sqrt{589}$) R 14.5° lattice on Au(111). b) 32×20 nm² and pseudo-3D 20×20 nm² STM images of C_{60} islands deposited at room temperature on Au(111). The highlighted rhombus defines a unit cell. The dashed lines indicate equivalent cells [175]. c) Top: pseudo-3D STM image (0.8×8 nm²) of the C_{60} line marked by a blue rectangle in b). Middle: side view model of molecular orientation. Bottom: top view model of the lateral arrangement of the molecules [175].

Due to thermal drift the sample area slightly changed from one image to the next. The red frames in Figure 6.14 mark the common regions of the four STM images. Localizing fixed positions, visible by the orange circles, one can align the frames and calculate the difference images 2–1, 3–2 and 4–3. One clearly observes that most of the molecules have remained in the same orientation, which is represented by the grey areas, while a few have either turned from dark to bright (white dots) or from bright to dark, (black dots). This change in orientation at RT is in agreement with the observations by E. I. ALTMAN in [190].

In contrast, performing the same STM measurements at 77 K (see Figure 6.15) shows that the C_{60} film is completely stable on a timescale of hours and that not a single molecule changes its orientation. A much lower drift than at RT can also be observed.

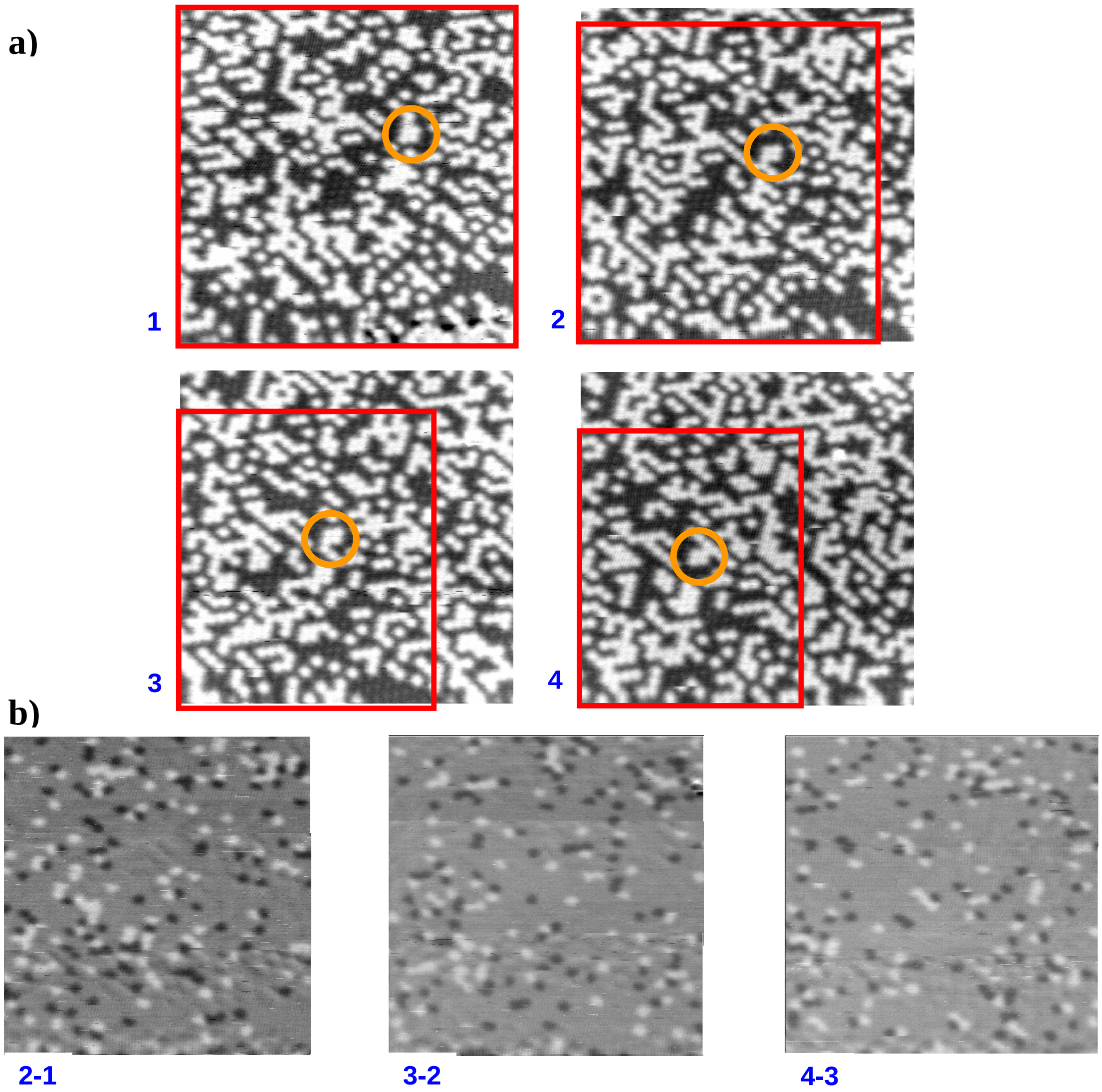

Figure 6.14: a) 33×33 nm² STM images of 1 ML C_{60}(1)/Au(111). Images 1, 2, 3 and 4 were imaged sequentially at RT at the same sample area and it took 22 min to take one image. Red frames mark the common sample area, changing slightly due to thermal drift. Orange circles mark fixed positions. b) Difference images indicating the switch of the C_{60} molecules from dark to bright or bright to dark [146].

In summary, at RT the C_{60} layer on both Au(111) and HOPG is a dynamic system with rotation of the molecules, which might enhance the diffusion of material on the layer, whereas at 77 K and at 5 K such effects can be safely neglected.

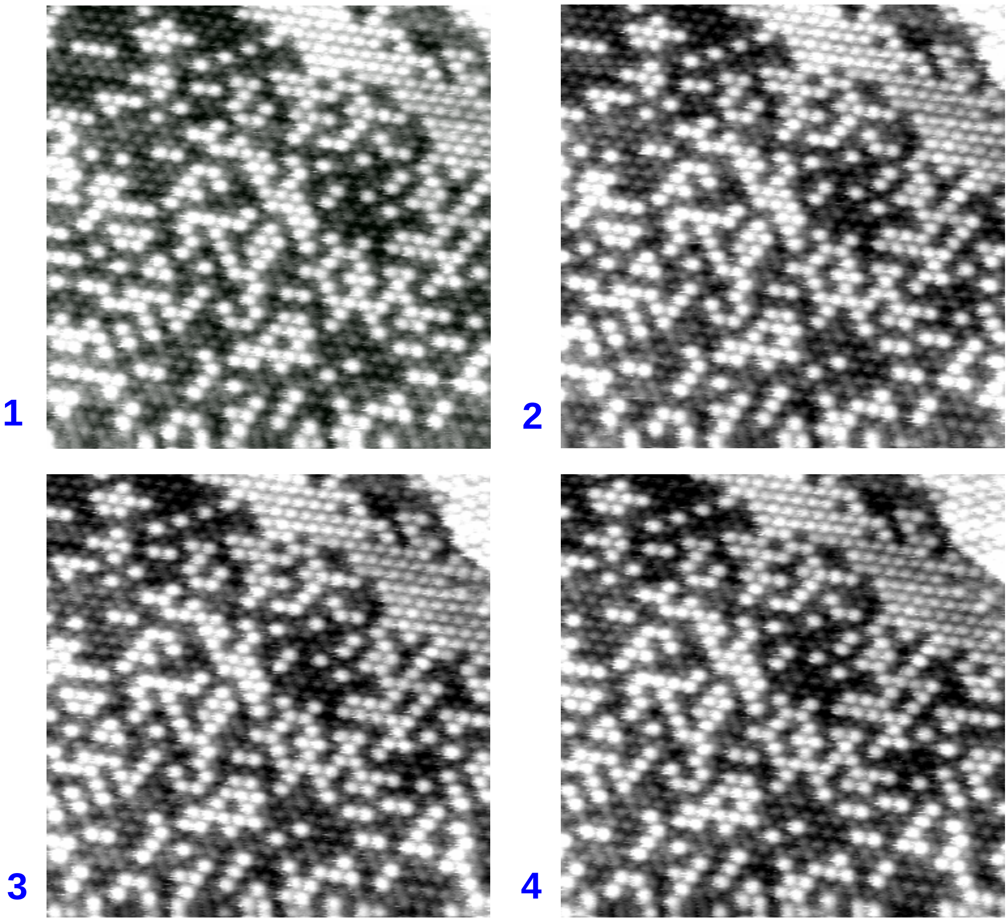

Figure 6.15: 33×33 nm² STM images of 1 ML C_{60}(1)/Au(111) measured consecutively at the same sample area at 77 K. The C_{60} film is long-time stable and the C_{60} orientations do not change.

6.3 Thermally activated processes of size selected Ag clusters

In this chapter the results for the deposition of size selected Ag clusters are presented and discussed concerning the thermally activated processes of the Ag clusters on C_{60}.

The experiments proceeded as follows: size selected Ag clusters were deposited on a C_{60} functionalized Au(111) or HOPG sample at low temperatures. The preparation steps and the details of the cluster deposition are presented in chapter 5. After deposition it took around 15 min to transfer the sample into the STM which was held at 77 K or 5 K. The sample was investigated with STM and the cluster heights were analyzed with the program *WSxM* (see section 6.1.1). Then the sample was annealed for different time intervals below and at RT and after every annealing step the sample was investigated with STM to study the cluster height.

The RT stability of size selected Ag clusters on C_{60} depends strongly on the sample substrate. If size selected *geometrically magic* clusters (section 6.3.1) are deposited on a metal surface like Au(111) functionalized with 1 ML C_{60}, the clusters decay during the annealing at RT, penetrate the C_{60} film and form Ag islands with the step height of 1 ML below the C_{60} (sections 6.3.1.1 – 6.3.1.5). The decay is explained by atomistic calculations done by MICHAEL MOSELER in section 6.3.1.8. During decay a metastable cluster size, which has an extremely narrow cluster height distribution, occurs. In contrast, if the clusters are deposited on 2 ML C_{60}/Au(111) or on 1 or 2 ML C_{60}/HOPG, the Ag clusters are long-time stable at RT and do not decay (sections 6.3.1.4 – 6.3.1.7)

The thermally activated processes of size selected *geometrically non-magic* Ag clusters (section 6.3.2) was studied as well and it was observed that geometrically non-magic clusters do not decay but show Ostwald ripening [191], which also leads to the same metastable cluster size which was observed for geometrically magic clusters. Due to the fact that we have indications for Ostwald ripening also for annealed Ag_{55} clusters, Ostwald ripening probably occurs in general for small clusters with less than 147 atoms.

6.3.1 Decay vs. stability of geometrically magic Ag clusters

6.3.1.1 Ag_N (N=55, 309, 561) / 1 ML C_{60} / Au(111)

Ag_{309} and Ag_{561} were deposited at 165 K on 1 ML C_{60}/Au(111) to guarantee the stability of the clusters. Ag_{55} was deposited at a lower temperature of 115 K because there were indications that the decay of Ag_{55} clusters already starts below RT. Contamination of the sample at low temperatures gets more critical below 100 K because a number of gases forming the residual pressure condense below this temperature [192]. STM images and height distributions after the low temperature deposition of Ag_{55}, Ag_{309} and Ag_{561} on 1 ML C_{60}/Au(111) are shown in Figure 6.16 and Figure 6.17.

After the low temperature deposition the cluster heights in the different images shown result in narrow cluster height distributions with cluster heights of $h = (1.38 \pm 0.15)$ nm for Ag_{55}, $h = (2.35 \pm 0.15)$ nm for Ag_{309} and $h = (2.77 \pm 0.02)$ nm or $h = (2.67 \pm 0.20)$ nm, respectively, for Ag_{561}. The narrow height distributions show that the mass selection and soft landing of the clusters was successful. Only some clusters which coalesced in the center of the deposition spot have larger heights. In Figure 6.17 it is shown that the cluster height is independent from the cluster density. The STM images in Figure 6.17 a) and b) were measured in a region with lower and higher cluster density. As represented by the height distributions the clusters measured in the low and high covered region have the same height [146]. The larger width of the cluster height distribution measured from clusters in the region with higher cluster coverage is due to the coalescence of some clusters. The difference of the mean values of the heights (2.77 nm and 2.67 nm) is within the error of 5 % of the STM measurement. A non negligible factor is the shape of the STM tip which has some influence on the cluster height [193,194].

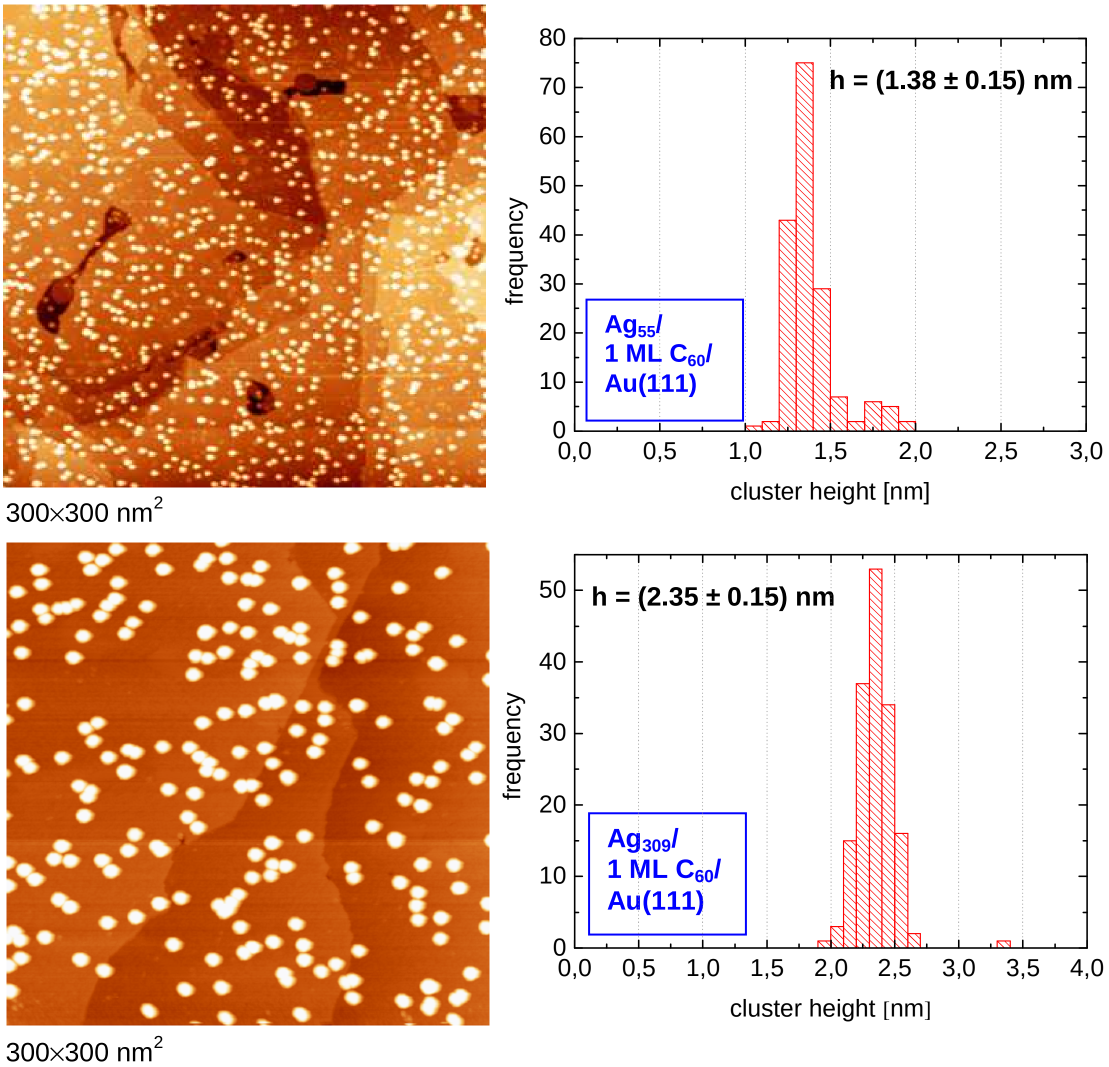
300×300 nm^2

300×300 nm^2

Figure 6.16: STM image at 77 K and height distribution of Ag_{55}/1 ML C_{60}/Au(111) ater the deposition at 115 K (top) and Ag_{309}/1 ML C_{60}/Au(111) (bottom) after deposition at 165 K.

Much stronger the STM tip influences the width of an object. As it is visible in the two STM images in Figure 6.17, the clusters in the region with low and high coverage have the same height but a different width. This is due to different condition of the STM tip. The width of an object is always a convolution of its real width and the shape of the STM tip, as it is explained in section 4.1. If there are two different cluster sizes on the same sample one observes a different width of the smaller and larger clusters showing mainly the relative heights. To get information about the width of a cluster there are different possibilities. In order to investigate the absolute width of the clusters some groups deconvolute the tip shape from the STM image of clusters with special programs algorithms. Another more precise experimental method to measure the cluster width is Transmission Electron Microscopy (TEM).

The results show that Ag_{55}, Ag_{309} and Ag_{561}/1 ML C_{60}/Au(111) are long-time stable at 77 K and that they have a narrow height distribution. Only in regions with a higher cluster density some clusters coalesced. As already discussed the RT stability of clusters on surfaces is of great importance for applications.

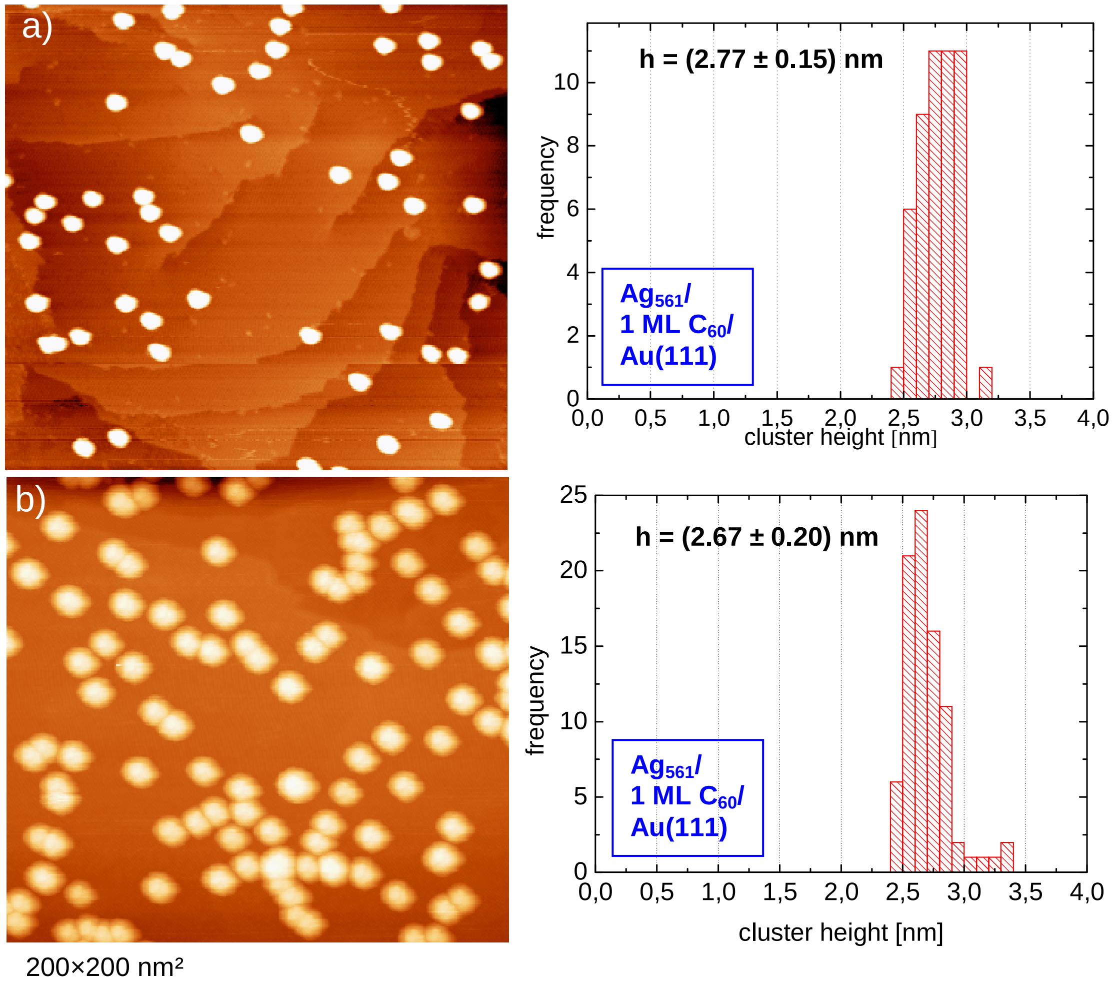

Figure 6.17: 77 K STM images of Ag_{561}/1 ML C_{60}/Au(111) scanned in a region with low (a)) and high (b)) coverage and corresponding height distributions. The cluster height is independent of the cluster density. The different width of the clusters is due to different shapes of the STM tip [146].

For this reason the Ag_N/1 ML C_{60}/Au(111) samples were annealed and after that imaged with STM at 77 K in order to investigate possible changes of the cluster heights. The height distributions of Ag_{309}/1 ML C_{60}/Au(111) after different annealing steps together with two STM images are shown in Figure 6.18. The sample was annealed for 45 min at 265 K and for 10, 25, 45, 90 and 180 min at RT and imaged with STM at 77 K after each annealing step. After 45 min at 265 K the cluster heights did not change significantly, but after annealing for 10 min at RT the broadened height distribution shows that that cluster heights shrink. After 25 min at RT a second maximum in the height distribution is formed and after 45 min at RT one clearly observes two maxima at 1.55 nm and at 2.05 nm. In the STM image taken after 45 min at RT the two different cluster sizes are visible by different colors and different cluster widths. Besides, below the C_{60} film one observes islands with the height of 1 ML Ag which indicate that the decrease of the cluster height is due to a thermally activated decay of the clusters on 1 ML C_{60}. After 90 min and 180 min at RT, respectively, the clusters completely decayed to a height of around 1.5 nm. In the STM image in Figure 6.18 taken after 90 min at RT the islands below the C_{60} are well visible and only one cluster size is observable. A few larger clusters due to coalescence are visible because after the decay the STM images were taken in a region with higher cluster coverage to gain good statistics for the height measurement. The cluster size of ≈ 1.5 nm height was also observed after the RT deposition of Ag_{309}, Ag_{561} and Ag_{923} [165, 86] and seems to be a metastable height.

After deposition of geometrically magic clusters/1 ML C_{60}/Au(111) at RT instead of 165 K, the sample was annealed for 12 h at RT and it was observed that nearly all clusters decayed on 1 ML C_{60}.

An STM image taken in the center of the deposition spot after annealing for 90 min at RT is depicted in Figure 6.19. The Ag which penetrated the C_{60} film has formed a network below the C_{60}. An interesting aspect concerning the decay of the clusters is the fact that the clusters decay in a shorter time on the C_{60}(2) surface, which matches the crystallographic directions of the Au(111) substrate. In contrast, on C_{60}(1) which has the typical $(2\sqrt{3} \times 2\sqrt{3})$ R30° structure, the clusters are stable for a longer time. The two STM images in Figure 6.20 show several clusters on 1 ML C_{60}(1) and only a few clusters on 1 ML C_{60}(2) together with Ag islands below the C_{60} due to clusters which penetrated the C_{60}(2) film. The cluster heights on C_{60}(1) and C_{60}(2) after 45 min at RT are depicted by the height distribution in Figure 6.20. The heights on the two phases of C_{60} do not differ significantly. Both larger and smaller clusters were observed on C_{60}(1) and C_{60}(2), before the clusters completely penetrated the C_{60} film.

For the deposition of Ag_{561}/1 ML C_{60}/Au(111) similar results were observed [146]. In order to check the stability of the deposited clusters, the sample was subsequently annealed in the same way as the Ag_{309} clusters, this time at 215 K, 265 K and RT, each time for 45 min, and for 15 h at RT. Below RT we did not observe a significant change of the cluster height distribution. After 45 min at RT, the cluster heights have significantly decreased (see Figure 6.21). The effective Ag coverage is observed to be lower than after deposition, because together with a smaller cluster height the number of clusters per area is constant or even lower than before annealing.

The two-peak structure of the height distribution after annealing Ag_{561}/1 ML C_{60}/Au(111) for 45 min at RT is similar to the height distribution of Ag_{309}/1 ML C_{60}/Au(111) after 45 min at RT. Additionally it is clearly corroborated by the height distribution in Figure 6.21, which was measured for Ag_{561} clusters deposited at RT and transferred into the 77 K STM, after about 45 min [146].

The metastable cluster size of ≈ 1.5 nm height is visible in the height distribution after annealing for 45 min at RT. Due to the fact that this experiment was made earlier than the deposition experiment of Ag_{309}, the sample was not annealed for 3 h at RT but directly for 15 h at RT, so that a height histogram which might show a narrow distribution at only 1.5 nm could not be observed.

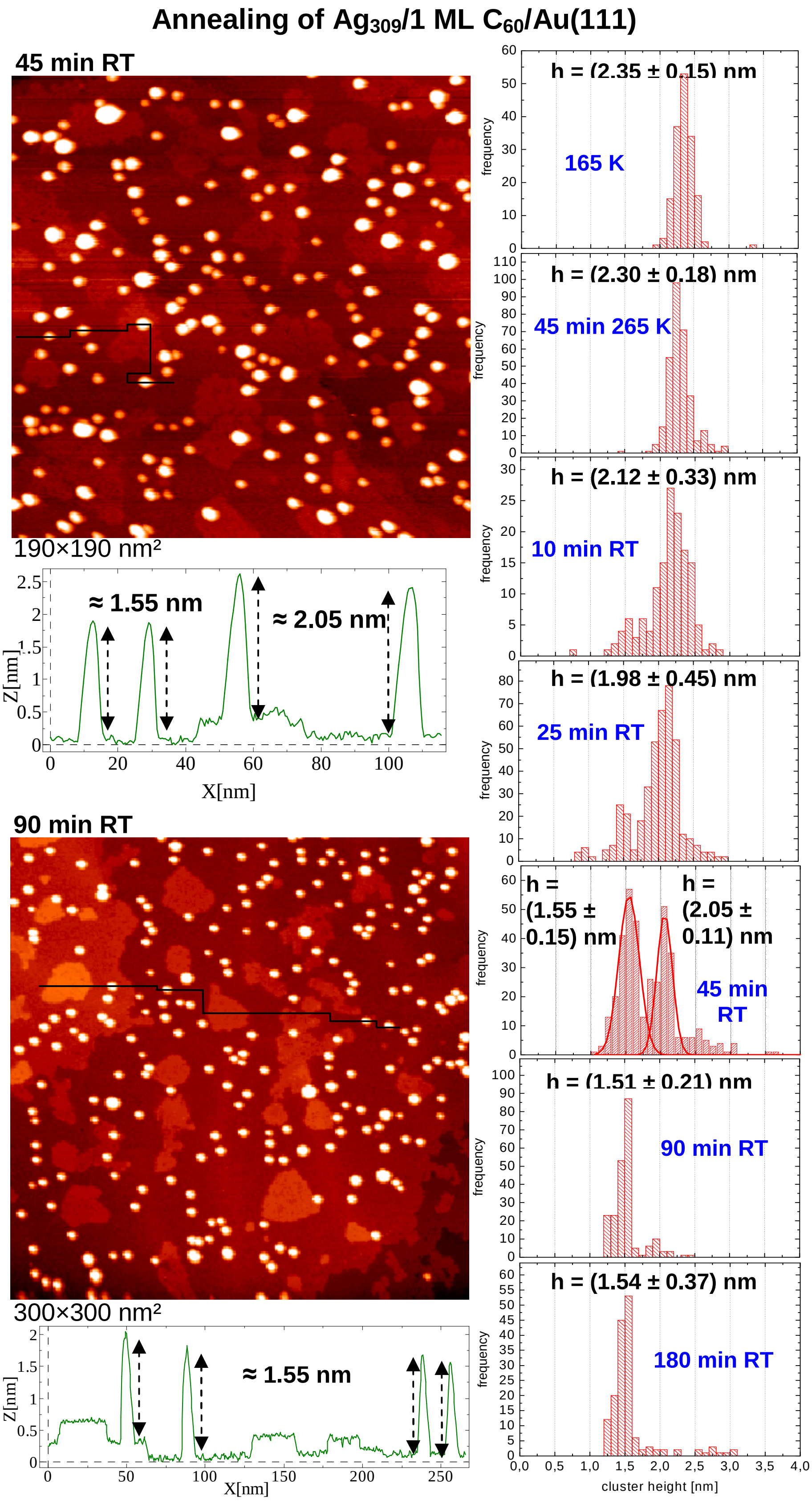

Figure 6.18: Height distributions, STM images and line profiles after annealing Ag_{309}/1 ML C_{60}/Au(111) for 45 min at 265 K and 10, 25, 45, 90 and 180 min at RT.

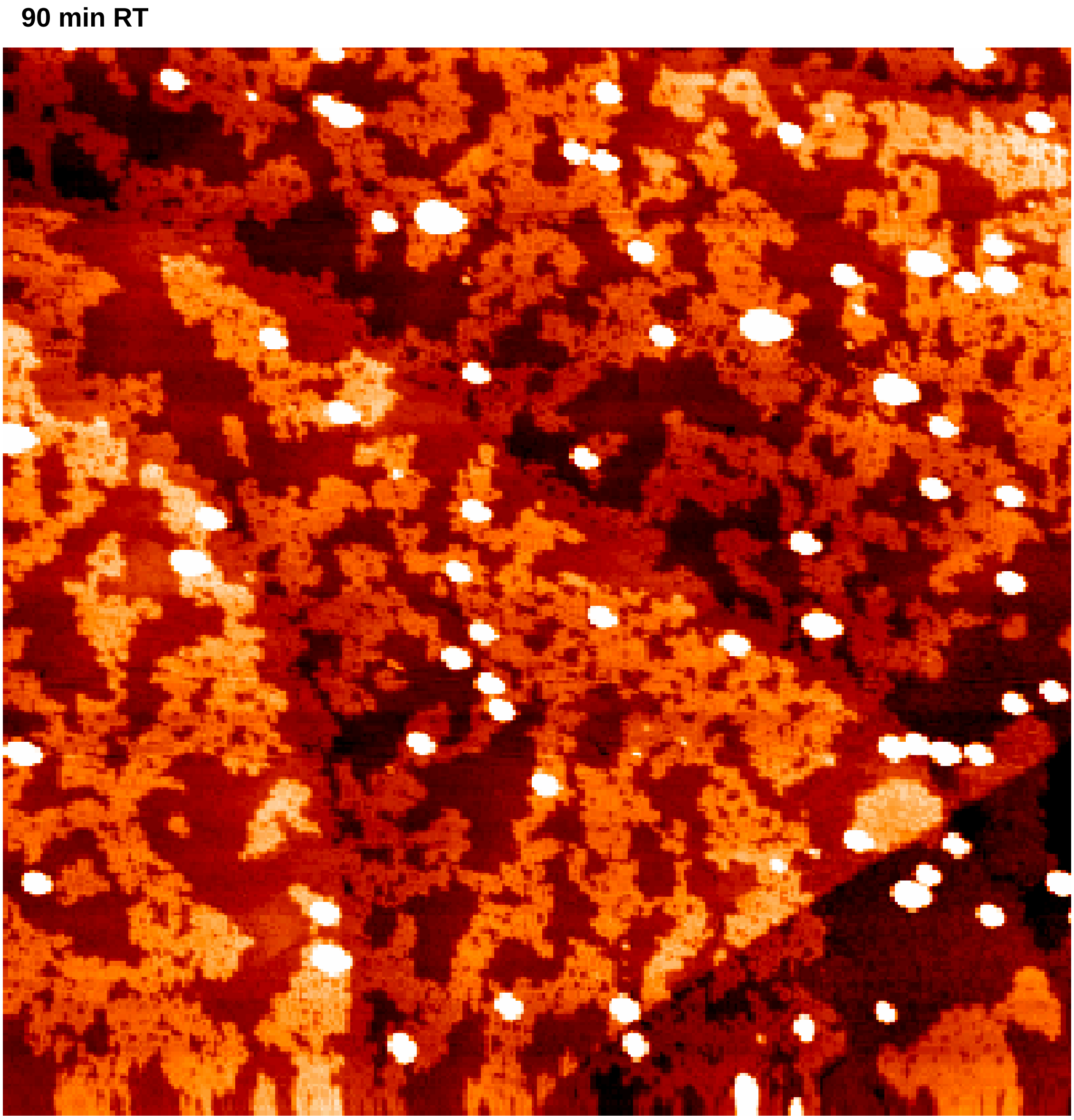

Figure 6.19: 300×300 nm² STM image of Ag_{309}/1 ML C_{60}/Au(111) taken at 77 K in the deposition spot after 90 min at RT. A network of Ag islands below C_{60} is visible.

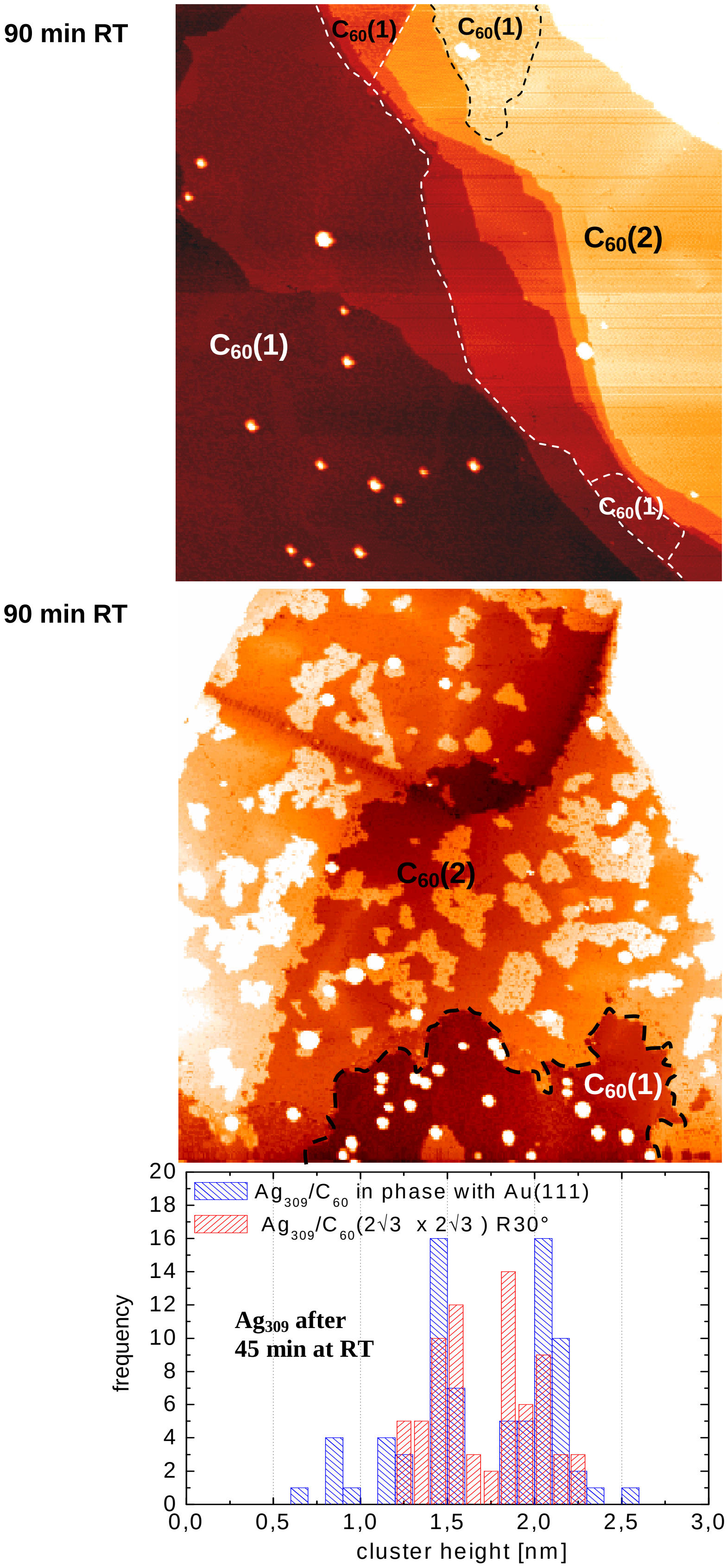

Figure 6.20: 263×263 nm² (left) and 300×300 nm² (right) STM images of Ag$_{309}$/1 ML C$_{60}$/Au(111) after 90 min at RT and height distributions after 45 min at RT. On C$_{60}$(1) Ag$_{309}$ clusters are stable for a longer time than on C$_{60}$(2). The cluster height is independent from the C$_{60}$ phase.

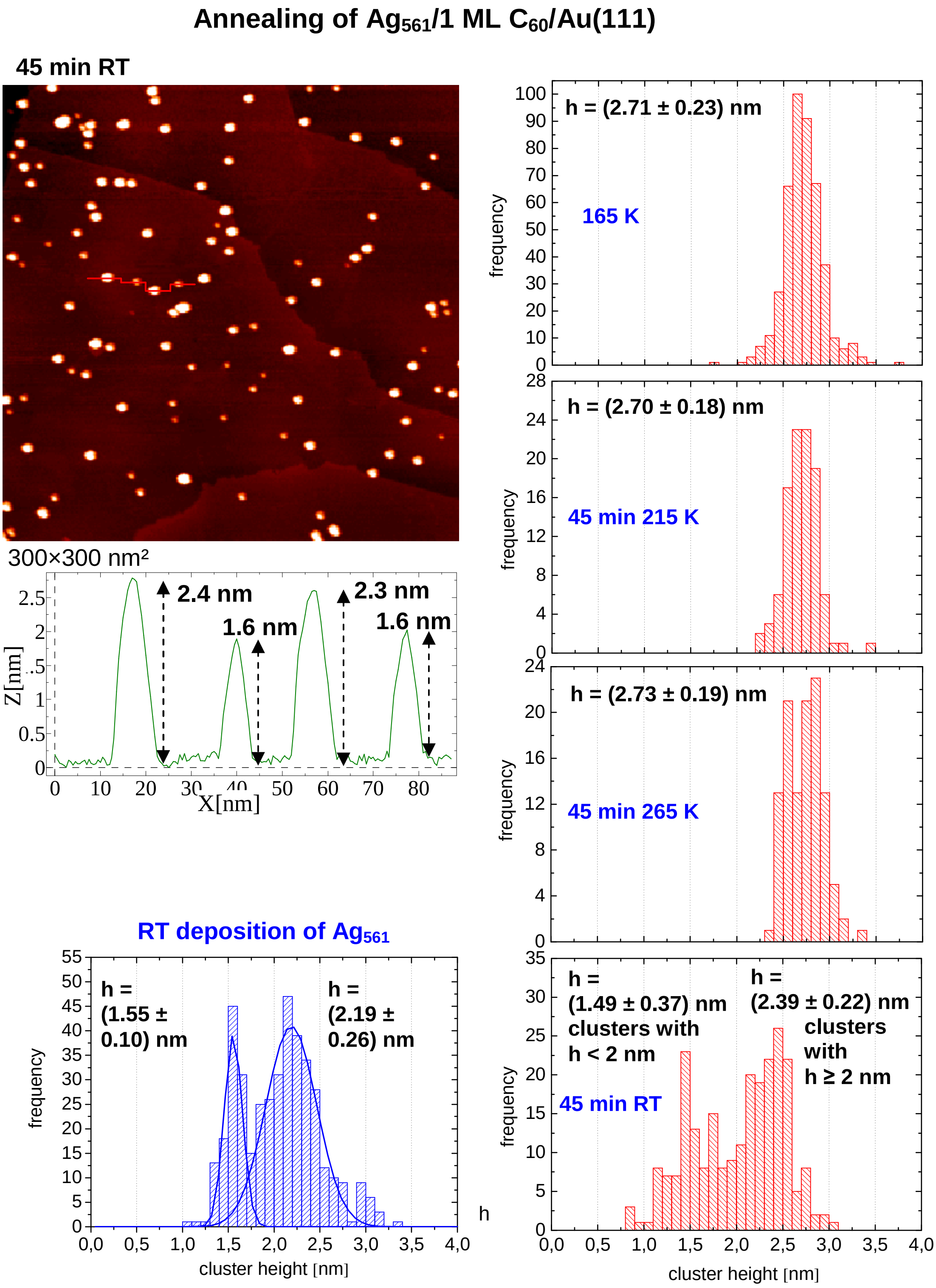

Figure 6.21: Height distributions after annealing Ag_{561}/1 ML C_{60}/Au(111) for 45 min at 200 K, 215 K, 265 K and RT and STM image and line profile after annealing for 45 min at RT. The two different cluster heights are clearly visible [146].

Keeping the samples with the Ag_{561} clusters deposited at 165 K for 15 h at RT finally leads to the disappearance of almost all clusters. Only in the areas in the center of the deposition spot some small clusters remained [146]. For this reason there is no height distribution for clusters after 15 h at RT due to poor statistics. The STM image in Figure 6.22 imaged after annealing for 15 h at RT shows Ag islands below the C_{60} film of about 0.3 nm height which result from the decayed Ag_{561} clusters on 1 ML C_{60}.

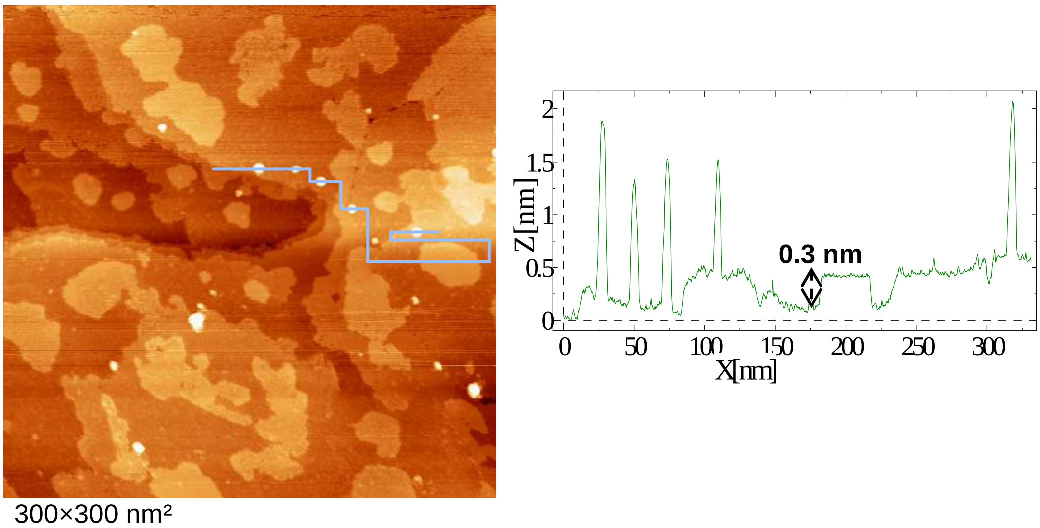

Figure 6.22: STM image and line profile of Ag_{561}/1 ML C_{60}/Au(111) after annealing for 15 h at RT.

The results of annealing Ag_{55}/1 ML C_{60}/Au(111) are slightly different. After deposition at 115 K Ag_{55} has a height of 1.38 nm which is smaller than the metastable cluster size of $h \approx 1.5$ nm. Therefore a decay of Ag_{55} would not lead to the metastable size. But, after annealing Ag_{55}/1 ML C_{60}/Au(111) for 3 h at RT, the height distribution shows a small maximum at $h \approx 1.5$ nm, together with a second maximum at 1.16 nm (see Figure 6.23). This indicates that the metastable cluster size might be reached by another process for Ag_{55}. The maximum at 1.16 nm lets assume that some Ag_{55} clusters decayed while other seemed to ripe to larger clusters. A possible explanation for this phenomenon is Ostwald ripening [191], which is explained in more detail in section 6.3.1.5 and 6.2.2 together with the results for geometrically non-magic clusters.

In summary the results of this section show that geometrically magic Ag clusters are not stable at RT on 1 ML C_{60}/Au(111). A thermally activated decay or thermally activated ripening of the clusters, respectively, lets the clusters change their size. During this processes a metastable cluster size occured, which is more stable at RT than the clusters as deposited. This metastable size stayed stable for some hours at RT before all clusters finally penetrated the C_{60} film. The cluster density decreased and finally only Ag islands below the C_{60} remained.

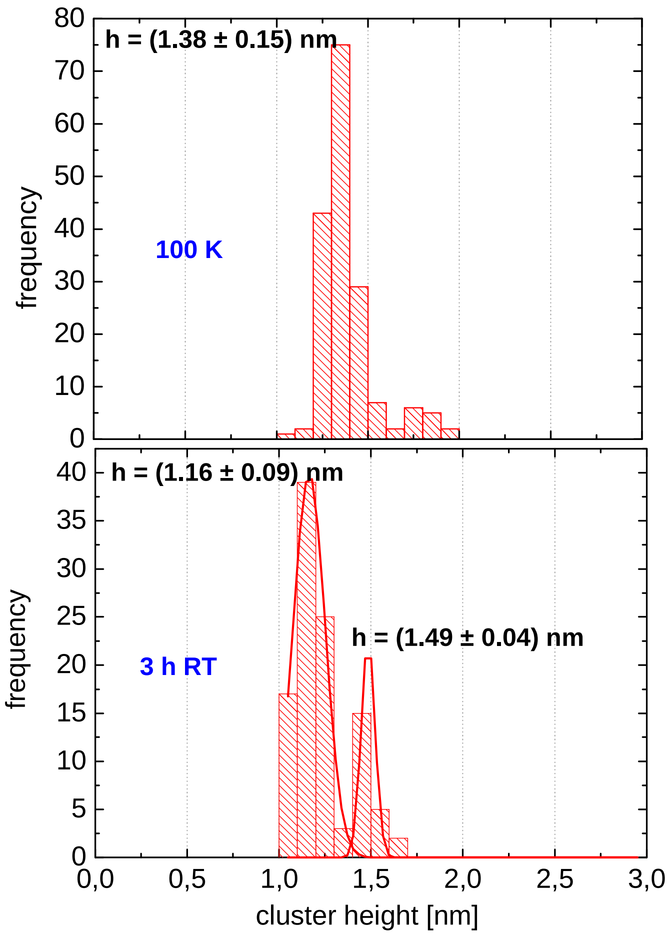

Figure 6.23: Height distributions of Ag_{55}/1 ML C_{60}/Au(111) after deposition and after 3 h at RT.

6.3.1.2 Ag_N (N=147, 309) / 1 and 2 ML C_{60} / Au(111)

In order to observe if geometrically magic Ag clusters also decay if they are deposited on more than 1 ML C_{60}, Ag_{309} clusters, and in a later experiment also Ag_{147} clusters, were deposited on Au(111) covered with one closed ML C_{60} and less than an additional second ML C_{60}. For the deposition of Ag_{309} in total 1.7 ML C_{60} were evaporated on Au(111) so that one had regions covered with 1 ML C_{60} and areas with 2 ML C_{60} (see section 5.2.1.1). This had the advantage that the results of Ag_{309} on 1 ML C_{60}/Au(111) could be corroborated and additional information for Ag_{309} on 2 ML C_{60}/Au(111) was obtained. Ag_{309} was deposited at 165 K on 1 and 2 ML C_{60}/Au(111) and a cluster height of around 2.2 nm was measured on 1 and 2 ML C_{60} [195]. The height is smaller than for Ag_{309} deposited on only 1 ML C_{60}. In this experiment (see section 6.3.1.1) a cluster height of 2.35 nm was measured. This deviation is possibly due to the fact that the measurements were made with another STM tip, which can influence the height measurement. Also another Au(111)/mica substrate was used. Small influences of the elastic properties of these flexible substrates on the STM control loop and therefore on the z-calibration cannot be excluded. STM images and height distributions after deposition and after annealing Ag_{309}/1 and 2 ML C_{60}/Au(111) are shown in Figure 6.24, Figure 6.25 and Figure 6.26.

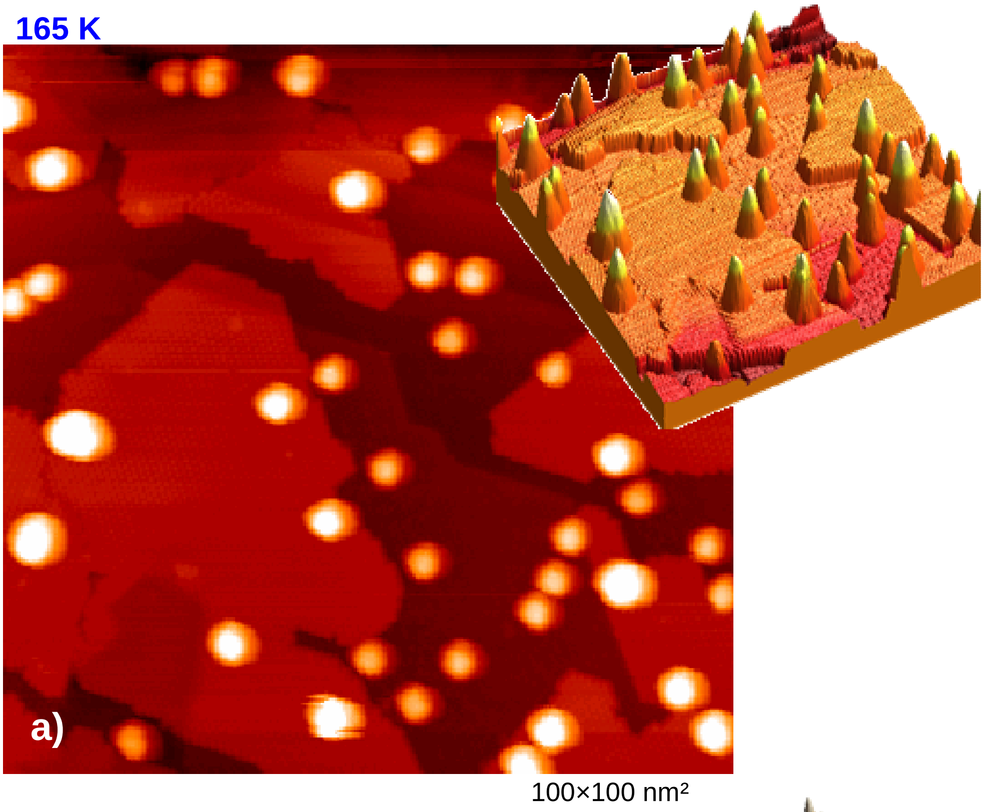

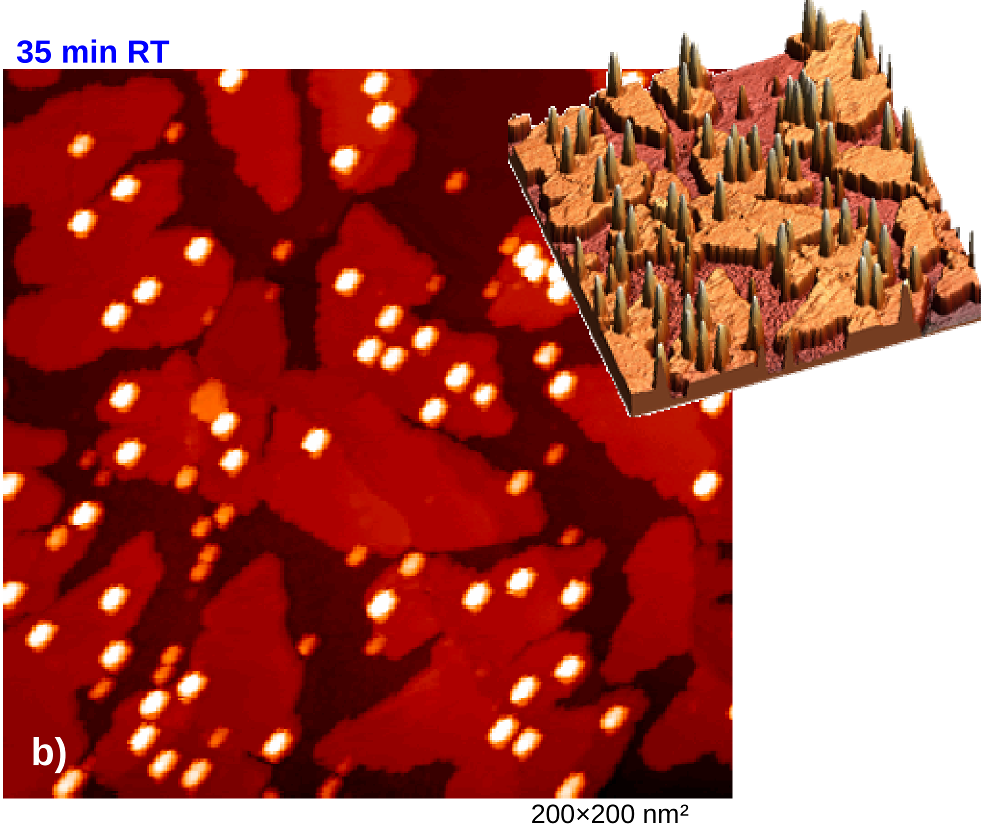

Figure 6.24: 77 K STM images of Ag_{309}/1 and 2 ML C_{60}/Au(111) a) after deposition at 165 K, b) after annealing for 35 min at RT.

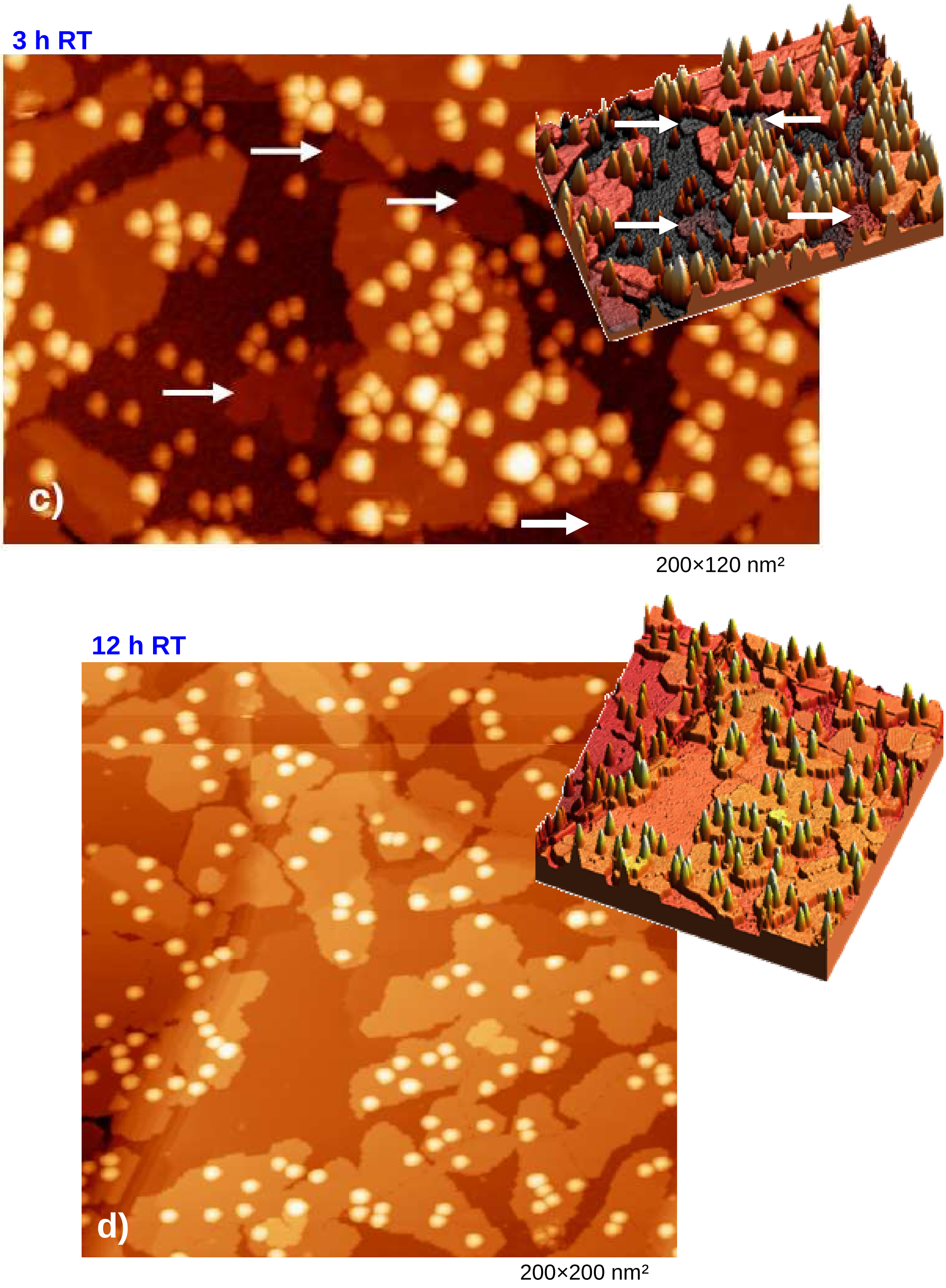

Figure 6.25: 77 K STM images of Ag_{309}/1 and 2 ML C_{60}/Au(111) c) after 3 h at RT, d) after annealing for 12 h at RT.

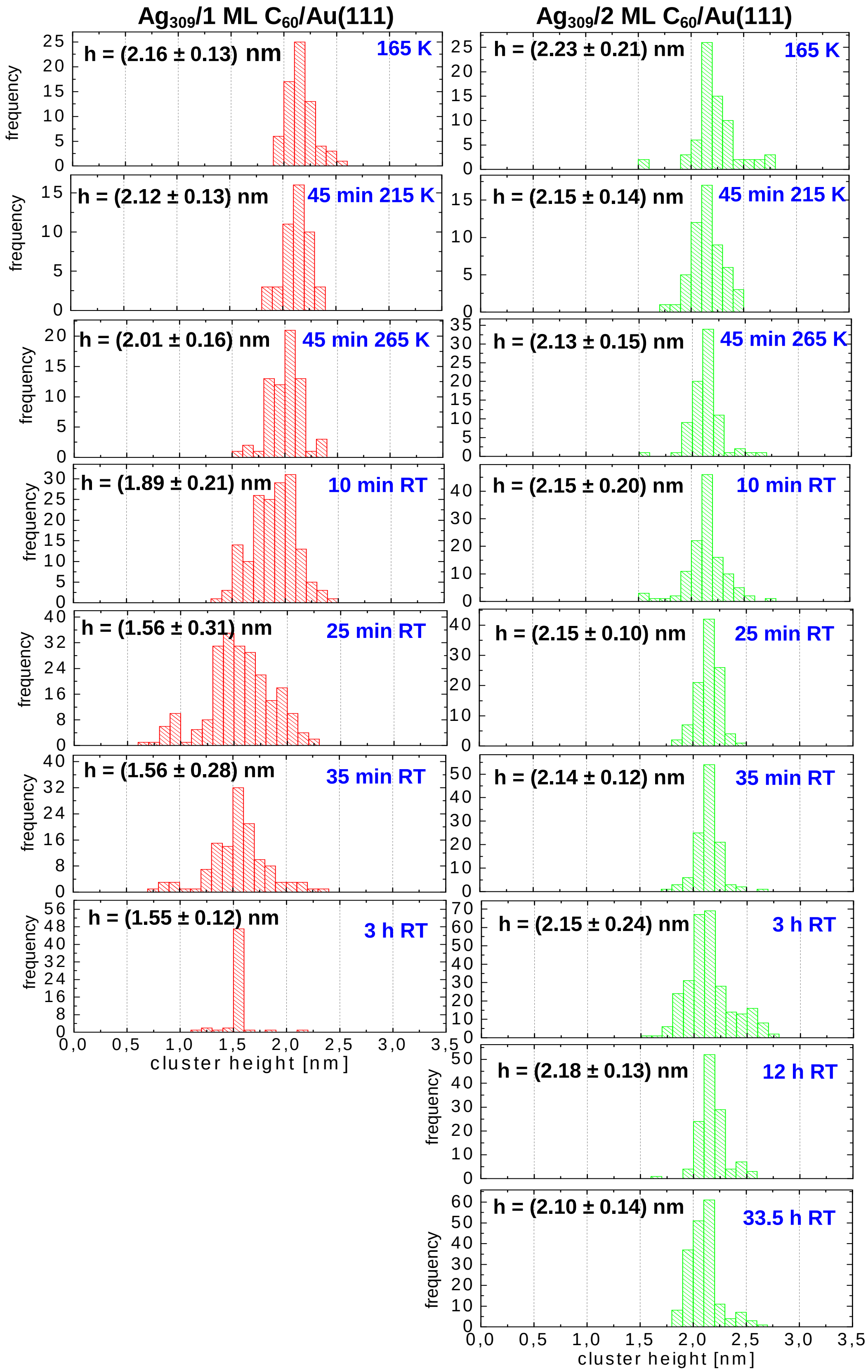

Figure 6.26: Height distributions of Ag$_{309}$/1 and 2 ML C$_{60}$/Au(111) after deposition and after every annealing step. Ag$_{309}$ on 1 ML C$_{60}$ decays, whereas Ag$_{309}$ on 2 ML C$_{60}$ stays stable [195].

In order to study the expected decay of Ag_{309} in detail on 1 ML C_{60} and the behavior of Ag_{309} on 2 ML C_{60} the sample was annealed in small steps. First the sample was annealed at 215 K and 265 K for 45 min each time. Then it was warmed up to RT for different time intervals, amounting to total times at RT of 10 min, 25 min, 35 min, 3 h, 12 h, and 33 h 30 min, respectively. After each annealing step the sample was transferred back into the STM where it was imaged at 77 K [195]. For Ag_{309} deposited on 1 ML C_{60}, first changes in the height distribution occur after heating the sample to 265 K for 45 min. The mean cluster height shifts to lower values and the distribution gets broader (see Figure 6.26). After a total time of 25 min at RT the height distribution is centered at 1.56 nm and ranges from below 1 nm to more than 2.2 nm (see Figure 6.26). After 35 min at RT the cluster height distribution gets narrower again, but the mean cluster height stays at 1.56 nm. After 3 h at RT an extremely narrow height distribution with a maximum at ≈ 1.5 nm was observed which was much narrower than the height distribution of Ag_{309} measured directly after deposition (see Figure 6.26). This phenomenon is an indication that the metastable clusters not only have a uniform size, but also a fixed orientation relative to the C_{60}. The width of the measured height distributions after deposition is assumed to be due to different orientations of the clusters to the C_{60}, because the number of atoms is the same and the error of the mass selection equals only 1 % of the selected cluster size (section 3.1.3.1). After 3 h at RT the number of clusters per area had decreased significantly on the 1 ML C_{60} areas and small Ag islands at the C_{60}/Au(111) interface were observed as shown in Figure 6.25. After annealing for 12 h at RT the clusters on 1 ML C_{60} have penetrated the C_{60} film completely as depicted in Figure 6.25. Thus, there exist no height distributions on 1 ML C_{60} after annealing for 12 and 33.5 h at RT.

The results for Ag_{309}/2 ML C_{60}/Au(111) were different. The cluster height was measured after every annealing step, but no changes of the cluster height were observed. The height stayed identical within the experimental errors for all annealing steps [195]. This means, that the Ag_{309} clusters on 2 ML C_{60} stayed stable, the cluster density remained constant and no Ag islands below 2 ML C_{60} were observed. The height distribution measured after annealing for 3 h at RT is broader due to coalescence of clusters in the center of the deposition spot. The data were taken at this position because only in the center there were still enough clusters on 1 ML C_{60} to get good statistics for the height distribution. The little change of the cluster height after 33.5 h at RT (from $h = 2.18 \pm 0.13$ nm to $h = 2.10 \pm 0.14$ nm) is possibly due to the fact that the clusters subside a little bit into the C_{60} or simply to another condition of the STM tip. The larger mean value after deposition and the larger width of the height distribution are due to cluster coalescence in the center of the deposition spot. The mean value of the cluster height distributions with a small width is always around 2.15 nm.

For Ag_{147} deposited at 165 K on 1.3 ML C_{60}/Au(111) similar results were observed. After taking STM images at 77 K directly after deposition, the sample was annealed for 45 min at 265 K and for 15, 45, 90, 180 min, 3 h and 12 h at RT. The height distributions after deposition at 165 K, after 45 min at 265 K and after 3 h and 12 h at RT are depicted in Figure 6.27. One problem was that the cooling of the cluster source was interrupted during the deposition so that the source warmed up which lead to contamination of the sample.

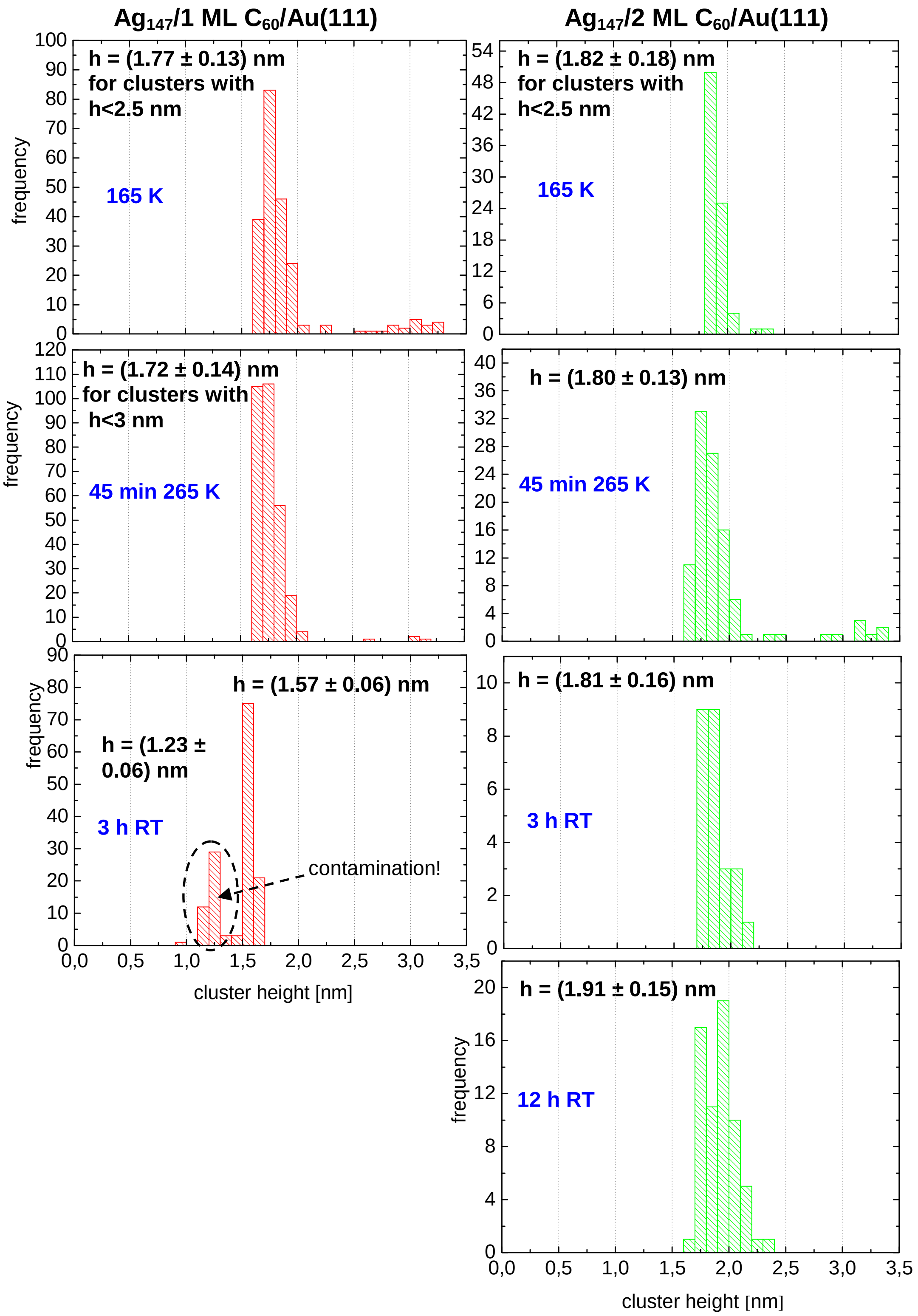

Figure 6.27: Height distributions of Ag$_{147}$/1 and 2 ML C$_{60}$/Au(111) after deposition at 165 K and after 45 min at 265 K and 3 and 12 h at RT. For Ag$_{147}$/1 ML C$_{60}$/Au(111) a decay is observed, the clusters on 2 ML C$_{60}$ stayed stable.

After deposition at 165 K the contamination was only observed on the free Au(111) areas on the sample which interacts stronger with adsorbates than C$_{60}$. Due to contamination the herringbone reconstruction of Au(111) was not visible. After annealing, the adsorbates partly coalesced with the clusters or diffused onto the C_{60} planes. This leads to an additional peak at $h = (1.23 \pm 0.06)$ nm in the height distribution of Ag_{147}/1 ML C_{60}/Au(111) measured after annealing for 3 h at RT and to the larger mean value of Ag_{147}/2 ML C_{60}/Au(111) measured after annealing for 12 h at RT due to coalescence of adsorbates and clusters. The height distributions in Figure 6.27 were measured in the outer regions of the deposition spot, where the contamination was lower. Apart from the contamination, the decay of Ag_{147} and the metastable cluster size of $h \approx 1.5$ nm were observed. After deposition extremely narrow height distributions were observed and a height of $h \approx 1.8$ nm was measured on 1 and 2 ML C_{60}/Au(111). After annealing for 45 min at RT there were no significant changes of the cluster height. The height distributions after 15, 45 and 90 min at RT indicate the decay of the clusters on 1 ML C_{60} and the stability of Ag_{147} on 2 ML C_{60}, but due to the fact that the STM images were taken in a region with strong contamination, no clear structures in the histograms could be pointed out. After annealing for 3 h at RT the STM measurements were taken in a region with lower contamination which leads to a height distribution for Ag_{147}/1 ML C_{60}/Au(111) showing a peak at the metastable cluster size of $h \approx 1.5$ nm, whereas the clusters on 2 ML C_{60} showed no changes in height. After 12 h at RT the Ag_{147} clusters on 1 ML C_{60} completely decayed and in contrast the clusters on 2 ML C_{60} stayed stable. An STM image of Ag_{147}/1 and 2 ML C_{60}/Au(111) annealed for 3 h at RT is shown in Figure 6.28. It is visible that the clusters on 2 ML C_{60} are larger than on 1 ML C_{60}. Ag islands below 1 ML C_{60} and the contamination on Au(111) and 1 ML C_{60} are visible.

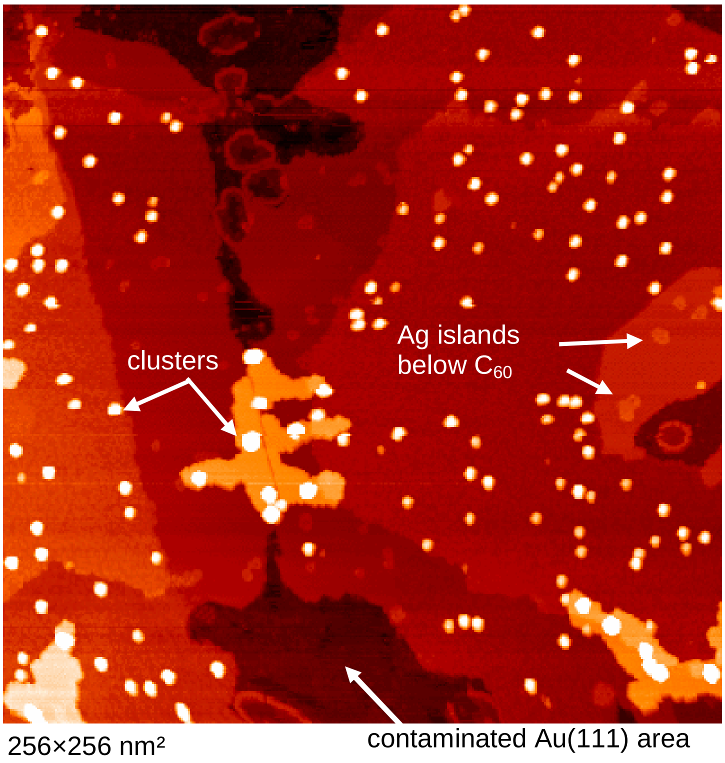

Figure 6.28: STM image of Ag_{147}/1 and 2 ML C_{60}/Au(111) after anneling for 3 h at RT.

6.3.1.3 The´magic` metastable cluster size

The cluster height distributions peaked at 1.5 nm, which were observed on 1 ML C_{60}/Au(111) after 25 min and 35 min at RT for Ag_{309} or, getting extremely narrow, after 3 h at RT for Ag_{147} and Ag_{309} hint at a metastable configuration with higher stability than larger and smaller clusters. In analogy to free clusters one could call this size a ´magic number` [46, 47]. It is not clear a priori that it will correspond to a configuration already known from gas phase clusters; in any case the extremely narrow height distribution after 3 h at RT suggests that the position and orientation of these clusters on the substrate may be more homogeneous than for the clusters as deposited. Neither Ag_{55} (with a height of (1 3 ± 0.2) nm after deposition at 115 K) nor Ag_{147} (with a height of (1.8 ± 0.2) nm after deposition at 165 K) directly correspond to the peak at 1.5 nm cluster height; these sizes therefore do not qualify as candidates for the metastable ’magic’ structure. It would be very interesting and useful to find out the number of atoms of the metastable size which could help to explain its stability and its preferred binding orientation relative to the C_{60}. The knowledge of the width could also be helpful in order to make - together with the known height of ≈ 1.5 nm - an approximation for the number of atoms per cluster for the metastable cluster size. With STM it is neither possible to count the number of atoms per cluster, nor to measure the absolute width. Thus, other methods, e.g. TEM, are required to define the width and consequently the number of atoms of the metastable cluster size.

A possibility to get information about the width of the mestable cluster size from STM would be the production of a so called *C_{60} necklace*. After depositing Ag_{309} on 1.7 ML C_{60}/Au(111) and after the different annealing steps up to 33.5 h at RT, 0.1 ML C_{60} were evaporated at RT. Due to the fact that the interaction between the clusters and C_{60} is stronger than the interaction beween the already existing C_{60} and the additionally evaporated C_{60}, it was expected that the 0.1 ML C_{60} are located around the clusters like a necklace. This behavior is known from rare gases (rare gas necklace) and is achieved by desorbing a rare gas from a surface covered with clusters [196]. Before the rare gas is completely desorbed, the last rare gas atoms build necklaces around the clusters due to the stronger interaction with metal clusters. The C_{60} necklace might help to define the cluster width by counting the number of C_{60} atoms around a cluster. Thus, due to the well known diameter of a C_{60} molecule, one could calculate the cluster diameter. In the case of the Ag_{309} clusters on 1.7 ML C_{60}, the metastable clusters on 1 ML nearly all decayed completely after anneling for a few hours at RT. Therefore, only the stable Ag_{309} clusters on 2 ML C_{60} were on the sample and the C_{60} growth could be observed only for the Ag_{309} clusters, not for the metastable size. But if this method would be successful, it could also be used in other experiments for the metastable clusters

In Figure 6.29 two STM images are shown taken after evaporating the additional 0.1 ML C_{60}. It is visible that the additional 0.1 ML C_{60} is indeed located around the Ag_{309} clusters on 2 ML C_{60} and nowhere else. No necklaces but small islands decorate the clusters which means that the coverage of 0.1 ML C_{60} was too high. The most crucial condition for the success of this method is an extremely sharp STM tip. During the experiment the STM tip was not sharp enough to make the single C_{60} molecules next to the clusters visible.

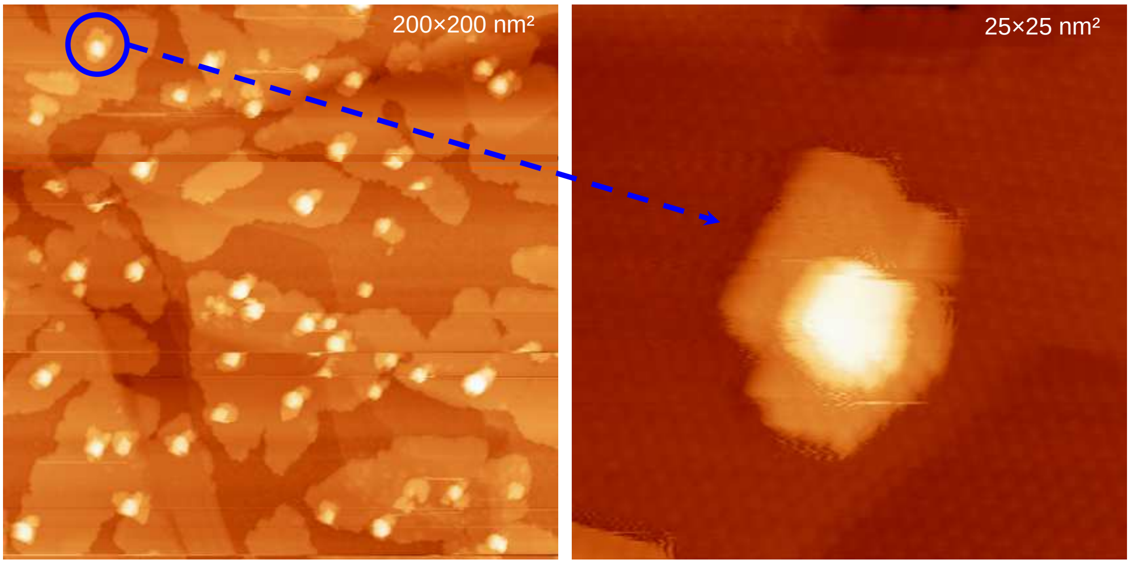

Figure 6.29: STM images of 0.1 ML C_{60} evaporated on Ag_{309}/1.7 ML C_{60}/Au(111) which has been annelaed for 33.5 h at RT. C_{60} islands around the clusters are visible.

6.3.1.4 Molecular dynamics and atomistic calculations

During this thesis we worked together with MICHAEL MOSELER from Freiburg who simulated the deposition process by molecular dynamics (MD) and explained the decay of the clusters on 1 ML C_{60}/Au(111) by atomistic calculations.

In order to elucidate whether the experimental setup allows for a softlanding of silver clusters, the potential energy surface of the Ag/Au/C system was modeled by the following analytic potentials. The metallic interactions (Ag-Ag, Au-Au and Ag-Au) were described by the Gupta many body potential [197]. Intrafullerene forces were treated with the Tersoff potential [198, 199] and the inter-fullerene (van der Waals) interactions with the Girifalco pair potential [200]. In order to parameterize the Ag-C and Au-C interaction, a Morse potential was fitted to the (ab-initio derived) equilibrium distance and adhesive energy of fullerenes adsorbed on Ag(111) and Au(111) surfaces [201], respectively, and to the experimental oscillation frequency of a fullerene charge shuttle between gold contacts [202]. The model of the substrate consisted of a block of 9 Au(111) monolayers (with a lateral dimension of 6.95 nm times 8.03 nm) covered by 64 C_{60} molecules. Periodic boundary conditions were applied in the lateral directions. The lowest gold monolayer was held fixed while a Langevin thermostat was applied to the next 3 layers [203]. Prior to deposition, both the substrate and the icosahedral Ag_{561} cluster were thermalized to the experimental temperatures $T_{substrate} = 165$ K and $T_{cluster} = 120$ K, respectively. The cluster trajectory was started 1 nm above the substrate with a kinetic energy of 18 eV (the experimental value) and the deposition dynamics was followed for 50 ps.

Figure 6.30 displays the final configuration 50 ps after deposition. Although the cluster mainly kept its global icosahedral shape (Figure 6.30 a)), structural damage can be observed in the vicinity of the carbon-silver interface (Figure 6.30 b)) [146]. The distortion of Ag_{561} can be explained by the relatively high adsorption strength of 1.5 eV

[201] of the fullerenes to an Ag(111) surface resulting in the observed partial wetting of the fullerenes by the silver atoms. The resulting denticulation of the Ag_{561} and the fullerene layer (Fig. 7b) indicates strong friction forces for lateral motion of the silver clusters corroborating the experimental observation that the clusters are not displaced during scanning with STM.

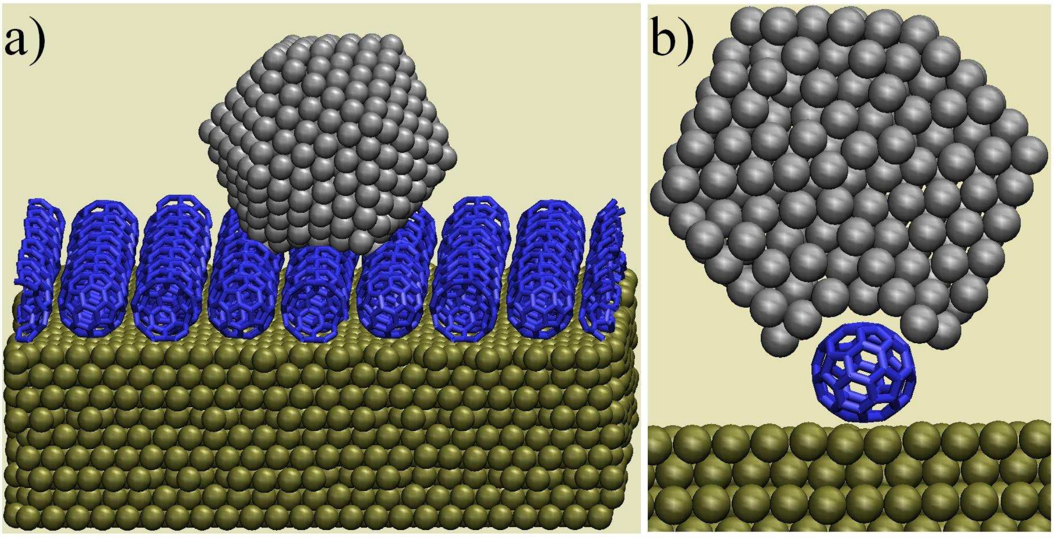

Figure 6.30: Final configuration of a molecular dynamics simulation of Ag_{561} impinging on a gold supported monolayer of C_{60}. (a) Snapshot of the system after 50 ps. (b) A 0.8 nm thick slice of the cluster from (a) showing the wetting of the central fullerene (the other fullerenes are not shown) by the silver atoms. Silver atoms are depicted by grey spheres, the fullerenes by blue cages and the gold atoms are plotted in gold.

The geometrical height of the cluster was calculated as the vertical (z-) distance between the highest atom of the fullerene layer and the highest silver atom. A value of 2.3 nm is obtained, which is around 0.4 nm smaller than the STM derived value of ≈ 2.7 nm [146]. In order to check the sensitivity of the final cluster height to variations in the Ag-C interaction strength an additional simulation using the weaker (Lennard-Jones type) interaction of Garrison et al. [204] was carried out. Although the wetting was less pronounced, the final height of the silver cluster turned out to be essentially the same as calculated with the stronger interaction. These findings point out difficulties in the use of an STM to determine cluster heights in heterogenous cluster-surface systems, which here are probably due to the different LDOS contours of the cluster and the C_{60} surface. MD simulations of soft-landing Ag_{561} on 2 ML C_{60}/Au(111) showed similar results.

The mechanism which allows the penetration of Ag through the C_{60} film was investigated by atomistic simulations using the Sutton-Chen potential for Ag and Au [205], the Brenner potential [206] for the intra-C_{60} and the Girifalco potential [200] for the inter-C_{60} forces as well as Ag-C and Au-C Morse potentials. Barriers for Ag penetration were calculated for several undercoordinated Ag atoms at the C_{60}/Ag_{309} interface by a constrained optimization with the distance of the Ag atom to the Au surface as reaction coordinate. A minimum barrier height of $E_b = 1.1$ eV for Ag_{309}/1 ML C_{60}/Au(111) clearly indicates that the timescale for penetration is of the order of hours for RT tempering, while the barrier of $E_b = 2.4$ eV for Ag_{309} / 2 ML C_{60} / Au(111) is impenetrable at RT [195]. The reason for the low E_b of the former can be inferred from the transition state in Figure 6.31. The penetrating Ag is accompanied by another silver atom that is still in contact with the cluster. At the transition state the breaking of the bond between these two atoms is facilitated by a concurrent adhesion of the penetrating Ag to Au(111) thus lowering the barrier. On the other hand, for Ag_{309}/2 ML C_{60}/Au(111) the longer distance to the Au(111) prevents barrier lowering. The Ag dimer has to break while the Ag is still far away from the gold [195].

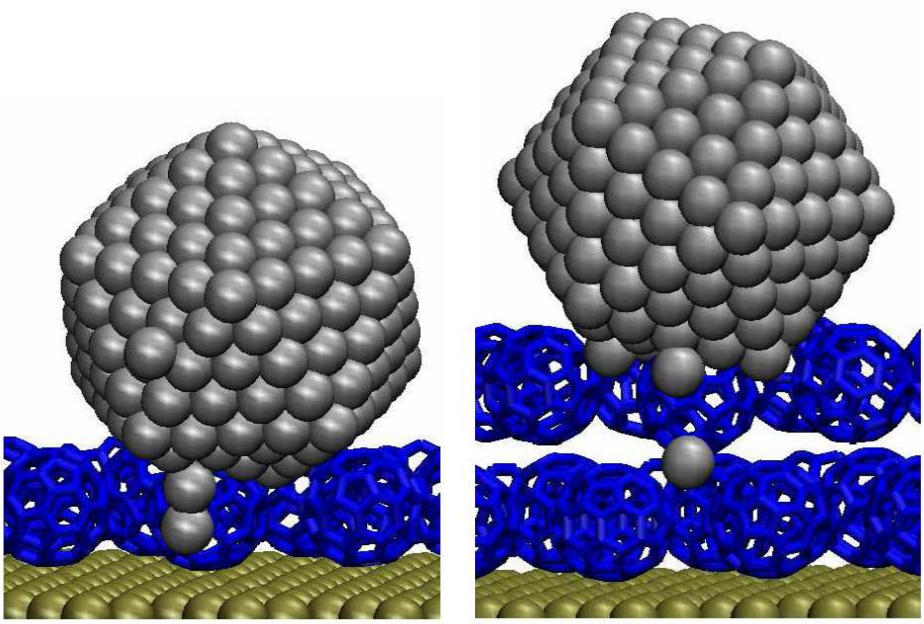

Figure 6.31: Atomistic calculations reveal a process by which the clusters (in this picture Ag_{309}) decay atom by atom through 1 ML C_{60}/Au(111) at RT. Ag atoms are depicted in grey, C_{60} in blue, Au in gold. For clarity parts of the C_{60} are not shown.

This behavior was calculated for Ag_{309} and Ag_{55} clusters. The further interpretation of the atomistic calculations is based on the Arrhenius equation which describes the temperature dependence on the rate of a chemical reaction or a physical process:

$$\frac{1}{\tau} = \omega_D \cdot \exp\left(-E_b / k_B \cdot T\right) \tag{6.2}$$

where τ is the decay time, ω_D a constant defined by the Debye temperature of Ag, E_b the barrier height, $k_B = 1.38065 \cdot 10^{-23}$ J/K the Boltzmann constant and T the temperature. In the case of the clusters which decay at RT, T has a value of ≈ 300 K in equation (6.2) and thus $k_B \cdot T \approx 1/40$ eV. The Debye frequency can be calculated as follows

$$\omega_D = \frac{k_B \cdot T_D}{\hbar}. \tag{6.3}$$

$T_D = 226$ K is the Debye temperature of Ag, and therefore $\omega_D \approx 3 \cdot 10^{13}$ 1/s. This means that for a barrier of $E_b = 1.0$ eV τ amounts to around 2 h which is a realistic timescale for the observed decay. A difference in the barrier height of only 0.1 eV leads to a drastic change of τ. A barrier of e.g. 0.9 eV leads to $\tau \approx 144$ s and $E_b = 1.1$ eV to

$\tau \approx 5$ d. The calculated barrier for Ag_{309} on 2 ML C_{60}/Au(111) of 2.4 eV leads to the decay time of $\tau \approx 5 \cdot 10^{20}$ years.

In future experiments it is planned to use another cluster material, e.g. Au. An interesting question would be if Au clusters show the same behavior on 1 and 2 ML C_{60} at RT as Ag clusters. For this reason the MD simulations concerning the soft landing as well as the atomistic calculations concerning the stability on 2 ML C_{60} were also performed for Au clusters. The results were similar as for Ag clusters. The barrier for Au clusters on 2 ML C_{60}/Au(111) is lower than for Ag clusters (only around 2 eV) but still high enough to guarantee stability on 2 ML C_{60}.

6.3.1.5 Ag_N (N=147, 309, 923) / 1 and 2 ML C_{60} / HOPG

Since the decay of Ag clusters on 1 ML C_{60} is strongly influenced by the the Au(111) substrate, it was assumed that the decay does not take place if the substrate is not metallic. For this reason geometrically magic Ag clusters were deposited at 165 K on an HOPG surface functionalized with 1 and 2 ML C_{60}.

For the direct comparison to the results on C_{60}/Au(111) Ag_{309} was deposited on C_{60}/HOPG [195] and in a later experiment Ag_{923}. After deposition of Ag_{309} on 1 and 2 ML C_{60}/HOPG a cluster height of ≈ 2.2 nm was measured with STM at 77 K on 1 and 2 ML C_{60} which agrees with the height of Ag_{309} measured on C_{60}/Au(111). On the free HOPG areas no clusters were observed which is due to the fact that the clusters on bare HOPG are too mobile to image them with STM. The tip displaces the clusters during scanning because the interaction between clusters and HOPG is very weak. To study the RT stability of the clusters, the Ag_{309}/C_{60}/HOPG sample was annealed for 45 min at 265 K and for 15 min, 45 min, 3 h and 12 h at RT and the heights were measured after every annealing step. The results of the height measurement are displayed by the height distributions in Figure 6.32. The clusters stayed stable on 2 ML C_{60} after annealing for 12 h at RT. Also on 1 ML C_{60} the clusters did not decay [195]. The small changes in the mean value of the cluster height are within 5 % error, which is typical for the STM measurement. The only change of the sample was visible after annealing for 45 min at 265 K. The clusters which were deposited on free HOPG areas moved to the step edges of the 1 ML C_{60} islands and coalesced continuously after each annealing step. Five STM images of different annealing steps are shown in Figure 6.33 and Figure 6.34. They represent the status of the sample during the whole experiment.

Due to the stability of the clusters STS measurements of Ag_{309} and Ag_{923} on C_{60}/HOPG were performed which are presented in section 6.5.

At the end of the experiment the sample was taken out of the surface science facility and was stored in an exsiccator. After three months the sample was transferred into the UHV chamber again, heated for 1 h at 100°C and scanned with STM at 77 K in order to find out if the clusters are still visible after such a long time at RT. The sample was contaminated because it was exposed to air and the heating for 1 h at 100°C removed only the water film.

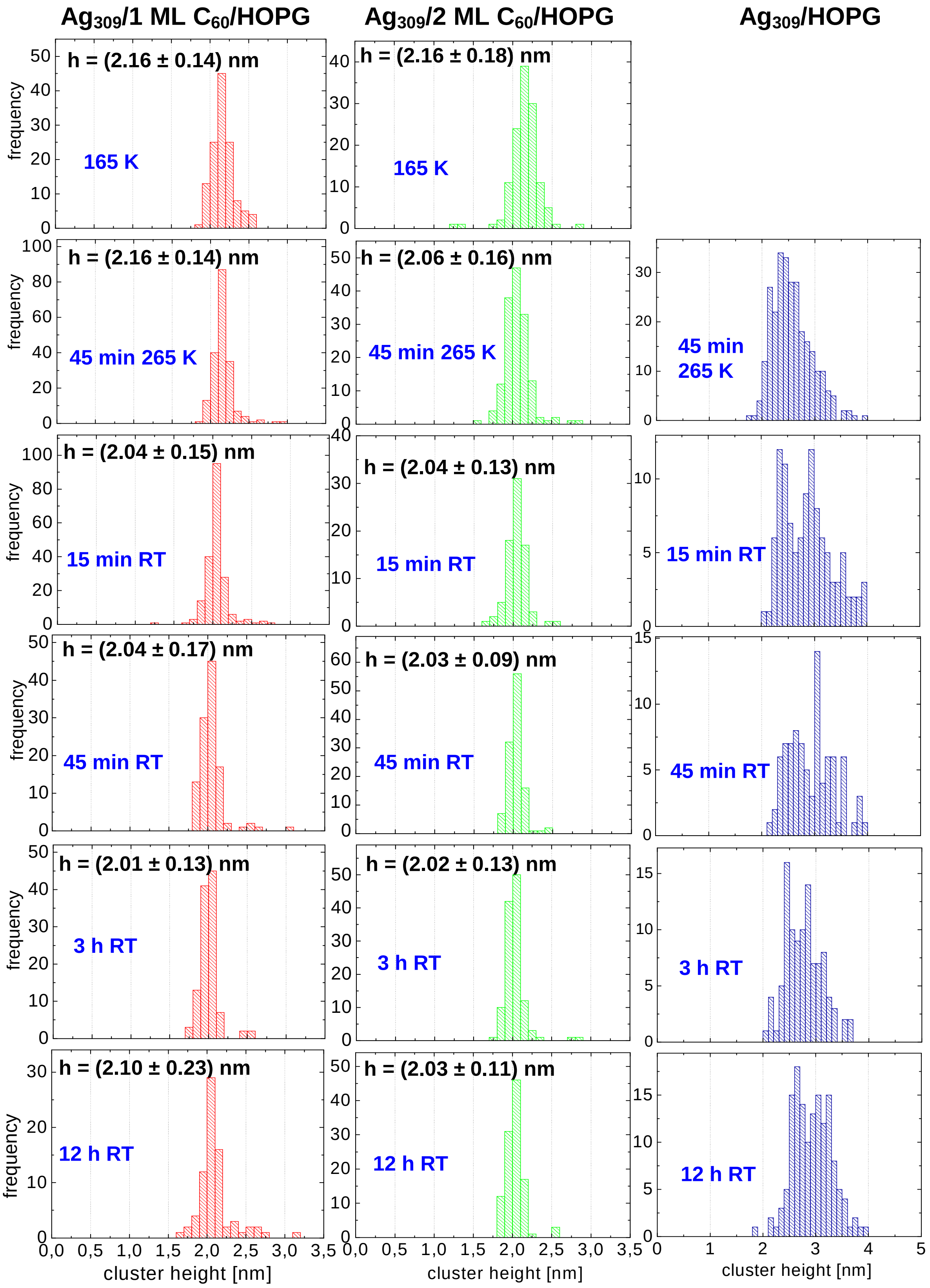

Figure 6.32: Height distributions of Ag_{309} on 1 ML C_{60} (left column), on 2 ML C_{60} (middle column) and coalesced Ag_{309} clusters on HOPG (right column). The clusters on 1 and 2 ML C_{60} are stable for 12 h at RT [195].

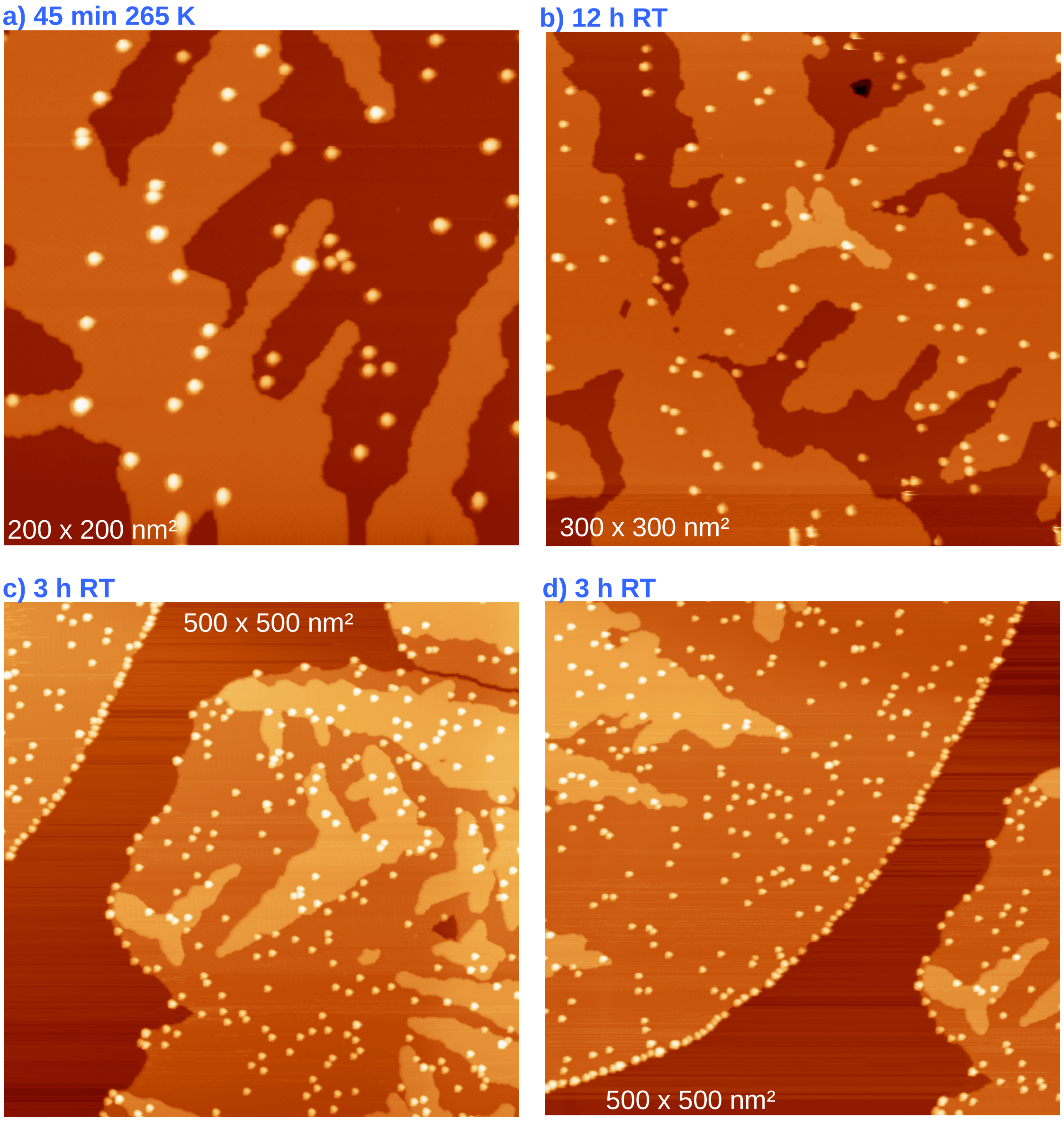

Figure 6.33: STM image of Ag_{309}/C_{60}/HOPG a) after annealing for 45 min at 265 K, b) after annealing for 12 h at RT, c)+d) after annealing for 3 h at RT.

Nevertheless the Ag_{309} clusters kept stable and could be imaged with STM. A change was visible in the C_{60} structure. There seemed to be more 3 ML C_{60} islands which before were partly observed only on large 2 ML C_{60} islands. This phenomenon is probably due to a change in the order of the C_{60} film during the heating to 100°C or due to contamination. Three STM images of Ag_{309}/C_{60}/HOPG taken at 77 K after three months at RT and after a heating step of 1 h at 100°C are shown in Figure 6.35.

On another sample covered with C_{60}/HOPG Ag_{923} clusters were deposited at RT, because with HOPG as sample substrate the clusters stay stable at RT. STM images at 77 K were taken and for Ag_{923} a cluster height of about 3 nm on 1 and 2 ML C_{60}/HOPG was measured after deposition. Narrow height distributions were observed which are shown in Figure 6.36.

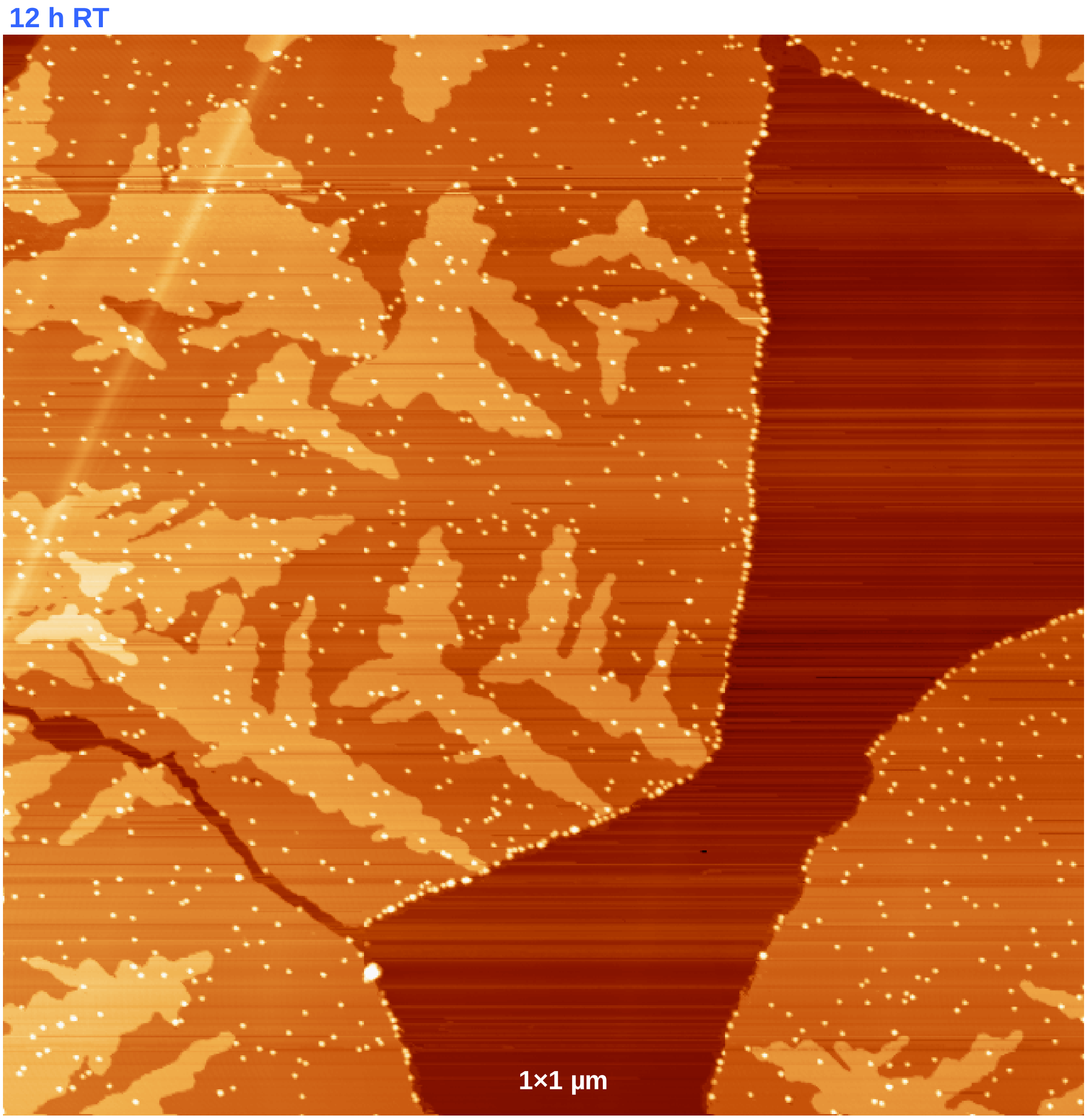

Figure 6.34: STM image of Ag_{309}/C_{60}/HOPG after annealing for 12 h at RT.

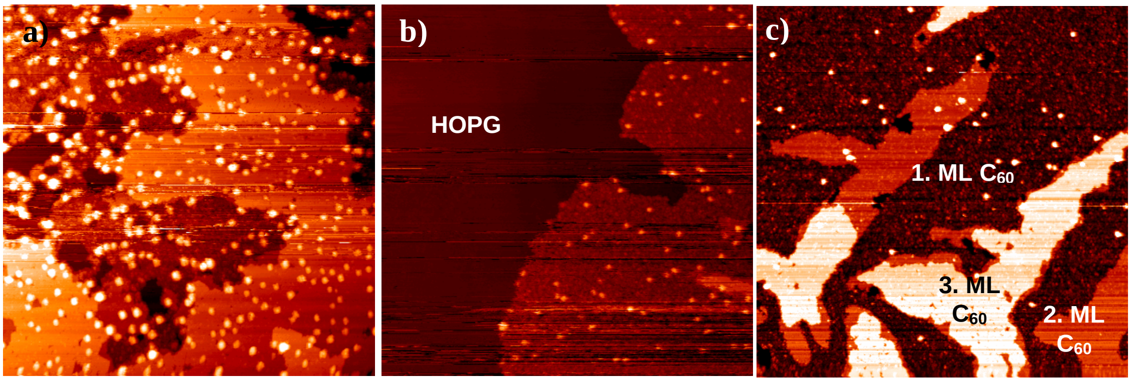

Figure 6.35: a) 300×300 nm² b) + c) 400×400 nm² STM image of Ag_{309}/C_{60}/HOPG after three months at RT and exposure to air. Contamination is visible, but also the stable Ag_{309} clusters with the same height as after deposition at 165 K. The order of the C_{60} film changed and more 3 ML islands are visible than before.

The few larger clusters are due to coalescence of clusters in highly covered regions of the deposition spot.

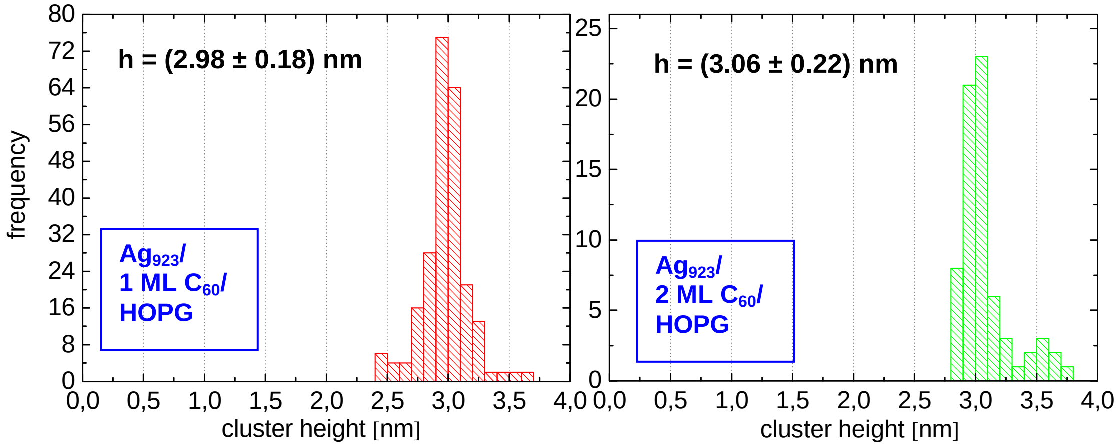

Figure 6.36: Height distributions of Ag_{923} deposited on 1 (left image) and 2 (right image) ML C_{60}/HOPG at RT, imaged with STM at 77 K.

This time the sample was not annealed up to different temperatures because it was expected that Ag_{923}/C_{60}/HOPG - as well as Ag_{309} - stays stable at RT. Instead, additionally to Ag_{923}, Ag_{147} clusters were deposited at RT onto the sample in order to study if the clusters interact with each other at RT, i. e. if they exchange atoms or if both types of clusters stay stable. Ag_{147} clusters were chosen because they can be distinguished very well from Ag_{923} due to their smaller height. After the additional deposition of Ag_{147} STM images were taken at 77 K and the clusters heights were measured. The corresponding height distributions are depicted in Figure 6.37.

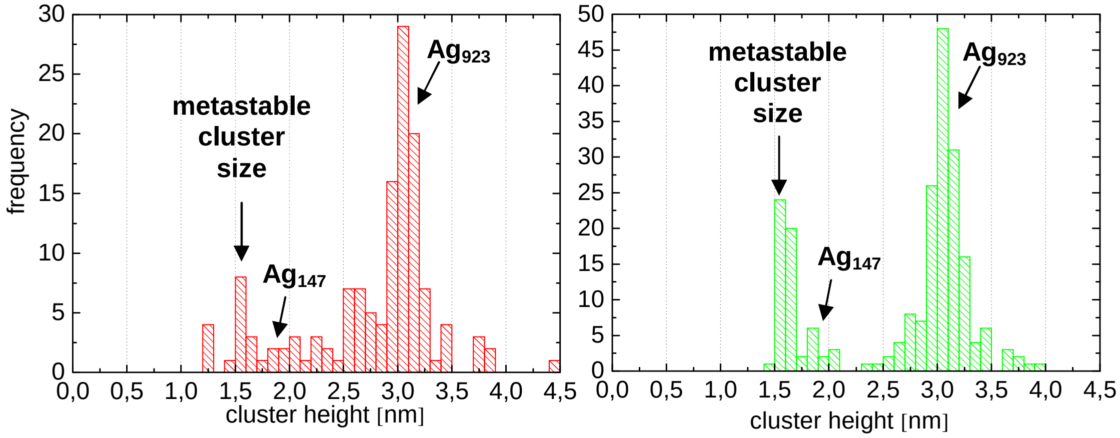

Figure 6.37: Height distributions measured after the RT deposition of Ag_{147} and Ag_{923} clusters on 1 (left image) and 2 (right image) ML C_{60}/HOPG.

Surprisingly the height distributions show a maximum at around 3 nm which corresponds to Ag_{923} and a maximum at ≈ 1.5 nm which corresponds to the metastable cluster size. A maximum at abut 1.8 nm was expected, which would represent the Ag_{147} clusters, but only a few clusters have the typical height of Ag_{147} clusters. Two possible explanations could interpret the results.

The first explanation is that the deposition temperature – RT – was too high for the smaller Ag_{147} clusters, which means that Ag_{147} is probably not stable on C_{60}/HOPG at RT, in contrast to the larger Ag_{309} or Ag_{923} clusters. In this case the peak in the height distribution at the metastable size of $h \approx 1.5$ nm is due to the decay of Ag_{147} and the few clusters which were higher than Ag_{923} clusters are due to coalescence. If this explanation is correct, it can be studied in a future experiment by depositing Ag_{147} at low temperatures on C_{60}/HOPG, followed by a step-by-step annealing as for Ag_{309}.

The second explanation is that the two clusters sizes on the same sample area interacted with each other and thus were not stable. This phenomenon can be explained by Ostwald ripening, which describes that larger clusters grow by drawing material from smaller clusters, which shrink. This process is described schematically in Figure 6.38, together with the principle of coalescence.

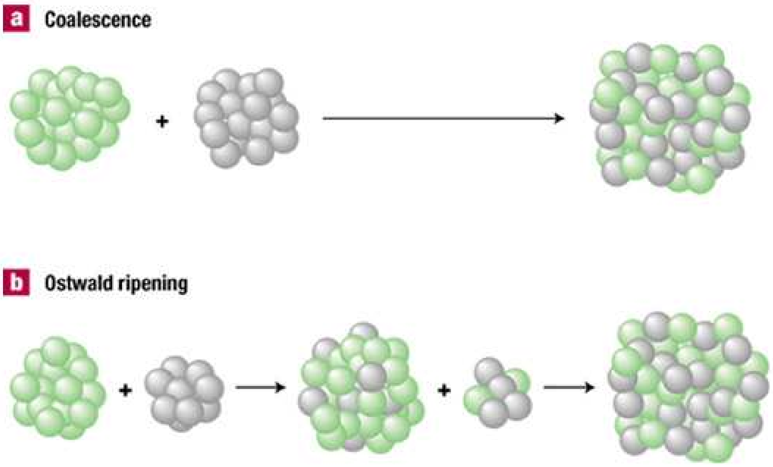

Figure 6.38: Schematical overview about the different processes of coalescence and Ostwald ripening [207].

In contrast to coalescence, which means that two particles unify and build one larger particle which consists of all atoms of both particles, Ostwald ripening is an inhomogenous process. Smaller clusters have a lower binding energy per atom due to a higher contribution of the surface energy for a larger surface to volume ratio. Therefore, larger clusters are energetically favored.

The results of the experiment with Ag_{147} and Ag_{923} being on the same sample region show that the smaller cluster size – Ag_{147} – is not really visible anymore, whereas the larger cluster size – Ag_{923} – is represented by a large peak in the height distribution. Additionally larger clusters were built during the Ostwald ripening process. During this process several atoms formed clusters which have the metastable height of 1.5 nm. It would be energetically favored that finally all Ag_{147} clusters disappear to the expense of the growth of the Ag_{923} clusters, but during this process again the formation of the metastable cluster size seems to be preferred.

These observations raise the question what makes the cluster with the metastable size stable, how many atoms they have and which effects (orientation, binding etc.) play a role for the formation of the clusters.

6.3.1.6 Overview about the results of geometrically magic Ag clusters

In summary we have successfully deposited Ag_{55}, Ag_{147}, Ag_{309}, Ag_{561} and Ag_{923} on C_{60} functionalized Au(111) or HOPG surfaces and observed narrow cluster height distributions after deposition. The histograms of all deposited geometrically magic cluster sizes are shown in Figure 6.39.

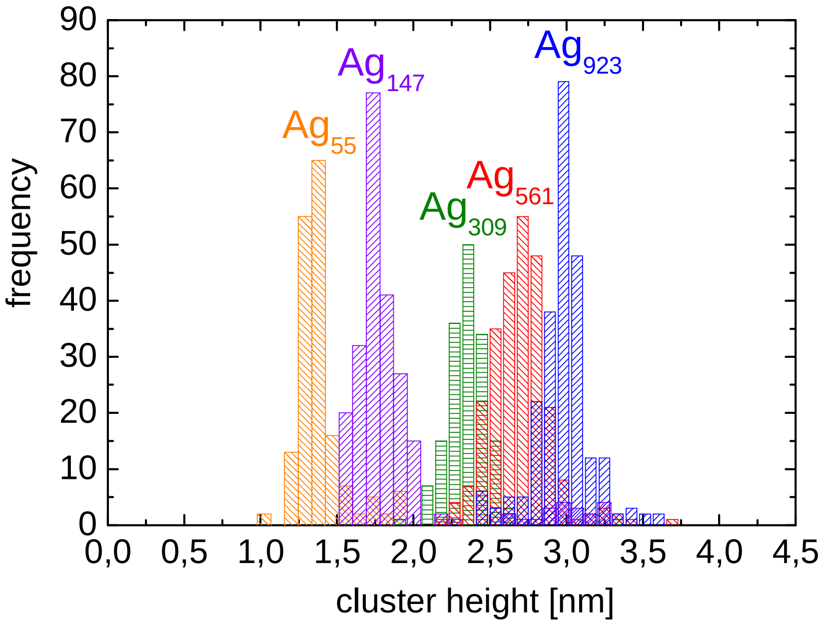

Figure 6.39: Overview of the height distributions of Ag_{55}, Ag_{147}, Ag_{309}, Ag_{561} and Ag_{923}.

The measured cluster heights are plotted against the number of closed geometrical shells in Figure 6.40 together with calculated heights by assuming a spherical shape of the clusters (see Figure 2.8 in section 2.1.3). The heights of the clusters which were deposited on C_{60}/HOPG are a bit smaller than the heights of the clusters deposited on C_{60}/Au(111). This is probably due to different electronic properties of the substrate which influences both C_{60} and clusters due to different types of interactions with Au(111) and HOPG. In general the measured cluster heights are similar to the calculated heights of spherical clusters. The height of Ag_{561} calculated by the MD simulations is significantly smaller than the height of a spherical Ag_{561} cluster. This shows that assuming a sphere is an upper limit. It is more probable that the clusters are slightly flattened when they are deposited onto the sample.

Due to the fact that the MD simulations showed that the clusters kept their icosahedral shape and that only at the interface to the C_{60} the clusters are distorted due to a denticulation of clusters and C_{60}, these cluster heights show the change in height from one closed shell to the next.

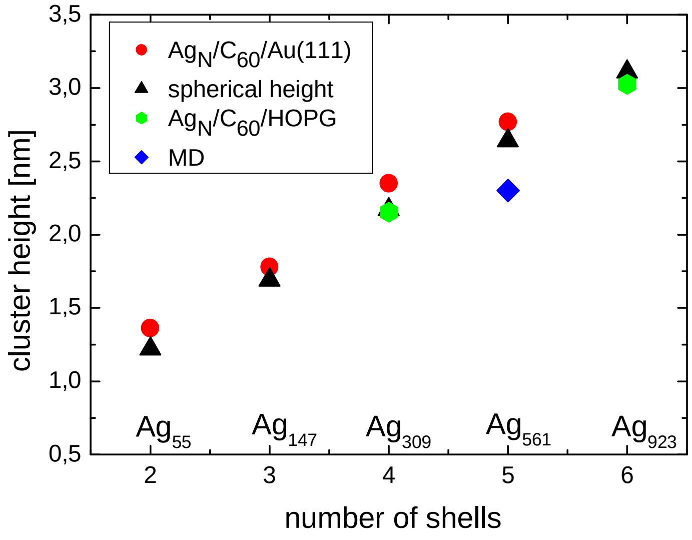

Ag_N	$h_{meas.}$ [nm]	$h_{spher.}$ [nm]	h_{MD} [nm]
Ag_{55}	1.36	1.22	
Ag_{147}	1.78	1.69	
Ag_{309}	2.15/ 2.35	2.17	
Ag_{561}	2.76	2.64	2.3
Ag_{923}	3.03	3.11	

Figure 6.40: Measured and calculated heights (spherical and MD) of geometrically magic Ag_N clusters vs. the number of closed shells per cluster.

6.3.2 Ostwald ripening of geometrically non-magic Ag clusters

This second part of section 6.3 deals with the results of deposited geometrically non-magic Ag clusters on C_{60} functionalized Au(111). In order to find out more details about the metastable cluster size of $h \approx 1.5$ nm, clusters between Ag_{55} and Ag_{147} were deposited. The height of Ag_{55} was measured as $h \approx (1.38 \pm 0.15)$ nm and the height of Ag_{147} as $h \approx (1.80 \pm 0.16)$ nm. Thus, the clusters with the metastable size are expected to have a number of atoms between 55 and 147. For this reason two geometrically non-magic cluster sizes were deposited with a number of atoms between 55 and 147.

6.3.2.1 Ag_N (N=68, 80) / 1 and 2 ML C_{60} / Au(111)

Ag_{68} was deposited on 1.2 ML C_{60}/Au(111) and Ag_{80} on 1.1 ML C_{60}/Au(111). In order to have enough areas with 1 ML C_{60}, only slightly more than 1 ML C_{60} was evaporated on Au(111). This is due to the fact that the clusters on 1 ML C_{60} were expected to decay after annealing up to RT which would lead to a shrinking of the cluster density and thus to poor statistics for the height distributions. The clusters were deposited at 165 K on C_{60}/Au(111), scanned with STM at 77 K and then annealed for different time intervals. The Ag_{68} clusters were annealed for 45 min at 265 K, for 15 and 45 min and for 3 h, 9 h and 33 h at RT. Ag_{80} was annealed in larger steps, namely for 45 min and for 12 h at RT. The observations for both clusters sizes were similar and are visualized by the height distributions after the different annealing steps, which are visible in Figure 6.41 and Figure 6.42.

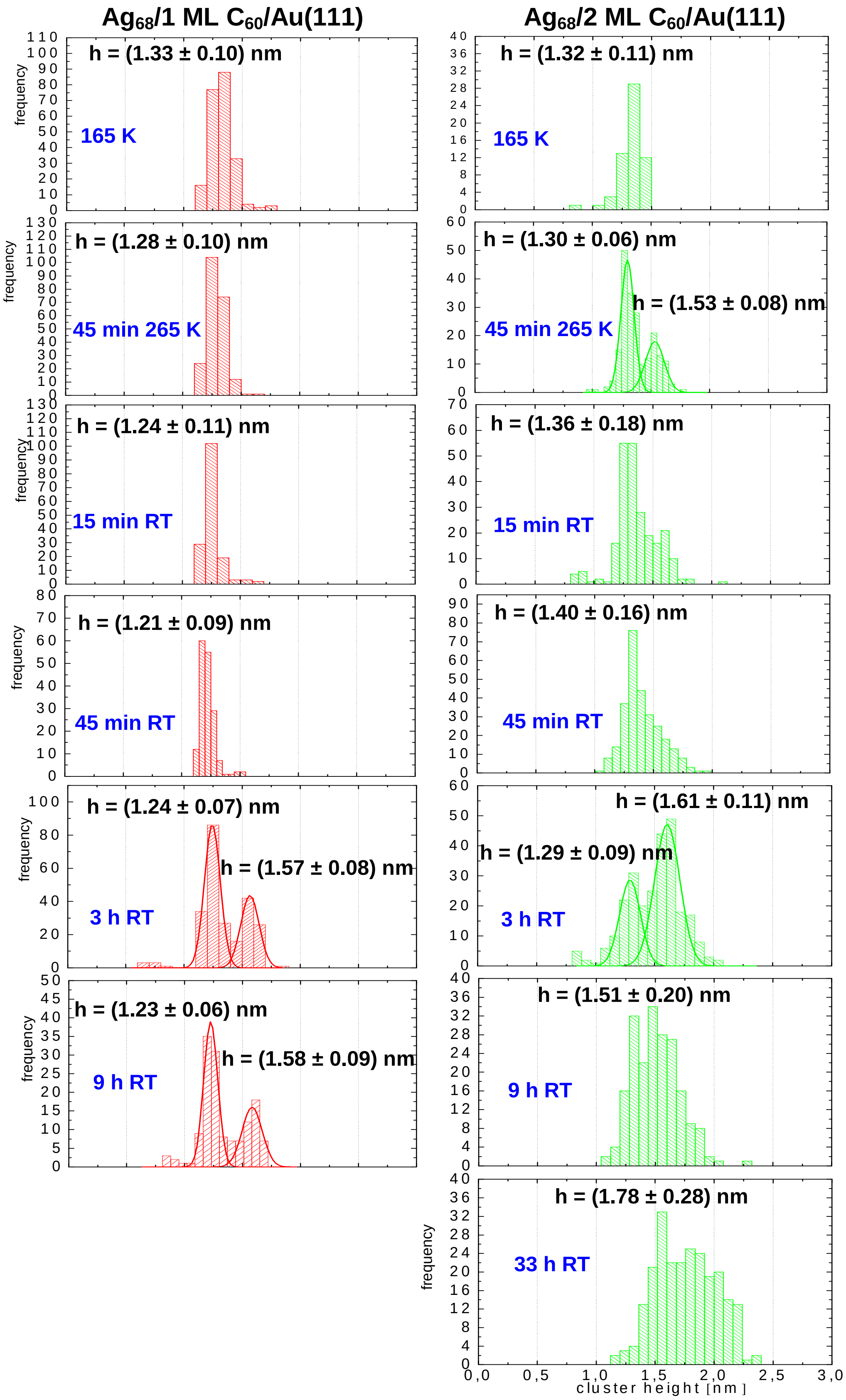

Figure 6.41: Height distributions of Ag_{68} on 1 ML C_{60} (left column) and 2 ML C_{60} (right column) on Au(111).

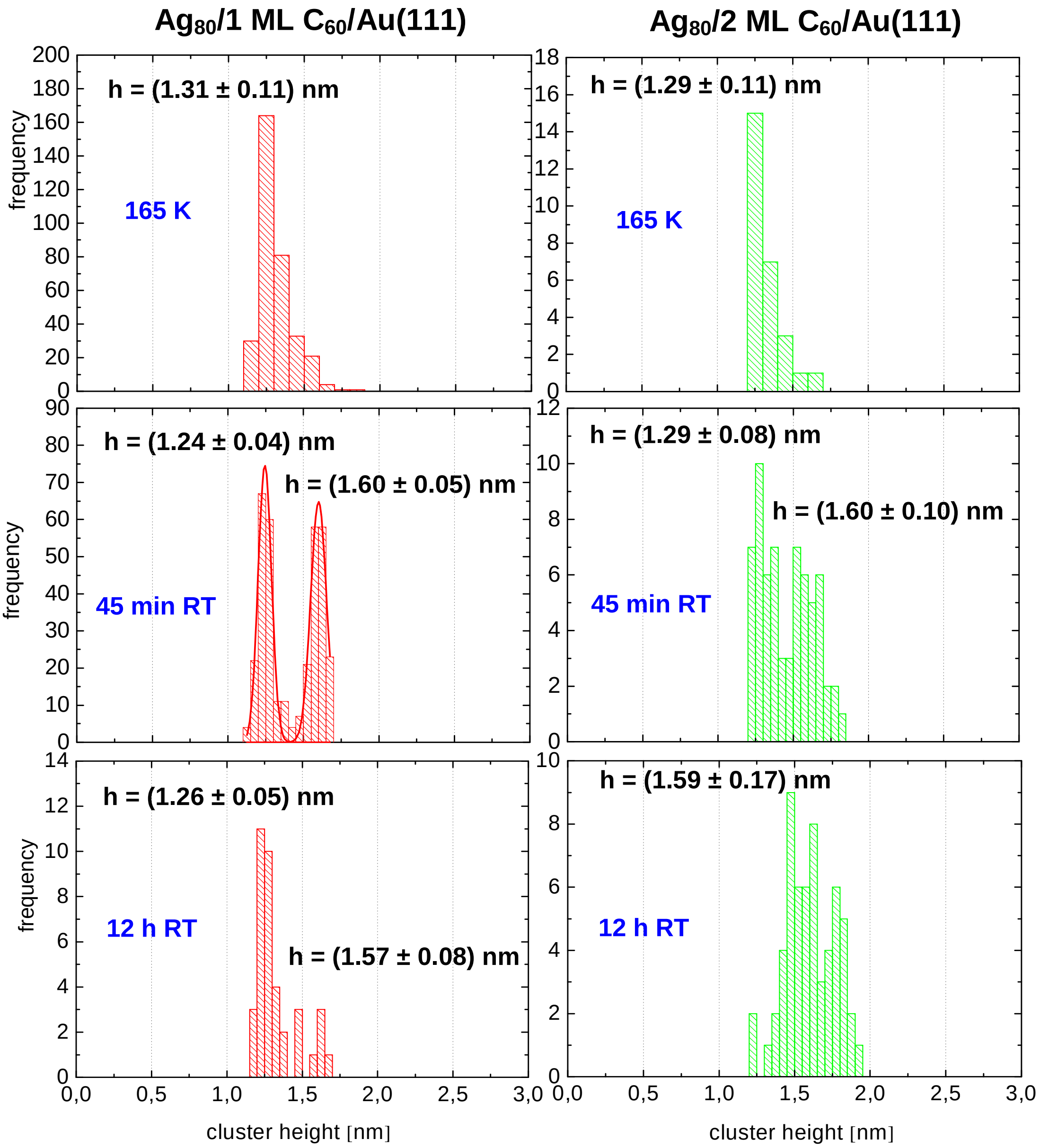

Figure 6.42: Height distributions of Ag_{80} on 1 ML C_{60} (left column) and 2 ML C_{60} (right column) on Au(111).

After deposition the Ag_{68} as well as the Ag_{80} clusters have a height of ≈ 1.3 nm on 1 and 2 ML C_{60}/Au(111) which is the same height as for Ag_{55}, which was measured to be (1.38 ± 0.15) nm (see subsection 6.3.1.1). At first glance this fact seems to be conflicting, but can be explained by a study of B. v. ISSENDORFF and M. MOSELER [54]. As mentioned in subsection 2.1.4 the group of BERND VON ISSENDORFF takes photo electron spectra of size selected clusters. For Na clusters of several sizes – from 39 up to 309 atoms – photo electron spectra were taken and compared with simulated spectra studied with density functional theory by MICHAEL MOSELER who determined the geometrical structure for the different clusters by comparison of measured and calculated photoemission spectra. Na clusters have a very similar structure to Ag clusters, they for example have the same geometrically magic cluster sizes at 55, 147, 309 atoms. The study shows that e.g. Na_{71} looks like a Na_{55} cluster with a 16-atom cap overlayer, so the additional atoms to Na_{55} build a cap at one side of the cluster. For the Ag_{68} and Ag_{80} clusters which probably look similar to a cluster with 71 or 92 atoms as shown in Figure 6.43 we assume that the clusters, after landing on the sample surface, are not standing uprightly on their smallest side but lie down so that the longer side has contact to the surface, because this is an energetically preferred state for the clusters. This would mean that the measured cluster height is not the length including the additional atoms as markes by the green arrow in Figure 6.43, but the height of an Ag_{55} cluster (yellow arrow). This could explain why the same heights for Ag_{55}, Ag_{68} and Ag_{80} are measured.

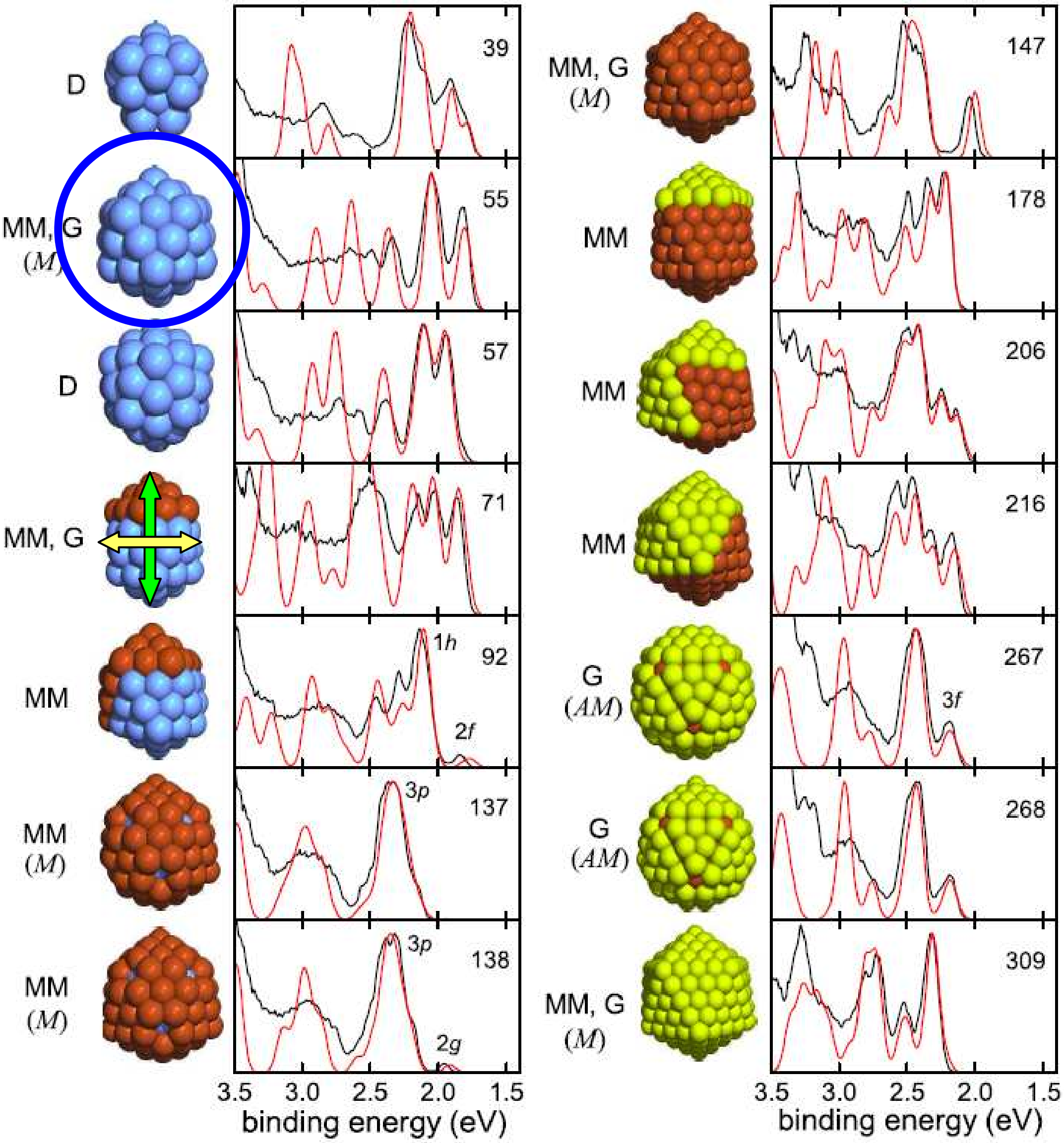

Figure 6.43: Comparison of photoelectron spectra (black lines) to calculated electron density of states (colored or shaded lines). The structures used in the calculations are indicated. The Na_{55} cluster is marked by the blue circle [54].

After annealing $Ag_{68}/C_{60}/Au(111)$ and $Ag_{80}/C_{60}/Au(111)$ different results than for geometrically magic clusters were observed. The clusters on 1 and this time also on 2 ML $C_{60}/Au(111)$ were not stable after annealing.

The Ag_{68} clusters deposited on 1 ML C_{60} were stable up to 45 min at RT which is shown by the narrow height distributions with a maximum at ≈ 1.3 nm in Figure 6.41. Figure 6.44 shows an STM image of Ag_{68}/C_{60}/Au(111) taken after deposition at 165 K. After 3 h and after 9 h at RT a bimodal height distribution was observed on 1 ML C_{60} with a maximum at 1.24 nm which is the height of Ag_{68} and a maximum at 1.57 nm which represents the height of the metastable cluster size. The metastable size has a larger height than Ag_{68}, thus the formation of the metastable size is due to a thermally activated growth process, most likely Ostwald ripening. On 2 ML C_{60} the growth of Ag_{68} was already visible after 45 min at 265 K by a smaller peak at 1.53 nm together with a larger peak at 1.30 nm. After 3 h at RT most of the clusters on 2 ML C_{60} had the height of the metastable size. After 9 and 33 h at RT the STM images were taken in a region with higher cluster density in order to get good statistics for clusters on 1 ML C_{60} which finally nearly all penetrated the C_{60} and formed Ag islands below the C_{60}, as it was observed for geometrically magic clusters. For this reason the height distribution for clusters on 2 ML C_{60} are broader and include coalesced clusters. After 33 h there is no height distribution for clusters on 1 ML C_{60} due to poor statistics because nearly all cluster had penetrated the C_{60} film.

The results for Ag_{80}/1.1 ML C_{60}/Au(111) were similar. After annealing for 45 min at RT a bimodal height distribution was observed for clusters on 1 and 2 ML C_{60}/Au(111) which shows a maximum at about 1.3 nm and 1.6 nm which is due to Ostwald ripening of the Ag_{80} clusters. Ag islands below the C_{60} were visible as it is depicted in the STM images in Figure 6.44. The STM image taken after 45 min at RT shows the two different cluster sizes properly which can be distinguished by brighter or darker spots on 1 ML C_{60}. After 12 h at RT there are only a few clusters on 1 ML C_{60}, but many Ag islands below the C_{60}, whereas the cluster density on 2 ML C_{60} did not change. This STM images clearly show differences between the strongly patterned $C_{60}(1)$ and the weaker patterned $C_{60}(2)$. The Ag islands are located below the $C_{60}(2)$ film, whereas on $C_{60}(1)$ some clusters are still visible. After 12 h at RT and for clusters on 2 ML C_{60} also after 45 min at RT the statistics for the height distributions are poor due to the fact that only 0.1 ML of the second ML C_{60} were evaporated and that the clusters on 1 ML C_{60} decayed after 12 h at RT. Nevertheless the observations for Ag_{68} and Ag_{80} are significantly and different as compared to geometrically magic clusters on C_{60}/Au(111) from Ag_{147} to Ag_{923}.

Two different competing processes at RT seem to influence the behavior of Ag_{68} and Ag_{80}. On the one hand thermally induced Ostwald ripening lets the clusters interchange atoms. The metastable size, which seems to be energetically favored, is formed and stayed stable for a timescale of hours. On the other hand, on 1 ML C_{60} the influence of the Au(111) substrate activates the atom-by-atom decay of the clusters at RT. Therefore, on a short timescale Ostwald ripening is the dominating process which lets the clusters grow up to the metastable size, but on a longer timescale of hours the decay of clusters on 1 ML C_{60} dominates.

For the explanation of the different behavior of Ag_{68} and Ag_{80} on C_{60}/Au(111) in contrast to Ag_{147}, Ag_{309}, Ag_{561} and Ag_{923} there are two possible interpretations. The first explanation is that the Ostwald ripening is due to instability of geometrically non-magic clusters. Geometrically magic clusters have closed atomic shells which lead to a large stability against interactions with each other. Only external conditions – like the strong influence of the Au(111) substrate and the rotation of the C_{60} molecules at RT – disturb the stability. Due to less stability of geometrically non-magic clusters, it is energetically favored to interchange atoms and to form more stable sizes. After this process, the sample is in the same status as it is for geometrically magic clusters, which *decayed* to the metastable size.

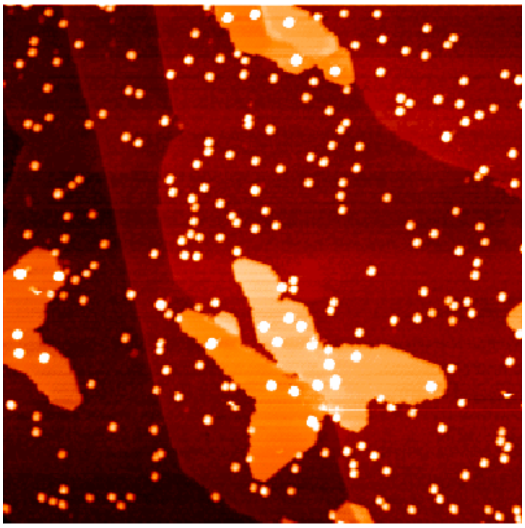

Ag_{68}/C_{60}/Au(111) – 165 K – 200×200 nm^2

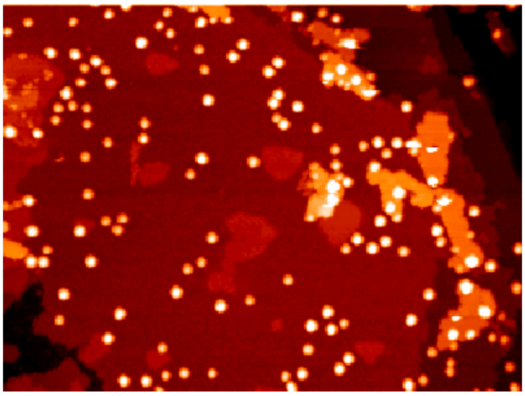

Ag_{80}/C_{60}/Au(111) – 45 min RT – 200×149 nm^2

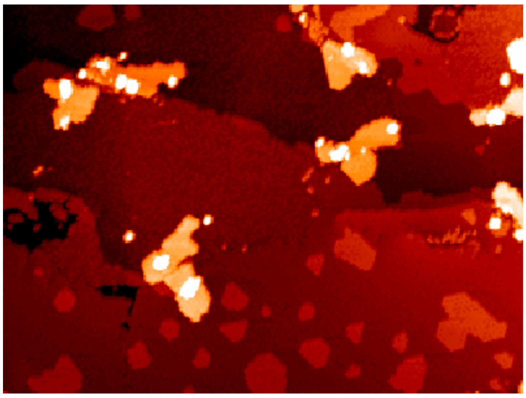

Ag_{80}/C_{60}/Au(111) – 12 h RT – 200×150 nm^2

Figure 6.44: STM images of Ag_{68}/1.2 ML C_{60}/Au(111) (left) and Ag_{80}/1.1 ML C_{60}/Au(111) (right).

The second interpretation is that the Ostwald ripening is independent from more or less stability of the clusters due to closed atomic shells, but is the dominant process for all clusters up to a certain size. An indication for this is the observation that annealed Ag_{55} clusters also form the metastable size of $h \approx 1.5$ nm by a growth process, although they are geometrically magic. But in this case the annealing process was not studied in detail and another explanation for the clusters with $h \approx 1.5$ nm after 3 h at RT is that some larger clusters were deposited together with Ag_{55} because it is difficult to chose a waiting time τ_W between two acceleration pulses of the mass selector which only selects small clusters like Ag_{55} with a still high cluster current. For the deposition of Ag_{55} the value of τ_W was acceptable and the height distribution after deposition was narrow. But a few higher clusters are still visible (see Figure 6.16 in section 6.3.1.1) and the peak in the height distribution after 3 h at RT could also be due to larger clusters which formed clusters with $h \approx 1.5$ nm in the decay process. To study this in detail, an annealing of Ag_{55} in smaller steps is necessary. Ag_{55} was only deposited on 1 ML C_{60}/Au(111) and a study of thermally activated processes of Ag_{55} on 2 ML C_{60} can be revealing as well and will be studied in future experiments.

To find out which of both interpretations is right, it is planned to deposit larger geometrically non-magic clusters between two magic numbers, e.g. between Ag_{147} and Ag_{309}, between Ag_{309} and Ag_{561} or between Ag_{561} and Ag_{923}. Due to the fact that Ostwald ripening takes place for clusters on 1 and 2 ML C_{60}, it seems to be a substrate independent process. Therefore, a deposition and annealing of Ag_{68} or Ag_{80} on C_{60}/HOPG can also be instructive.

6.4 Thermally activated processes of grown metal islands

In addition to the deposition of size selected Ag clusters the thermally activated processes of grown Ag and Pb islands on C_{60} functionalized Au(111) surfaces were investigated within this thesis. The metal atoms were evaporated on C_{60}/Au(111) by an evaporator with integrated flux monitor (EFM) which is presented in section 3.2.2.

6.4.1 Ag islands on C_{60} / Au(111)

The first part of this section deals with grown Ag islands on 1.3 ML C_{60}/Au(111). The experiments were carried out similar as for size selected clusters in order to compare the results of grown Ag islands and deposited size selected Ag clusters with each other. Of great interest is the question, if the metastable cluster size is also formed by grown Ag islands and whether the Ag islands finally decay on 1 ML C_{60}/Au(111) but stay stable or grow on 2 ML C_{60}/Au(111). Another interesting question is, if very large Ag islands which are stable on 1 ML C_{60} can be achieved.

6.4.1.1 Calibration of the Ag EFM

After melting Ag granulate in the crucible of the evaporator a calibration is necessary to determine the evaporated amount of Ag and with this the calibration constant κ. The effective Ag coverage is given by

$$\Gamma_{EFM}\,[ML] = \kappa \cdot \frac{I_{Flux}}{I_{em}} \cdot \Delta t\,, \tag{6.4}$$

where Δt is the evaporation time, I_{em} the measured electron emission current and I_{Flux} the measured Ag ion current. For the calibration of the evaporator Ag was evaporated at 250 K on an Ag(111) single crystal, which leads to Ag islands on Ag(111). A height histogram gives information about the Ag coverage which can be compared to the nominally evaporated amount. First nominally 0.3 ML Ag were evaporated on Ag(111) using $\kappa_1 = 933$ ML/sec, the value of a former calibration. STM images at 77 K and histograms revealed that only 0.1 ML Ag were evaporated on Ag(111) which lets assume that the new value for κ is smaller by a factor of 3. Again nominally 0.3 ML were evaporated at 230 K in order to achieve a smaller Ag island size and now the measurements showed that totaling 0.2 ML Ag covered the surface of the Ag(111) single crystal. Therefore, κ_1 was corrected by a factor 3.

To verify these results, in a second experimental run using κ_2 = 311 ML/sec 0.3 ML Ag were evaporated on the clean sputtered and heated Ag(111) single crystal at T = 230 K. STM images and histograms revealed a coverage of 0.3 ML Ag on Ag(111) which corroborates the results of the first measurement. In Figure 6.45 an STM image of 0.3 ML Ag/Ag(111) is shown together with histograms of two plane areas of the STM image.

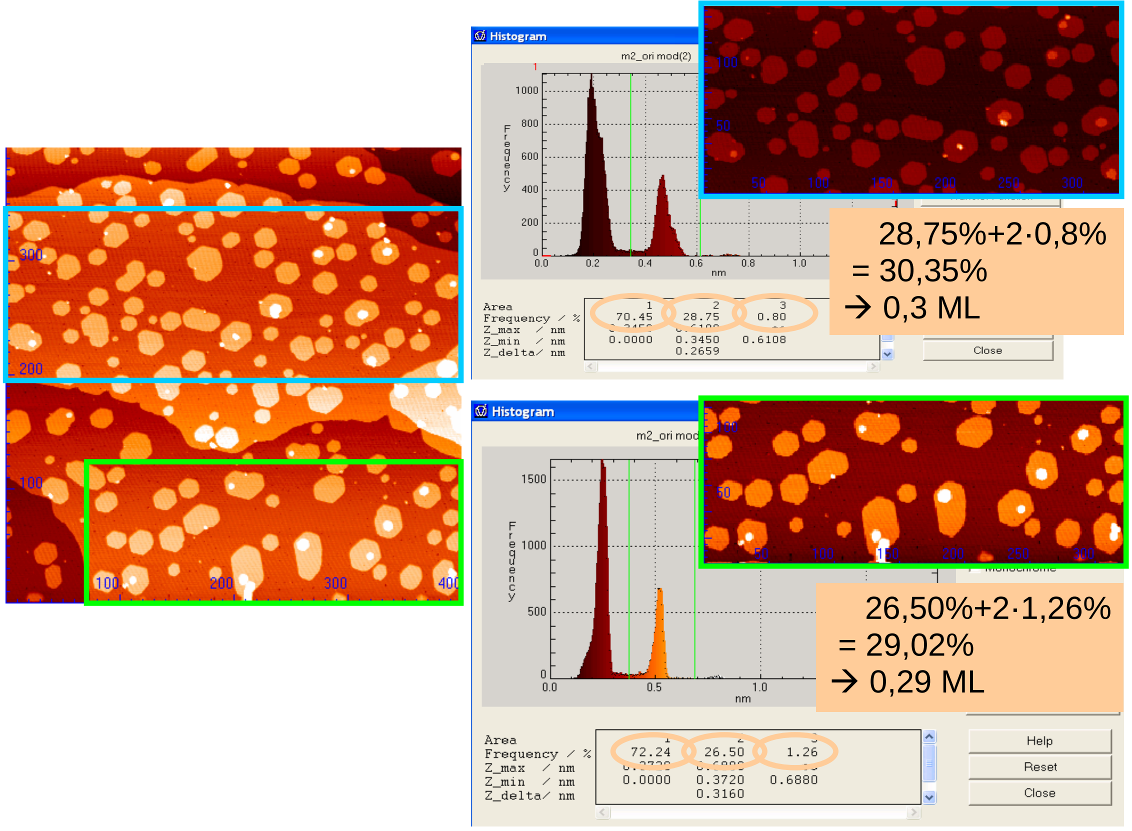

```
Area                1        2        3
Frequency / %   70.45    28.75     0.80
Z_max   / nm
Z_min   / nm   0.0000   0.3450   0.6108
Z_delta/ nm             0.2659
```

28,75%+2·0,8%
= 30,35%
→ 0,3 ML

```
Area                1        2        3
Frequency / %   72.24    26.50     1.26
Z_max   / nm
Z_min   / nm   0.0000   0.3720   0.6880
Z_delta/ nm             0.3160
```

26,50%+2·1,26%
= 29,02%
→ 0,29 ML

Figure 6.45: STM image of 0.3 ML Ag/Ag(111) and histograms to define the real coverage of Ag on the Ag(111) single crystal.

The analysis showed that in the first case 70.45 % of the cut out area of the STM image is bare Ag(111). 28.75 % of the area is covered with 1 ML Ag islands and 0.8 % with an Ag double layer, which means that this amount has to be multiplied by a factor 2. Thus, 28.75 % + 2·0.8 % = 30.35 % of the area are covered with Ag islands which equals about a third of 1 ML. In the second case 26.50 % + 2·1.26 % = 29.02 % of the area are covered with Ag islands. The same result was achieved for the first calibration experiment. Hence, the new value for κ is a third of the former value:

$$\kappa = 311 \text{ ML/sec} \tag{6.5}$$

In preparation for the annealing experiments of Ag/C_{60}/Au(111) the sample with 0.2 ML Ag/Ag(111) was annealed for 15 min at RT in order to study the thermally activated processes of Ag islands. Figure 6.46 shows STM images taken at 77 K before and after annealing for 15 min at RT.

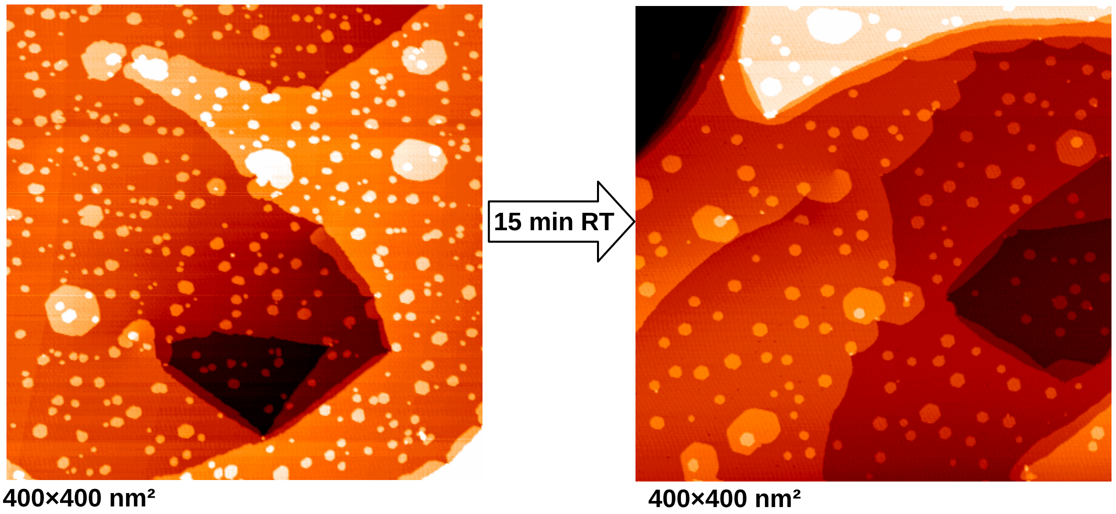

Figure 6.46: STM image of 0.6 ML Ag/Ag(111) before (left) and after annealing for 15 min at RT (right).

As it was expected Ag islands grow due to Ostwald ripening. In the STM image taken before annealing a number of small Ag islands are visible which are not visible after 15 min at RT. This is due to the fact that larger islands have drawn atoms from smaller islands.

6.4.1.2 0.026 ML Ag / 1.3 ML C_{60} / Au(111)

In a first evaporation experiment 0.013 ML Ag were evaporated at $T < 50$ K on 1.3 ML C_{60}/Au(111). The effective coverage Γ given in atomic monolayers was evaluated from equation (6.4), using $\kappa = 311$ ML/sec.

At this low coverage small dots which might represent e.g. Ag atoms, dimers or trimers were visible in the STM images taken at 77 K on 1 and 2 ML C_{60}. Slightly larger islands were observed at grain boundaries, step edges or defects which served as nucleation centers (see Figure 6.47). For this reason an additional coverage of 0.013 ML Ag was evaporated onto the sample which leads to a coverage of 0.026 ML Ag on 1.3 ML C_{60}/Au(111). The STM images taken at 77 K look similar as for 0.013 ML Ag. The Ag islands did not grow significantly, but more dots were observed on 1 and 2 ML C_{60}/Au(111). After that the sample was annealed for 45 min at 165 K, and for 15 min and 3 h at RT. STM images of every annealing step were depicted in Figure 6.47. After annealing for 45 min at 165 K, Ag on 1 ML C_{60} penetrated the C_{60} film, whereas Ag on 2 ML C_{60} stayed stable.

After annealing for 15 min at RT also the Ag dots on 2 ML C_{60} penetrated the C_{60} film and finally the STM images show clean C_{60} areas on Au(111). Only Ag islands at step edges, grain boundaries or defects are still stable indicating that the stability of these larger Ag islands is higher.

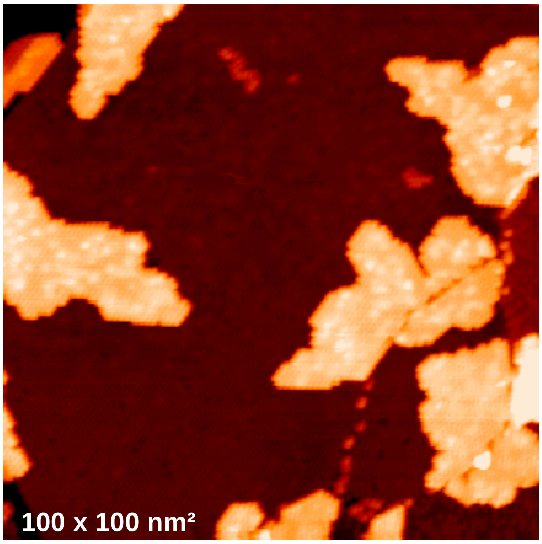

0.013 ML Ag - 77 K

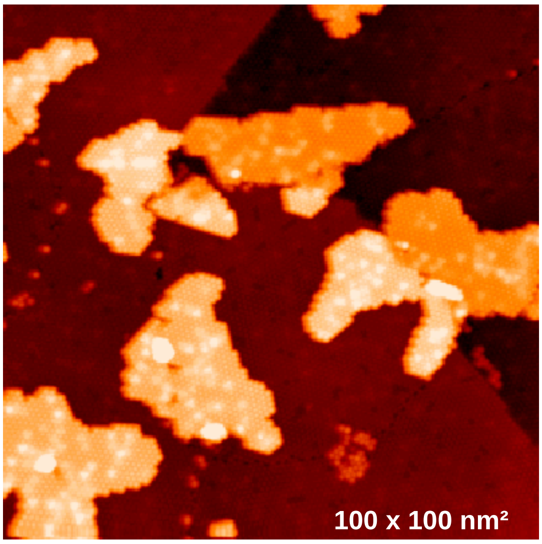

0.026 ML Ag - 77 K

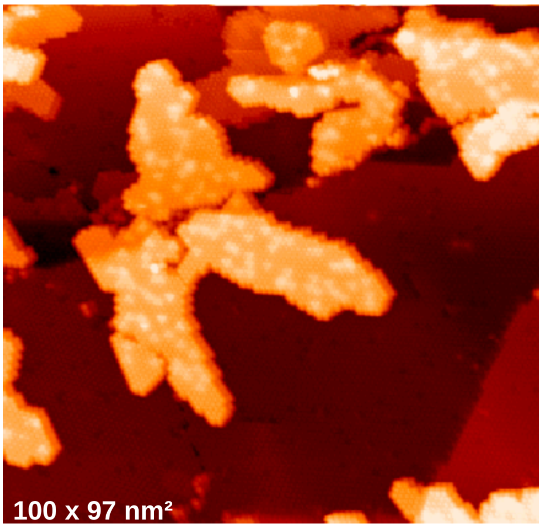

0.026 ML Ag - 45 min 165 K

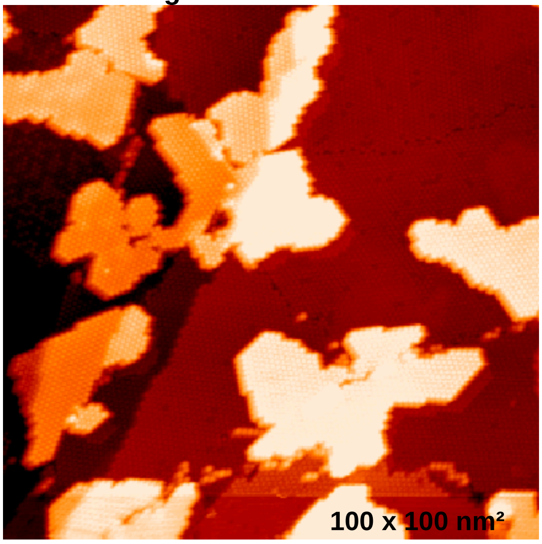

0.026 ML Ag - 15 min RT

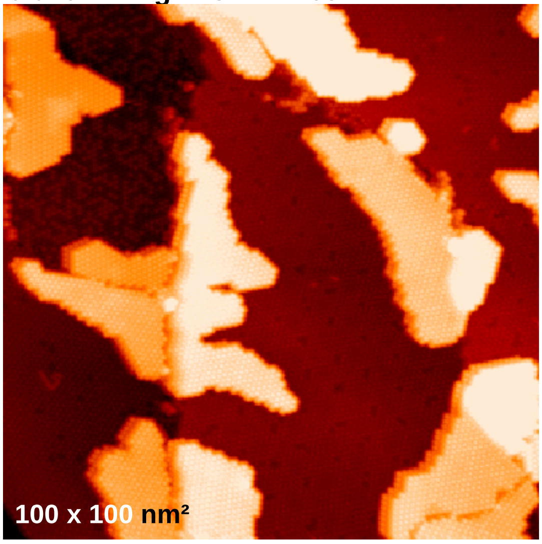

0.026 ML Ag - 3 h RT

Figure 6.47: STM images of 0.013 ML Ag and 0.026 ML Ag on 1.3 ML C_{60}/Au(111) after the evaporation below 50 K and after annealing for 45 min at 165 K, 15 min and 3 h at RT.

6.4.1.3 0.5 ML Ag / 1.3 ML C_{60} / Au(111)

Due to the fact that the Ag coverage of the first experiment was too low to observe stable sizes or growth of larger islands, in a second experiment 0.5 ML Ag were evaporated on 1.3 ML C_{60}/Au(111) at T < 50 K. After the evaporation the sample was covered with Ag islands with a height of several Å up to about 1 nm as it is shown in Figure 6.48

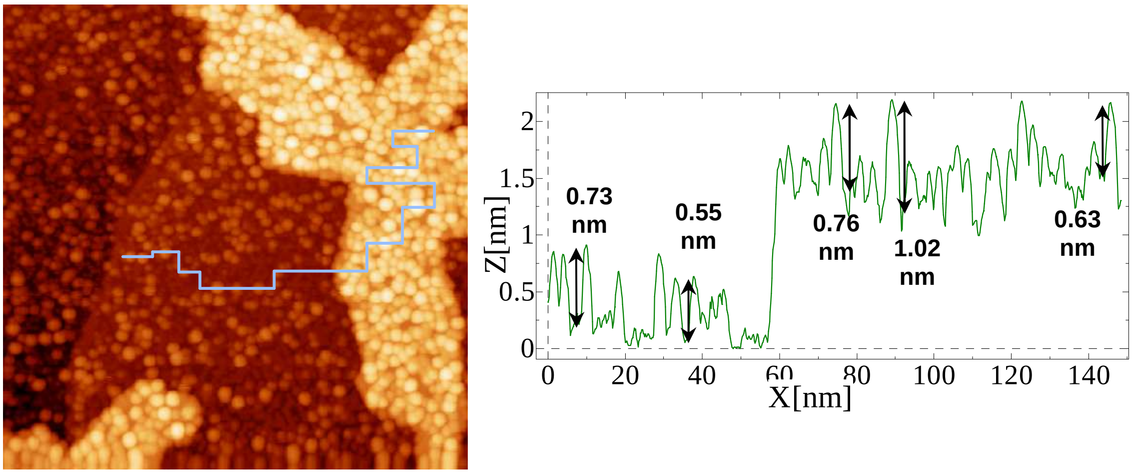

Figure 6.48: 100×100 nm² STM image taken at 77 K and line profile of 0.5 ML Ag/1.3 ML C_{60}/Au(111) deposited at T <50 K. Small Ag islands are visible on 1 and 2 ML C_{60}/Au(111).

After STM at 77 K, the sample was annealed for 45 min at 165 K, for 45 min at 215 K, and for 15 min, 45 min, 3 h, 12 h and 14 d at RT. STM images at 77 K were taken after every annealing step and the heights of the Ag islands on C_{60}/Au(111) were measured. STM images of the Ag islands after the annealing steps and the corresponding height distributions are visible in Figure 6.49 and Figure 6.50, respectively.

In the STM image taken after annealing for 45 min at 165 K it is clearly visible that the island density on 1 ML C_{60} shrunk, whereas the Ag islands on 2 ML C_{60} grew due to coalescence and Ostwald ripening. Some more stable Ag islands on 1 ML C_{60} coalesced to larger islands but most of the Ag islands already penetrated the 1 ML C_{60} film and a mixed phase of Ag and C_{60} was visible. For this annealing step the heights of only a few Ag islands were measured, consequently there is no height distribution due to poor statistics. This is due to the fact that the island density on 2 ML was extremely high and a measurement of the heights difficult because one could hardly find free C_{60} areas. On 1 ML C_{60} most of the Ag islands formed a mixed phase together with 1 ML C_{60} molecules and thus a height measurement of the coalesced Ag islands on 1 ML C_{60} which was difficult as well.

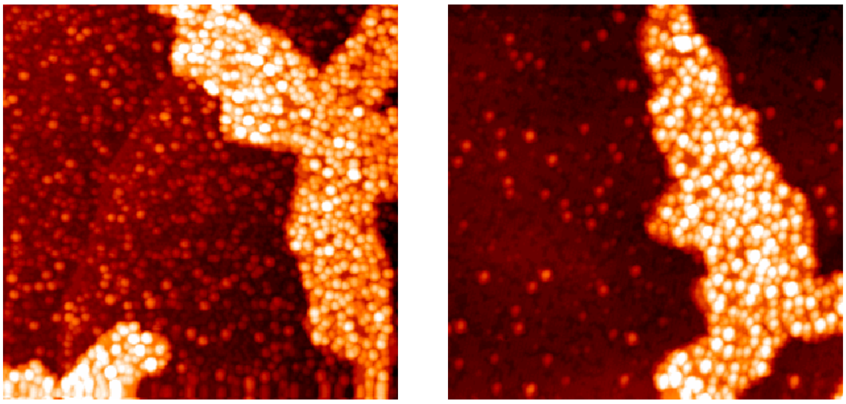

100×100 nm^2 - 77 K

100×100 nm^2 - 45 min 165 K

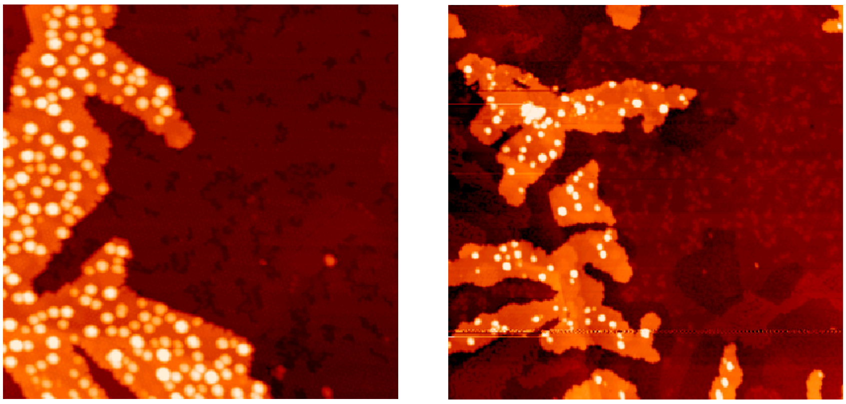

100×100 nm^2 - 45 min 215 K

200×200 nm^2 - 15 min RT

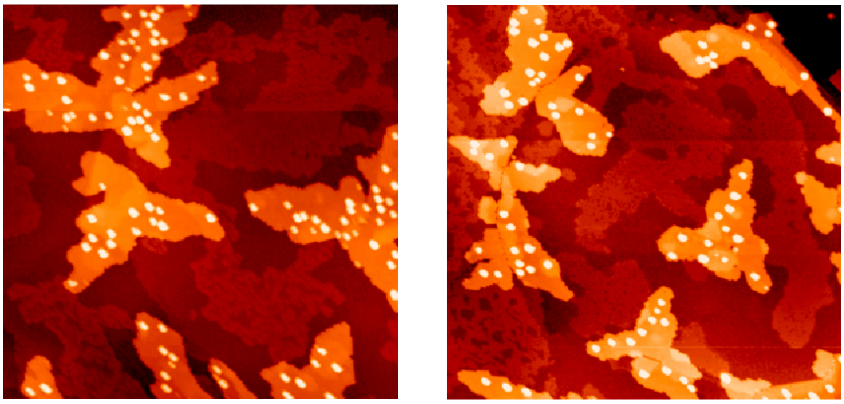

200×200 nm^2 - 45 min RT

200×200 nm^2 - 3 h RT

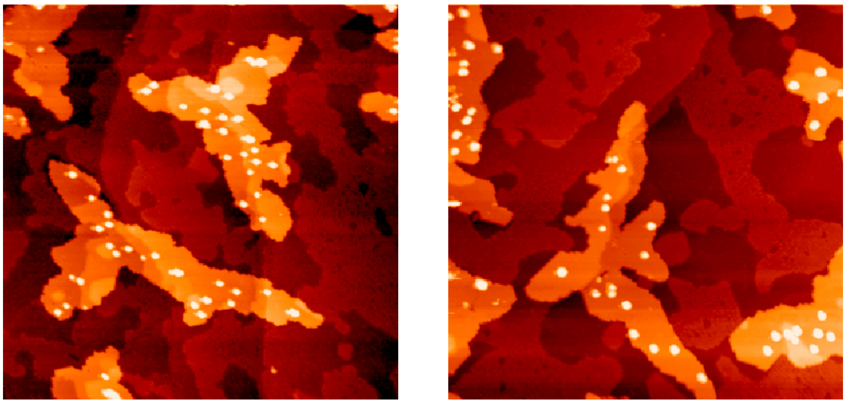

200×200 nm^2 - 12 h RT

200×200 nm^2 - 14 d RT

Figure 6.49: STM images of 0.5 ML Ag/1.3 ML C_{60}/Au(111) after different annealing steps.

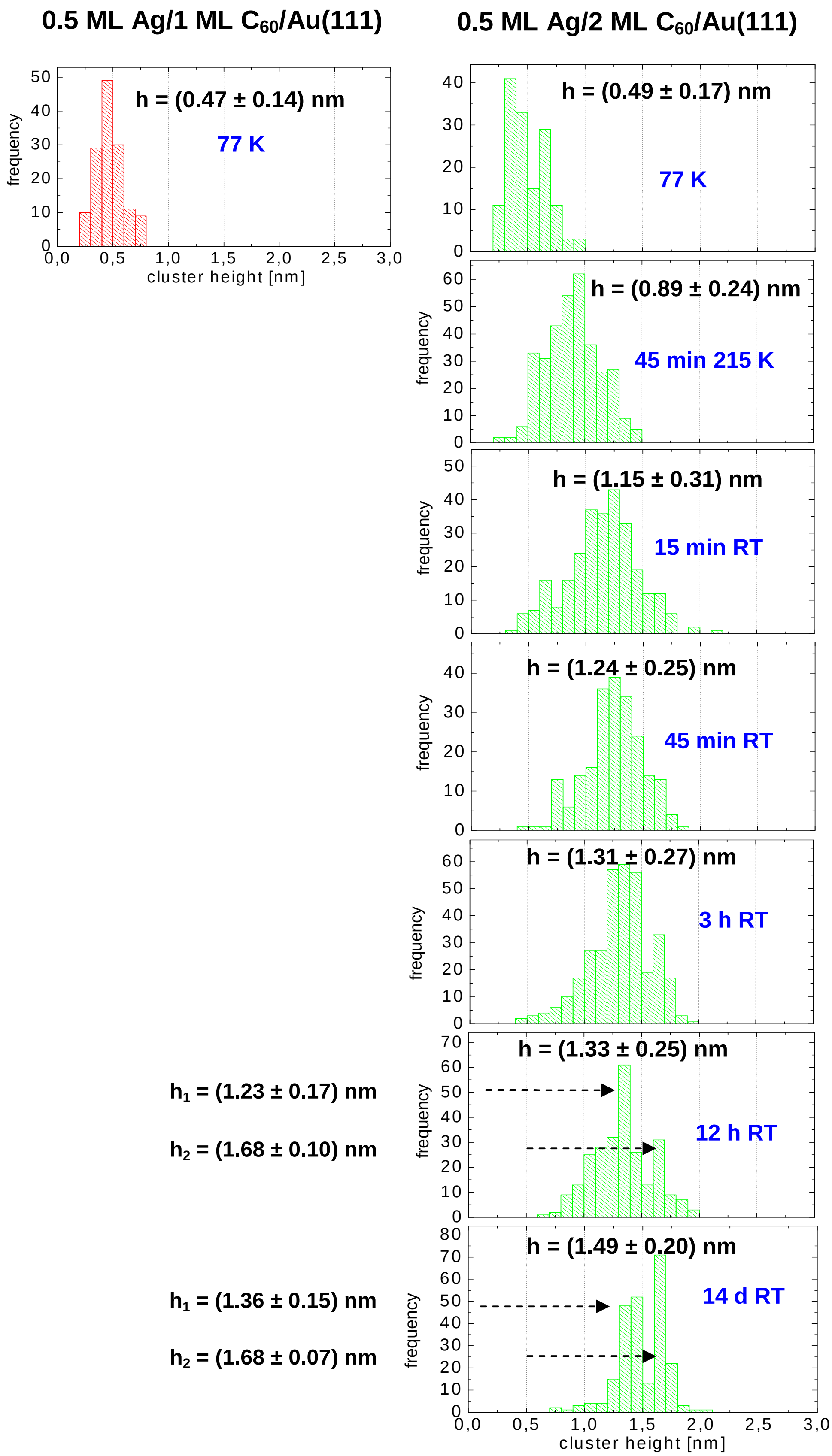

Figure 6.50: Height distributions of 0.5 ML Ag/ 1 and 2 ML C_{60}/Au(111) after different annealing steps.

Therefore, only a qualitative interpretation is possible for this annealing step. For annealing at 77 K the same problems of the height measurement existed. But due to being the first step for which height measurements were performed, the heights for Ag islands on 1 and 2 ML C_{60} annealed at 77 K were analyzed in more detail. The difficulties of the height measurement possibly lead to more unprecise heights for the 77 K data than for the other annealing steps.

After annealing for 45 min at 215 K nearly all Ag islands on 1 ML C_{60}/Au(111) decayed and formed a network of 1 ML Ag on the Au(111) surface below the 1 ML C_{60}.

On 2 ML C_{60} the Ag islands grew during annealing, which is indcated by the STM image in Figure 6.49. The growth of Ag islands on 2 ML C_{60} is corroborated by the height distributions shown in Figure 6.50. Already for 45 min at 215 K the mean value for the height distribution is larger than after evaporation and storage in the STM at 77 K. Due to the fact that the nearly all Ag islands on 1 ML C_{60} penetrated the C_{60} at 215 K, no height distributions exist for this and all following annealing steps.

For the following annealing steps the processes which were described above continued. As presented by the STM images in Figure 6.49 and the height distributions in Figure 6.50, the Ag islands which were evaporated on 1 ML C_{60}/Au(111) formed multilayer Ag islands below the C_{60} monolayer. In contrast, the Ag islands on 2 ML C_{60} grew due to coalescence and Ostwald ripening. An interesting phenomenon is the formation of favored Ag island sizes on 2 ML C_{60}. After 3 h at RT two maxima are visible in the height distribution, which get more pronounced after annealing for 12 h and for 14 d at RT. After 14 d at RT a bimodal height distribution was observed with two narrow peaks and maxima at about 1.3 nm and 1.68 nm, and no larger islands are formed.

These results are similar to the results for deposited size selected Ag clusters on Au(111) functionalized with C_{60}. For both, deposited Ag clusters and grown Ag islands, the Ag material penetrated the 1 ML C_{60} film, whereas Ag remained on top of 2 ML C_{60}. Geometrically magic Ag clusters did not change their size on 2 ML C_{60}, whereas geometrically non-magic clusters and Ag islands grew due to Ostwald ripening. For Ag islands on 2 ML C_{60} favored sizes were observed which seem to block further island growth. But the stable island sizes do not agree with the height of $h \approx 1.5$ nm which was observed for geometrically magic Ag clusters on 1 ML C_{60} due to decay and for geometrically non-magic Ag clusters on 1 and 2 ML C_{60} due to Ostwald ripening.

During the experiments within this thesis, after annealing 0.5 ML Ag/C_{60}/Au(111) an interesting superstructure with threefold symmetry of 1 ML C_{60} was observed and is depicted in Figure 6.51. Ag islands below the C_{60} are visible which adapt the threefold superstructure of the C_{60}. Another observation was the formation of different structures of Ag islands below the C_{60} which depend on the C_{60} pattern (see Figure 6.52). Below the strongly patterned C_{60}(1) film the Ag islands formed larger closer packed 1 ML islands (see Figure 6.52 a)) than below the C_{60}(2) film, where more but smaller Ag islands were observed (Figure 6.52 b)).

Ostwald ripening is a process which was investigated in several publications. The growth of larger Ag islands on Ag(111) at the expense of smaller ones was e.g. also studied by K. Morgenstern et al. by studying the time evolution of cluster sizes and kinetic parameters [208, 209].

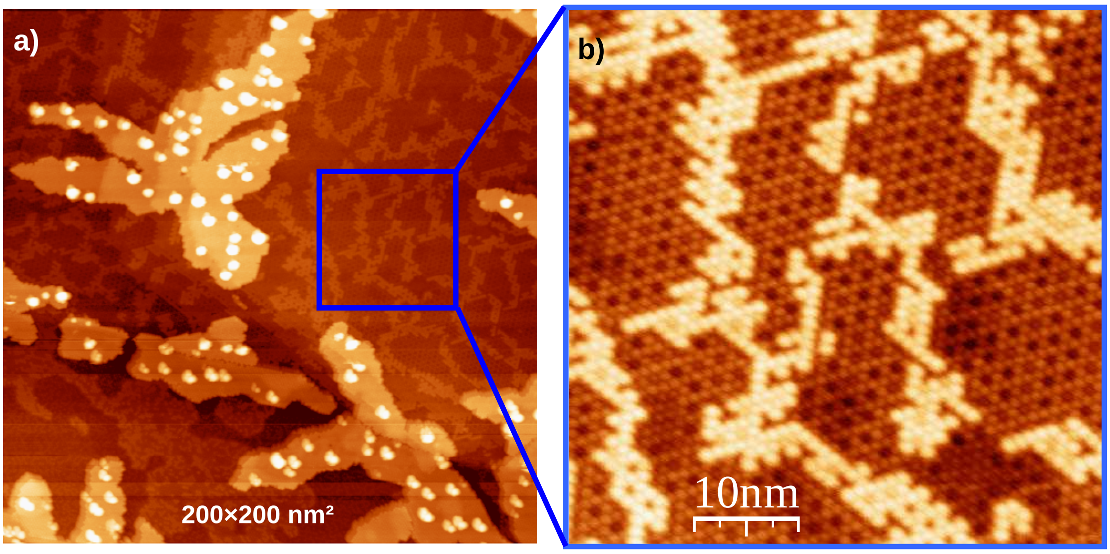

Figure 6.51: a) STM image of 0.5 ML Ag/1.3 ML C_{60}/Au(111) after 45 min at RT. The 1 ML C_{60} area shows a superstructure with threefold symmetry. Ag islands below the C_{60} are visible. b) Enlarged 26×26 nm² STM image of the threefold C_{60} superstructure.

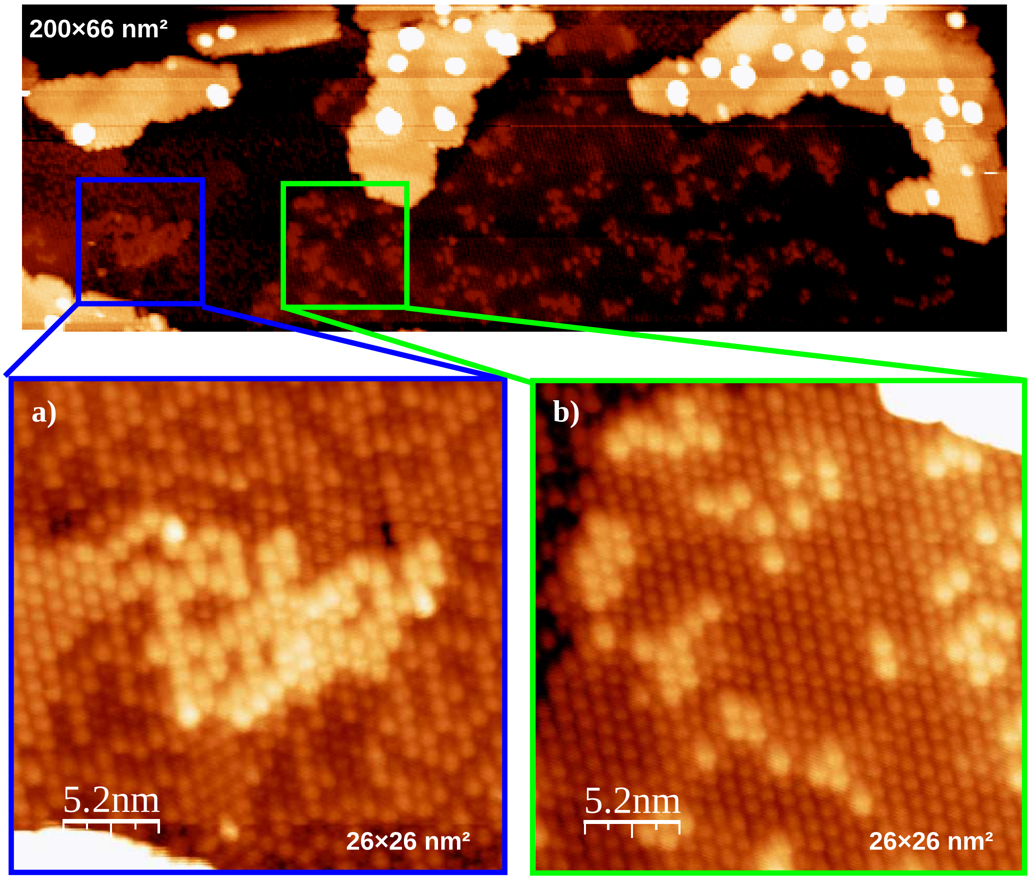

Figure 6.52: STM images of different Ag island structures below a) C_{60}(1) and b) C_{60}(2).

H. CERCELLIER et al and F. REINERT investigated the epitaxial growth of Ag films on Au(111) at low temperatures and at RT and observed similar island structures of Ag/Au(111) as observed within this thesis for Ag/Au(111) below 1 ML C_{60} (Figure 6.49). They found out that the first, second, and third Ag layers are reconstructed and that this surface reconstruction acts as a superlattice for surface state electrons. Since the mismatch is very weak, the driving force for such a reconstruction could be the small Ag-Au intermixing observed at room temperature [210].

6.4.1.4 4 ML Ag / 1.3 ML C_{60} / Au(111)

In order to find out if the decay of Ag islands on 1 ML C_{60} can be suppressed by growing islands which are large enough to stay stable or metastable at RT, 4 ML Ag were evaporated at $T < 50$ K on 1.2 ML C_{60}/Au(111). STM images were taken at 77 K, before the sample was annealed for 45 min at 165 K, 215 K, 265 K, for 15 min, 45 min, 3 h and 12 h at RT and for 45 min at 335 K. STM images for the most significant annealing steps are shown in Figure 6.53.

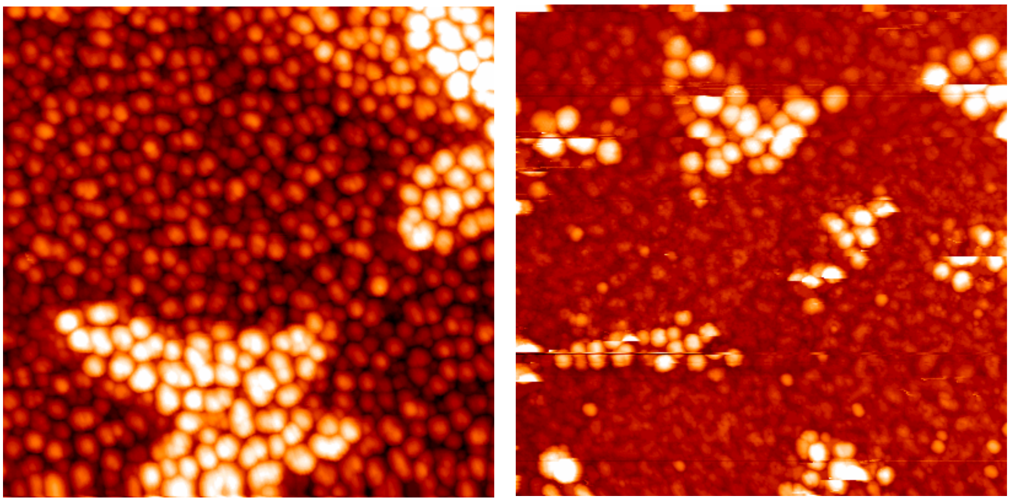

100×100 nm^2 - 77 K

200×200 nm^2 - 45 min 265 K

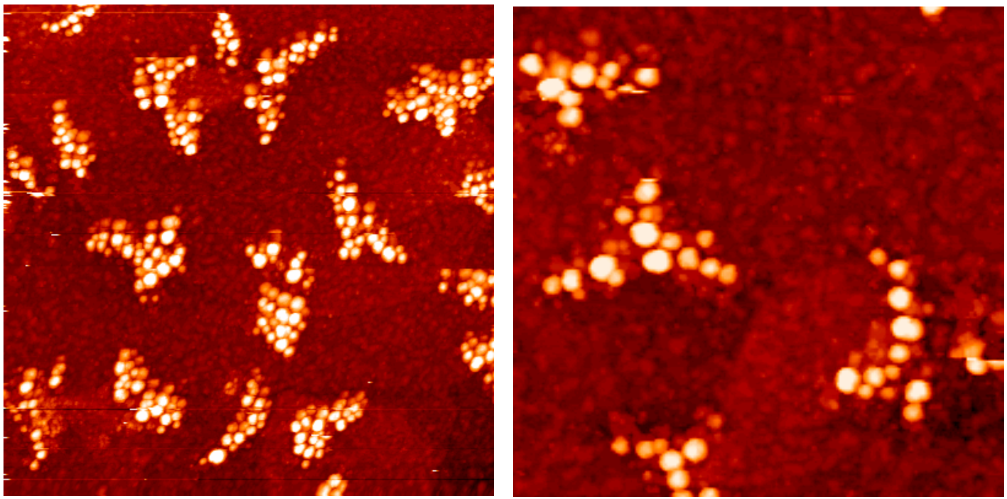

400×400 nm^2 - 3 h RT

200×200 nm^2 - 12 h RT

Figure 6.53: STM images taken at 77 K of 4 ML Ag/1.2 ML C_{60}/Au(111) after different annealing steps. On 1 ML C_{60} 4 ML Ag decayed at 265 K, whereas Ag islands on 2 ML C_{60} show ripening.

It is clearly visible that the cluster density is higher and the Ag islands are larger than for 0.5 ML Ag/C_{60}/Au(111). In contrast to 0.5 ML Ag islands, which decayed on 1 ML C_{60} after annealing for 45 min at 165 K, 4 ML Ag on 1 ML C_{60} stayed stable under these conditions. But after annealing for 45 min at 265 K the Ag islands on 1 ML C_{60} penetrated the fullerene layer and formed a C_{60}-Ag mixed phase. In contrast, the Ag islands on 2 ML C_{60} did not decay but grew after every annealing step due to Ostwald ripening and thermally induced mobility. Annealing above RT – for 45 min at 335 K – yielded no significant changes of the Ag islands. The Ag island heights were not measured explicitly because the island density was too high to find free C_{60} areas for the reference measurement. The results are comparable to the results of 0.5 ML Ag/C_{60}/Au(111), except for the fact that the larger Ag islands on 1 ML C_{60}/Au(111) decayed only at 265 K and not at 165 K, as observed for 0.5 ML Ag.

6.4.1.5 Calculation of the effective coverage

Using the experiment with 0.5 ML Ag/1.3 ML C_{60}/Au(111), the effective coverage after different annealing steps is calculated considering different assumptions [142]. The first assumption is that the Ag islands have the shape of a prolate spheroid. Due to the cluster-surface interaction, this is a reasonable approximation of the cluster shape. Ag islands with the shape of a prolate spheroid are defined by the height h, which was measured for the Ag islands, and the width w, which can not be measured with STM. Thus x, the ratio of width and height is a parameter which defines the volume of the Ag islands for given h. Figure 6.54 shows a schematic illustration for a prolate spheroid.

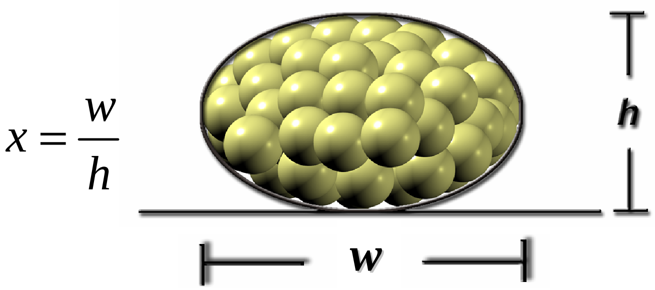

Figure 6.54: Schematical illustration of a prolate spheroid which is assumed for the shape of the Ag islands.

The volume of a prolate spheroid is given by

$$V_{prolate\ spheroid} = \frac{4}{3}\pi \cdot \frac{h}{2} \cdot \left(\frac{w}{2}\right)^2 = \frac{\pi}{6} \cdot x^2 \cdot h^3 \qquad (6.6)$$

The volume of the evaporated Ag islands is the product of the thickness of the Ag material in monolayer units N_{ML}, the height of an Ag monolayer h_{ML} and the area A considered:

$$V_{ev} = N_{ML} \cdot h_{ML} \cdot A \qquad (6.7)$$

The volume of the evaporated Ag has to equal the sum of the volume of all Ag islands with the shape of a prolate spheroid:

$$N_{ML} \cdot h_{ML} \cdot A = \frac{\pi}{6} \cdot x^2 \cdot \sum_{i=1}^{n} h_i{}^3 . \tag{6.8}$$

Thus, it follows:

$$x = \sqrt{\frac{6 \cdot N_{ML} \cdot h_{ML} \cdot A}{\pi \cdot \sum_{i=1}^{n} h_i^3}} . \tag{6.9}$$

The measurement of the Ag island heights on 1 ML C_{60} were not as precise as on 2 ML C_{60} because it was often difficult to find free C_{60} areas for the reference measurement of the cluster heights on 1 ML C_{60}. Additionally it is possible that after the evaporation at $T < 50$ K or in the STM at 77 K a part of the Ag islands already decayed. For this reason the calculation of *x* is made by regarding Ag islands on 2 ML C_{60} at $T < 50$ K (77 K in the STM) and the result is used for both Ag islands on 1 and 2 ML C_{60}, and at all annealing steps.

For the calculation of *x* the measured Ag islands heights *h* are considered (see Figure 6.50). N_{ML} equals 0.5 ML, $h_{ML} = 0.236$ ML and the area *A* on which the Ag island heights were measured on 2 ML C_{60} equals 688.32 nm². This leads to $x = 2.53$.

By knowing *x*, the volume of the Ag islands can be calculated by assuming a prolate spheroidal shape with constant *x* and thus the effective coverage on 1 and 2 ML C_{60} after different annealing steps. The results are visualized in Figure 6.55.

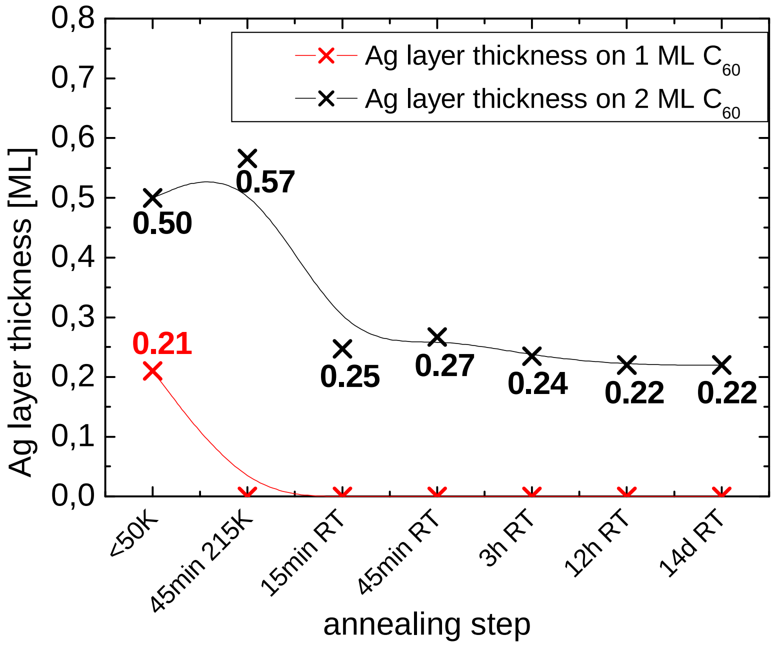

Figure 6.55: Ag layer thickness on 1 and 2 ML C_{60} after every annealing step by assuming a constant value of 2.53 for the ratio of width and height of the Ag islands. A spline interpolation visualizes the change of the Ag layer thickness [142].

By definition on 2 ML C_{60} the calculation of the Ag layer thickness for T < 50 K equals 0.5 ML but on 1 ML C_{60} only 0.21 ML. This can be due to the fact that on the one hand Ag has penetrated the 1 ML C_{60} film already at 77 K. On the other hand the value of 2.53 for x based on different approximations. It is probable that the shape of the Ag islands on 1 ML C_{60} changes for 1 or 2 ML C_{60}, or at different temperatures, and therefore the model of the prolate spheroid is not valid for Ag islands on 1 ML C_{60}. An interesting observation is that for both Ag islands on 1 and on 2 ML C_{60} a decrease of the Ag layer thickness was calculated. Ag islands on 1 ML C_{60} penetrated the C_{60} after annealing for 45 min at 215 K, whereas there is a decrease for Ag islands on 2 ML C_{60} after annealing for 15 min at RT. For all following annealing steps the Ag layer thickness on 2 ML C_{60} stayed constant although the density and heights of the Ag islands change due to the growth of the islands. Therefore, it is very likely that for these data points the assumption $x = \text{constant}$ is correct. For the growth process of the Ag islands both coalescence and Ostwald ripening may play an important role.

6.4.2 Pb islands on C_{60} / Au(111)

In [211] the stability of Pd particles on $TiO_2(110)$ were investigated. Upon heating, the number of particles per area decreased and the particle size increased due to coalescence at 830 K. In [212] it was shown that Ag monomers or dimers which are deposited on TiO_2 are very mobile at RT and sintered to form large islands of approximately 50 atoms in size. In contrast, Ag_3 clusters deposited on TiO_2 stayed stable trimers and showed a limited mobility at RT. This shows that different metals often behave differently on the same kind of substrate and in the case of Ag the mobility strongly depends on the clusters size.

In order to study the thermally activated processes of another kind of metal on C_{60}/Au(111), Pb atoms were evaporated which results in three dimensional Pb islands on C_{60}/Au(111). The calibration constant κ for Pb was taken from a former calibration and equals

$$\kappa = 131 \text{ ML/sec.} \tag{6.10}$$

0.04 ML Pb were evaporated at T < 50 K on an Au(111) surface functionalized with 1 ML C_{60} in order to study the thermally induced processes of Pb islands. For an investigation of the Pb islands STM images were taken at 77 K followed by annealing at different temperatures up to RT and investigation of the Pb island heights. Figure 6.56 shows three significant STM images and height distributions measured after each annealing step.

First STM images were taken directly after the evaporation at T < 50 K. Small Pb islands with heights below 1 nm and a mean value of (0.33 ± 0.18) nm were observed (see Figure 6.56). Then STM images were taken after storage in the STM at 77 K for 16 h in order to study, if an annealing at 77 K causes a change of the island heights. As it is visible by the height distribution measured after 16 h at 77 K, the heights of the Pb islands did not change significantly, the mean value is h = (0.35 ± 0.18) nm.

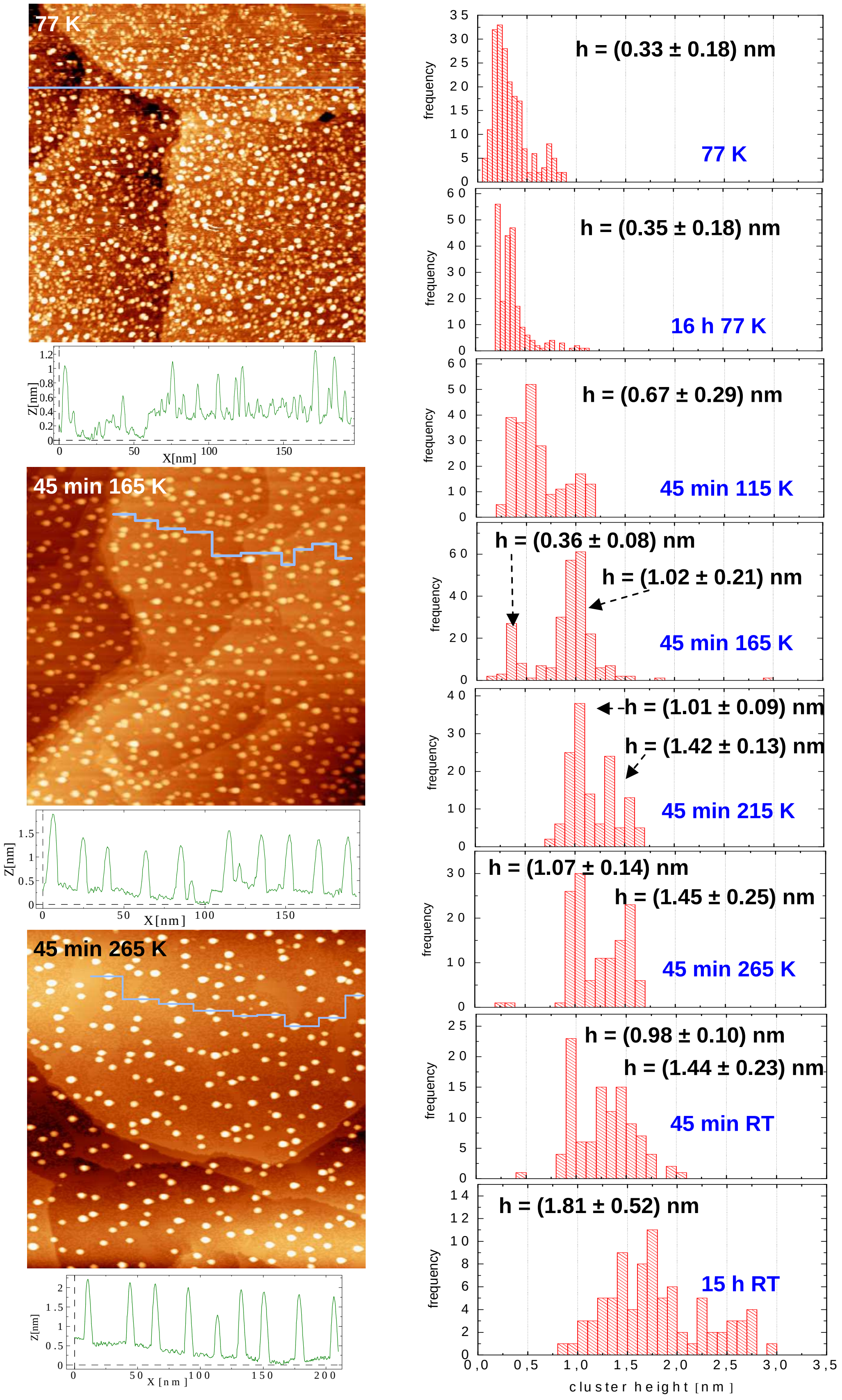

Figure 6.56: 200×200 nm² STM images taken at 77 K and height distributions of 0.04 ML Pb/1 ML C_{60}/Au(111) after different annealing steps.

The Pb islands were furthermore annealed for 45 min at 115 K, 165 K, 215 K and 265 K and for 45 min and 15 h at RT. After annealing for 45 min at 115 K the Pb islands started to grow and the mean value of the islands heights shifted to h = (0.67 ± 0.29) nm. The Pb islands grew after every annealing step and metastable cluster sizes became visible in the height distributions. After 45 min at 165 K two maxima in the height distribution at h = (0.36 ± 0.08) nm and h = (1.02 ± 0.21) nm were visible (see Figure 6.56). The STM image in Figure 6.56 taken after annealing for 45 min at 165 K shows a lower cluster density as in the STM image taken directly after the evaporation, but larger Pb islands with larger height. The fact that less small but more larger islands were observed is an indication for Ostwald ripening of the Pb islands. It is also possible that in addition to Ostwald ripening coalescence of Pb islands occurred. Metastable islands of about 1 nm height were also visible after annealing for 45 min at 215 K, 265 K and RT, only after 15 h at RT these islands grew to larger ones. The maximum at h = 0.36 nm vanished after annealing for 45 min at 215 K, but another metastable size of h ≈ 1.4 nm was visible after 45 min at 215 K, 265 K, RT and 15 h at RT. The results were corroborated by evaporating 0.04 ML Pb on 1 ML C_{60}/Au(111) within a second experiment.

In summary Pb islands on 1 ML C_{60}/Au(111) formed small islands after the low temperature evaporation and grew after every annealing step up to RT. It is striking that no thermally induced decay of the Pb islands took place as observed for Ag islands on 1 ML C_{60}/Au(111). Due to the fact that no Pb islands below the C_{60} were observed and that the effective coverage of Pb islands on 1 ML C_{60}/Au(111) stayed in the same order of magnitude after annealing [104], a penetration of Pb through 1 ML C_{60} can be safely neglected.

The decisive question is why Pb islands on 1 ML C_{60}/Au(111) behave such differently than Ag islands. In order to answer this question it can help to regard the different properties of Pb/Au(111) and Ag/Au(111). The growth of Ag on Au(111) was studied in [213]. At submonolayer coverage growth in fingerlike rows locked to the Au(111) reconstruction was observed. One monolayer of Ag removes the substrate surface reconstruction. Experimental results for Pb on Au(111) indicate that initial sites for Pb adsorption are located at the herringbone kinks. For higher coverages, Pb prefers hcp and fcc stacking regions, avoiding the herringbone ridges. The reconstruction is removed for a coverage between 0.05 and 0.2 monolayers [214]. Hence, Pb removes the Au(111) reconstruction for much less coverage as Ag, which lets assume that Pb is more mobile than Ag which leads to a stronger self-ordering of Pb, independent from the Au(111) reconstruction. Other differences between Pb and Ag are the surface free energy which is 0.59 eV for Pb [215] and 0.50 eV for Ag and the fact that Pb atoms localize at the surface defects (elbows) of the Au(111) reconstruction in contrast to Ag atoms [213, 216].

Due to the fact that Pb melts at about 600 K (1235 K for Ag) desorption experiments are difficult. The desorption of 1 ML C_{60}/Ag(111) starts above 675 K, the desorption of C_{60}/polycrystalline Ag above 750 K [217]. The low melting point of Pb leads to a higher mobility of Pb atoms at RT in contrast to Ag atoms. Hence, the mobile Pb atoms tend to grow or coalesce and ignore the Au(111) interaction.

GOLDONI et al. reported on a strong predominantly ionic bonding between C_{60} and Ag(110) [217] whereas there exists an ionic bonding with intermediate strength between Ag(100) and C_{60} [218, 219]. Ionic bondings are characterized by charge transfer from the metal to the LUMO (lowest unoccupied molecular orbital) of C_{60}. WANG et al. studied the charge transfer of Ag islands to C_{60} molecules [220] and reported that Ag is weakly bounded by van der Waals interactions up to a critical island size. For Ag clusters larger than this critical size, which is above 4 nm, charge transfer from Ag to C_{60} will occur. For the Ag island experiment within this thesis these observations mean that the small Ag islands on 1 ML C_{60}/Au(111) are stronger influenced by the metal-metal interaction with the Au(111) substrate than by the van der Waals interaction with C_{60}, which leads to a penetration of Ag islands through the C_{60}. In contrast UPS spectra of Pb islands on C_{60}/Si(111)-7×7 show a metallic character of C_{60} due to charge transfer from Pb to C_{60} for less than one ML Pb on C_{60} [221]. Hence, the Pb-C_{60} interactions are stronger compared to the Ag-C_{60} interactions which lead for Pb to Ostwald ripening and coalescence, respectively, at RT.

There is also a stronger charge transfer from Pb to C_{60} than from Au(111) to C_{60}. The degree of charge transfer from Au, Cu and Pb, respectively to the C_{60} molecules was studied in ref [222]. It increases from Au(111) to Pb(111) which is visible in STS spectra of C_{60}/Pb(111) and C_{60}/Au(111). Figure 6.57: shows STS spectra of C_{60}/Cu(110), C_{60}/Pb(111) and C_{60}/Au(111) which show different degrees of charge transfer between metal and C_{60}.

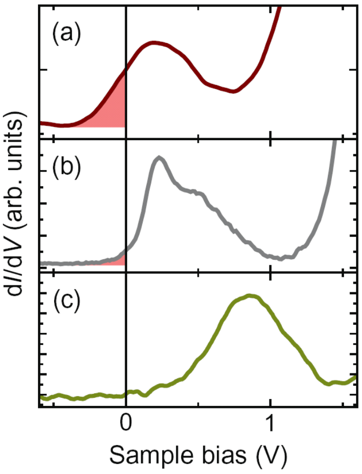

Figure 6.57: d*I*/d*V* curves showing the LUMO of C_{60} on (a) Cu(110), (b) Pb(111) and (c) Au(111). The shaded areas mark the occupied portions of the LUMO peaks. From this a decreasing amount of electron transfer into the C_{60} molecule can be expected for Cu(110) to Pb(111) to Au(111) [222].

If the charge transfer between C_{60}/Ag(111) would be stronger than for C_{60}/Au(111), one could conclude that the charge transfer of C_{60}/Ag(111) is also stronger than for C_{60}/Pb(111) (see Figure 6.57). But in [190] E. I. ALTMAN et al. showed that adsorbed C_{60} molecules were found to rotate faster on Au(111) than on Ag(111) which indicates a stronger interaction between C_{60} and Ag(111). However, annealing studies showed that C_{60} desorbs from both Au(111) and Ag(111) at approximately the same temperature indicating that differences in interaction strength between the two surfaces cannot be large. This result is corroborated by large-scale density functional theory (DFT) calculations, which predict an adsorption energy of –1.5 eV for C_{60}/Ag(111) and

–1.2 eV for C_{60}/Au(111), respectively [223]. Therefore, the similar interaction strength of Ag(111) and Au(111) with C_{60} might indicate that the stronger charge transfer between C_{60} and Pb islands is stronger than for Ag islands, as mentioned above.

With this explanations one can try to understand why Ag and Pb behave differently on 1 ML C_{60}/Au(111) at RT. But possibly also other properties and mechanisms are responsible for the decay of Ag islands and the growth of Pb islands on 1 ML C_{60}/Au(111).

6.4.3 Comparison: Size selected Ag clusters vs. grown metal islands

The results of grown Ag islands on C_{60}/Au(111) showed that it was impossible to evaporate enough Ag to grow large islands which do not penetrate the C_{60} film. But it was observed that larger Ag islands on 1 ML C_{60}/Au(111) (see subsection 6.4.1.4) decay at higher temperatures than smaller Ag islands (see subsection 6.4.1.3). The calculation of the effective coverage indicates a decay of small Ag islands also on 2 ML C_{60}/Au(111). But finally long-time stability and favored island sizes at RT are obtained, if a certain island size is reached due to coalescence or Ostwald ripening. In contrast for Pb islands on 1 ML C_{60}/Au(111) only the growth of Pb islands was observed.

For size selected Ag clusters on 1 ML C_{60}/Au(111) there are also indications of an earlier decay for smaller clusters than for larger clusters on 1 ML C_{60}. Within this thesis it was observed that Ag_{55} and Ag_{147} decay faster than Ag_{309}, Ag_{561} [146] and Ag_{923} [165], as depicted by the height distributions after different annealing steps. Especially geometrically non-magic clusters show instability below RT. A large difference to grown Ag islands is the formation of the metastable cluster size of ≈ 1.5 nm height and the absolute RT stability of geometrically magic Ag clusters from Ag_{147} to Ag_{923} on 2 ML C_{60}/Au(111) and on 1 and 2 ML C_{60}/HOPG. Mass selection enables the production of clusters with the same size which can not be achieved by evaporating a metal atom-by-atom onto a surface. The STM images in Figure 6.58 visualize this difference of size selected clusters and grown islands.

Hence, mass selected clusters with their tailored properties and especially the system Ag_N on C_{60}/HOPG, which is long-time stable at RT, are promising for technical applications.

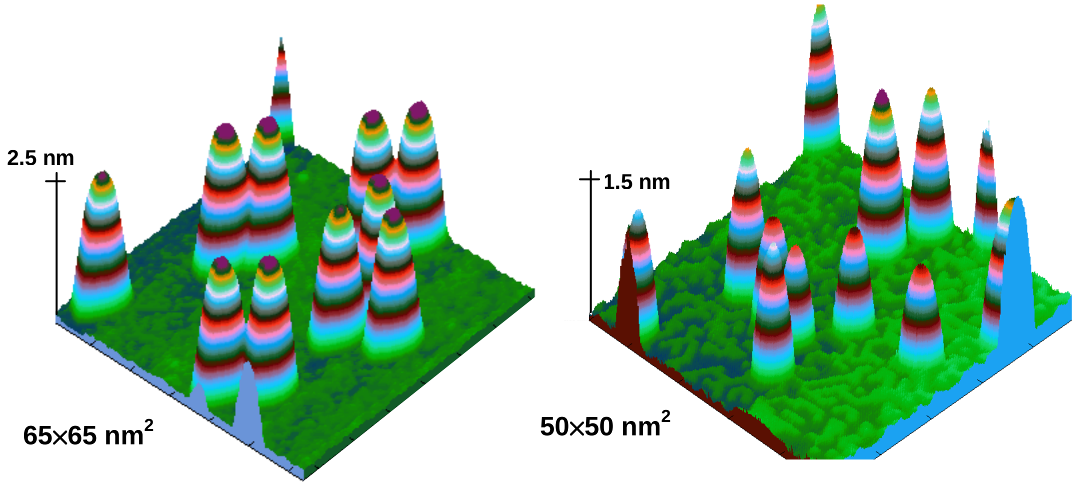

Figure 6.58: 3D STM images of Ag_{309}/1 ML C_{60}/Au(111) after deposition at 165 K (left) and grown Pb islands on 1 ML C_{60}/Au(111) (right). The color shading show clearly that size selected clusters all have the same height, whereas the heights of grown metal islands are different.

6.5 STS spectra of size selected Ag clusters

In addition to the thermally activated processes of size selected Ag clusters and the investigated geometrical properties, STS spectra of single size selected Ag clusters on 1 and 2 ML C_{60}/HOPG were taken in order to get information about the electronic structure of size selected Ag clusters. Due to the fact that on the C_{60} functionalized HOPG surface size selected clusters stay stable at RT also on 1 ML C_{60}, this sample system is well suited for taking STS spectra. Because the thermal drift must be low and the tip has to be extremely stable for taking STS spectra the measurements were performed at 5 K. At this temperature Ag clusters on 1 ML C_{60}/Au(111) are stable as well, but the sample and the STM are easier to handle, if the sample can be stored at RT e.g. for a change of the STM tip

The STS technique is described in detail in section 4.2. Shortly, during taking an STM image the tip is positioned on an Ag clusters with given setpoint values, the loop gain is switched off and by varying the tunneling voltage between two defined values with constant tip-cluster distance, the corresponding current is measured. As represented by equation (4.7) the dI/dV curves give information about the LDOS of the sample. Extreme changes of the current lead to peaks in the dI/dV curves, which indicate the existence of cluster orbitals.

6.5.1 STS spectra of Ag_{309} and Ag_{923}/C_{60}/HOPG

Within this thesis STS spectra at 5 K of Ag_{309} and Ag_{923} on C_{60}/HOPG were taken. The spectra are shown in Figure 6.64 - Figure 6.68. They were taken on the highest position of an Ag clusters and also on the C_{60} as a reference measurement as depicted in Figure 6.59. STS spectra of C_{60} were taken before and after taking STS spectra of an Ag cluster in order to observe if the tip shape changed during the measurement. Measured and calculated STS spectra of C_{60} are well known from literature [178, 179, 224-226] and can therefore be used for reference measurements. The tip always influences the structure of an STS spectrum and thus it is important to know if the tip is stable or changes from measurement to measurement. If several C_{60} spectra look similar one can assume that the shape of the STM tip did not change during the measurement. Hence, STS spectra of clusters, which were measured between these C_{60} spectra, were also measured with the same tip shape. If the structure of the C_{60} spectra changes during the measurement, this is an indication that the shape of the STM tip changed, which has to be considered during analysis of the STS spectra. STS spectra of C_{60} which are similar were marked by identical colors. STS spectra of clusters which were measured in between have the same color as the corresponding C_{60} spectra.

The STS spectra of C_{60} (see Figure 6.64, Figure 6.66 and Figure 6.67) show mainly three peaks, which indicate transitions of electrons from the STM tip into a molecule orbital of a C_{60} molecule. At 0 V the Fermi levels of tip and sample are aligned. The peaks between 1 and 2 V represent the lowest unoccupied molecule orbital (LUMO) of C_{60} and the peaks at about 3 V the LUMO+1. The peaks at about –2.5 V, which are particularly visible in Figure 6.67 at the negative edge of the voltage range, correspond to electron transistions from the highest occupied molecule orbital (HOMO) of C_{60} into the tip. Peak shifts in calculated STS spectra of C_{60}/Ag(111) due to different shapes of the STM tip are modeled in [224].

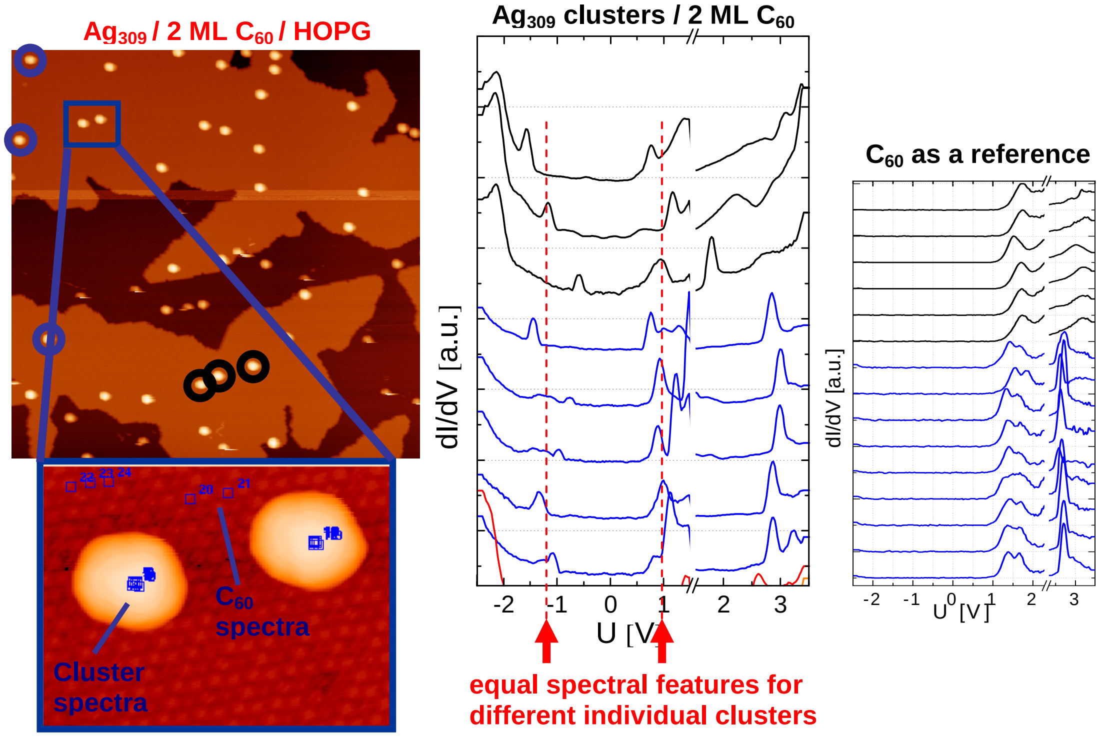

Figure 6.59: STM images (200×200 nm² and 22×15 nm²) of Ag_{309}/C_{60}/HOPG and STS spectra of Ag_{309} and C_{60} showing equal spectral features for individual clusters.

The most striking features in the STS spectra of the Ag clusters are two pairs of peaks which are visible for Ag_{309} at about –1 V and 1 V and at about – 2 V and 2.5 V and for Ag_{923} at –0.5 V and 1 V and at about –2 V and 1.5 V. Only some spectra show all four peaks, in most cases only the inner or the outer peaks are visible. If and how precisely the peaks are visible depends on the STM tip, stable tunneling conditions and the exact tip position on the cluster during the measurement. In Figure 6.59 the position of the peaks at – 1 V and 1 V for Ag_{309} clusters are marked by the red dashed lines. In Figure 6.61 STS spectra of Ag_{309} and Ag_{923} clusters are shown. The position of the inner peaks at – 1 V and 1 V for Ag_{309} and at – 0.5 V and 1 V for Ag_{923} is clearly visible. This means, that the distance of the peaks equals 2.0 eV for Ag_{309} and 1.5 eV for Ag_{923}.

There are different possible explanations for the existence of the observed peaks. One explanation is the so called Coulomb staircase due to charging effects as presented in section 2.1.4 for free Al clusters [56]. Coulomb charging effects are induced by the presence of two tunneling barriers, which might characterize the tip-cluster-surface system (see Figure 6.60). In [227, 228, 229] the two-barrier tunneling junction is decribed theoretically as a series of two resistor-capacitor pairs. The different energies of different charge states of the cluster lead to a stepwise increment of the current as a function of the bias voltage.

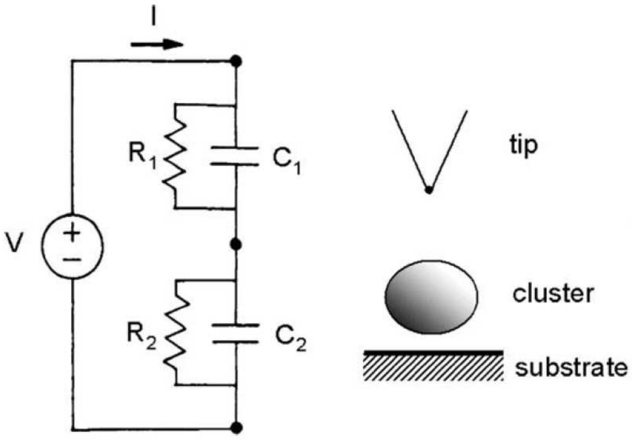

Figure 6.60: Cicuit diagram of a double barrier tunneling junction (left) and STM setup (right). R_1 and C_1 correspond to the tunneling path between tip and cluster, R_2 and C_2 determine the electron transport from the cluster into the substrate [158].

For free clusters different charge states are due to the emittance of electrons after the photo ionization process. For UPS of clusters on surfaces different charge states were also observed, but due to the coupling to a surface the charge is absorbed by the substrate after a certain time. During the STS process different charge states of clusters occur due to the transport of electrons from the cluster to the tip and into the substrate. In the dI/dV spectra the different charge states are visible as peaks at different voltage values. As shown in [56] the energy difference ΔE_0 of the Fermi edges due to different charge states of clusters is given by

$$\Delta E_0 = \frac{e^2}{4\pi\varepsilon_0 \cdot R}, \qquad (6.11)$$

where e is the elementary charge, ε_0 the electric constant and R the cluster radius. The distance of the Fermi edges visible in UPS measurements roughly corresponds to the distance of peaks in the dI/dV spectra. Due to equation (6.11), the peak distance for small clusters is larger. In [55] ΔE_0 equals 0.66 eV for Al_{2000}^{-} clusters and 0.272 eV for Al_{32000}^{-} clusters. For spherical Ag_{309} clusters with $R = 1.09$ nm, the calculated peak distance ΔE_0 equals 1.32 eV and for spherical Ag_{923} clusters with $R = 1.50$ nm ΔE_0 equals 0.96 eV. The peak distance of measured STS spectra of Ag_{309} and Ag_{923} is 2.0 eV for Ag_{309} and 1.5 eV for Ag_{923}. The deviations might be due to the fact that the geometric and electronic radius of a cluster is not equal [55], but much larger deviations are likely to occur because of using equation (6.11) for an estimation of ΔE_0 which assumes spherical clusters and neglects all cluster-substrate and cluster-tip interactions. There are two other indications for the existence of the peaks being due to Coulomb charging effect. One hint is the gap of zero conductance around the Fermi level, which is visible in nearly all measured STS data. This effect is called Coulomb blockade and reflects the blocked tunneling current for electron energies smaller than the charging energy. The other indication is the observation that in some spectra the inner or outer peaks shift by a constant value relative to the corresponding peaks of another spectrum, so that the distance between the inner or outer peaks remains equal, but the energetic positions are different relative to the other spectrum. This phenomenon is visible by the red and blue colored spectra of Ag_{923} clusters in Figure 6.61 and might be due to an offset charge in the Coulomb-charging picture.

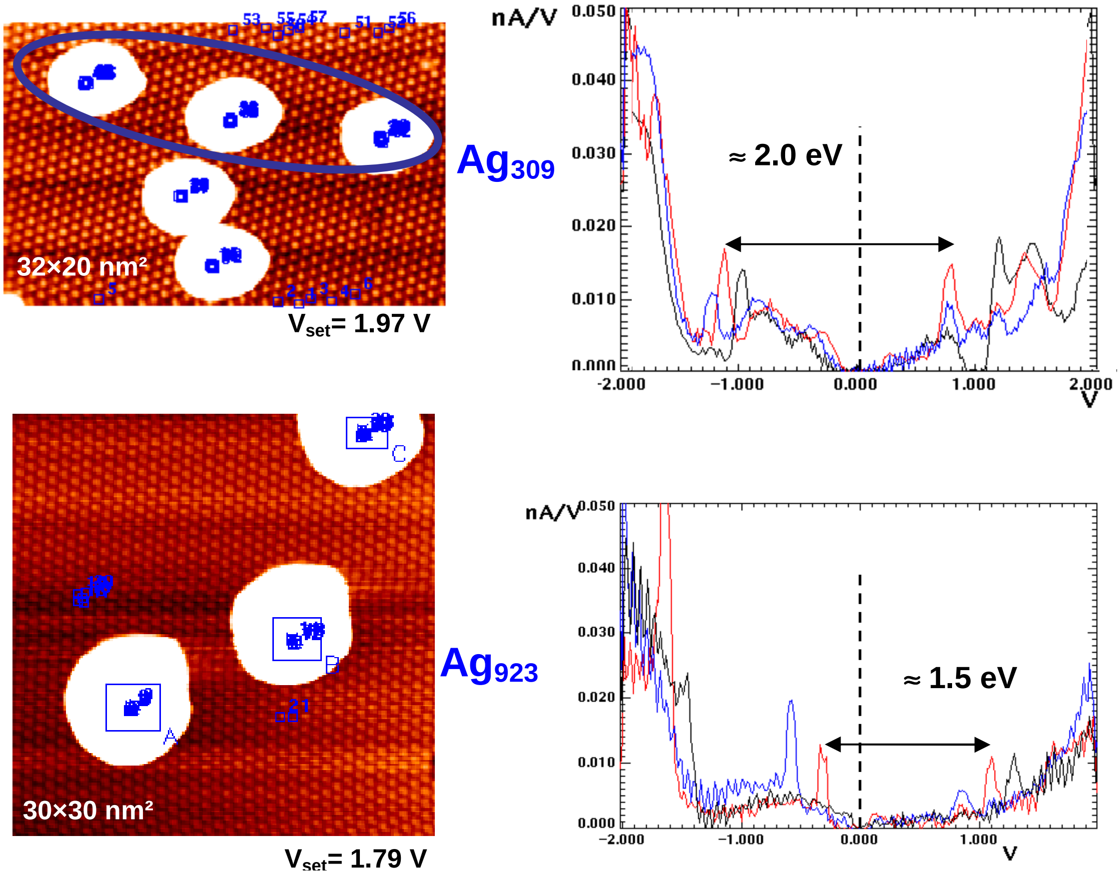

Figure 6.61: STM images and STS spectra of Ag_{309} and Ag_{923}. The peak distance in the STS spectra depends on the clusters radius.

A different interpretation of the observed peaks in the STS data is the assignment to a size-dependent quantization of electronic states within the clusters. As mentioned in chapter 2 clusters have - depending on their size - quantized or bulk-like properties. For clusters with several thousands of atoms the bulk-like properties dominate, which means that single peaks pass into the band structure. The ratio of the radii for Ag_{923} and Ag_{309}, which is the cubic root of the number of atoms, equals 1.4, the ratio of the inner and outer peaks in Figure 6.61 equals 1.3. For the estimation of energy level spacings close to the Fermi energy in Ag_N clusters an upper and lower bound have to be considered [230]. As an upper bound, in the case of highly symmetric particles which can be described by the spherical jellium model (see chapter 2), the multiple degeneracy enlarges the mean level distance. In a simple periodic orbit approach the mean length <L> of classical orbits determines the main shell oscillation periodicity. For a spherical cluster of the radius R one gets <L> = 5.42·R [231], which results in an energy spacing of

$$\Delta E = \frac{\hbar^2 \, k_F \, \pi}{2.71 m_e \, R}, \tag{6.12}$$

where m_e is the electron mass, k_F the Fermi wave vector ($1.20 \cdot 10^{10} \mathrm{m}^{-1}$ for Ag [232]), and $\hbar$ the Planck constant. These main shell closings for high symmetry particles give an upper limit for the observed peak distances.

For particles with low symmetry for non-degenerated electron states the mean energy spacing near the Fermi edge is

$$\delta E = \frac{2\pi^2 \hbar^2}{m \, k_F \, V}, \tag{6.13}$$

where V is the cluster volume. From equation (2.2) and (2.3) follows for the shell structure that $\Delta E \propto 1/N^{1/3}$ and for the spacing of individual energy levels $\delta E \propto 1/N$. This leads to an expansion of the region between the two limits for increasing cluster size, which is demonstrated in Figure 6.62. Because an atomic shell structure is assumed for Ag_{309} and Ag_{923}, the energy level spacing might be expected below but close to the upper bound ΔE. But the smallest energy level spacings observed in the STS data for Ag_{923} of 1.5 eV and for Ag_{309} of 2.0 eV are above the upper bound.

This phenomenon is probably due to the fact that many states of metal clusters are invisible to STS measurements. This also includes peaks with smaller energy level spacings between δE and ΔE. In [233] M. DE MENECH et al. describe the absence of metal cluster states in STS measurements. By means of fully self-consistent quantum transport calculations, using realistic tunneling tips, they show that, depending on the tip shape, only a small fraction of the electronic states contribute to the STS spectra. A more unambiguous characterization of the states on the supported metal clusters could be achieved with energy-resolved images, as it was shown with a theoretical analysis which mimics the experimental imaging procedure. They also report that the tip position on the clusters influences the spectra, as it was also observed in STS spectra measured within this thesis (see Figure 6.63). Additonally to experimental STS results, a theoretical study is necessary and planned for future experiments in order to understand

and classify the observed peaks and features and to characterize the electronic properties of clusters.

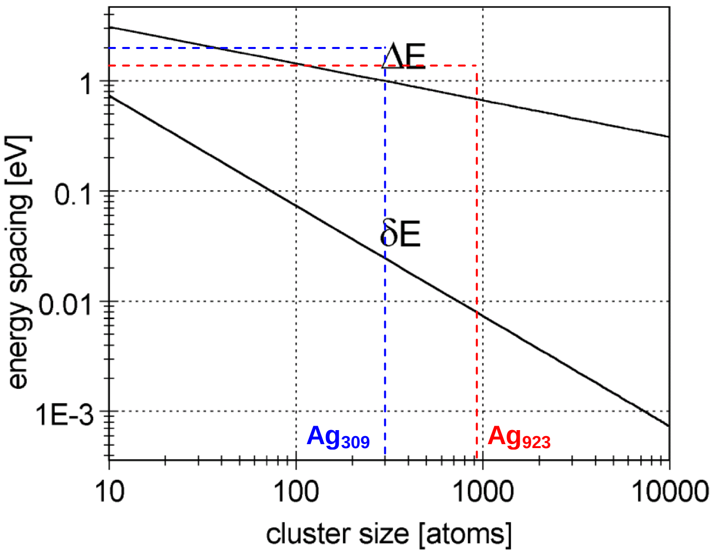

Figure 6.62: Estimated energy level spacing close to the Fermi energy in silver clusters with the upper bound ΔE and the lower bound δE.

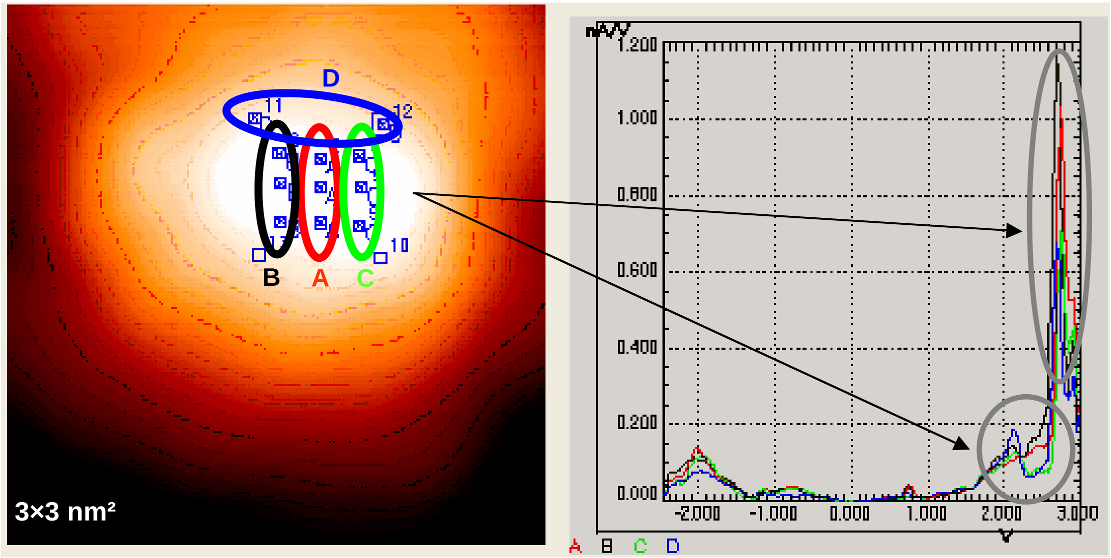

Figure 6.63: STM image of an Ag_{309} cluster on 1ML C_{60}/HOPG. STS spectra were measured on different positions on top of the cluster. STS spectra which were taken in the regions A, B and C, respectively, look equal but have shifts relative to each other (see text).

It is often difficult to assign the peaks in STS spectra of clusters to either Coulomb charging effect or quantization of electron states. One mostly observes indications for both interpretations. In [234] D. C. RALPH et al. observed discrete electronic states in STS data of single Al particles. In contrast, the peaks in STS spectra of oxide-supported silver particles were first assigned to single electron states [235] but later the interpretation was modified and the peaks were attributed to Coulomb charging effects [236]. It is also possible that there exists a combination of both effects which would lead to an even more complex analysis of STS data.

Even if the C_{60} spectra look almost equal, which indicates the same shape of the STM tip, the corresponding Ag_{309} and Ag_{923} spectra sometimes differ from each other. In addition to sharp peaks broader structures were observed in the STS data which might also characterize properties of the cluster-surface system. Due to the cluster-surface interaction a simple jellium model is not sufficient to describe the STS data. It might be possible that the broader structures are due to the combination of Coulomb charging and quantization effects. As it is visible e.g. for the Ag_{309} spectra in Figure 6.61 the sharp peaks shift whereas the broad structures at ≈ -0.5 V remain at the same position. The peak positions depend on the exact position of the STM tip during taking a spectrum. If the tip is not located on the highest point of the cluster, the result often is a spectrum with peaks which are shifted relative to the peaks of a spectrum taken on the highest point of the cluster. This phenomenon is shown in Figure 6.63. It was observed that spectra which were taken on similar cluster positions look equal to each other whereas differences occur for positions with a larger distance to each other. In Figure 6.63 each three spectra located in the regions marked with A, B and C and the two spectra in the region marked with D look equal and were therefore averaged to one spectrum. The four resulting spectra show peak shifts or varying features at the same voltage values.

Another reason for differences in STS spectra of size selected clusters can be the different possible orientations of the clusters relative to the C_{60} film, which influence the electronic structure of the clusters.

In general, the measured spectra of different individual Ag_{309} clusters on C_{60}/HOPG look very similar to each other, as it was expected for size selected clusters. In particular this is the case for stable STM tip conditions, as monitored by C_{60} spectra taken in between (see e.g. Figure 6.66 left column). For comparison STS spectra of non size selected clusters which were taken formerly in Dortmund [237] are much less identical, even if their height is similar. STS spectra of Ag_{923} clusters are also similar to each other, but are less identical than STS spectra of Ag_{309} clusters. This might be due to the fact that Ag_{923} clusters have more isomers than Ag_{309} and the number of atoms after mass selection is more precise for $Ag_{309(\pm 3)}$ than for $Ag_{923(\pm 9)}$. Additionally it is more difficult to get stable tunneling conditions for Ag_{923} due to their large height in comparison to Ag_{309}. The contact with the STM tip or the displacement of Ag_{923} clusters by the tip could lead to a destruction or deformation of the clusters. Systematic deviations between STS spectra taken on clusters/1 ML C_{60} and clusters/2 ML C_{60} were not observed. For both Ag_{309} and Ag_{923} more STS spectra on 1 than on 2 ML C_{60} were measured. This is due to the fact that the tunneling conditions were often better for clusters on 1 ML C_{60}/HOPG than for clusters on 2 ML C_{60}/HOPG, probably due to another coupling of metal clusters to 1 ML C_{60}/HOPG. This behavior depends strongly on the condition of the STM tip. However, the quality of the Ag_{309} and Ag_{923} spectra on 2 ML C_{60} is better compared to spectra taken on 1 ML C_{60}.

As presented in section 2.1.4 UPS spectra of free Cu_{55}, Ag_{55} and Au_{55} clusters [9] show sharp peaks due to closed atomic shells with energy shifts of about 0.5 eV. This is much less than the 1/R-extrapolation of the experimentally observed peak distances for Ag_{923} and Ag_{309} would suggest. The Coulomb charging energy estimated using equation (6.11) to 2.36 eV with R = 0.61 nm for spherical Ag_{55} clusters. With peak distances of more than 2 eV it would be difficult to collect enough information in the energy range available in STS experiments. However, it might be possible that sharp peaks or broader structures of Ag_{55} clusters are visible in STS spectra and a suppression of peaks [224] will not occur. STS spectra of clusters with the metastable cluster size of 1.5 nm height on C_{60}/Au(111) could also be very interesting. Due to the fact that the height distribution of these clusters is extremely narrow, which hints to the same binding orientations relative to the C_{60}, it is possible that STS spectra of the metastable clusters might be even more identical than STS spectra of Ag_{309} and Ag_{923}. Due to the fact that the metastable clusters decay at RT, but are stable at 77 K and at 5 K, the measurement of STS spectra should be possible.

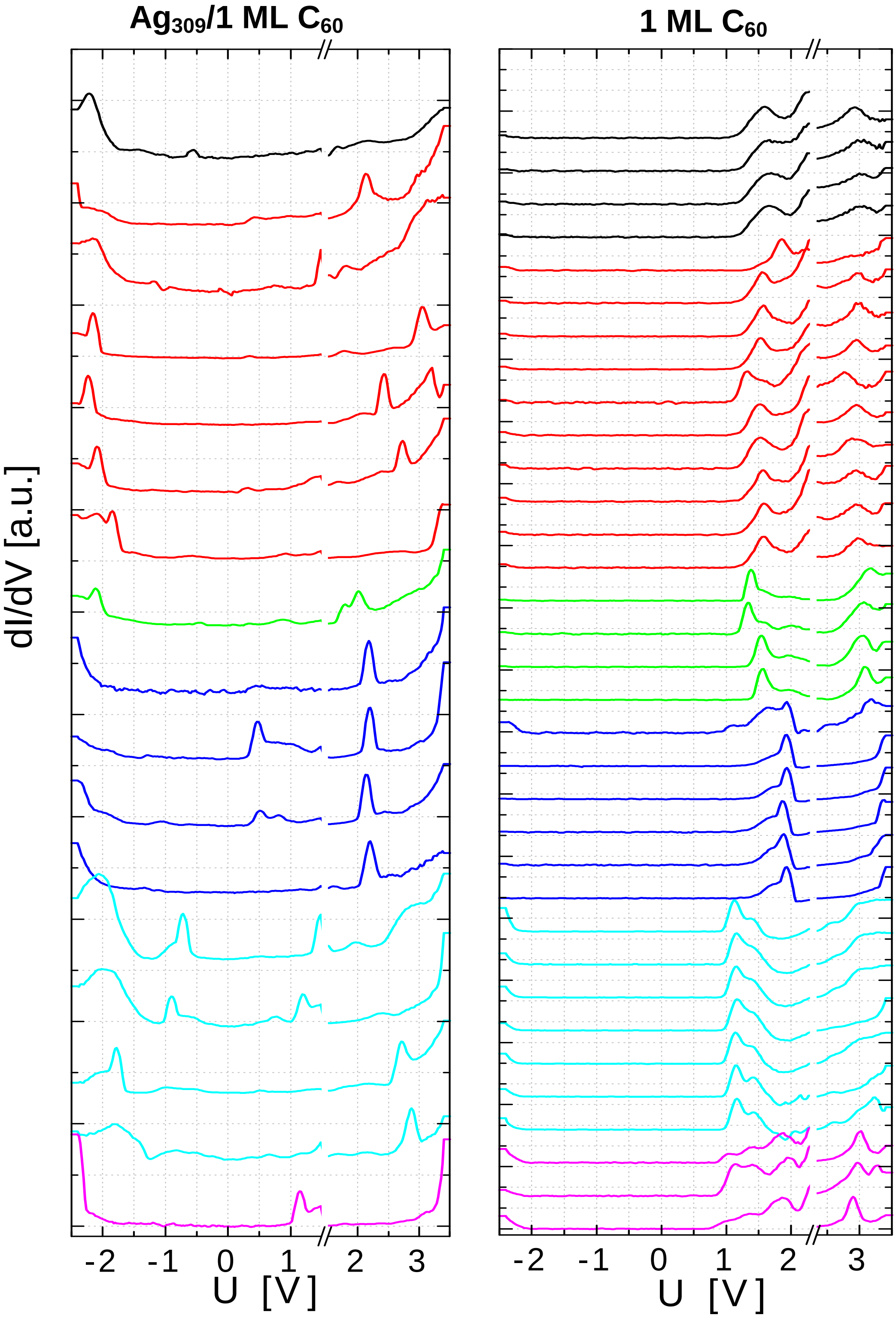

Figure 6.64: STS spectra of Ag_{309} on 1 ML C_{60} and STS spectra of 1 ML C_{60}, measured as a reference. The spectra were normalized in order to emphasize special features, e.g. peaks. The break of the x-axis denotes a different normalization right and left from the break. Spectra which have identical colors were measured with the same tip shape as monitored by the C_{60} spectra. Different colors are due to different conditions of the STM tip during the measurement. It is striking that also the cluster spectra which were measured with the identical tip shape are very similar to each other.

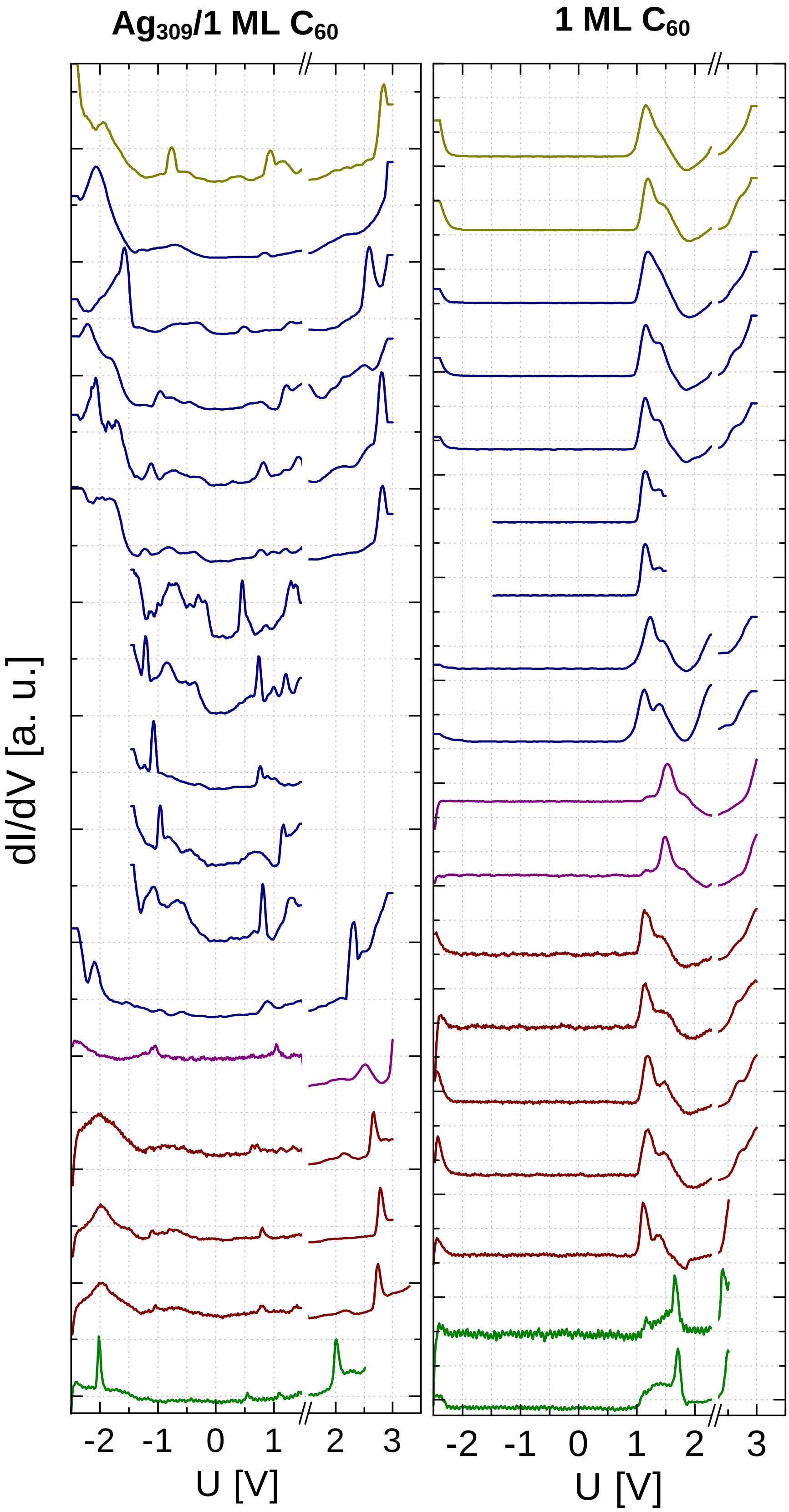

Figure 6.65: STS spectra of Ag_{309} on 1 ML C_{60} and STS spectra of 1 ML C_{60}, measured as a reference (see Figure 6.64).

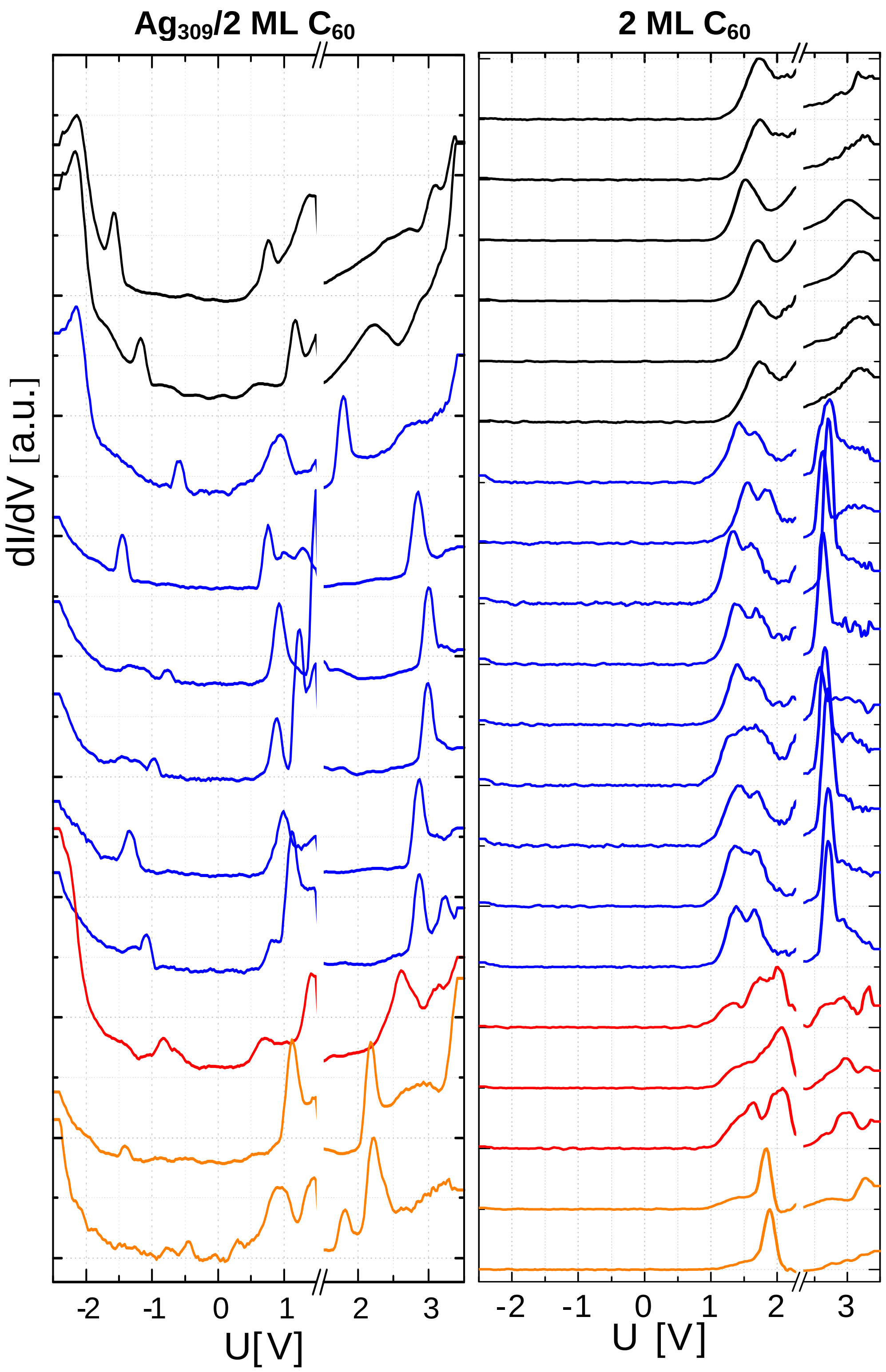

Figure 6.66: Normalized STS spectra of Ag$_{309}$ on 2 ML C$_{60}$ and STS spectra of 2 ML C$_{60}$, measured as a reference. Identical colors represent the same shapes of the STM tip as monitored by the C$_{60}$ spectra.

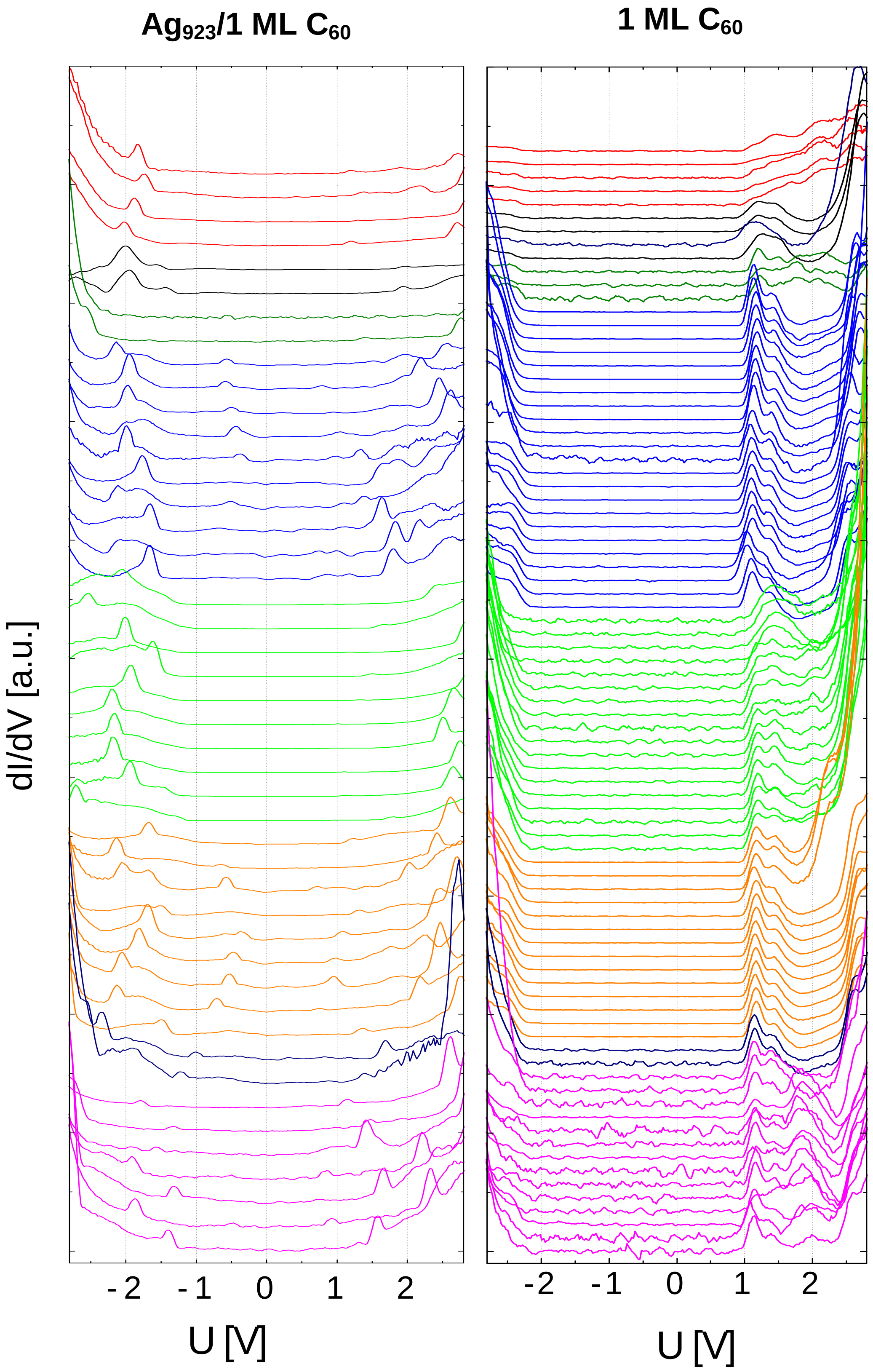

Figure 6.67: Normalized STS spectra of Ag_{923} on 1 ML C_{60} and STS spectra of 1 ML C_{60}, measured as a reference. Identical colors represent the same shapes of the STM tip as monitored by the C_{60} spectra.

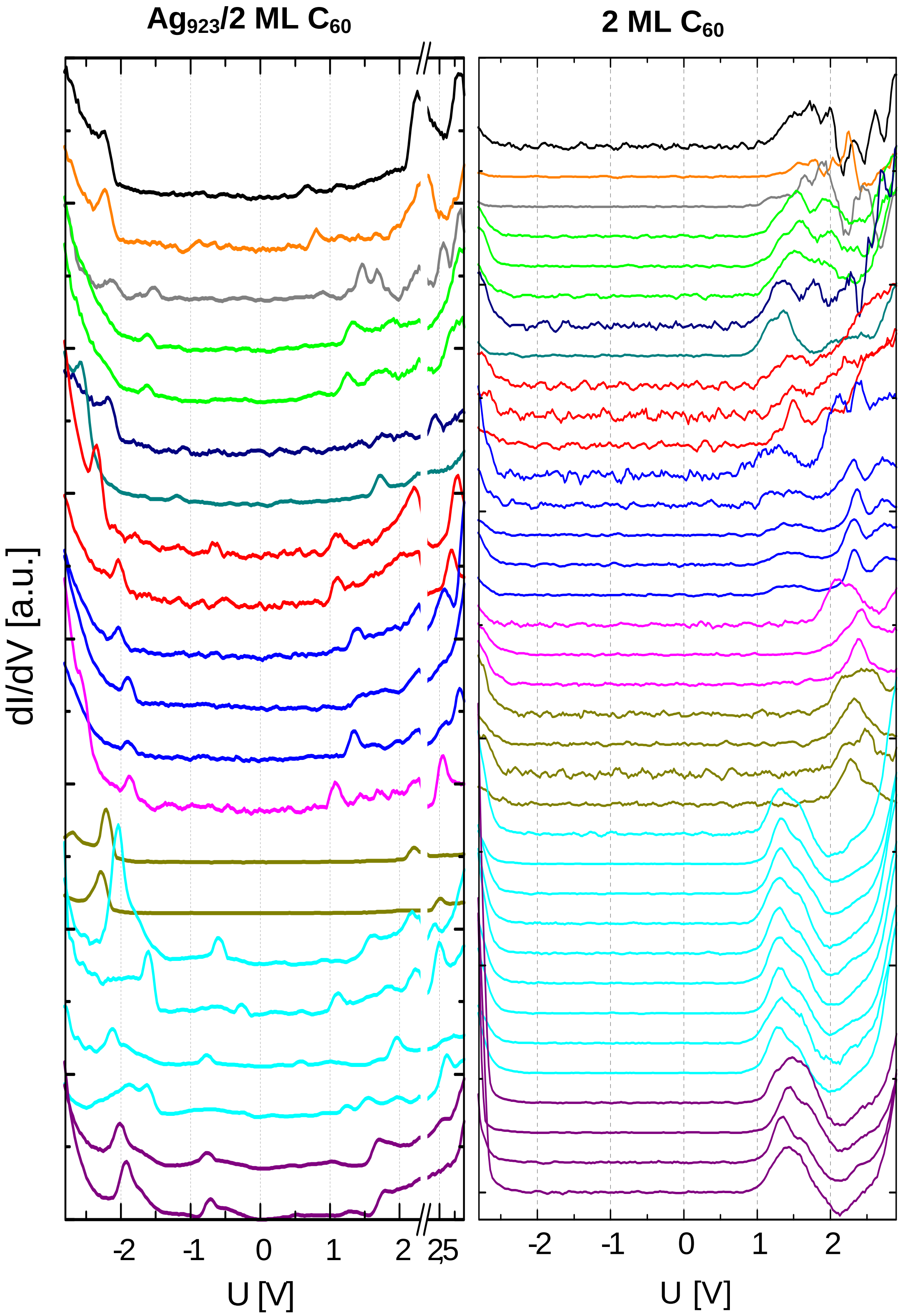

Figure 6.68: Normalized STS spectra of Ag$_{923}$ on 2 ML C$_{60}$ and STS spectra of 2 ML C$_{60}$, measured as a reference. Identical colors represent the same shapes of the STM tip as monitored by the C$_{60}$ spectra.

6.6 UPS spectra of size selected Ag clusters

In order to get information about the electronic properties of size selected Ag clusters, additionally to STS spectra UPS spectra were taken. Theoretical and experimental details about this technique are described in section 4.3. In contrast to STS which allows the study of the electronic structure of a single cluster, UPS yields spectra which average the electronic structure of all Ag clusters within the measurement spot of 1 mm².

6.6.1 UPS of Ag_{55} and Ag_{923}/C_{60}/HOPG

Within this thesis several sample systems are used for UPS measurements. Due to the function as a buffer layer and the RT stability of C_{60} surfaces, C_{60} functionalized surfaces are an optimal substrate for the deposition of size selected Ag clusters. For this reason this sample system was used for the first UPS measurements of size selected Ag clusters. Due to the fact that the UPS signal of C_{60} is very strong and shows peaks at the same energy as silver, UPS spectra of Ag clusters on bare HOPG were also measured at low temperatures in further experiments.

In section 2.1.4 UPS spectra of size selected geometrically magic Na clusters in a free beam are shown, which were taken by the group of BERND VON ISSENDORFF in Freiburg. These spectra clearly show the closed atomic shells resulting in a strongly degenerated electronic structure due to their high symmetry, and other spectral features which are typical for size selected clusters. Similar results are expected for UPS spectra of geometrically magic Ag clusters on surfaces. Such spectra are much harder to obtain than spectra of clusters in a free beam. This is due to the fact that the clusters must not coalesce in order to keep the mass selection, but the cluster density should be high enough to get a UPS signal of Ag clusters with reasonable signal to noise ratio.

UPS spectra of grown Ag and Au islands on nanostructured HOPG were measured in Dortmund in former experiments [158, 159]. UPS spectra of Ag and Au islands – here also named “clusters” – are depicted in Figure 6.69.

Similar UPS spectra as shown for $N = 2 \cdot 10^2$ in Figure 6.69 (left) were expected for size selected geometrically magic Ag clusters. Before the deposition of Ag clusters UPS spectra of the sample substrate were taken which later were subtracted from the UPS signal of Ag clusters on the substrate. Figure 6.70 shows four UPS spectra taken within this thesis of bulk Au(111) and 1 ML C_{60}/Au(111) at 165 K as well as bare HOPG and 3 ML C_{60}/HOPG at RT. 1 ML C_{60}/Au(111) is sufficient to cover the whole Au(111) surface, whereas for HOPG 3 ML are needed to avoid free HOPG areas due to the different growth of C_{60} on Au(111) or HOPG. The UPS spectra of Au(111) and C_{60}/Au(111) were taken at 165 K, the spectrum of HOPG at 100 K and the spectrum of C_{60}/HOPG at RT. The spectra were taken by employing He I radiation with $h\nu = 21.2$ eV.

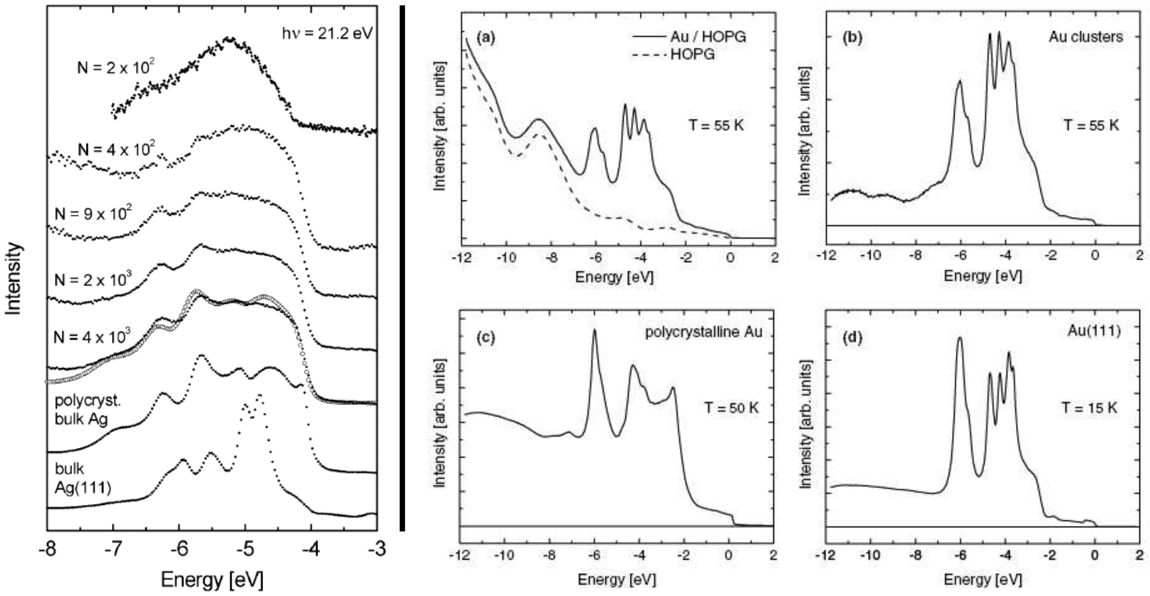

Figure 6.69: Left: solid dots: UPS spectra of Ag clusters for different cluster sizes given as the mean number N of atoms in one cluster and of polycrystalline bulk Ag and an Ag(111) bulk crystal. Open dots: calculated curve corresponding to clusters with N = 4·10^3 atoms [159]. Right: (a) UPS spectra of the Au d band structure with about 1.3 ML evaporated Au. Solid curve: measured spectrum of the cluster sample. Dashed curve: spectrum of the bare HOPG substrate. (b) Difference signal of the two spectra in (a). (c) UPS signal of a polycrystalline gold sample. (d) UPS signal of a Au(111) single crystal [158].

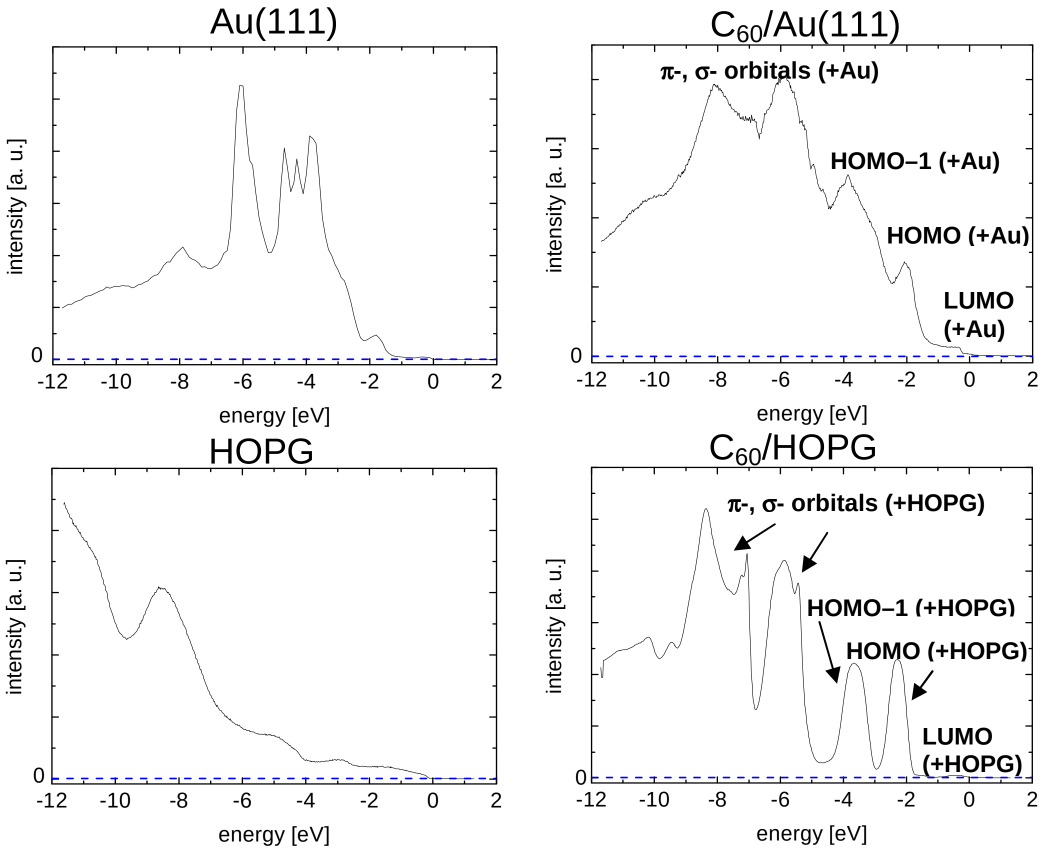

Figure 6.70: UPS spectra of Au(111), 1 ML C_{60}/Au(111), HOPG and 3 ML C_{60}/HOPG. The UPS spectrum of Au(111) shows the typical d band, the spectra of C_{60} clearly show the different occupied orbitals.

UPS spectra of C_{60}/Au(111) [238, 239] and C_{60}/HOPG [240] are well-known from literature and the UPS spectra taken within this thesis look very similar. In Figure 6.70 and all the following UPS spectra a defect of the UPS electronics which led to shifts in the kinetic energy scale limited the accuracy of the energy to about ± 0.2 eV, which however is not important for the following discussion.

The UPS signal of silver shows a high intensity at an energy of –5 eV (see Figure 6.69 left). Unfortunately the π- and σ-orbitals of C_{60} show a high intensity in UPS spectra also at $E \approx -5$ eV and the measurements showed that the signal of Ag clusters on C_{60} was not detectable. A larger intensity of Ag could be obtained by increasing the number of deposited Ag clusters. But in order to avoid coalescence, the number of deposited Ag clusters should not be too high. A coverage of $I_{cluster} \cdot t_{depo} = 600$ pAmin was deposited, which is three times of the ‘normal’ number of Ag clusters (see subsection 5.3.1.2, equation (5.1)) which already leads to coalescence in the deposition center. But even with this coverage no UPS spectra of Ag_{55}/1 ML C_{60}/Au(111) or Ag_{923}/3 ML C_{60}/HOPG could be measured due to the strong UPS signal of C_{60}.

6.6.2 UPS of Ag_{55} and Ag_{923}/HOPG

Due to the fact that the UPS signal of Ag clusters on C_{60} was not visible Ag_{923} and within a second experiment Ag_{55} clusters were deposited on bare HOPG at low temperatures with $I_{cluster} \cdot t_{depo} = 600$ pAmin and a deposition energy of $E \approx 0.02$eV/atom in order to guarantee soft landing. Ag clusters are extremely mobile on HOPG and coalesce at RT. The deposition at low temperatures should hinder the diffusion and thus the coalescence of the clusters. First UPS spectra of bare HOPG were taken and later subtracted from the Ag_N/HOPG signal in order to get the UPS signal of Ag_N clusters. The spectra of Ag_{923}/HOPG were taken at 100 K, the spectra of Ag_{55}/HOPG at 50 K. Below 50 K contamination of the sample due to the adsorption of residual gas was visible with UPS. The UPS spectra of Ag_{923}/HOPG, Ag_{923}, Ag_{55}/HOPG and Ag_{55} are depicted in Figure 6.71 and Figure 6.72.

The spectra were taken at different sample positions. At some positions the Ag_{923} and Ag_{55} clusters could be identified which is clearly visible in Figure 6.71 and Figure 6.72. The Ag clusters are visible by a broad shoulder in the HOPG spectrum for low coverage or for higher coverages by a structure which is similar to the d band of bulk silver. The shape of the spectra varies depending on the cluster density. Remembering the UPS spectra measured for grown Ag islands of different sizes [158, 159] (see Figure 6.69), several Ag_{55} and Ag_{923} spectra are similar to the spectra measured for Ag islands with about 200 and 900 atoms, respectively. But some spectra are very similar to spectra of Ag islands with much more atoms, which lets assume that especially in the deposition center the Ag_{55} and Ag_{923} clusters might be coalesced on the bare HOPG substrate in spite of the low temperature of 50 K and 100 K, respectively. The spectra of Ag_{55} and Ag_{923}, visible within the waterfall diagrams (Figure 6.71 and Figure 6.72) represent an increasing cluster density from top to bottom. The four Ag_{923} spectra (blue, light blue, pink and yellow colored in Figure 6.71), were probably measured at positions with no or only a few Ag clusters which might be considered during the interpretation of the spectra.

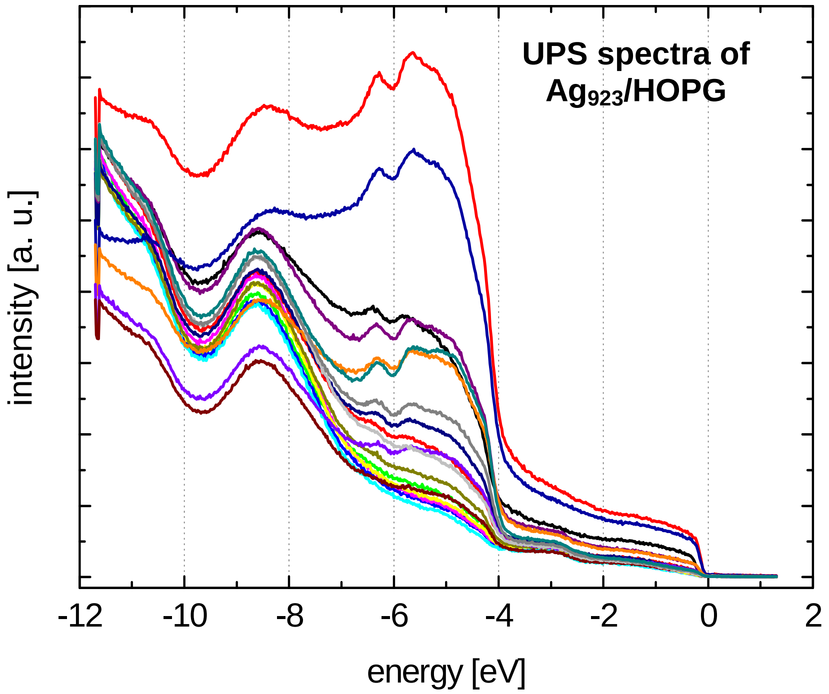

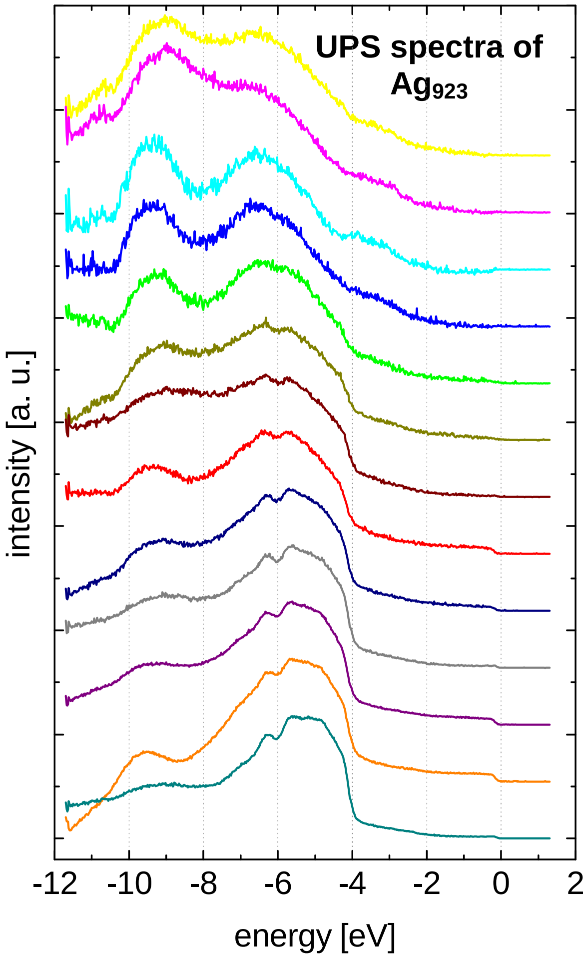

Figure 6.71: UPS spectra of Ag_{923}/HOPG (as measured) and Ag_{923} (HOPG spectra substracted and normalized) taken at 100 K. Different Ag coverages were observed at different sample positions.

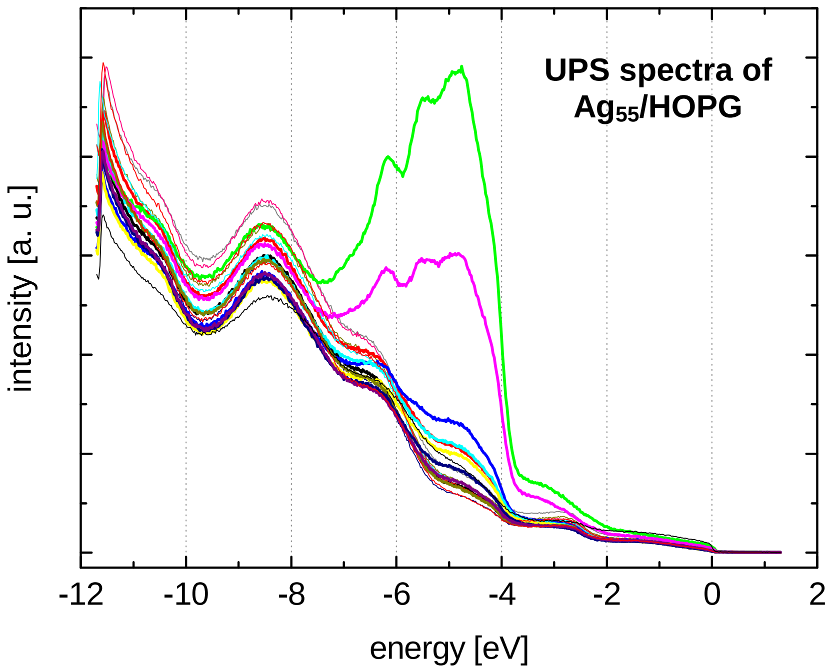

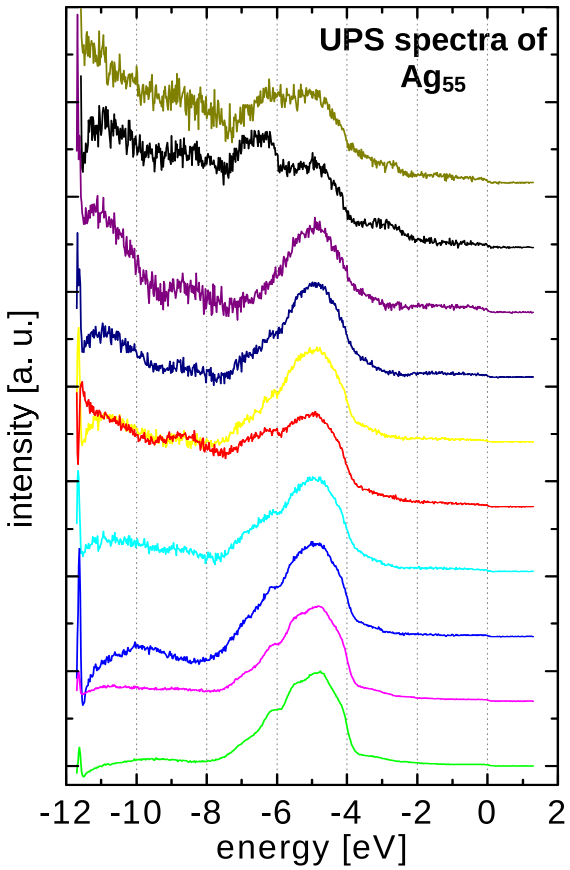

Figure 6.72: UPS spectra of Ag_{55}/HOPG (as measured) and Ag_{55} (HOPG and contamination signal substracted and normalized) taken at 50 K. Different Ag coverages were observed at different sample positions.

An observation, which corroborates the assumption of cluster coalescence in the center of the deposition, is the shift of the Ag signal to larger binding energies for decreasing cluster density, which is particularly visible in the Ag_{923} data. The shift can be explained by the so called “dynamic final state effect”. In the case of free clusters or clusters coupled to a poorly conducting surface, like HOPG, the final state is characterized by the excited photoelectron and the corresponding hole in the cluster. The shift to larger binding energies has its origin in a remaining positive charge on the cluster. The lifetime of the positive charge on the isolated cluster is large compared to other timescales of the experiment. The resulting Coulomb attraction therefore increases the apparent binding energy of the Ag electrons by $\sim e^2/R$ (see equation (6.11)), where R is the cluster radius. If clusters are coupled to a well conducting surface, the lifetime of the remaining charge is smaller due to a stronger charge transfer between cluster and substrate which leads to neutralization of the clusters. Ref [241], [242] and [243] first reported on a final state effect of Ag, Pt, Pd and Au clusters on amorphous carbon. Due to the dependency of the shift on the cluster radius R, the shift is larger for smaller clusters. In the case of the photoemission spectra of Ag_{55} and Ag_{923} clusters, the spectra of Ag_{923} clusters show larger shifts to each other than the spectra of Ag_{55} clusters. This could be an indication that the Ag_{55} clusters coalesced more than the Ag_{923} clusters, probably due to larger mobility on the bare HOPG. A possible reason could be that the deposition energy of Ag_{55} was slightly larger and for Ag_{923} slightly lower than 0.02 eV/atom. After taking UPS spectra of Ag_{55}/HOPG at 50 K, STM images were taken which show that the Ag_{55} clusters indeed coalesced on the bare HOPG substrate.

During the measurement of UPS spectra of Ag_{55} clusters at different sample positions with 1 mm distance to each other it was observed that a large Ag coverage was measured at two positions and much lower coverages at the remaining positions, which is visible in Figure 6.73. Together with the 1 mm diameter of the measurement spot this result corroborates a deposition spot size of about 2 mm.

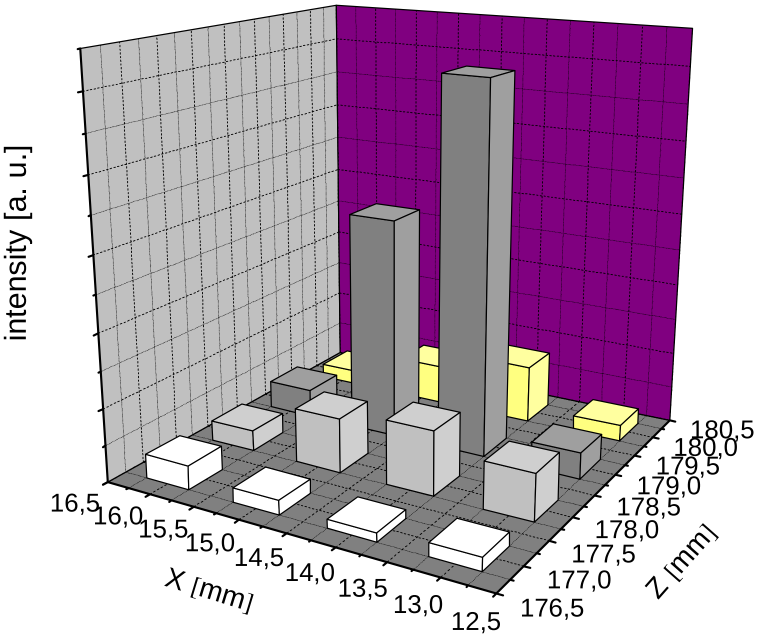

Figure 6.73: 3D plot of the UPS intensity of Ag_{55}/HOPG depending on the sample position.

The spectra of Ag_{55} and Ag_{923} which were shown in this section show qualitatively that it is possible to take UPS spectra of size selected clusters. The spectra do not show features which point to the quantized electronic structure of geometrically magic clusters, but show structures which are similar to those for grown Ag clusters in nanopits which were measured in former experiments in Dortmund. Due to the defect in the UPS electronics the position of the peaks and features in the spectra is approximately right, but not as precise as it would be necessary for a quantitative analysis of size dependent peak shifts e.g. in the d band. In addition the cluster size selection is at least partly lost due to coalescence for the deposition on bare HOPG. To solve the coalescence problem currently Ag_{55} clusters were deposited on 1 ML Xe/HOPG in order to hinder the cluster diffusion and to guarantee an ultra soft landing. STM images showed that the clusters remain separated on 1 ML Xe/HOPG which is an optimal condition for taking UPS spectra of size selected clusters. Contamination of Xe/HOPG due to residual gas adsorption was observed only at temperatures below 40 K so that the spectra can be taken at 40 K.

Figure 6.74 depicts two STM images of Ag_{55}/1 ML Xe/HOPG taken at 5 K. Some clusters in the deposition spot coalesced, but most of the clusters remained separated and have a height of about 1.4 nm, which is in agreement with the height of Ag_{55} measured on 1 ML C_{60}/Au(111).

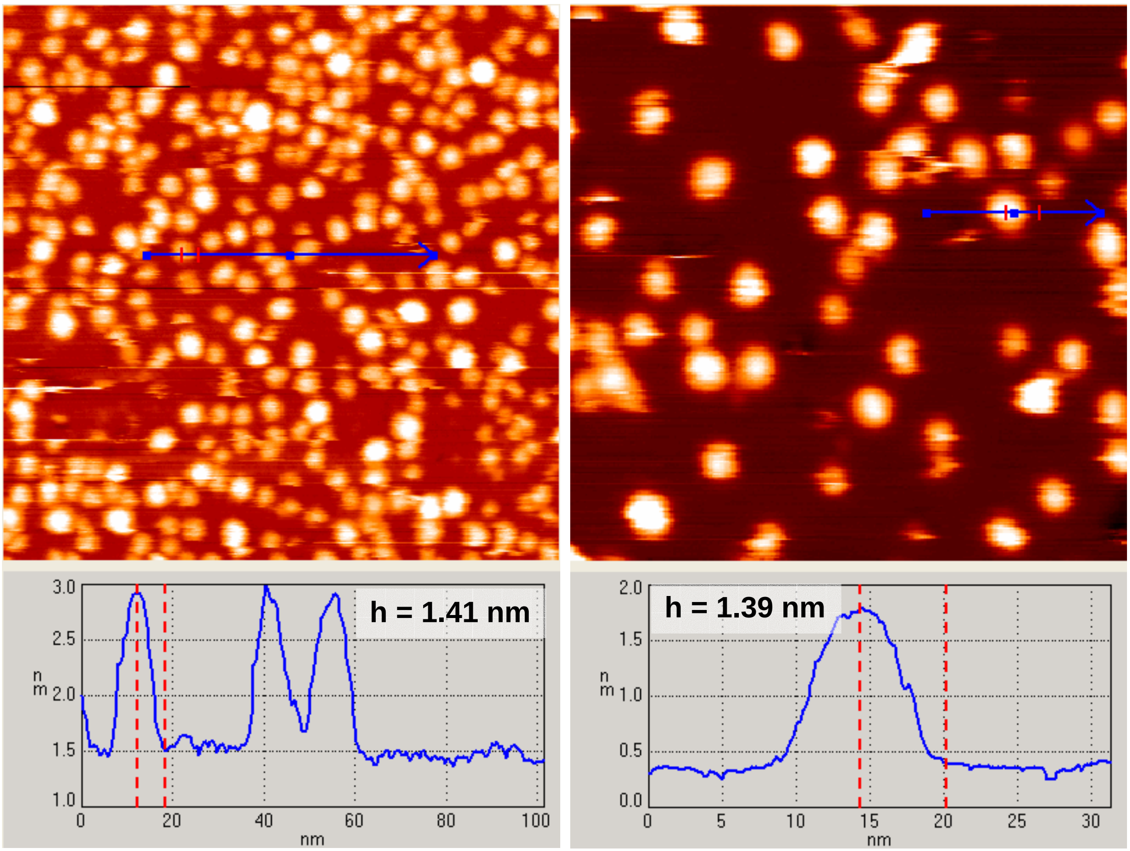

Figure 6.74: 200×200 nm² (left) and 100×100 nm² STM image (right) of Ag_{55}/1 ML Xe/HOPG taken at 5 K.

7 SUMMARY AND OUTLOOK

7.1 Summary

The results presented within this thesis were achieved within the priority program SPP 1153: “Clusters in Contact with Surfaces – Electronic Structure and Magnetism” of the Deutsche Forschungsgemeinschaft (DFG). We collaborated with two groups from Freiburg in order to study geometric and electronic properties of size selected clusters on surfaces: the experimental group of BERND VON ISSENDORFF and MICHAEL MOSELER, who performed molecular dynamics simulations and atomistic calculations. The ambitions concerning the geometrical properties were the stability and thermally induced processes of size selected clusters and a comparison concerning these aspects with grown metal islands. Regarding the electronic properties of size selected clusters one aim was a comparison between UPS spectra of clusters in a free beam and clusters on surfaces. For geometrically magic metal clusters in a free beam UPS spectra showing closed shell structures were taken in the group of BERND VON ISSENDORFF [54, 55, 9].

7.1.1 Setup, sample systems

We deposited size selected geometrically magic Ag_N clusters with an icosahedral shape from Ag_{55} to Ag_{923}, which are very stable due to closed atomic shells (see chapter 2). In comparison to size selected Ag clusters grown Ag and Pb metal islands were investigated.

The Ag_N clusters were produced, mass separated and finally soft landed on surfaces (section 5.3.1.4) with a cluster deposition machine consisting of a magnetron sputter gas aggregation source [98], an acceleration stage and a special time-of-flight mass selector [99] (section 3.1 and 5.3). The size selected Ag_N clusters were investigated with different experimental techniques, namely STM (section 4.1), STS (section 4.2) and UPS (section 4.3).

For the soft landing of the clusters and the production of grown metal islands we used an Au(111) or HOPG surface functionalized with 1 and 2 ordered monolayers of C_{60}. Due to the properties of C_{60}, the fullerenes work as a buffer layer in order to support the soft landing and due to their corrugation period of about 1 nm they hinder the cluster diffusion on the surface. The C_{60} film is long-time stable at RT and decouples the Ag_N clusters electronically from the substrate.

The results for fullerene layers on surfaces were presented in section 6.2. First STM images and properties of C_{58} on HOPG were discussed. C_{58}/HOPG was investigated

within a collaboration with ARTUR BÖTTCHER from Universität Karlsruhe. The observations showed that C_{58} forms fractal-like islands which lead to a very stable network, stabilized by significantly stronger fullerene-fullerene bonds than found for 1 ML C_{60} van der Waals films
The different orientations of C_{60} molecules on Au(111) and HOPG were depicted in subsections 6.2.2 and 6.2.3. It was observed that 1 ML C_{60} molecules on HOPG all have the same orientation, whereas for 2 ML C_{60}/HOPG three different orientations including in-plane orientations of single C_{60} molecules were observed by taking highly resolved STM images at 5 K of occupied and unoccupied C_{60} states. The orientations showed a three-lobe, a dumbbell-like and a bright spherical intramolecular pattern which can be assigned to the hexagons and pentagons of a C_{60} molecule.
For C_{60}/Au(111), three different C_{60} patterns were observed for certain areas of 1 ML C_{60} islands. The three patterns show arrangements of C_{60} molecules with different orientations. The C_{60}(1) surface shows a pattern with both dark and bright molecules representing different C_{60} orientations and is assigned to a $(2\sqrt{3}\times 2\sqrt{3})$ R30° structure, whereas the C_{60}(2) matches the crystallographic directions of the Au(111) units and has a 38×38 unit cell containing 11 C_{60} molecules [143, 188]. C_{60}(3) is organized in a supramolecular $(\sqrt{589}\times\sqrt{589})$ R 14.5° lattice on Au(111) and its unit cell is composed of 49 molecules in (7×7) array [175]. STM images of 1 ML C_{60}/Au(111) at RT taken consecutively at the same sample area within this thesis revealed that the C_{60} molecules change their orientations and rotate at RT [190], whereas at 77 K such effects can be neglected. This observation was important to explain the thermally induced processes of clusters on C_{60}. Due to the dynamics of the C_{60} film at RT the diffusion of clusters might be enhanced.

7.1.2 Softlanding, thermal stability

In subsection 6.3.1 geometrical properties and thermally activated processes of size selected geometrically magic Ag clusters on 1 and 2 ML C_{60} on Au(111) and HOPG were presented. The clusters were deposited at low temperatures because in [165] and [86] it was shown that Ag_N clusters on C_{60}/Au(111) seem to be not stable after RT deposition. Ag_{147}, Ag_{309}, Ag_{561} and Ag_{923} were deposited at 165 K and Ag_{55} at 115 K. The results show that it is possible to land size selected Ag clusters softly on C_{60}/Au(111) and C_{60}/HOPG and to keep the mass selection. After the low temperature deposition a narrow height distribution for every cluster size was observed and for Ag_{55} to Ag_{923} different cluster heights were measured. The measured heights are similar to calculated heights by assuming a spherical shape of the clusters. These heights are slightly higher than the spherical heights, which have to be taken as an upper limit. This difference can be due to different LDOS on the clusters and on the C_{60}. Molecular dynamics calculations by MICHAEL MOSELER, assuming the same parameters as in the experiments, showed that the Ag_N clusters kept their global icosahedral shape after deposition. Only at the interface of clusters and C_{60} there was a small distortion which leads to a denticulation of cluster and C_{60} [146].
Because former experiments indicated a change of the cluster height at RT for Ag_N/1 ML C_{60}/Au(111), the samples were annealed for different time intervals up to RT. During annealing a decrease of the height for Ag_N clusters on 1 ML C_{60} was

observed and after a few hours at RT a metastable cluster size of about 1.5 nm height was observed. After annealing Ag_{309}/1 ML C_{60}/Au(111) for 3 h at RT, a height distribution was observed, which was narrower than the height distribution measured directly after deposition [195]. This is an indication that these metastable clusters not only have the same number of atoms but also the same orientations relative to the C_{60}, which do not has to be the case for Ag_N clusters after deposition. The metastable cluster height was observed after RT annealing of Ag_{55}, Ag_{147}, Ag_{309}, Ag_{561} and in Ref. [165] also of Ag_{923} on 1 ML C_{60}/Au(111) and is due to a decay of the clusters at RT. During RT annealing islands below 1 ML C_{60} with the height of an Ag monolayer were observed which indicated that the Ag material penetrated the C_{60} film. Atomistic calculations by MICHAEL MOSELER revealed a process by which the clusters decay atom-by-atom through the C_{60} film. The penetrating Ag is accompanied by another silver atom that is still in contact with the cluster and at the transition state the bond between the two atoms breaks. After annealing for 12 or more hours at RT it was observed that also the metastable clusters finally penetrated 1 ML C_{60}, so that in the end a network of Ag islands below the C_{60} was visible with STM.
The observations for Ag_{55} were slightly different. After deposition Ag_{55} had a smaller cluster height than 1.5 nm, but nevertheless the metastable cluster size was observed after annealing, together with clusters with heights smaller than Ag_{55} clusters. One explanation for this observation is that the metastable cluster size is formed by Ostwald ripening of Ag_{55} clusters. Another explanation is that some larger clusters were deposited together with Ag_{55} due to a non optimal waiting time τ_W between two acceleration pulses of the mass selector. In this case the metastable cluster size would be formed after annealing of these larger clusters.

Because the height of the metastable cluster size is between the height of Ag_{55} and Ag_{147}, geometrically non-magic clusters between Ag_{55} and Ag_{147} were deposited. Ag_{68} was deposited on 1.2 ML C_{60} and Ag_{80} on 1.1 ML C_{60}. The same height as for Ag_{55} was measured for both Ag_{68} and Ag_{80} after deposition at 165 K [54]. During annealing of Ag_{68} and Ag_{80} on C_{60}/Au(111) the metastable cluster size with 1.5 nm height was visible in the height distributions for clusters on 1 and also on 2 ML C_{60}/Au(111). This behavior indicates thermally induced Ostwald ripening and coalescence of Ag_{68} and Ag_{80} or other geometrically non-magic clusters. It might also be a property of clusters up to a certain size. After annealing for 12 h at RT Ag_{68} and Ag_{80} clusters on 1 ML C_{60} finally decayed and penetrated the C_{60} film, whereas clusters on 2 ML C_{60} grew. Therefore, decay and Ostwald ripening play an important role for Ag_{68} and Ag_{80} on 1 ML C_{60} - Ostwald ripening on a short and decay on a longer timescale.

Additionally to the thermally induced mechanisms for size selected Ag clusters, the thermally activated processes of grown Ag and Pb islands, evaporated at $T < 50$ K, were studied (section 6.4). It was observed that 0.026 ML Ag decayed on 1 ML C_{60} after annealing for 45 min at $T = 165$ K and on 2 ML C_{60} after annealing for 15 min at RT. In contrast, for 0.5 ML Ag on 1 ML C_{60} the islands completely decayed after 45 min at 215 K. A part of the Ag islands on 2 ML C_{60} also decayed, whereas another part grew and stayed stable for 14 d at RT. Evaporating 4 ML Ag on C_{60}/Au(111) showed that Ag islands on 1 ML C_{60} decayed after 45 min at 265 K, whereas the Ag islands on 2 ML C_{60} grew and stayed stable for at least 12 h at RT.

In contrast, evaporating Pb on 1 ML C_{60}/Au(111) at T < 50 K and annealing up to RT showed that Pb islands did not decay, but grew and stayed stable up to 15 h at RT. The different behavior of Ag and Pb on C_{60}/Au(111) is probably due to the fact that the mobility of Pb on C_{60} is large, whereas for Ag islands on C_{60}/Au(111) the Ag-Au(111) interaction dominates.

7.1.3 Spectroscopy

In order to study the electronic properties of size selected clusters STS spectra at 5 K of Ag_{309} and Ag_{923} were taken (section 6.5). The spectra of individual different clusters looked similar to each other as it was expected for size selected clusters. But changes due to different shapes of the STM tip were observed. For this reason STS spectra of C_{60} were taken as a reference. STS spectra of clusters which were taken with the same condition of the STM tip as monitored by the C_{60} spectra showed identical features. Taking STS spectra on different positions on a cluster revealed that the spectra are not only dependent on the STM tip but also on the tip position on the clusters during the STS measurements. Peak shifts occurred for different tip positions on a cluster. The STS spectra of Ag_{309} and Ag_{923} show two characteristic peaks. The distance of the peaks of Ag_{923} and Ag_{309} seems to be proportional to the inverse radii of Ag_{923} and Ag_{309}, and might be due to Coulomb staircase effects, quantized electronic properties or a combination of both interpretations (see section 6.5.1).

In addition to STS spectra, UPS spectra of Ag_{55} and Ag_{923} were taken within this thesis (section 6.6). Due to the fact that the strong UPS signal of C_{60} superposes the UPS signal of Ag clusters, UPS spectra of Ag_{55} and Ag_{923} on bare HOPG were taken at low temperatures. The Ag signal was visible and looked similar to the signal for grown Ag islands on HOPG. For Ag_{923} the so called ‘dynamic final state effect’ was visible by shifts to larger binding energy of the spectra taken for different cluster coverages (section 6.6.2). STM images of Ag_{55}/HOPG revealed that the clusters coalesced. For this reason Ag_{55} was deposited on 1 ML Xe/HOPG. STM images showed that the clusters stayed separated due to the surrounding xenon.

7.2 Outlook

Within future experiments the investigation of electronic and geometric properties of size selected Ag clusters and metal islands and properties of the metastable cluster sizes will continue.

The metastable cluster size will be studied in more detail concerning its geometry, number of atoms and electronic properties. In order to study its exact size, information about its width can be useful. Producing a C_{60} necklace for the study of the width of Ag_{309} by counting the surrounding C_{60} molecules (subsection 6.3.1.2) was not as successful as expected, but may be improved in future experiments. A promising alternative to investigate the width of the metastable cluster size are TEM (Transmission Electron Microscopy) measurements. TEM measurements and the widths of geometrically magic clusters might also reveal information about the geometric shape of Ag clusters on a surface. MD calculations showed that the global icosahedral shape is kept after deposition, but an additional flattening of the clusters on the surface is possible due to cluster-surface interactions.

Another experiment which will help to understand the thermally activated processes of size selected clusters is the low temperature deposition of Ag_{55} on 1 and 2 ML C_{60}/Au(111) followed by a detailed annealing and STM study. The deposition of Ag_{55} on only 1 ML C_{60} and annealing for 3 h at RT (subsection 6.3.1.1) raised the question, whether the thermally activated instability of Ag_{55} can be compared to the thermally activated Ostwald ripening of Ag_{68} and Ag_{80} or if annealed Ag_{55} clusters show similarities to other geometrically magic clusters after annealing. In this context the deposition and thermally activated processes for larger geometrically non-magic clusters are interesting in order to observe more details about the differences of geometrically magic and non-magic as well as smaller and larger clusters.

For the comparison between size selected Ag clusters and grown Ag islands future investigations of Ag islands on C_{60}/HOPG are an interesting topic. If the Ag-Au(111) interaction is the decisive factor for the decay, we expect that Ag islands on 1 ML C_{60}/HOPG do not decay due to the weak Ag-HOPG interaction but show coalescence and Ostwald ripening. Because Pb islands on 1 ML C_{60}/Au(111) did not decay after annealing (subsection 6.4.2), the growth of other kinds of metal islands on C_{60}/Au(111) can give information about metal-Au(111) and metal-C_{60} interactions.

Further STS and UPS spectra of size selected Ag clusters will be taken in order to obtain information about the electronic structure. The observation of electronic closed shell structures of deposited geometrically magic Ag clusters would be an important result for the use of cluster-specific properties on surfaces. But also charging effects like Coulomb staircase, dynamic final state effect or transport of single electrons will be investigated in more detail. It is expected that STS and UPS studies of the metastable cluster size, which occurred after annealing Ag_{147}, Ag_{309}, Ag_{561} and Ag_{923}, look even more similar than spectra of deposited size selected clusters, because the narrow height distribution of these cluster size indicates that the clusters not only have the same number of atoms but also the same orientation relative to the C_{60} and therefore even more similar electronic properties.

For UPS measurements size selected Ag clusters will be deposited on HOPG functionalized with rare gases in order to keep the mass selection, which was not given for the low temperature deposition of Ag clusters on bare HOPG. By desorbing the rare gas layer after the cluster deposition a rare gas necklace might be produced which can help to define the width of the clusters [196]. By desorbing the rare gas an ultra soft landing on HOPG can be achieved.

The deposition of size selected Ag clusters on C_{60}/Ag(111) will be interesting for collaborations with theoretical groups because only two different materials have to be modeled. The decay mechanism of Ag_N clusters or metal islands on C_{60}/Ag(111) can be compared with the results achieved within this thesis for Ag_N and metal islands on C_{60}/Au(111). The comparison of STS spectra of Ag_N clusters measured in Dortmund with calculated STS spectra of Ag_N clusters within a future collaboration may help to understand the observed peaks and features and to reveal more information about the electronic structure.

Due to the fact that a buffer layer like C_{60} is useful to decouple the clusters from the substrate, it is planned to replace C_{60} by oxide layers or self-assembled monolayers (SAMs) and to study the thermally activated mechanisms and properties of Ag_N clusters on these kinds of samples.

At long sight, depositions with another kind of cluster material are planned. Due to the fact that Pb islands on 1 ML C_{60}/Au(111) are stable after annealing, thermally activated processes of size selected Pb clusters on C_{60}/Au(111) are interesting, but also other metals like Au, Cu, Pt or Na will be considered, especially for the comparison with UPS spectra of size selected clusters in the free beam taken in Freiburg.

Cluster assembled materials are of great impact for future applications. Particularly size selected clusters with tailored properties can be used for different purposes. The RT stability of these materials is a necessary condition because most processes and technical applications need materials which are long-time stable at RT. For this reason the investigation of geometric and electronic properties of supported size selected clusters and the RT stability of these systems is of great promise for progress in science and technology.

8 APPENDIX

8.1 Overview about deposition parameters and annealing steps

8.1.1 Deposition of Ag_N / C_{60} / Au(111)

8.1.1.1 Deposition of Ag_{55} / 1 ML C_{60} / Au(111)

DEPOSITION PARAMETERS	
Deposition time	20 min
Cluster current before deposition	10 pA
Deposition temperature	115 K
τ_w	100
U_{Bias}	–15 V

ANNEALING STEPS	
1st annealing step	3 h RT

8.1.1.2 Deposition of Ag_{309} / 1 ML C_{60} / Au(111)

DEPOSITION PARAMETERS	
Deposition time	5 min
Cluster current before deposition	30 pA
Deposition temperature	165 K
τ_w	17
U_{Bias}	0 V

ANNEALING STEPS	
1st annealing step	45 min 215 K
2nd annealing step	45 min 265 K
3rd annealing step	10 min RT
4th annealing step	25 min RT
5th annealing step	45 min RT
6th annealing step	90 min RT
7th annealing step	180 min RT

8.1.1.3 Deposition of Ag_{561} / 1 ML C_{60} / Au(111)

DEPOSITION PARAMETERS	
Deposition time	10 min
Cluster current before deposition	16 pA
Deposition temperature	165 K
τ_w	17
U_{Bias}	0 V

ANNEALING STEPS	
1st annealing step	45 min 215 K
2nd annealing step	45 min 265 K
3rd annealing step	45 min RT
4th annealing step	15 h RT

8.1.1.4 Deposition of Ag_{147} / 1.3 ML C_{60} / Au(111)

DEPOSITION PARAMETERS	
Deposition time	60 min
Cluster current before deposition	3 pA
Deposition temperature	165 K
τ_w	20
U_{Bias}	–10 V

ANNEALING STEPS	
1st annealing step	45 min 265 K
2nd annealing step	15 min RT
3rd annealing step	45 min RT
4th annealing step	90 min RT
5th annealing step	180 min RT
6th annealing step	3 h RT
7th annealing step	12 h RT

8.1.1.5 Deposition of Ag_{309} / 1.7 ML C_{60} / Au(111)

DEPOSITION PARAMETERS	
Deposition time	27 min
Cluster current before deposition	7 pA
Deposition temperature	165 K
τ_w	25
U_{Bias}	0 V

ANNEALING STEPS	
1st annealing step	45 min 215 K
2nd annealing step	45 min 265 K
3rd annealing step	10 min RT
4th annealing step	25 min RT
5th annealing step	35 min RT
6th annealing step	3 h RT
7th annealing step	12 h RT
8th annealing step	33.5 h RT

8.1.1.6 Deposition of Ag_{68} / 1.2 ML C_{60} / Au(111)

DEPOSITION PARAMETERS	
Deposition time	40 min
Cluster current before deposition	8 pA
Deposition temperature	165 K
τ_w	35
U_{Bias}	+12 V

ANNEALING STEPS	
1st annealing step	45 min 265 K
2nd annealing step	15 min RT
3rd annealing step	45 min RT
4th annealing step	3 h RT
5th annealing step	9 h RT
6th annealing step	33 h RT

8.1.1.7 Deposition of Ag_{80} / 1.1 ML C_{60} / Au(111)

DEPOSITION PARAMETERS	
Deposition time	12.5 min
Cluster current before deposition	16.5 pA
Deposition temperature	165 K
τ_w	35
U_{Bias}	–2 V

ANNEALING STEPS	
1st annealing step	45 min RT
2nd annealing step	12 h RT

8.1.2 Deposition of Ag_N / C_{60} / HOPG

8.1.2.1 Deposition of Ag_{147} / C_{60} / HOPG

DEPOSITION PARAMETERS	
Deposition time	15 min
Cluster current before deposition	13 pA
Deposition temperature	RT
τ_w	20
U_{Bias}	–20 V

NO ANNEALING

8.1.2.2 Deposition of Ag_{309} / C_{60} / HOPG

DEPOSITION PARAMETERS	
Deposition time	2 min
Cluster current before deposition	8.3 pA
Deposition temperature	165 K
τ_w	20
U_{Bias}	0 V

ANNEALING STEPS	
1st annealing step	45 min 265 K
2nd annealing step	15 min RT
3rd annealing step	45 min RT
4th annealing step	3 h RT
5th annealing step	12 h RT

8.1.2.3 Deposition of Ag_{923} / C_{60} / HOPG

DEPOSITION PARAMETERS	
Deposition time	25 min /18 min / 42 min
Cluster current before deposition	7.5 pA / 11.7 pA / 14.3 pA
Deposition temperature	RT
τ_w	15
U_{Bias}	0 V

NO ANNEALING

8.1.3 Deposition of Ag_N / HOPG

8.1.3.1 Deposition of Ag_{55} / HOPG

DEPOSITION PARAMETERS	
Deposition time	50 min
Cluster current before deposition	12 pA
Deposition temperature	50 K
τ_w	100
U_{Bias}	–7 V

NO ANNEALING

8.1.3.2 Deposition of Ag_{923} / HOPG

DEPOSITION PARAMETERS	
Deposition time	52 min
Cluster current before deposition	11.5 pA
Deposition temperature	140 K
τ_w	15
U_{Bias}	0 V

NO ANNEALING

8.1.4 Growth of metal islands / C_{60} / Au(111)

8.1.4.1 Growth of 0.026 ML Ag / 1.3 ML C_{60} / Au(111)

DEPOSITION PARAMETERS	
Deposition time	28.6 sec
Deposition temperature	< 50 K
$I_{emission}$	8 mA
I_{flux}	12 nA
$I_{filament}$	1.7 A
U_{bias}	700 V

ANNEALING STEPS	
1st annealing step	77 K (STM)
2nd annealing step	45 min 165 K
3rd annealing step	15 min RT
4th annealing step	3 h RT

8.1.4.2 Growth of 0.5 ML Ag / 1.3 ML C_{60} / Au(111)

DEPOSITION PARAMETERS	
Deposition time	17 min 52 sec
Deposition temperature	< 50 K
$I_{emission}$	8 mA
I_{flux}	12 nA
$I_{filament}$	1.7 A
U_{bias}	700 V

ANNEALING STEPS	
1st annealing step	77 K (STM)
2nd annealing step	45 min 165 K
3rd annealing step	45 min 215 K
4th annealing step	15 min RT
5th annealing step	45 min RT
6th annealing step	3 h RT
7th annealing step	12 h RT
8th annealing step	14 d RT

8.1.4.3 Growth of 4 ML Ag / 1.3 ML C_{60} / Au(111)

DEPOSITION PARAMETERS	
Deposition time	2 h 22 min 54 sec
Deposition temperature	< 50 K
$I_{emission}$	8 mA
I_{flux}	12 nA
$I_{filament}$	1.7 A
U_{bias}	700 V

ANNEALING STEPS	
1st annealing step	77 K (STM)
2nd annealing step	45 min 165 K
3rd annealing step	45 min 215 K
4th annealing step	45 min 265 K
5th annealing step	15 min RT
6th annealing step	45 min RT
7th annealing step	3 h RT
8th annealing step	12 h RT
9th annealing step	45 min 335 K

8.1.4.4 Growth of 0.04 ML Pb / 1 ML C_{60} / Au(111)

DEPOSITION PARAMETERS	
Deposition time	90 sec
Deposition temperature	< 50 K
$I_{emission}$	2.75 mA
I_{flux}	10 nA
$I_{filament}$	1.7 A
U_{bias}	610 V

ANNEALING STEPS	
1st annealing step	77 K (STM)
2nd annealing step	45 min 115 K
3rd annealing step	45 min 165 K
4th annealing step	45 min 215 K
5th annealing step	45 min 265 K
6th annealing step	45 min RT
7th annealing step	15 h RT

9 REFERENCES

[1] C.R. Henry,
Surface studies of supported model catalysts,
Surf. Sci. Rep. **31**, 231 (1998)

[2] U. Heiz and E. Bullock,
Fundamental aspects of catalysis on supported metal clusters,
J. Mater. Chem. **14**, 564 (2004)

[3] W. Lu and C. M. Lieber,
Nanoelectronics from the bottom up,
Nature Materials **6**, 841 (2007)

[4] J. van Lith, A. Lassesson, S. A. Brown, M. Schulze, J. G. Partridge, and A. Ayesh,
A hydrogen sensor based on tunneling between palladium clusters,
Appl. Phys. Lett. **91**, 181910 (2007)

[5] J. Bansmann et al.,
Magnetic and structural properties of isolated and assembled clusters,
Surf. Sci. Rep. **56**, 189 (2005)

[6] Chenyong Ju, Dieter Suter, and Jiangfeng Du,
Two-qubit gates between noninteracting qubits in endohedral-fullerene-based quantum computation,
Phys. Rev. A **75**, 012318 (2007)

[7] Dieter Suter and Kyungwon Lim,
Scalable architecture for spin-based quantum computers with a single type of gate,
Phys. Rev. A **65**, 052309 (2002)

[8] DFG priority program SPP 1153
"*Clusters in Contact with Surfaces – Electronic Structure and Magnetism*":
http://www.physik.uni-rostock.de/spp1153

[9] Hannu Häkkinen, Michael Moseler, Oleg Kostko, Nina Morgner, Margarita Astruc Hoffmann, and Bernd von Issendorff,
Symmetry and Electronic Structure of Noble-Metal Nanoparticles and the Role of Relativity,
Phys. Rev. Lett. **93**, 093401 (2004)

[10] S. Helveg, C. López-Cartes, J. Sehested, P. L. Hansen, B. S. Clausen, J. R. Rostrup-Nielsen, F. Abild-Pedersen, and J. K. Nørskov,
Atomic-scale imaging of carbon nanofibre growth,
Nature **427**, 426 (2004).

[11] P. Serp, M. Corrias, and P. Kalck,
Carbon nanotubes and nanofibers in catalysis,
Appl. Catal. A **253**, 337 (2003).

[12] H. Haberland:
Cluster. In *Lehrbuch der Experimentalphysik*,
W. Raith, de Gruyter (1992)

[13] W. P. Halperin,
Quantum size effects in metal particles,
Rev. Mod. Phys. **58**, 533 (1986)

[14] W. A. de Heer,
The physics of simple metal clusters: experimental aspects and simple models,
Rev. Mod. Phys. **65**, 611 (1993)

[15] ed. K.-H. Meiwes-Broer
Metal Clusters at Surfaces,
(Springer, Berlin Heidelberg, 2000)

[16] J. L. Martins, R. Car and J. Buttet,
Electronic and structural properties of sodium clusters,
Phys. Rev. B **31**, 1804 (1985)

[17] B. K. Rao, P. Jena, M. Manninen, and R.M. Nieminen,
Spontaneous fragmentation of multiply charged metal clusters,
Phys. Rev. Lett. **58**, 1188 (1987)

[18] M. Cini,
Ionization potentials and electron affinities of metal clusters,
J. Catalysis **37**, 187 (1975)

[19] W. Ekardt,
Work function of small metal particles: self-consistent spherical Jellium-background model,
Phys. Rev. B **29**, 1558 (1984)

[20] W. Ekardt,
Dynamical Polarizability of Small Metal Particles: Self-Consistent Spherical Jellium Background Model,
Phys. Rev. Lett. **52**, 1925 (1984)

[21] D. E. Beck,
Self-consistent calculation of the electronic structure of small Jellium spheres,
Solid State Commun. **49**, 381 (1984)

[22] D. E. Beck,
Self-consistent calculation of the polarizability of small jellium spheres,
Phys. Rev. B **30**, 6935 (1984)

[23] M. M. Kappes, R. W. Kunz, and E. Schumacher,
Production of large sodium clusters (Na_x, $x \leq 65$) by seeded beam expansions,
Chem. Phys. Lett. **91**, 413 (1982)

[24] W. D. Knight, K. Clemenger, W. A. de Heer, W. A. Saunders, M. Y. Chou, M. L. Cohen,
Electronic Shell Structure and Abundances of Sodium Clusters, Phys. Rev. Lett. **52**, 2141 (1984)

[25] W. D. Knight, W. A. de Heer, K. Clemenger,
Electronic shell structure in potassium clusters,
Solid State Commun. **53**, 445 (1985)

[26] J. Pederson, S. Bjornholm, J. Borggreen, K. Hansen, T. P. Martin, and H. D. Rasmussen,
Observation of quantum supershells in clusters of sodium atoms,
Nature **353**, 733 (1991)

[27] W. A. de Heer, W. D. Knight, M. Y. Chou, M. L. Cohen,
in *Solid State Physics*, ed. by H. Ehrenreich and D. Turnbull (Academic, New York), Vol. **40**, p. 30, 1987

[28] Stefanie Duffe (former Krause),
Massenselektierte Cluster deponiert auf Oberflächen,
Diploma thesis, Technische Universität Dortmund (2006)

[29] D. Mendeleeff,
The Principle of Chemistry, 3rd Ed. (Longmans, Green and Co., London, 1905)

[30] T. E. Thorpe,
Scientific worthies XXVI. Dimitri Wanowitch Mendeleeff.
Nature XL, 193-197 (1889)

[31] H. A. Jahn and E. Teller,
Stability of Polyatomic Molecules in Degenerate Electronic States. I. Orbital Degeneracy,
Proceedings of the Royal Society of London. Series A, Mathematical and Physical Science, **161**, 220 (1937)

[32] D. F. Shriver and P. W. Atkins,
Inorganic Chemistry, (3rd ed.), 235, (Oxford University Press)

[33] B. R. Mottelson and S. G. Nilsson,
Classification of the Nucleonic States in Deformed Nuclei,
Phys. Rev. **99**, 1615 (1955)

[34] A. Bohr and B. R. Mottelson,
Nuclear Structure, (Benjamin, New York, 1975), Vol II

[35] K. Clemenger,
Elipsoidal shell structure in free-electron metal clusters,
Phys. Rev. B **32**, 1359 (1985)

[36] C. Bréchignac, Ph. Cahuzac, J. Leygnier, and J. Weiner,
Dynamics of unimolecular dissociation of sodium cluster ions,
J. Chem. Phys. **90**, 1492 (1989)

[37] M. P. J. van Staveren, H. B. Brom, L. J. de Jong, Y. Ishii,
Energetics of charged small metal particles,
Phys. Rev. B **35**, 7749 (1987)

[38] K. Manninen, T. Santa-Nokki, H. Häkinnen, and M. Manninen,
Magic clusters Na_{57}^- *and* Na_{59}^+,
Eur. Phys. J. D, **34**, 43 (2005)

[39] George Alameddin, Joanna Hunter, Douglas Cameron, and Manfred M. Kappes,
Electronic and geometric structure in silver clusters,
Chem. Phys Lett. **192**, 122 (1992)

[40] C. Pettiette, S. Yang, M. Craycraft, J. Conceicao, R. Laaksonen, O. Cheshnovsky and R. Smalley,
Ultraviolet photoelectron spectroscopy of copper clusters,
J. Chem. Phys. **88**, 5377 (1988)

[41] O. Cheshnovsky, K. Taylor, J. Conceicao and R. Smalley,
Ultraviolet Photoelectron Spectra of Mass-Selected Copper Clusters: Evolution of the 3d Band,
Phys. Rev. Lett. **64**, 1785 (1990)

[42] T. P. Martin, T. Bergmann, H. Gölich, T. Lange,
Observation of electronic shells and shells of atoms in large Na clusters,
Chem. Phys. Lett. **172**, 209 (1990)

[43] P. Stampfli, K. H. Bennemann,
Unified Model for the Shell Structure in the Cohesive Energy , Ionization Potential and Photoyield of Metallic Clusters,
Phys. Rev. Lett. **69**, 3471 (1992)

[44] P. Stampfli, K. H. Bennemann,
Simplified semiclassical theory for the electronic shell structure of metallic clusters,
Z. Phys. D **25**, 87 (1992)

[45] A. L. Mackay,
A dense non-crystallographic packing of equal spheres,
Acta Crystall. **15**, 916 (1962)

[46] O. Echt, K. Sattler, E. Recknagel,
Magic Numbers for Sphere Packings: Experimental Verification in free Xenon Clusters,
Phys. Rev. Lett **47**, 1121 (1981)

[47] D. Kreisle, O. Echt, M. Knapp, and E. Recknagel,
Time-dependent size distribution of Xe-cluster ions,
Phys. Rev. A **33**, 768 (1986)

[48] B. D. Hall, M. Flüeli, D. Reinhard, J.-P. Borel, R. Monot,
An electron diffraction apparatus for studies on small particles in a molecular beam,
Rev. Sci. Instr. **62**, 1481 (1991)

[49] C. Kittel,
Einführung in die Festkörperphysik,
Oldenbourg-Verlag (1998).

[50] M. R. Hoare,
*Structure and Dynamics of Simple Microcluster*s,
Adv. Chem. Phys. **40**, 49 (1979)

[51] J. Jortner,
Level structure dynamics of clusters,
Bericht der Bunsengesellschaft für Physikalische Chemie **88**, 188 (1984)

[52] M. Moseler, B. Huber, H. Häkkinen, U. Landman, G. Wrigge, M. Astruc Hoffmann, B. von Issendorff,
Thermal effects in the photoelectron spectra of Na_N*–clusters (N = 4 - 19),*
Phys. Rev. B **68**, 165413 (2003)

[53] G. Wrigge, M. A. Hoffmann, B. v. Issendorff,
Photoelectron spectroscopy of sodium clusters: Direct observation of the electronic shell structure,
Phys. Rev. A **65**, 063201 (2002)

[54] O. Kostko, B. Huber, M. Moseler, and B. v. Issendorff,
Structure Determination of Medium-Sized Sodium Clusters,
Phys. Rev. Lett **98**, 043401 (2007)

[55] Hellmut Haberland, Thomas Hippler, Jörn Donges, Oleg Kostko, Martin Schmidt, and Bernd von Issendorff,
Melting of Sodium Clusters: Where Do the Magic Numbers Come from?,
Phys. Rev. Lett. **94**, 035701 (2005)

[56] M. Astruc Hoffmann, G. Wrigge, and B. v. Issendorff,
Photoelectron spectroscopy of Al_{32000}^{-}*: Observation of a "Coulomb staircase" in a free cluster*,
Phys. Rev. B **66**, 041404 (2002)

[57] Hannu Häkkinen, Michael Moseler,
55-Atom clusters of silver and gold: Symmetry breaking by relativistic effects,
Comp. Mater. Sci. **35**, 332 (2006)

[58] D. M. Cox, R. Brickman, K. Creegan, A. Kaldor,
Gold clusters: reactions and deuterium uptake,
Z. Phys. D **19**, 353 (1991)

[59] D. M. Cox, R. Brickman, K. Creegan, A. Kaldor,
Mater. Res. Soc. Symp. Proc. **206**, 43 (1991)

[60] B. E. Salisbury, W. T. Wallace, R. L. Whetten,
Low-temperature activation of molecular oxygen by gold clusters: a stoichiometric process correlated to electron affinity,
Chem. Phys. **262**, 131 (2000)

[61] Y. D. Kim, M. Fischer, G. Ganteför,
Origin of unusual catalytic activities of Au-based catalysts,
Chem. Phys. Lett. **377**, 170 (2003)

[62] Bokwon Yoon, Pekka Koskinen, Bernd Huber, Oleg Kostko, Bernd von Issendorff, Hannu Häkkinen, Michael Moseler, and Uzi Landman,
Size-Dependent Structural Evolution and Chemical Reactivity of Gold Clusters,
Chem. Phys. Chem. **8**, 157 (2007)

[63] M. Turner, Vladimir B. Golovko, Owain P. H. Vaughan, Pavel Abdulkin, Angel Berenguer-Murcia, Mintcho S. Tikhov, Brian F. G. Johnson, and Richard M. Lambert,
Selective oxidation with dioxygen by gold nanoparticle catalysts derived from 55-atom clusters,
Nature **454**, 981 (2008)

[64] X. Y. Deng and C. M. Friend,
Selective oxidation of styrene on an oxygen-covered Au(111).
J. Am. Chem. Soc. **127**, 17178 (2005).

[65] R. M. Lambert, F. J. Williams, R. L. Cropley, and A. Palermo,
Heterogeneous alkene epoxidation: past, present and future,
J. Mol. Catalys. A **228**, 27 (2005)

[66] R. J. Chimentao et al.,
Sensitivity of styrene oxidation reaction to the catalyst structure of silver nanoparticles,
Appl. Surf. Sci. **252**, 793 (2005)

[67] F. J. Williams, D. P. C. Bird, A. Palermo, A. K. Santra, and R. M. Lambert,
Mechanism, selectivity promotion, and new ultraselective pathways in Ag-catalyzed heterogeneous epoxidation,
J. Am. Chem. Soc. **126**, 8509 (2004)

[68] Q. Tang et al.,
Co^{2+}*-exchanged faujasite zeolites as efficient heterogeneous catalysts for epoxidation of styrene with molecular oxygen*,
Chem. Commun. **4**, 440 (2004)

[69] J. Sebastian, K. M. Jinka, and R. V. Jasra,
Effect of alkali and alkaline earth metalions on the catalytic epoxidation of styrene with molecular oxygen using cobalt (II)-exchanged zeolite X,
J. Catalys. **244**, 208 (2006)

[70] B. Huber, P. Koskinen, H. Häkkinen, M. Moseler,
Oxidation of magnesia-supported Pd-clusters leads to the ultimate limit of epitaxy with a catalytic function,
Nature Materials **5**, 44 (2006)

[71] M. Moseler, H. Häkkinen, U. Landman,
Supported Magnetic Nanoclusters: Soft Landing of Pd Clusters on a MgO Surface,
Phys. Rev. Lett. **89**, 176103 (2002)

[72] K. S. Novoselov, D. Jiang, F. Schedin, T. J. Booth, V. V. Khotkevich, S. V. Morozov, and A. K. Geim,
Two-dimensional atomic crystals,
Proc. Natl. Acad. Sci. USA **102,** 10451 (2005)

[73] K. S. Novoselov, A. K. Geim, S. V. Morozov, D. Jiang, Y. Zhang, S. V. Dubonos, I. V. Grigorieva, A. A. Firsov,
Electric Field Effect in Atomically Thin Carbon Films,
Science **306**, 666 (2004)

[74] S. Iijima,
Helical microtubules of graphitic carbon,
Nature **354**, 56 (1991)

[75] Albert G. Nasibulin et al.,
A novel hybrid carbon material,
Nature Nanotechnology **2**, 156 (2006)

[76] Albert G. Nasibulin, Anton S. Anisimov, Peter V. Pikhitsa, Hua Jiang, David P. Brown, Mansoo Choi, Esko I. Kauppinen,
Investigations of NanoBud formation,
Chem. Phys. Lett **446**, 109 (2007)

[77] Ricardo Vieira, Marc-Jacques Ledoux and Cuong Pham-Huu,
Synthesis and characterisation of carbon nanofibres with macroscopic shaping formed by catalytic decomposition of C_2H_6/H_2 over nickel catalyst,
Appl. Catal. A, **247**, 1 (2004)

[78] E. Osawa,
Superaromaticity,
Kagaku **25**, 854 (1970)

[79] Z. Yoshida and E. Osawa,
Aromaticity
Chemical Monograph Series **22**, 174 Kagaku Dojin: Kyoto, Japan (1971), only available in Japanese

[80] H. W. Kroto, J. R. Heath, S. C. O’Brien, R. E. Curl, R. E. Smally,
C_{60}: Buckminsterfullerene,
Nature **318**, 162 (1985)

[81] Robert J. Ternansky, Douglas W. Balogh, and Leo A. Paquette,
Dodecahedrane,
J. Am. Chem. Soc. **104**, 4503 (1982)

[82] Leo A. Paquette, Robert J. Ternansky, Douglas W. Balogh, and Gary Kentgen,
Total Synthesis of Dodecahedrane,
J. Am. Chem. Soc. **105**, 5446 (1983)

[83] W. Krätschmer, K. Fostiropoulos and Donald R. Huffman,
The infrared and ultraviolet absorption spectra of laboratory-produced carbon dust: evidence for the presence of the C_{60} molecule,
Chem. Phys. Lett. **170**, 167 (1990)

[84] L. P. F. Chibante, Andreas Thess, J. M. Alford, M. D. Diener, and R. E. Smalley,
Solar Generation of the Fullerenes,
J. Phys. Chem. **97**, 8696 (1993)

[85] L. Fulcheri, Y. Schwob, F. Fabry, G. Flamant, L. F. P. Chibante, D. Laplaze,
Fullerene production in a 3-phase AC plasma process,
Carbon **38**, 797 (2000)

[86] Markus Bieletzki,
Rastertunnelmikroskopie an massenselektierten Clustern auf C_{60},
Diploma thesis, Technische Universität Dortmund (2006)

[87] S. Bandow, M. Takizawa, H. Kato, T. Okazaki, H. Shinohara, and S. Iijima,
Smallest limit of tube diameters for encasing of particular fullerenes determined by radial breathing mode Raman scattering,
Chem. Phys. Lett. **347**, 23 (2001)

[88] H. W. Kroto,
The stability of the fullerenes C_n, *with* $n = 24, 28, 32, 36, 50, 60$ *and* 70,
Nature **329**, 529 (1987)

[89] R. C. Haddon,
Chemistry of the Fullerenes: The Manifestation of Strain in a Class of Continuous Aromatic Molecules,
Science **26**, 1545 (1993)

[90] W. Krätschmer, Lowell D. Lamb, K. Fostiropoulos, and Donald R. Huffman,
Solid C_{60}*: a new form of carbon,*
Nature **347**, 354 (1990)

[91] P. C. Eklund, Ping Zhou, Kai-Aa Wang, G. Dresselhaus, and M. S. Dresselhaus,
Optical phonon modes in solid and doped C_{60},
J. Phys. Chem. Solids **53**, 1391 (1992)

[92] A. F. Hebard, M. J. Rosseinsky, R. C. Haddon, D. W. Murphy, S. H. Glarum, T. T. M. Palstra, A. P. Ramirez, and A. R. Kortan,
Superconductivity at 18 K in potassium-doped C_{60},
Nature **350**, 600 (1991)

[93] Xin Lu and Zhongfang Chen,
Curved Pi-Conjugation, Aromaticity, and the Related Chemistry of Small Fullerenes ($<C_{60}$) *and Single-Walled Carbon Nanotubes,*
Chem. Rev. (Washington, D.C.) **105**, 3643 (2005)

[94] S. Diaz-Tendero, M. Alcami and F. Martin,
Theoretical study of ionization potentials and dissociation energies of C_n^{q+} *fullerenes* ($n = 50$ - 60, $q = 0$, 1 *and* 2),
J. Chem. Phys. **119**, 5545 (2003)

[95] Angela Bihlmeier, Claire C. M. Samson, and Wim Klopper,
DFT Study of Fullerene Dimers,
Chem. Phys. Chem. **6**, 2625 (2005)

[96] T. Becker, H.Hövel, M. Tschudy, and B. Reihl,
Applications with a new low-temperature UHV STM at 5 K,
Appl. Phys. A **66**, 27 (1998)

[97] H. Hövel, T. Becker, D. Funnemann, B. Grimm, C. Quitmann, B. Reihl,
High-resolution photoemission combined with low-temperature STM,
J. Elec. Spec. Rel. Phenom. **88-91**, 1015 (1998)

[98] H. Haberland, M. Mall, M. Moseler, Y. Qiang, Th. Reiners, and Y.Thurner,
Filling of micron-sized contact holes with copper by energetic cluster impact,
J. Vac. Sci. Technol. A **12**, 2925 (1994)

[99] B. von Issendorff and R. E. Palmer,
A new high transmission infinite range mass selector for cluster and nanoparticle beams,
Rev. Sci. Instr. **70**, 4497 (1999)

[100] Chunrong Yin,
Deposition and Characterization of Size-Selected Metal Clusters,
Dissertation, Albert Ludwig Universität Freiburg (2007)

[101] P. Sigmund,
Theory of Sputtering. I. Sputtering Yield of Amorphous and Polycrystalline Targets,
Phys. Rev. **184**, 383 (1969)

[102] SIMION, D. A. Dahl and J. E. Delmore, Idaho Engineering Laboratory, EG&G Idaho Inc., P. O. Box 1625, Idaho Falls, ID 83415

[103] Ingo Barke,
Edelgasschichten auf der Au(111)-Oberfläche: Präparation und lokale Tunnelspektroskopie,
Diploma thesis, Technische Universität Dortmund (2001)

[104] Torsten Richter,
*Untersuchung von deponierten und gewachsenen Silberclustern auf Fullerenschichten mittels Rastertunnelmikrosk*opie,
Diploma thesis, Technische Universität Dortmund (2007)

[105] G. Binnig, H. Rohrer, Ch. Gerber, and E. Weibel,
Tunneling through a controllable vacuum gap,
Appl. Phys. Lett. **40**, 178 (1982)

[106] G. Binnig, H. Rohrer, Ch. Gerber, and E. Weibel,
Surface Studies by Scanning Tunneling Microscopy,
Phys. Rev. Lett. **49**, 57 (1982)

[107] G. Binnig and H. Rohrer,
Scanning Tunneling Microscopy,
Surf. Sci. **126**, 236 (1983)

[108] R. W. Gurney, E. U. Condon,
Wave Mechanics and Radioactive Disintegration,
Nature **122**, 439 (1928)

[109] R. W. Gurney, E. U. Condon,
Quantum Mechanics and Radioactive Disintegration,
Phys. Rev. **33**, 127 (1929)

[110] G. Gamow,
Zur Quantentheorie des Atomkernes,
Z. Phys. A **51**, 204 (1928)

[111] R. W. Wood,
A new form of cathode discharge and the production of x-rays, together with some notes of diffraction,
Phys. Rev. **5**, 1 (1897)

[112] H. Bethe and A. Sommerfeld,
Handbuch *der Physik*, ed. by Geiger and Schied,
Verlag Julius Springer, 2nd ed. Vol. **24**, Part 2, p. 450 (1933)

[113] R. Holm, B. Kirschstein,
Über den Widerstand dünnster Fremdschichten in Metallkontakten,
Zeit. Techn. Phys. **16**, 488 (1935)

[114] R. Holm,
*The Electric Tunnel Effect across Thin Insulator Films in Contac*t,
J. Appl. Phys. **22**, 569 (1951)

[115] J. Simmons,
Generalized Formula for the Electric Tunnel Effect between Similar Electrodes Separated by a Thin Insulating Film,
J. Appl. Phys. **34**, 1793 (1963)

[116] J. Bardeen,
Tunneling from a many-particle point of view,
Phys. Rev. Lett. **6**, 57 (1961)

[117] J. Tersoff and D. R. Hamann,
Theory and Application for the Scanning Tunneling Microscope,
Phys. Rev. Lett. **50**, 1998 (1983)

[118] J. Tersoff and D. R. Hamann,
Theory of the scanning tunneling microscope,
Phys. Rev. B **31**, 805 (1985)

[119] Léon Brillouin,
La mécanique ondulatoire de Schrödinger: une méthode générale de resolution par approximations successives,
Comptes Rendus de l'Academie des Sciences **183**, 24 (1926)

[120] Hendrik A. Kramers,
Wellenmechanik und halbzählige Quantisierung,
Z. d. Phys. **39**, 828 (1926)

[121] Gregor Wentzel,
Eine Verallgemeinerung der Quantenbedingungen für die Zwecke der Wellenmechanik,
Zeitschrift der Physik **38**, 518 (1926)

[122] G. Binnig, K. H. Frank, H. Fuchs, N. Garcia, B. Reihl, H. Rohrer, F. Salvan, and A. R. Williams,
Tunneling Spectroscopy and Inverse Photoemission: Image and Field States,
Phys. Rev. Lett. **55**, 991 (1985)

[123] Hans-Christoph Ploigt, Christophe Brun, Marina Pivetta, François Patthey, and Wolf-Dieter Schneider,
Local work function changes determined by field emission resonances: NaCl/Ag(100),
Phys. Rev. B **76**, 195404 (2007)

[124] I. S. Tilinin, M. K. Rose, J. C. Dunphy, M. Salmeron, M. A. Van Hove,
Identification of adatoms on metal surfaces by STM: experiment and theory,
Surf. Sci. **418**, 511 (1998)

[125] Philippe Sautet,
Atomic adsorbate identification with the STM: a theoretical approach,
Surf. Sci. **374**, 406 (1997)

[126] Heinz Hövel, B. Grimm, and B. Reihl,
Modification of the Shockley-type surface state on Ag(111) by an adsorbed xenon layer,
Surf. Sci. **477**, 43 (2001)

[127] H. Hövel and I. Barke,
Large noble metal clusters: electron confinement and band structure effects,
New J. Phys. **5**, 31 (2003)

[128] I. Barke and H. Hövel,
Confined Shockley Surface States on the (111) Facets of Gold Clusters,
Phys. Rev. Lett **90**, 166801 (2003)

[129] B. Grimm,
Tunnelspektroskopie und Photoemission bei tiefen Temperaturen an Edelgas-Modellsystemen und Nanostrukturen,
Dissertation, Technische Universität Dortmund (2000)

[130] H. R. Hertz,
Über einen Einfluß des ultravioletten Lichtes auf die electrische Entladung,
Ann. Phys. u. Chem. **31**, 983 (1887)

[131] W. Hallwachs,
Über den Einfluß des Lichtes auf die electrostatisch geladenen Körper,
Ann. Phys. u. Chem. **33**, 301 (1888)

[132] J. J. Thomson,
Cathode Rays,
Philosophical Magazine **44**, 293 (1897).

[133] G. J. Stoney,
Of the "Electron," or Atom of Electricity,
Philosophical Magazine Series 5, **38**, 418 (1894)

[134] P. Lenard,
Erzeugung von Kathodenstrahlen durch ultraviolettes Licht,
Ann. Phys. **2**, 359 (1900)

[135] A. Einstein,
Über einen die Erzeugung und Verwandlung des Lichtes betreffenden heuristischen Gesichtspunkt,
Ann. Phys. **17**, 132 (1905)

[136] D. W. Turner and M. I. Al Jobory,
Determination of Ionization Potentials by Photoelectron Energy Measurement,
J. Chem. Phys. **37**, 3007 (1962)

[137] C. N. Berglund and W. E. Spicer,
Photoemission Studies of Copper and Silver: Theory,
Phys. Rev. **136**, A1030 (1964)

[138] L. Pauling,
The Nature of the Chemical Bond,
p. 235, 3rd Edition (1960)

[139] C. A. Lang, M. M. Dovek, J. Nogami, and C. F. Quate,
Au(111) autoepitaxy studied by scanning tunneling microscopy,
Surf. Sci. Lett. **224**, L947 (1989)

[140] K. Reichelt and H. O. Lutz,
Hetero-epitaxial growth of vacuum evaporated silver and gold,
J. Cryst. Growth **10**, 103 (1971)

[141] S. Narasimhan and D. Vanderbilt,
Elastic Stress Domains and the Herringbone Reconstruction on Au(111),
Phys. Rev. Lett **69**, 164 (1992)

[142] Lukas Patryarcha,
Massenselektierte Silbercluster und aufgedampftes Silber auf C_{60}*/HOPG und* C_{60}*/Au(111),*
Diploma thesis, Technische Universität Dortmund (2008)

[143] E. I. Altman and R. J. Colton,
Nucleation, Growth and Structure of Fullerene Films on Au(111),
Surf. Sci. **279**, 49 (1992)

[144] S. Szuba, R. Czajka, A. Kasuya, A. Wawro, and H. Rafii-Tabar,
Observation of C_{60} *film formation on a highly oriented pyrolitic graphite substrate via scanning tunnelling microscopy,*
Appl. Surf. Sci. **144**, 648 (1999)

[145] Hui Liu and Petra Reinke,
C_{60} *thin film growth on graphite: Coexistence of spherical and fractal-dendritic islands,*
J. Chem. Phys. **124**, 164707 (2006)

[146] Stefanie Duffe, Thomas Irawan, Markus Bieletzki, Torsten Richter, Benedikt Sieben, Chunrong Yin, Bernd von Issendorff, Michael Moseler, and Heinz Hövel,
Softlanding and STM imaging of Ag_{561} *clusters on a* C_{60} *monolayer,*
Eur. Phys. J. D **45**, 401 (2007)

[147] Artur Böttcher, Patrick Weis, Angela Bihlmeier, and Manfred M. Kappes,
C_{58} *on HOPG: Soft-landing adsorption and thermal desorption,*
Phys. Chem. Chem. Phys. **6**, 5213 (2004)

[148] Artur Böttcher, Patrick Weis, Stefan-S. Jester, Daniel Löffler, Angela Bihlmeier, Wim Klopper, and Manfred M. Kappes,
Solid C_{58} *films,*
Phys. Chem. Chem. Phys. **7**, 2816 (2005)

[149] Daniel Löffler, Stefan S. Jester, Patrick Weis, Artur Böttcher, and Manfred M. Kappes,
C_n *films (n=50, 52, 54, 56, and 58) on graphite: Cage size dependent electronic properties,*
J. Chem. Phys. **124**, 054705 (2006)

[150] Benedikt Sieben,
Rastertunnelmikroskopie an Clustersystemen,
Diploma thesis, Technische Universität Dortmund (2007)

[151] J. A. Venables,
Rate Equation Approaches to Thin Film Nucleation Kinetics,
Phil. Mag. **27**, 697 (1973)

[152] S. J. Chase, W. S. Bacsa, M. G. Mitch, L. J. Pilione, and J. S. Lannin,
Surface-enhanced Raman scattering and photoemission of C_{60} *on noble-metal surfaces,*
Phys. Rev. B **46**, 7873 (1992)

[153] S. Modesti, S. Cerasari, and P. Rudolf,
Determination of Charge States of C_{60} *Adsorbed on Metal Surfaces,*
Phys. Rev. Lett. **71**, 2469 (1993)

[154] M. W. Ruckman and Bo Xia,
Adsorption of C_{60} *on Ta(110): Photoemission and C K-edge studies,*
Phys. Rev. B **48**, 15457 (1993)

[155] A. Rosenberg,
Resonant second-order Raman spectra of C_{60} *on Ag and In surfaces,*
Phys. Rev. B **51**, 1961 (1995)

[156] M. R. C. Hunt, S. Modesti, P. Rudolf, and R. E. Palmer,
Charge transfer and structure in C_{60} *adsorption on metal surfaces,*
Phys. Rev. B, **51**, 10039 (1995)

[157] H. Hövel, T. Becker, A. Bettac, B. Reihl, M. Tschudy, and E. J. Williams,
Controlled cluster condensation into preformed nanometer-sized pits,
J. Appl. Phys. **81**, 154 (1997)

[158] H. Hövel and I. Barke,
Morphology and electronic structure of gold clusters on graphite: Scanning-tunneling techniques and photoemission,
Prog. Surf. Sci, **81**, 53 (2006)

[159] H. Hövel,
Clusters on Surfaces; high-resolution spectroscopy at low temperatures,
Appl. Phys. A **72**, 295 (2001)

[160] H. Hövel, T. Becker, A. Bettac, B. Reihl, M. Tschudy, and E. J. Williams,
Crystalline structure and orientation of gold clusters grown in preformed nanometer-sized pits,
Appl. Surf. Sci. **115**, 124 (1997)

[161] T. Irawan, I. Barke, and H. Hövel,
Size-dependent morphology of gold clusters grown on nanostructured graphite,
Appl. Phys. A **80**, 929 (2005)

[162] F. Ghaleh, R. Köster, H. Hövel, L. Bruchhaus, S. Bauerdick, J. Thiel, and R. Jede,
Controlled fabrication of nanopit patterns on a graphite surface using focused ion beams and oxidation,
J. Appl. Phys. **101**, 044301 (2007)

[163] L. E. C. van de Leemput, P. H. H. Rongen, B. H. Timmerman, and H. van Kempen,
Calibration and characterization of piezoelectric elements as used in scanning tunneling microscopy,
Rev. Sci. Instrum **62**, 989 (1991)

[164] S. Liu, Y.-J. Lu, M.M. Kappes, and J.A. Ibers,
The Structure of the C_{60} *Molecule*: *X-Ray Structure Determination of a Twin at 110 K*,
Science **254**, 408 (1991)

[165] Thomas Irawan,
Geometric and Electronic Properties of Size-Selected Metal Clusters on Surfaces,
Dissertation, Technische Universität Dortmund (2006)

[166] W. B. Pearson,
Handbook of Lattice Spacings and Structures of Metals and Alloys,
Pergamon, Vol. **2** (1967)

[167] K. O. McLean, C. A. Swenson, and C. R. Case,
Thermal Expansion of Copper, Silver and Gold Below 30 K,
J. Low Temp. Phys. **7**, 77 (1972)

[168] Ting Ning, Qingliang Yu and Yiying Ye,
Multilayer relaxation at the surface of fcc metals: Cu, Ag, Au, Ni, Pd, Pt, Al,
Surf. Sci. **206**, L857 (1988)

[169] C. E. D. Chidsey, D. N. Loiacono, T. Sleator, and Sho Nakahara,
STM Study of the surface morphology of gold on mica,
Surf. Sci. **200**, 45 (1988)

[170] V. M. Hallmark, S. Chiang, J. F. Rabolt, J. D. Swalen, R. J. Wilson,
Observation of Atomic Corrugation on Au(111) by Scanning Tunneling Microscopy,
Phys. Rev. Lett. **59**, 2879 (1987)

[171] R. D. Jaklevic and L. Elie,
Scanning-Tunneling-Microscope Observation of Surface Diffusion on an Atomic Scale: Au on Au(111),
Phys. Rev. Lett. **60**, 120 (1988)

[172] I. Horcas and R. Fernández, J. M. Gómez-Rodríguez, J. Colchero, J. Gómez-Herrero, and A. M. Baro,
WSXM: A software for scanning probe microscopy and a tool for nanotechnology,
Rev. Sci. Instrum. **78**, 013705 (2007)

[173] P. Meakin,
Diffusion-controlled flocculation: The effects of attractive and repulsive interactions,
J. Chem. Phys. **79**, 2426 (1983)

[174] B. Yoon, V. M. Akulin, Ph. Cahuzac, F. Carlier, M. de Frutos, A. Masson, C. Mory, C. Colliex and C. Brechignac,
Morphology control of the supported islands grown from soft-landed clusters,
Surf. Sci. **443**, 76 (1999)

[175] G. Schull and R. Berndt,
Orientationally Ordered (7×7) Superstructure of C_{60} on Au(111),
Phys. Rev. Lett **99**, 226105 (2007)

[176] Haiqian Wang, Changgan Zeng, Bing Wang, and J. G. Hou,
Orientational configurations of the C_{60} molecules in the (2×2) superlattice on a solid C_{60} (111) surface at low temperature,
Phys. Rev. B **63**, 085417 (2001)

[177] G. Schull, N. Néel, M. Becker, J. Kröger and R. Berndt,
Spatially resolved conductance of oriented C_{60},
New J. Phys. **10,** 065012 (2008)

[178] Xinghua Lu, M. Grobis, K. H. Khoo, Steven G. Louie, and M. F. Crommie,
Charge transfer and screening in individual C_{60} molecules on metal substrates: A scanning tunneling spectroscopy and theoretical study,
Phys. Rev. B **70**, 115418 (2004)

[179] Xinghua Lu, M. Grobis, K. H. Khoo, Steven G. Louie, and M. F. Crommie,
Spatially Mapping the Spectral Density of a Single C_{60} Molecule,
Phys. Rev. Lett. **90**, 096802 (2003)

[180] W. I. F. David, R. M. Ibberson, T. J. S. Dennis, J. P. Hare, and K. Prassides,
Structural Phase Transitions in the Fullerene C_{60},
Europhys. Lett. **18**, 219 (1992)

[181] Paul A. Heiney, John E. Fischer, Andrew R. McGhie, William, J. Romanow,
Orientational Ordering Transition in Solid C_{60},
Phys. Rev. Lett. **66**, 2911 (1991)

[182] R. Tycko, G. Dabbagh, R. M. Fleming, R. C. Haddon, A. V. Makhija, and S. M. Zahurak,
Molecular Dynamics and the Phase Transition in Solid C_{60},
Phys. Rev. Lett. **67**, 1886 (1991)

[183] C. S. Yannoni, R. D. Johnson, G. Meijer, D. S. Bethune, and J. R. Salem,
^{13}C *NMR Study of the* C_{60} *Cluster in the Solid State: Molecular Motion and Carbon Chemical Shift Anisotropy*,
J. Phys. Chem. **95**, 9 (1991)

[184] Robert D. Johnson, Costantino S. Yannoni, Harry C. Dorn, Jesse R. Salem, and Donald S. Bethune,
C_{60} *Rotation in the Solid State: Dynamics of a Faceted Spherical Top*,
Science **255**, 1235 (1992)

[185] D. A. Neumann et al.,
Coherent Quasielastic Scattering Study of the Rotational Dynamics of C_{60} *in the Orientationally Disordered Phase*,
Phys. Rev. Lett. **67**, 3808 (1991)

[186] William I. F. David, Richard M. Ibberson, Judy C. Matthewman, Kosmas Prassides, T. John S. Dennis, Jonathan P. Hare, Harold W. Kroto, Roger Taylor, and David R. M. Walton,
Crystal structure and bonding of ordered C_{60},
Nature **353**, 147 (1991)

[187] D. Passerone and E. Tosatti,
Surface rotational disordering in crystalline C_{60},
Surf. Rev. Lett. **4**, 859 (1997)

[188] Eric I. Altman and Richard J. Colton,
Determination of the orientation of C_{60} *adsorbed on Au(111) and Ag(111)*,
Phys. Rev. B **48**, 18244 (1993)

[189] X. Zhang, F. Yin, R. E. Palmer, Q. Guo,
The C_{60}*/Au(111) interface at room temperature: A scanning tunnelling microscopy study*,
Surf. Sci. **602**, 885 (2008)

[190] E. I. Altman, R. J. Colton,
The interaction of C_{60} *with noble metal surfaces*,
Surf. Sci. **295**, 13 (1993)

[191] W. Ostwald,
Über die vermeintliche Isomerie des roten und gelben Quecksilberoxyd,
Z. Phys. Chem. (Leipzig) **34**, 495 (1900).

[192] M. Wutz, H. Adam, W. Walcher:
Theorie und Praxis der Vakuumtechnik,
Vieweg-Verlag (1988)

[193] Niklas Grönhagen,
Wachstum von Nanostrukturen auf strukturiertem Graphit,
Diploma thesis, Technische Universität Dortmund (2008)

[194] Farhad Ghaleh,
Characterization of Surface Defects Produced with Focused Ion Beams and Exploration of Applications for Controlled Growth of Nano-structures,
Dissertation, Technische Universität Dortmund (2009)

[195] Stefanie Duffe, Lukas Patryarcha, Benedikt Sieben, Chunrong Yin,
Bernd von Issendorff, Michael Moseler, and Heinz Hövel,
submitted for publication (2009)

[196] R. Schaub, H. Jödicke, F. Brunet, R. Monot, J. Buttet, and W. Harbich,
Decorated Ag_{19} *on Pt(111) or the "Rare Gas Necklace"*,
Phys. Rev. Lett. **86**, 3590 (2001)

[197] A. Rapallo, G. Rossi, R. Ferrando, A. Fortunelli, B.C. Curley, L.D. Lloyd, G.M. Tarbuck, R.L. Johnston,
Global optimization of bimetalliccluster structures. I. Size-mismatched Ag-Cu, Ag-Ni, and Au-Cu systems,
J. Chem. Phys. **122**, 194308 (2005)

[198] J. Tersoff,
New empirical model for the structural properties of silicon,
Phys. Rev. Lett. **56**, 632 (1986)

[199] J. Tersoff,
Modeling solid state chemistry: Interatomic potentials for multicomponent systems,
Phys. Rev. B **39**, 5566 (1989)

[200] L.A. Girifalco,
Molecular Properties of C_{60} *in the Gas and Solid Phases,*
J. Phys. Chem. **96**, 858 (1992)

[201] L.-L. Wang, H.-P. Cheng,
Density functional study of the adsorption of a C_{60} *monolayer on Ag(111) and Au(111) surfaces,*
Phys. Rev. B **69**, 165417 (2004)

[202] H. Park, J. Park, A.K.L. Lim, E.H. Anderson, A.P. Alivisatos, P.L. McEuen,
Nanomechanical oscillations in a single-C_{60} *transistor,*
Nature **407**, 57 (2000)

[203] M. Moseler, J. Nordiek, H. Haberland,
Reduction of the reflected pressure wave in the molecular-dynamics simulation of energetic particle-solid collisions,
Phys. Rev. B **56**, 15439 (1997)

[204] R. Chatterjee, Z. Postawa, N. Winograd, B. Garrison,
Molecular Dynamics Simulation Study of Molecular Ejection Mechanisms: keV Particle Bombardment of C_6H_6*/Ag{111},*
J. Phys. Chem. B **103**, 151 (1999)

[205] A. P. Sutton and J. Chen,
Long-range Finnis-Sinclair potentials,
Phil. Mag. Lett. **61**, 139 (1990)

[206] D. Brenner,
Empirical potential for hydrocarbons for use in simulating the chemical vapour deposition of diamond films,
Phys. Rev. B **42**, 9458 (1990)

[207] Michael Bowker,
Surface science: The going rate for catalysts,
Nature Materials **1**, 205 (2002)

[208] Karina Morgenstern, Georg Rosenfeld, and George Comsa,
Decay of Two-Dimensional Ag Islands on Ag(111),
Phys. Rev. Lett. **76**, 2113 (1996)

[209] Karina Morgenstern, Georg Rosenfeld, Erik Lægsgaard, Flemming Besenbacher, and George Comsa1,
Decay of Two-Dimensional Ag Islands on Ag(111),
Phys. Rev. Lett. **80**, 556 (1998)

[210] H. Cercellier, C. Didiot, Y. Fagot-Revurat, B. Kierren, L. Moreau, and D. Malterre, and F. Reinert,
Interplay between structural, chemical, and spectroscopic properties of Ag/Au(111) epitaxial ultrathin films: A way to tune the Rashba coupling,
Phys. Rev. B **73** , 195413 (2006)

[211] M. J. J. Jak, C. Konstapel, A. van Kreuningen, J. Verhoeven, J.W.M. Frenken,
Scanning tunnelling microscopy study of the growth of small palladium particles on TiO_2*(110),*
Surface Science **457**, 295 (2000)

[212] Lauren Benz, Xiao Tong, Paul Kemper, Yigal Lilach, Andrei Kolmakov, Horia Metiu, Michael T. Bowers, and Steven K. Buratto,
Landing of size-selected Ag_n^+ *clusters on single crystal* TiO_2 *(110)-(1×1) surfaces at room temperature,*
J. Chem. Phys. **122**, 081102 (2005)

[213] M. M. Dovek, C. A. Lang, J. Nogami, and C. F. Quate,
Epitaxial growth of Ag on Au(111) studied by scanning tunneling microscopy,
Phys. Rev. B **40**, 11973 (1989)

[214] M. C. Robinson and A. J. Slavin, and K. De'Bell,
A study of the diffusion of Pb on the Au(111) surface by STM and EAM-MD simulations,
Surf. Rev. Lett. **6**, 793 (1999)

[215] R. DeBoer et al.,
Cohesion in Metals,
p. 676. North-Holland (1988)

[216] J. A. Meyer, I. D. Baikie, E. Kopatzki, R.J. Behm,
Preferential island nucleation at the elbows of the Au(111) herringbone reconstruction through place exchange,
Surf. Sci. **365**, L647 (1996)

[217] A. Goldoni, G. Paolucci,
The interaction of C_{60} *with Ag(100): strong predominantly ionic bonding*,
Surf. Sci. **437**, 353 (1999)

[218] D. Purdie, H. Bernhoff, B. Reihl,
The electronic structure of Ag(110)c(4×4)C_{60} *and Au(110)(6×5)*C_{60}*,*
Surf. Sci. **364**, 279 (1996)

[219] E. Magnano, S. Vandré, C. Cepek, A. Goldoni, A.D. Laine, G.M. Curro, A. Santaniello, and M. Sancrotti,
Substrate-adlayer interaction at the C_{60}*/Ag(110) interface studied by high-resolution synchrotron radiation,*
Surf. Sci. **377–379**, 1066 (1997)

[220] Haiqian Wang and J. G. Hou, O. Takeuchi, Y. Fujisuku, and A. Kawazu,
STM observations of Ag-induced reconstruction of C_{60} *thin films,*
Phys. Rev. B **61**, 2199 (2000)

[221] Oliver Janzen,
Untersuchungen zur Wechselwirkung von Buckminsterfullerenen mit Siliziumoberflächen und zur Grenzflächendotierung von Metall-Silizium-Kontakten mit Buckminsterfullerenen,
Dissertation, Gerhard-Mercator-Universität - Gesamthochschule Duisburg (1999)

[222] Gunnar Schulze, Katharina J. Franke and Jose Ignacio Pascual,
Resonant heating and substrate-mediated cooling of a single C_{60} molecule in a tunnel junction,
New J. Phys. **10**, 065005 (2008)

[223] Lin-Lin Wang and Hai-Ping Cheng,
Density functional study of the adsorption of a C_{60} monolayer on Ag(111) and Au(111) surfaces,
Phys. Rev. B **69**, 165417 (2004)

[224] Mario De Menech, Ulf Saalmann, and Martin E. Garcia,
Energy-resolved STM mapping of C_{60} on metal surfaces: A theoretical study,
Phys. Rev. B **73**, 155407 (2006)

[225] M. Grobis, X. Lu, and M. F. Crommie,
Local electronic properties of a molecular monolayer: C_{60} on Ag(001),
Phys. Rev. B **66**, 161408 (2002)

[226] J. Andreas Larsson, Simon D. Elliott, James C. Greer, Jascha Repp, Gerhard Meyer, and Rolf Allenspach,
Orientation of individual C_{60} molecules adsorbed on Cu(111): Low-temperature scanning tunneling microscopy and density functional calculations,
Phys. Rev. B **77**, 115434 (2008)

[227] A. E. Hanna, M. Tinkham,
Variation of the Coulomb staircase in a two-junction system by fractional electron charge,
Phys. Rev. B **44**, 5919 (1991)

[228] M. Amman, R. Wilkins, E. Ben-Jacob, P. D. Maker, R. C. Jaklevic,
Analytic solution for the current-voltage characteristic of two mesoscopic tunnel junctions coupled in series,
Phys. Rev. B 43, 1146 (1991)

[229] M. Amman, K. Mullen, and E. Ben-Jacob,
The charge-effect transistor,
J. Appl. Phys. **65**, 339 (1989)

[230] H. Hövel, B. Grimm, M. Bödecker, K. Fiefer, and B. Reihl,
Tunneling spectroscopy on silver clusters at T = 5 K: size dependence and spatial anergy shifts,
Surf. Sci. Lett. **463**, L603 (2000)

[231] Matthias Brack,
The physics of simple metal clusters: self-consistent jellium model and semiclassical approaches,
Rev. Mod. Phys. **65**, 677 (1993)

[232] N. W. Ashcroft, N. D. Mermin,
Solid state Physics,
Holt-Saunders, Philadelphia (1976)

[233] Mario De Menech, Ulf Saalmann, and Martin E Garcia,
Recovering hidden electronic states using energy-resolved imaging of metal clusters at surfaces,
New J. Phys. **9**, 340 (2007)

[234] D. C. Ralph, C. T. Black, and M. Tinkham,
Spectroscopic Measurements of Discrete Electronic States in Single Metal Particles,
Phys. Rev. Lett. **74**, 3241 (1995)

[235] Niklas Nilius, Maria Kulawik, Hans-Peter Rust, Hans-Joachim Freund,
Quantization of electronic states in individual oxide-supported silver particles,
Surf. Sci. **572**, 347 (2004)

[236] Niklas Nilius, Maria Kulawik, Hans-Peter Rust, Hans-Joachim Freund,
Erratum to: Quantization of electronic states in individual oxide-supported silver particles,
Surf. Sci. **600**, 3522 (2006)

[237] Heinz Hövel, Ingo Barke,
Morphology and electronic structure of gold clusters on graphite: scanning-tunneling techniques and photoemission,
Prog. Surf. Sci. **81**, 53 (2006)

[238] C.-T. Tzeng, W.-S. Lo and J.-Y. Yuh, R.-Y. Chu, K.-D. Tsuei,
Photoemission, near-edge x-ray-absorption spectroscopy, and low-energy electron-diffraction study of C_{60} on Au(111) surfaces,
Phys. Rev. B **61**, 2263 (2000)

[239] B. W. Hoogenboom, R. Hesper, L. H. Tjeng, and G. A. Sawatzky,
Charge transfer and doping-dependent hybridization of C_{60} on noble metals,
Phys. Rev. B **57**, 11939 (1998)

[240] P. Reinke , H. Feldermann , P. Oelhafen,
C_{60} bonding to graphite and boron nitride surfaces,
J. Chem. Phys. **119**, 12547 (2003)

[241] G. K. Wertheim, S. B. DiCenzo, and S. E. Youngquist,
Unit Charge on Supported Gold Clusters in Photoemission Final State,
Phys. Rev. Lett. **51**, 2310 (1983)

[242] G. K. Wertheim, S. B. DiCenzo, and N. D. E. Buchanan,
Noble- and transition-metal clusters: The d bands of silver and palladium,
Phys. Rev. B **33**, 5384 (1986)

[243] M. G. Mason, L. J. Gerenser, and S.-T. Lee,
Electronic Structure of Catalytic Metal Clusters Studied by X-Ray Photoemission Spectroscopy,
Phys. Rev. Lett. **39**, 288 (1977)

10 PUBLICATIONS

[1] Stefanie Duffe, Thomas Irawan, Markus Bieletzki, Torsten Richter, Benedikt Sieben, Chunrong Yin, Bernd von Issendorff, Michael Moseler, and Heinz Hövel,
Softlanding and STM imaging of Ag_{561} *clusters on a* C_{60} *monolayer,*
Eur. Phys. J. D **45**, 401 (2007).

Abstract:

The low energy deposition of silver cluster cations with 561 (±5) atoms on a cold fullerene covered gold surface has been studied both by scanning tunneling microscopy and molecular dynamics simulation. The special properties of the C_{60}/Au(111) surface result in a noticeable fixation of the clusters without a significant change of the cluster shape. Upon heating to room temperature we observe a flattening or shrinking of the cluster samples due to thermal activation. Similar changes were observed also for mass selected Ag clusters with other sizes. For comparison we also studied Ag islands of similar size, grown by low temperature deposition of Ag atoms and subsequent annealing. A completely different behavior is observed with much broader size distributions and a qualitatively different response to annealing.

[2] Stefanie Duffe, Lukas Patryarcha, Benedikt Sieben, Chunrong Yin, Bernd von Issendorff, Michael Moseler, and Heinz Hövel,
Finite size effect for the penetration of nanoscopic barriers in metal-carbon systems,
submitted for publication

Abstract:

Room temperature (RT) nanostructure stability is of paramount importance for applications in catalysis [3,4], sensors [5] or magnetic recording devises [6]. Metal particles on carbon nanosubstrates are of particular interest [7,8]. Here, a well defined representative is studied. Size selected $Ag_{309\pm3}$ clusters were softlanded on C_{60} films supported on Au(111) and graphite is studied. For one monolayer (ML) C_{60} on Au(111), the Ag clusters shrunk within minutes at RT. Two ML C_{60} on Au(111) or the use of HOPG below one ML C_{60} stabilizes the clusters over days at RT. Supported by atomistic calculations these results reveal a finite-size effect for the penetration of a nanoscopic barrier in which ametal dimmer, still in contact with the metal cluster, gets into the attractive potential of the metal substrate. This lowers the energy barrier for an atom-by-atom cluster decay at RT. Similar effects will be important for other nanosystems in technology or biology.

11 GLOSSARY

12 ACKNOWLEDGMENTS

An dieser Stelle möchte ich mich bei allen bedanken, die zum Erfolg dieser Arbeit beigetragen haben.

Prof. Dr. Metin Tolan danke ich dafür, die Doktorarbeit ebenso wie bereits meine Diplomarbeit an seinem Lehrstuhl anfertigen zu können, und für die Möglichkeit, in der ersten Zeit nach meiner Promotion eine Postdoc-Stelle an seinem Lehrstuhl antreten zu dürfen. Außerdem danke ich ihm für den gelungenen Zusammenhalt der ganzen Gruppe und die gute Lehrstuhlatmosphäre.

Am allermeisten danke ich meinem Betreuer PD Dr. Heinz Hövel. Durch seine freundschaftliche, humorvolle und aufheiternde Art hat er eine Atmosphäre geschaffen, in der ich Tag für Tag sehr gerne gearbeitet habe. Aufgrund seiner enormen Erfahrung und Kompetenz hat er dazu beigetragen, unser Projekt immer weiter nach vorne zu führen. Ich danke ihm, dass er trotz seiner vielfältigen Aufgaben immer ein offenes Ohr hatte und Zeit gefunden hat, bei Problemen und Fragen mit Handgriffen und Ratschlägen im Labor zu helfen und auch aus der Ferne immer erreichbar zu sein. Schließlich danke ich ihm für die Möglichkeit, auf vielen nationalen und internationalen Tagungen unser Projekt präsentieren zu dürfen, die Cluster-Community kennen zu lernen, viele Kontakte zu knüpfen, einen großen Überblick zu bekommen und neue Flecke der Welt kennen zu lernen. Auch danke ich ihm für die Möglichkeit, nach der Promotion eine Postdoc-Stelle am Lehrstuhl E1 zu antreten zu können.

Prof. Dr. Thomas Weis danke ich für die freundliche Bereitschaft, das Zweitgutachten anzufertigen, und das Interesse an meiner Arbeit.

Unseren Kooperationspartnern Prof. Dr. Michael Moseler, Prof. Dr. Bernd von Issendorff und Dr. Chunrong Yin danke ich für die gelungene Zusammenarbeit. Michael Moseler danke ich sehr für die anregenden Gespräche und die Rechnungen, mit deren Hilfe wir den Zerfall der Cluster erklären und deuten konnten. Ohne seine Hilfe wäre hinter vielen Aspekten ein Fragezeichen geblieben. Bernd von Issendorff und Chunrong Yin danke ich für die Hilfe bei technischen und physikalischen Fragen der Clusterstrahlanlage, für die anregenden Diskussionen und für die Freistrahl-Messungen, die uns vor allem helfen werden, wenn wir weitere UPS-Daten von Clustern auf Oberflächen haben.

Dipl.-Phys. Torsten Richter danke ich für seinen unermüdlichen Einsatz und seine enorme Motivation und Tatkraft, mit der er unser Projekt im ersten Jahr meiner Doktorarbeit vorangetrieben hat. Erwähnen möchte ich unter anderem die Ausarbeitung, Konstruktion und den Aufbau des C_{60}-Verdampfers, der mir 3 Jahre lang treue Dienste geleistet hat. Vor allem durch die freundschaftliche Zusammenarbeit und seine unkomplizierte Art haben mir die gute Büroatmosphäre und Zusammenarbeit während des ersten Jahres meiner Doktorarbeit außerordentlich viel Freude bereitet.

Weiterhin danke ich Dipl.-Phys. Benedikt Sieben für die Zusammenarbeit, vor allem für die Konstruktion des Ventils im Massenselektor, die Simulationen zur Cluster-Positionsbestimmung und für viele Anregungen und Ideen.

Bei Dipl.-Phys. Lukas Patryarcha bedanke ich mich für die gute Zusammenarbeit im Labor und seine große Motivation und Einsatzbereitschaft. Vor allem schätze ich sehr seine Ausdauer beim langwierigen Messen der Clusterhöhen. Mit seiner Konstruktion der Stickstoff-Nachfüllautomatik wurde uns das Nachfüllen von Stickstoff am Wochenende erspart.

Außerdem möchte ich mich bei Ben Wortmann bedanken, mit dem ich in der Endphase meiner Doktorarbeit zusammenarbeiten durfte. Besonders danke ich ihm für seine hohe Motivation und seine humorvolle, geduldige Art, mit der er sich auch vor langen Messtagen nicht abschrecken ließ.

Dipl.-Phys. Niklas Grönhagen und Kolja Mende danke ich ebenfalls für die gute und produktive Zusammenarbeit im Labor und freue mich, dass Niklas als mein Nachfolger das Cluster-Projekt weiter vorantreibt.

Ebenfalls bedanke ich mich bei Dr. Farhad Ghaleh für die gute Zusammenarbeit im Labor. Er hat mir oft mit Rat und Tat zur Seite gestanden. Sehr viel Freude haben mir die vielen Fotos seiner Tochter Samansa gemacht.

Auch bei dem Rest der STM-Gruppe – Sabrina Hennes und Stefan Balk– möchte ich mich für die gute Stimmung, die heiteren Gespräche und Anregungen bedanken.

Besonders erwähnen möchte ich Dr. Thomas Irawan, Dipl.-Phys. Markus Bieletzki und Dipl.-Phys. Robert Köster. Mit Ihnen hatte ich die beste und lustigste Zeit in der STM-Gruppe. Die erfolgreiche Zusammenarbeit, die großartige Zeit auf Konferenzen, die außerphysikalischen Treffen und viele lustige Begebenheiten haben uns gute Freunde werden lassen.

Aus der Röntgengruppe möchte ich mich vor allem bei Dipl.-Phys. Martin Schroer, Dipl.-Phys. Christoph Sahle und Dipl.-Phys. Florian Wieland bedanken, die mich beim Zusammenschreiben motiviert haben und die mich in den Schreibpausen sinnvoll abgelenkt und unterhalten haben. Martin Schroer möchte ich außerdem für die oftmals benötigte Hilfe beim Nachfüllen von flüssigem Helium danken.

Manuela Linke und Monika Voits-Besli danke ich für die Hilfe bei allen administrativen Aufgaben, sowie Thorsten Witt und Georg Jülicher für die Hilfe bei technischen Fragen.

Natürlich möchte ich mich bei dem gesamten Lehrstuhl EIa für die großartige Atmosphäre, die Zusammenarbeit und die außerphysikalischen Aktivitäten bedanken.

Herrn Wydinski danke ich für die Bereitstellung von flüssigem und gasförmigem Stickstoff und Helium, vor allem für seine Hilfe, wenn es mal schnell gehen musste.

Bei der mechanischen und elektronischen Werkstatt bedanke ich mich für die Hilfe, die Entwicklung, den Bau und die Reparatur von Geräten und Werkstoffen.

Zuletzt aber nicht weniger möchte ich mich bei meiner Familie bedanken. Meinen Eltern danke ich für ihre großartige Unterstützung, ihre Motivation und die Freude an meiner Arbeit. Auch meinen Schwiegereltern danke ich für ihr offenes Ohr und Ihr Interesse.

Ganz besonders danke ich meinem Mann Sebastian. Mit seiner liebevollen Art hat er mich enorm unterstützt und unsere Freizeit zu einem entspannenden Ausgleich werden lassen. Außerdem danke ich ihm für die fachlichen Diskussionen und für seine Motivation und Aufheiterung in allen Situationen. Besonders möchte ich seine Geduld erwähnen, die er gezeigt hat, wenn ich nach langen Messtagen später nach Hause kam oder wenn am Wochenende Ausflüge zur Uni zum Helium- oder Stickstoff-Nachfüllen mit in unsere Freizeitplanung eingeflossen sind.